

ISTANBUL TECHNICAL UNIVERSITY ★ GRADUATE SCHOOL OF SCIENCE
ENGINEERING AND TECHNOLOGY

**A STUDY ON UPPER ATMOSPHERIC JOULE HEATING USING
OBSERVATIONS AND COUPLED MODELS AND A SPACE WEATHER
CONSEQUENCE: GEOMAGNETICALLY INDUCED CURRENTS**



Ph.D. THESIS

Emine Ceren EYİGÜLER

Department of Meteorological Engineering

Atmospheric Sciences Programme

SEPTEMBER 2018

ISTANBUL TECHNICAL UNIVERSITY ★ GRADUATE SCHOOL OF SCIENCE
ENGINEERING AND TECHNOLOGY

**A STUDY ON UPPER ATMOSPHERIC JOULE HEATING USING
OBSERVATIONS AND COUPLED MODELS AND A SPACE WEATHER
CONSEQUENCE: GEOMAGNETICALLY INDUCED CURRENTS**

Ph.D. THESIS

Emine Ceren EYİGÜLER
(511092008)

Department of Meteorological Engineering

Atmospheric Sciences Programme

Thesis Advisor: Prof. Dr. Zerefşan KAYMAZ

SEPTEMBER 2018

İSTANBUL TEKNİK ÜNİVERSİTESİ ★ FEN BİLİMLERİ ENSTİTÜSÜ

**YUKARI ATMOSFER JOULE ISINMASININ GÖZLEM VE UZAY HAVASI
MODELLERİ KULLANARAK KAPSAMLI İNCELENMESİ VE BİR UZAY
HAVASI UYGULAMASI: JEOMANYETİK AKIMLAR**

DOKTORA TEZİ

**Emine Ceren EYİĞÜLER
(511092008)**

Meteoroloji Mühendisliği Anabilim Dalı

Atmosfer Bilimleri Programı

Tez Danışmanı: Prof. Dr. Zerefşan KAYMAZ

EYLÜL 2018

Emine Ceren EYİGÜLER, a Ph.D. student of İTÜ Graduate School of Science Engineering and Technology student ID 511092008, successfully defended the thesis entitled “A STUDY ON UPPER ATMOSPHERIC JOULE HEATING USING OBSERVATIONS AND COUPLED MODELS AND A SPACE WEATHER CONSEQUENCE: GEOMAGNETICALLY INDUCED CURRENTS”, which she prepared after fulfilling the requirements specified in the associated legislations, before the jury whose signatures are below.

Thesis Advisor : **Prof. Dr. Zerefşan KAYMAZ**
İstanbul Technical University

Jury Members : **Prof. Dr. Sema TOPÇU**
İstanbul Technical University

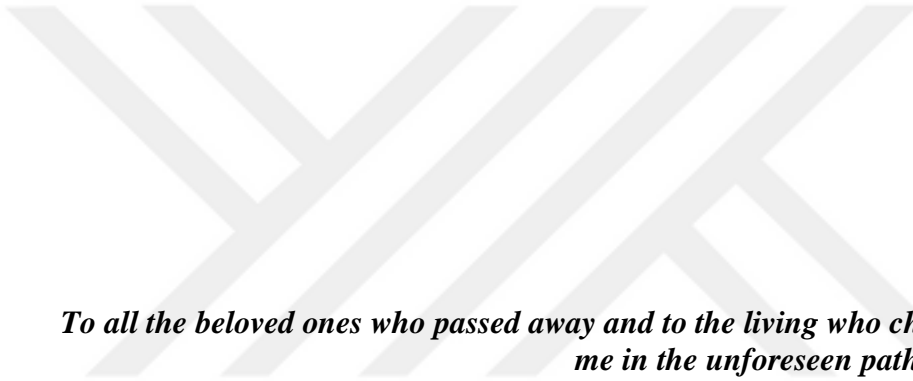
Prof. Dr. Zafer ASLAN
İstanbul Aydın University

Prof. Dr. Kasım KOÇAK
Istanbul Technical University

Dr. Maria M. KUZNETSOVA
NASA/GSFC Space Weather Lab.

Date of Submission : 26 July 2018
Date of Defense: 17 September 2018





To all the beloved ones who passed away and to the living who chose to walk with me in the unforeseen pathways of this life,



FOREWORD

This work is a comprehensive study of the variations at thermospheric altitudes and ground level during geomagnetically disturbed time intervals. Our effort to understand how the interactions between the magnetosphere-ionosphere-thermosphere domains occur and how they project themselves on the ground has been cumbersome at times, but it has always been exciting and full of ambition.

My advisor, Prof. Zerefşan Kaymaz, not only provided me lots of opportunities since the year we started working, 2005, but also let my ability to independently work grow throughout the process. I have been lucky enough to be a part of the team who worked on the expansion of Upper Atmosphere and Space Weather Laboratory which is one of the first of its kind in Turkey on upper atmosphere and space weather. During the years, we built two Sudden Ionospheric Disturbance (SID) antennas, setup an ionosonde and a magnetotelluric station and began tracking geomagnetic disturbances and sunspots with our own observations and measurements. We additionally started to run some space weather models in our lab. Even though the abovementioned are, themselves, specific study areas, being a part of the teams working on the instrument setups opened up new realms for me; expanded my vision and perception in our field of study and created fresh ideas in my mind to explore as future works. I am always grateful to my advisor for being such a compassionate, supportive and caring person throughout my growing up process.

During the years I have been at ITU, which roughly is half of my life now (2002-2018), I had many gains and losses. My gains are my friends and experiences. My losses are members of my family whom I was deeply attached to. I believe that it is a blessing to have had the chance to spend time for quiet a period of time together with all the people who had been in my life. I will always remember my grandmothers lovingly and my grandfather with smiles. I thank especially my parents, Vedat and Emine Kalafatoğlu, for letting be myself. My father was an exceptional man. He knew about people, analyzed situations, was always solution-oriented and had no girl-boy favoritism. I will always miss him deeply. His words and kind soul remain still alive in my mind and heart. My mother, thank to God she is still here, was and is always supportive of me and helped me when I am really in need. I am grateful to the free and nonjudgmental environment they provided for me. My husband, Ahmet Eyigüler; he always knows how to calm me down. I always felt his continuous support and love throughout my thesis study. Thank you for entering my life. I also would like to thank to my daughter Bilge Filiz who already started to teach and remind me of valuable life lessons. I am blessed to have relatives who were with me during the difficult times of my life. All of my uncles and their wives; especially, Ahmet Baki Akkartal, Sevil Akkartal, Bilgehan Akkartal, Hanife Akkartal, Turhan Akkartal and İnci Akkartal, my cousins: Fatma Cihan and İlker Akkartal: you are precious. I also want to thank to my eldest uncle Mustafa Akkartal for his support and intellectual discussions during the previous years. My friends, Deniz Bilgili, Zeynep Oral Savkurt, Attila Yalazkan, Mert Dalokay; you were always there for me. I cannot share every moment of kindness and amity here: we have a page limit. Not to forget my colleagues, who actually are not only colleagues but are also like my siblings, Filiz Türk Katırcıoğlu, İklim Gençtürk Akay,

Özlem Baydarođlu, Ceyhan Kahya, Sedef akır, Filiz Bektař, Dođa Can Su Öztürk and my lab brothers, Yiđit ay and Necmi Cihan Örger: you made my days full of joy and made my coming to work a pleasure.

I thank Prof. Sema Topçu and Prof. Zafer Aslan for their valuable comments, continuous support and encouragement throughout the stages of this work.

During the years, I also had the chance to attend many conferences (AGU, EGU, AOGS, ATMOS, AIAA, UHUK) and meetings (GEM, CEDAR) as well as NSF supported summer schools such as the Center for Integrated Space Weather Modeling Summer School, Heliophysics Summer School, Space Weather Research, Education, Development Initiative Summer School (SW-REDI). Here, I must mention that GEM and CEDAR meetings hold a special place for me. By means of these meetings, I had the opportunity to attend many valuable talks as well as seeing beloved friends regularly. Thus, I must emphasize the importance of these meetings for our space physics community. I want to state that I also met very special people during my stay in USA and work at NASA. First of all, Maria M. Kuznetsova, with her welcoming nature, she was always a great mentor for me. She helped me to stay focused and gave valuable insights on our research. Secondly, Ja Soon Shim, her positive attitude always made my mood rise. It was a privelege to have the chance to work with both Masha and Ja Soon. I am also thankful to Antti Pulkkinen who provided me with valuable feedback on our geomagnetically induced current studies at the very initial stages of our work. Elsayed Talaat was there whenever we were in need and saved the day. Things would have been more difficult unless he was there. Speaking of USA, NASA, meetings and Maryland, David G. Sibeck and Ray Lin cannot be forgotten. They were so nice to gently introduce us the environment. Not only they informed us of places, what to do, how to do but they also integrated us to their weekend activity team. It was a great pleasure to have shared such wonderful times with them.

Lastly, we are grateful to the data providers and open access data repositories, Space Physics Interactive Data Resource (SPIDR), World Data Center (WDC), Kyoto, NASA Coordinated Data Analysis Web (CDAWEB), Satellite Situation Center Web (SSCWEB). Our research could not have been done without them. We are also thankful to our collaborators. Their experience and perspectives provided us valuable feedback. NASA/Space Weather Laboratory/Community Coordinated Modeling Center (CCMC) has been one of our main collaborators. Being able to run simulations from CCMC computers quickened this research. Additionally, our close collaboration with the Super Dual Auroral Radar Network (SuperDARN) team at Virginia Tech made one of the major outputs of this thesis possible. Throughout the study years, our work was supported by numerous agencies: TÜBİTAK (The Scientific and Technological Research Council of Turkey) by projects 109Y058, 113Y213, 2214-A; TUJJB-TUMEHAP (Turkish National Geodesy and Geophysics Union-Turkish National Meteorological and Hydrological Disaster Programme) by project number 01-12; and lastly ITU-BAP (Istanbul Technical University-Scientific Research Programme). We thank them for their support.

September 2018

Emine Ceren EYİĞÜLER
M.Sc., Researcher

TABLE OF CONTENTS

FOREWORD	ix
TABLE OF CONTENTS	xi
ABBREVIATIONS	xiii
SYMBOLS	xv
LIST OF TABLES	xvii
LIST OF FIGURES	xix
SUMMARY	xxiii
ÖZET	xxvii
1. INTRODUCTION	1
1.1 Purpose of the Thesis	3
1.2 Structure of the Thesis	4
1.3 Solar Wind-Magnetosphere Interaction on Average	5
1.4 Magnetosphere-Ionosphere-Thermosphere Coupling	7
1.5 Geomagnetic Activity and Its Effects in the Near-Earth Space Environment ...	9
2. LITERATURE REVIEW	13
2.1 Upper Atmospheric Joule Heating	13
2.2 Joule Heating Effects on Thermospheric Neutral Density	19
2.3 Thermospheric Neutral Density Variations	20
2.4 Geomagnetically Induced Currents	22
3. DATA	27
3.1 Super Dual Auroral Radar Network (SuperDARN)	27
3.2 Challenging Mini Satellite Payload (CHAMP)	28
4. MODELS	29
4.1 Magnetohydrodynamic (MHD) Models: SWMF/BATSRUS	29
4.2 Physics-based Models of the Ionosphere-Thermosphere	30
4.2.1 Thermosphere Ionosphere Electrodynamics General Circulation Model (TIEGCM)	30
4.2.2 Coupled Thermosphere Ionosphere Plasmasphere Electrodynamics (CTIPe)	31
4.2.3 Global-Ionosphere-Thermosphere Model (GITM)	31
4.3 Empirical Models of the Ionosphere and Thermosphere	32
4.3.1 Weimer model: Weimer05	32
4.3.2 International Reference Ionosphere-2012: IRI2012	32
4.3.3 Mass Spectrometer and Incoherent Scatter Radar Exosphere (NRLMSISE- 00)	33
4.3.4 Jacchia-Bowman 2008: JB2008	33
4.3.5 OVATION Prime	33
4.4 Inputs to Models	34
5. UPPER ATMOSPHERIC JOULE HEATING	35
5.1 Selected Substorm Cases	35
5.2 Indice-based Methods	37

5.3 New Combinative Methods	39
5.4 Methods with the Neutral Wind.....	41
5.5 Detailed Analysis on March 8, 2008 Substorm Cases	42
5.5.1 Temporal variations	43
5.5.2 Substorm phase dependence	46
5.5.3 Spatial distribution	48
5.5.4 MLT and Magnetic latitude dependence	51
5.5.5 Role of conductance and electric fields.....	55
5.5.6 Role of the neutral wind	59
5.6 Discussion on Joule Heating Variability	61
6. NEUTRAL DENSITY VARIABILITY	73
6.1 Orbit Averaging Tool (OAT).....	77
6.2 Baseline Shifting Tool (BAST)	79
6.3 Performance Assessment Tool (PAT).....	85
6.4 Characteristics of the Thermospheric Neutral Density from the Models Before the Shifts	87
6.5 Demonstration of the Methods: A Case Example	89
6.6 Evaluation of the Model Performances	91
6.7 Discussion on the Performances of the Methods.....	98
7. ON THE RELATION BETWEEN JOULE HEATING AND NEUTRAL DENSITY	101
7.1 Relation between the Instantaneous JH and Neutral Density	102
7.2 Storm-time Relation Between the JH and Neutral Density.....	104
7.3 Relation Between the Integrated JH and Neutral Density.....	106
7.4 Discussion on the relation between JH and neutral density	107
8. FIELD WORK.....	109
8.1 Magnetotelluric Measurements in Bozcaada.....	109
8.2 Event Selection and Data Preparation.....	112
8.3 Case Examples	118
8.4 Discussion on the Geomagnetically Induced Currents at Mid-Latitudes.....	143
9. CONCLUSION AND FUTURE RESEARCH.....	149
9.1 Thesis Summary and Conclusions	149
9.2 Future Work and Recommendations.....	153
REFERENCES	155
APPENDICES	177
CURRICULUM VITAE.....	185

ABBREVIATIONS

ACE	:	Advanced Composition Explorer spacecraft
AE	:	Auroral electrojet index
BATSRUS (SWMF)	:	Space Weather Modeling Framework / Block-Adaptive-Tree-Solarwind-Roe-Upwind-Scheme
BB (BB_{crmc})	:	BATSRUS/CRCM conductances + BATSRUS/CRCM ionospheric electric field
BB_{rcm}	:	BATSRUS/RCM conductances + ionospheric electric field
BB_{nw_crm}	:	BATSRUS/CRCM conductances + BATSRUS/CRCM horizontal ionospheric current
BB_{nw_rcm}	:	BATSRUS/RCM conductances and BATSRUS/RCM horizontal ionospheric current
BCRCM	:	BATSRUS coupled with Comprehensive Ring Current Model
BRCM	:	BATSRUS coupled with Rice Convection Model
BS	:	BATSRUS/CRCM conductances + SuperDARN ionospheric electric field
CCMC	:	Community Coordinated Modeling Center
CDAWEB	:	Coordinated Data Analysis Web
CHAMP	:	Challenging Mini Satellite Payload spacecraft
CME	:	Coronal Mass Ejection
CPCP	:	Cross Polar Cap Potential
CRCM	:	Comprehensive Ring Current Model
CTIPe	:	Coupled Thermosphere-Ionosphere-Plasmasphere model
DMSP	:	Defense Meteorological Satellite Program
Dst	:	Disturbance storm-time index
EISCAT	:	European Incoherent Scatter Radar
ESA	:	European Space Agency
FAC	:	Field-aligned currents
GIC	:	Geomagnetically induced currents
GITM	:	Global Ionosphere-Thermosphere Electrodynamics model
GSWM	:	Global Scale Wave Model
GUMICS	:	Grand-Unified Magnetosphere-Ionosphere Coupling Simulation
HP	:	Hemispheric Power
HSS	:	High Speed Stream
HWM93	:	Horizontal Wind Model 93
IB_{rcm,crmc}	:	IRI2012 conductances + BATSRUS (RCM/CRCM) model ionospheric electric field
IE	:	Ionospheric Electrodynamics
IL	:	IMAGE magnetometer electrojet index
IMF	:	Interplanetary Magnetic Field

IRI	:	International Reference Ionosphere
IS	:	Joule heating method with IRI2012 conductances and SuperDARN ionospheric electric field
ISS	:	International Space Station
iSWA	:	Integrated Space Weather Analysis
JB-2008	:	Jacchia-Bowman 2008 thermosphere model
JH	:	Joule heating
JH_{nw}	:	Neutral wind contribution to Joule heating
KP	:	Kenziffer index
LEMI	:	Laboratory for Electromagnetic Innovation
LFM	:	Lyon-Feddery-Mobarry model
MFI	:	Magnetic Field instrument
MLT	:	Magnetic Local Time
NASA	:	National Aeronautics and Space Administration
NCAR-HAO	:	National Center for Atmospheric Research- High Altitude Observatory
NOAA	:	National Oceanic and Atmospheric Administration
NRLMSISE-00 (MSIS)	:	Naval Research Laboratory Mass Spectrometer and Incoherent Scatter Radar Exosphere
OB	:	OVATION Prime conductances + BATSRUS model ionospheric electric field
OS	:	OVATION Prime conductances + SuperDARN ionospheric electric field
OIB	:	OVATION Prime+IRI1012 conductances + BATSRUS model ionospheric electric field
OIS	:	OVATION Prime+IRI1012 conductances + SuperDARN model ionospheric electric field
OP	:	OVATION Prime
OpenGGCM	:	Open Geospace General Circulation model
OPI	:	OVATION Prime + IRI-2012 conductances
POES	:	Polar-orbiting Operational Environmental Satellite
RCM	:	Rice Convection Model
SC	:	Sudden Commencement
SI	:	Sudden Impulse
Sq	:	Solar quiet current
SP	:	Polar spacecraft conductances + SuperDARN electric field
SSCWEB	:	Satellite Situation Center Web
SuperDARN	:	Super Dual Auroral Network
SWE	:	Solar Wind Experiment
TIEGCM	:	Thermosphere-Ionosphere-Electrodynamics General Circulation Model
UT	:	Universal Time
WDC	:	World Data Center
W05	:	Weimer 2005 model

SYMBOLS

a_p	: Equivalent range (geomagnetic) index
B_x, B_y, B_z	: x, y, z components of the Earth's magnetic field
E_{\perp}	: Ionospheric electric field
E, E_x, E_y	: Geoelectric field of the Earth; north-south and east-west components
F10.7	: Solar indice: Solar radio flux at 10.7 cm (2800 MHz)
F10.7A	: 3-month average of F10.7
H	: Horizontal component of the Earth's magnetic field
$J, J_{\perp}, J_{//}$: Total ionospheric current, horizontal ionospheric current field-aligned currents
M10.7	: Solar indice which is a measure of chromospheric and some photospheric solar active region activity that uses Mg II solar emissions in mid-ultraviolet wavelengths (~280 nm)
P_{dyn}	: Dynamic pressure of the solar wind
Q_j	: Local Joule heating
R_e	: Earth's radius
S10.7	: Solar indice, which is derived from solar emission between 26 and 34 nm
U_i, U_n	: Zonal component of the velocity for ions and neutrals
V_i, V_n	: Meridional component of the velocity for ions and neutrals
Y10.7	: Solar indice, which is a mix of X10 (flare component removed GOES X-ray Spectrometer measurements) and Lyman- α measurements.
σ_P	: Pedersen conductivity
σ_H	: Hall conductivity
σ_C	: Cowling conductivity
Σ_P	: Height-integrated Pedersen conductivity
Φ	: Ionospheric Potential field



LIST OF TABLES

	<u>Page</u>
Table 4.1 : Inputs to the ionosphere-thermosphere models.....	34
Table 5.1 : Summary of the methods for JH based on geomagnetic indices.	38
Table 5.2 : Summary of the methods for JH without the neutral wind.	39
Table 5.3 : Methods to determine the neutral wind contribution and the resultant Joule heating.....	42
Table 5.4 : The amount of JH due to the dayside and nightside conductances (%). .	56
Table 5.5 : Average ratios of JH obtained from the methods with respect to substorm phases (G: growth, E: expansion, R: recovery, F: full interval).....	57
Table 5.6 : Average ratios of JH: BB_{crem}/BS and BB_{crem}/OIS when SuperDARN has data in the midnight sector.	57
Table 6.1 : GEM-CEDAR Challenge events. Table shows the maximum values of geomagnetic and solar indices (KPmax, F10.7, Dstmax, HPmax), solar wind sources of the events and quiet and disturbed intervals.	75
Table 6.2 : Model runs at the CCMC for each event.	76
Table 6.3 : Baseline shifts. ρ_{old} is the original orbit-averaged time series whereas ρ_{new} is the baseline shifted time series.	80
Table 6.4 : Shift amounts for S1 and S2 (kg/m^3).....	84
Table 7.1 : Properties of the correlation between model JH and CHAMP neutral density.....	105
Table 8.1 : Selected events and corresponding maximum KP, Dst and AE index during the period of ground level fluctuations.	113
Table 8.2 : Average characteristics of magnetic and electric field fluctuations measured at Bozcaada station at the time of the maximum time derivative of magnetic field components during geomagnetic disturbances.....	145
Table 8.3 : Solar wind plasma and IMF data at the CME shock corresponding to the large amplitude ground level magnetic and electric field fluctuations at the time of the sudden commencement or the magnetospheric compression.....	147



LIST OF FIGURES

	<u>Page</u>
Figure 1.1 : Solar wind and the Earth's magnetosphere (Url-1).....	5
Figure 1.2 : a) Magnetosphere and the current systems (Russell, 2007) b) Layers of the atmosphere and their classifications (Dieminger et al., 1996).	6
Figure 1.3 : a) Region-1 currents (shown in red) b) Region-2 currents and partial ring current (purple) and the banana current (orange) (Ganushkina et al., 2018).....	7
Figure 1.4 : Ionospheric convection driven by the solar wind (Cowley, 1996).	8
Figure 1.5 : Diagram showing the means of interaction and mechanisms in the ionosphere (reproduced from Kamide et al., 1993).....	8
Figure 1.6 : Energy sources and sinks in the IT system (Forbes, 2007).	9
Figure 1.7 : Geomagnetic storm effects in space, Earth's atmosphere and on the ground level.....	10
Figure 1.8 : Dst variation during geomagnetically active and disturbed intervals.	11
Figure 1.9 : The variation of the AU and AL components of the AE index during a substorm (McPherron, 1995).....	11
Figure 3.1 : The SuperDARN radar locations in a) Northern b) Southern hemispheres (Url-2).	27
Figure 5.1 : Top five panels: IMF and solar wind upstream data in GSM coordinates from ACE spacecraft. Bottom two panels: Epsilon parameter and geomagnetic indices (AU/AL, AE, KP, Dst).	36
Figure 5.2 : Epsilon and Joule heating from the methods.....	44
Figure 5.3 : JH from the Methods a) averaged over the substorm phases b) integrated over the substorm phases.	47
Figure 5.4 : Spatial distribution of JH and associated parameters at 18:20 UT.	49
Figure 5.5 : Variation in maximum Joule heating with a) MLT, b) Magnetic Latitude (MLat) and c) the distribution of JH maxima in MLT vs MLat.....	52
Figure 5.6 : Magnetic sector dependence of JH. a) evaluation with respect to methods (OIB, OIS, BS, BB _{crim}) b) evaluation with respect to the magnetic local time sectors.	54
Figure 5.7 : Comparison of JH, Pedersen conductance and CPCP.	56
Figure 5.8 : JH with neutral wind, without neutral wind and neutral wind effect. Top: BCRCM, bottom: BRCM results.	59
Figure 5.9 : Joule heating from BCRCM and BRCM with and without the neutral wind.	60
Figure 5.10 : Neutral wind contribution to JH for March 8, 2008 substorms.	61
Figure 5.11 : Comparisons of the JH estimations from different combinative methods which use BCRCM and BRCM outputs.	63
Figure 6.1 : Differences in orbit-averaged neutral densities in two consecutive orbits on quiet day cases.	74
Figure 6.2 : KP and Dst variations during the GEM-CEDAR storm intervals.	74

Figure 6.3 : CHAMP satellite daily orbital parameters.....	77
Figure 6.4 : Neutral density estimates from different models and the observations from CHAMP during the December 13, 2006 storm.	78
Figure 6.5 : Orbit-averaged neutral densities from the models and CHAMP as a product of the OAT.	79
Figure 6.6 : An example of climatological baseline shift for 2006-348 event.	82
Figure 6.7 : Generated background series for 2006-348 event.....	85
Figure 6.8 : From left to right: storm-time maximum in neutral density, storm-time average neutral density, timing difference between the peak of models and M2017 (without shift).	88
Figure 6.9 : An example event: 2006-348. First row, from left to right: a) top: Neutral density from the model and observations without shift; below: KP and Dst indices, neutral density estimations from the models and M2017 after b) S1, c) S2, d) S3. Second row, from left to right: e) Background series for the persistent method, neutral density estimations from the methods and M2017 after f) S4, g) S5, h) S6.	90
Figure 6.10 : Skill scores. From left to right: storm-time ratio of maximum neutral density of the models to M2017, storm-time ratio of average neutral density from the models to M2017, timing difference between the peak of models and M2017. From top to bottom: SV2.3, MSIS, JB2008, TIEGCM, CTIPe, GITM.	92
Figure 6.11 : From top to bottom: storm-time orbit and time integrated neutral density, storm-time change in maximum neutral density, storm-time change in mean neutral density.	94
Figure 6.12 : Skill scores: From left to right: MAE, NRMSE, PE. KP scales, axis labels, colors and symbols are the same as Figure 6.10.....	97
Figure 7.1 : Temporal variation of neutral density from CHAMP, TIEGCM and CTIPe and superposed JH from TIEGCM and CTIPe (2006-348) a) before the time shift, b) after the time shift c) time delays.....	103
Figure 7.2 : Correlation between the JH from the models and neutral density estimations a) TIEGCM and CHAMP b) CTIPe and CHAMP.	103
Figure 7.3 : Storm-time correlation between the JH and neutral density for all events.	105
Figure 7.4 : Integrated storm-time neutral density response from models and CHAMP for GEM-CEDAR events vs. integrated JH from IT models. From left to right: a) TIEGCM and CHAMP b) CTIPe and CHAMP. .	106
Figure 8.1 : (a) A map of the region and island Bozcaada, Çanakkale, Turkey, where the instruments were installed. (b) Plan of the instrumental set up in the field. (c) Instruments that came with magnetotelluric station; (1) Magnetometer, (2) GPS receiver, (3) Electrometer, (4) Electrodes, (5) Station, (6) An example of raw data.....	110
Figure 8.2 : Number of events between September 2013 and September 2014 according to KP index.	112
Figure 8.3 : Example of variations in B_x , B_y , B_z , E_x and E_y from top to bottom for a quiet day: October 6, 2013. The last panel gives the geomagnetic activity indices: KP on the left, Dst and AE on the right.....	115
Figure 8.4 : Magnetic and electric field measurements for April 20, 2014, a sudden commencement event with substorm scale geomagnetic activity. From top to bottom: variations in B_x , B_y , B_z , E_x and E_y , and geomagnetic activity indices: KP on the left, Dst and AE on the right.	119

Figure 8.5 : North-south and east-west components of the magnetic field (top panels), dB/dt (second panels), associated electric field variations (third panels) during the geomagnetic activity and geomagnetic activity indices on April 20, 2014. From the top, B_x , dB_x/dt , E_y , and activity indices (KP, Dst and AE) are on the left panels, and B_y , dB_y/dt , E_x and activity indices (KP, Dst and AE) are on the right panels.....	120
Figure 8.6 : Magnetic field deviations from the background, ΔB_x (left) and ΔB_y (right). (Bottom): Electric field deviations from the best fit curves for electric field components given in Figure 8.4, ΔE_y (left) and ΔE_x (right).	123
Figure 8.7 : Magnetic field and electric field variations during the April 20, 2014 sudden commencement event for an expanded interval. On the top: the variations between north-south component of magnetic field, B_x (left), and east west component of electric field, E_y (right). On the bottom: the variations between the east-west component of magnetic field, B_y (left), and north-south component of electric field, E_x (right).	124
Figure 8.8 : Electric field variations in the east-west (E_y) and north-south (E_x) components during the April 20, 2014 sudden commencement event for the expanded period.	125
Figure 8.9 : Variations of the horizontal component of geoelectric field and the derivative of the horizontal component of the geomagnetic field for April, 20, 2014 event.	126
Figure 8.10 : IMF and solar wind parameters for April 20, 2014 event. From top to bottom: Interplanetary magnetic field (IMF B, IMF B_z), solar wind density, solar wind velocity, solar wind temperature, solar wind dynamic pressure, and horizontal components of the electric field and magnetic field given along with the AE index.	127
Figure 8.11 : Magnetic and electric field measurements extending from October 8 to 11, 2013 during weak-to-moderately disturbed geomagnetic activity. From top to bottom: variations in B_x , B_y , B_z , E_x and E_y , and geomagnetic activity indices: KP on the left, Dst and AE on the right.....	131
Figure 8.12 : North-south and east-west components of the magnetic field (top panels), dB/dt (second panels), and associated electric field variations (third panels) during the geomagnetic activity on October 8, 2013. From the top, B_x , dB_x/dt , E_y , and activity indices (KP, Dst and AE) are on the left panels, and B_y , dB_y/dt , E_x and activity indices (KP, Dst and AE) are on the right panels.....	132
Figure 8.13 : Electric field variations in the east-west (E_y) and north-south (E_x) components during the October 8, 2013 sudden commencement event for an expanded interval.	134
Figure 8.14 : IMF and solar wind parameters for October 8, 2013 event. From top to bottom: Interplanetary magnetic field (IMF B, IMF B_z), solar wind density, solar wind velocity, solar wind temperature, solar wind dynamic pressure, and horizontal components of the electric field and magnetic field given along with the AE index.	135
Figure 8.15 : Magnetic and electric field measurements from June 7 to June 9, 2014 during a weak geomagnetic storm. From top to bottom: variations in B_x , B_y , B_z , E_x and E_y , and geomagnetic activity indices: KP on the left, Dst and AE on the right.	137

Figure 8.16 : North-south and east-west components of the magnetic field (top panels), dB/dt (second panels), and associated electric field variations (third panels) during the geomagnetic activity on June 8, 2014. From the top, B_x , dB_x/dt , E_y , and activity indices (KP, Dst and AE) are on the left panels, and B_y , dB_y/dt , E_x and activity indices (KP, Dst and AE) are on the right panels.	138
Figure 8.17 : Magnetic field deviations from the background, ΔB_x (left) and ΔB_y (right). (Bottom): Electric field deviations from the best fit curves for electric field components given in Figure 8.13, ΔE_y (left) and ΔE_x (right).	140
Figure 8.18 : IMF and solar wind parameters for June 8, 2014 event. From top to bottom: Interplanetary magnetic field (IMF B , IMF B_z), solar wind density, solar wind velocity, solar wind temperature, solar wind dynamic pressure, and horizontal components of the electric field and magnetic field given along with the AE index.....	142
Figure A.1 : Baseline shifts: 2005-135.....	178
Figure A.2 : Baseline shifts: 2005-190.....	178
Figure A.3 : Baseline shifts: 2005-243.....	178
Figure A.4 : Baseline shifts: 2007-142.....	179
Figure A.5 : Baseline shifts: 2007-91.....	179
Figure B.1 : Temporal shifts for the GEM-CEDAR events. From left to right; Top: 2005-135 and 2005-190; Middle: 2005-243 and 2007-142 Bottom: 2007-91 and 2006-348.....	171
Figure C.1 : B_x , E_y and B_y , E_x . Top: October 8, 2013, bottom: June 8, 2014.	172
Figure C.2 : E and dH/dt . Top: October 8, 2013, bottom: June 8, 2014.	173
Figure C.3 : E_x and E_y . Top: October 8, 2013, bottom: June 8, 2014.	174

A STUDY ON UPPER ATMOSPHERIC JOULE HEATING USING OBSERVATIONS AND COUPLED MODELS AND A SPACE WEATHER CONSEQUENCE: GEOMAGNETICALLY INDUCED CURRENTS

SUMMARY

Space weather has immediate consequences on today's space borne and ground-based technological infrastructure. In the long term, it, as well, affects the health of the aircrew on aircraft and astronauts on space missions. Thus, it is essential to quantify the extent and limits of space weather effects on Earth and near-Earth space environment. In this work, we study the space weather effects on the upper atmosphere and ground level during geomagnetically disturbed time intervals. Following, this thesis comprises three main parts: 1) investigation and comparison of different methods and data that were separately used and presented for JH in previous studies in the literature, 2) thermospheric neutral density variations that occur in response to the elevated temperatures during geomagnetic storms and substorms, 3) detection and initial quantification of low to mid-latitude geomagnetically induced currents using a magnetotelluric station located at Bozcaada, Çanakkale (in geographic coordinates: 37.5°N, 106°E).

JH is the frictional heating that arises from the collisions between the neutrals and ions in the ionospheric levels. Thus, it is crucial to have exact information on both species to be able to calculate JH precisely. Its exact determination depends on the simultaneous knowledge of the ionospheric electric fields, conductances, thermospheric neutral wind and ambient magnetic fields or in a second approach, conductances, ion drifts and neutral wind at the high latitudes. Previously, some studies were also conducted by assuming that the neutral wind contribution is negligible.

In our study, we investigate the JH with and without the neutral wind effects. For the calculations not involving the neutral wind, we get use of combinative methods. Electric field data from radars and an MHD model and conductance data from ionospheric electrodynamics (IE) module of an MHD model and an empirical model are combined interchangeably to calculate the JH. The most used indice-based methods are also investigated. Our aim is to present the alternative methods that give the best estimate for the JH rate in the absence of the global observations of the parameters needed for the calculation. Observational electric field data comes from Super Dual Auroral Radar Network (SuperDARN) radars and MHD model output is from the Space Weather Modeling Framework/Block-Adaptive-Tree-Solarwind-Roe-Upwind-Scheme (SWMF/BATSRUS, hereafter will be referred to as BATSRUS) model, whereas the conductances come from BATSRUS-IE and OVATION Prime + International Reference Ionosphere 2012 (IRI2012) models. For the calculations without the neutral wind, we find that with respect to the variations in Akasofu's Epsilon parameter, all combinative methods show a time lag varying between 10 to 20 minutes for the peak JH. However, the proxy method, which is based on the AE index,

shows the maximum time lag, which varies between 20 minutes to 1.5 hour. Qualitatively, all methods exhibit similar variations. AE proxies show the highest rate of JH while the combinations with International Reference Ionosphere 2012 (IRI2012) conductances result in the lowest. The differences between the combinations with SuperDARN and BATSRUS electric fields are the smallest when SuperDARN has data in the midnight sector.

In the second part of this thesis, we investigate the neutral density estimations from the empirical and physics-based IT models for GEM-CEDAR challenge events. We quantify the amount of errors using the neutral density observations from the Challenging Minisatellite Payload (CHAMP) satellite. We show that coupled ionosphere-thermosphere models and empirical models of the ionosphere give different neutral density climatologies and responses during geomagnetic storms. The storm effects are found as superimposed on the climatology. A performance assessment solely on the neutral density maxima leads to misleading performance assessments. A model overestimating the climatology but underestimating the storm-time response might well end up with a good performance record. Real time estimation of the atmospheric drag heavily relies on estimating the storm-time responses right. Following, we apply several techniques to separate the model climatology and storm-time response of the thermosphere from each other. Baselines for the thermospheric neutral densities are determined using the quiet periods preceding geomagnetic storms for both the CHAMP observations and the models. The data were shifted to baseline levels and effects due to the magnetic storm could be extracted. We obtain increases in skill scores up to 113% for the models, which differ from the quiet time climatology. Physics-based model neutral density variations show similar tendencies with CHAMP data. Physics-based models perform the worst for the low KP events, whereas they perform better for high KP events. Either CME or CIR induced, physics-based model results capture the variations in neutral densities very sufficiently. Empirical models are good in capturing the climatology and the baseline shifts do not affect the storm-time response considerably. However, despite attaining close values to the neutral density peaks, the shapes of the response curves are substantially different. For real time calculations of the satellite drag, we suggest using ensemble approach and background removal methods together to obtain reliable neutral density estimates. Furthermore, using the baseline shift method, we investigate the relationship between Joule heating and storm-time neutral density variations. A simple model using linear regression method is constructed by relating the JH estimations of the physics-based models of the thermosphere with CHAMP satellite neutral density observations.

In the last part of our work, we study the magnetic and electric field characteristics of the GICs at mid-latitudes using electric field and magnetic field observations in Turkey during the geomagnetically active intervals. A magnetotelluric station consisting of an electrometer and a magnetometer were set up in Bozcaada, Çanakkale (37.5°N, 106°E). Several cases that show large electric and magnetic field fluctuations during geomagnetic disturbances are selected. The effects of geomagnetic activity are studied using the time derivatives of horizontal component of the magnetic field and the deviations in the magnetic and electric field components from the quiet background. In magnetic field data, quiet day S_q variations are removed using cubic spline fits. Similarly, the magnitude of the deviations in the electric field are determined by subtracting the background electric field determined by using cubic spline. Corresponding to the strong geomagnetic activity identified using KP and Dst indices, high frequency, strong fluctuations in the magnetic field, its derivatives, and electric

field are observed. These fluctuations in horizontal magnetic and electric field are compared with those seen during a magnetically quiet day. The close association between the fluctuations of the time derivatives of the horizontal magnetic field and electric field components are demonstrated. Two types of variations in the electric and magnetic fields corresponding to the different phases of the geomagnetic activity are identified: those corresponding to the initial phase including the sudden commencement and those to the main phase of the geomagnetic storm. The fluctuations in both magnetic field and electric field corresponding to the sudden commencement and the initial phase indicate the effects of magnetopause currents driven by the large solar wind dynamic pressure as associated with the coronal mass ejection (CME) events. Each event shows increased levels of ground level magnetic and electric field fluctuations corresponding to the CME compression at the subsolar magnetopause. High frequency, large fluctuations continue subsequently during the main phase in the presence of the geomagnetic storms. GIC occurrences in our latitudes are shown to be associated with the sudden commencement and main phase of the geomagnetic storm activity.

To conclude, in this thesis, we analyse our current capabilities of estimating the thermospheric Joule heating and neutral density variations during geomagnetically disturbed intervals. For the first time, the magnetic and electric field variations during geomagnetically active intervals are determined in the Eurasia region for the detection of GICs. Our study aims to contribute to the worldwide understanding and modelling efforts on the space weather effects on the thermospheric altitudes and the ground level.



YUKARI ATMOSFER JOULE ISINMASININ GÖZLEM VE UZAY HAVASI MODELLERİ KULLANARAK KAPSAMLI İNCELENMESİ VE BİR UZAY HAVASI UYGULAMASI: JEOMANYETİK AKIMLAR

ÖZET

Uzay havasının yer ve uzay konulu günümüz teknolojik altyapısı üzerine doğrudan etkileri vardır. Uzun vadede, uçaklardaki kabin ekibi ve uzaydaki astronotların da sağlıklarını etkilemektedir. Bu nedenle, uzay havasının Dünya yüzeyine ve yere yakın Uzay ortamına olabilecek etkilerinin ve bu etkilerin sınırlarının belirlenmesi büyük önem taşımaktadır. Bu çalışmada, uzay havasının yukarı atmosfere ve yer seviyesinde jeomanyetik olarak üretilmiş (geomagnetically induced currents-GICs) akımlara etkisi çalışılmıştır. Takriben, bu tez çalışması üç ana bölümden oluşmaktadır: 1) Joule ısınması için literatürdeki daha önce yapılmış çalışmalarda kullanılmış yöntemlerin araştırılması ve birbirleriyle karşılaştırılması 2) jeomanyetik fırtınalar ve mikrofırtınalar esnasında yükselen termosferik nötral sıcaklıkların bir sonucu olarak artan termosferik nötral yoğunluk değişimlerinin incelenmesi 3) Bozcaada, Çanakkale’de (coğrafi koordinatlar: 37.5°K, 106°D) kurduğumuz bir manyetotellürik istasyonun verisini kullanarak aşağı-orta enlemlerde jeomanyetik olarak üretilmiş akımların (JOÜA) tespit edilmesi ve nicelleştirilmesi.

Joule ısınması (JI) iyonosferik seviyelerde nötraller ve iyonların çarpışması sonucunda ortaya çıkan sürtünme kaynaklı ısınmadır. JI'nın tam olarak belirlenebilmesi, anlık olarak elektrik alan, iyonosferik iletkenlik, termosferik nötral rüzgar ve ortamdaki manyetik alanın, ya da ikinci bir yaklaşımla; aynı anda iyonosferik iletkenliğin, nötral ve iyon hızlarının bilinmesini gerektirir. Literatürde, nötral rüzgarın katkısının düşük olduğu varsayılarak yapılan çalışmalar da mevcuttur.

Çalışmamızda, JIyı nötral rüzgar etkileri dahil edilmiş ve edilmemiş olarak iki türlü hesaplamaktayız. Nötral rüzgar etkisi içermeyen hesaplarımız için çaprazlama birleştirme yöntemi kullanılmıştır. Elektrik alan için gözlemsel radar datası ve bir manyetohidrokinamik modelin iyonosferik elektrodinamik modülü (MHD-IE) çıktısı; iyonosferik iletkenlikler için ise amprik bir model ve yine MHD-IE modülü verilerini değişimli kullanarak hesaplamaktayız. JI hesaplarında en çok kullanılan indis-bazlı yöntemler de çalışmamızda mercek altına alınmıştır. Amacımız, küresel bir gözlem ağının yokluğunda Joule ısınması için en iyi sonuçları veren alternatif yöntemleri ortaya koymaktır. Gözlemsel elektrik alan verisi Super Dual Auroral Radar Network (SuperDARN) radarlarından ve manyetohidrokinamik model verisi, Space Weather Modeling Framework/Block-Adaptive-Tree-Solarwind-Roe-Upwind-Scheme’den (SWMF / BATSRUS - buradan sonra sadece BATSRUS olarak anılacaktır) gelmektedir. İletkenlikler BATSRUS-IE modülünden ve OVATION Prime + Uluslararası Referans İyonosfer 2012 (International Reference Ionosphere 2012-IRI2012) modelinden alınmıştır. Nötral rüzgar içermeyen hesaplamalarda, Akasofu’nun Epsilon parametresi baz alındığında, Joule ısınması maksimum değeri

için bütün yöntemlerin 10 ila 20 dakika arasında değişen gecikmeler ortaya koyduğunu bulduk. Bununla birlikte, AE indisine dayalı olan dolaylı (proxy) yöntem, 20 dk ila 1.5 saat arası değişen en uzun gecikmeleri göstermektedir. Nitelik olarak baktığımızda, tüm yöntemler benzer değişimler göstermiştir. AE proxy yöntemi en yüksek, IRI2012 modeli iletkenliklerini kullanan yöntemler ise en düşük Joule ısınması değerlerini sergilemişlerdir. SuperDARN ve BATSRUS elektrik alanı kullanan yöntemler arasındaki farklar gece sektöründe radar gözlemi olması durumunda birbirine daha yakın sonuçlar vermiştir.

Tezin ikinci kısmında, güncel amprik ve fizik bazlı iyonosfer-termosfer modellerinin GEM-CEDAR topluluklarının seçtikleri olaylar için termosferik nötral yoğunluk tahminleri incelenmiştir. CHAMP (Challenging Minisatellite Payload) uydusu gözlemleri kullanılarak modellerin hata farkları nicelleştirilmiştir. Etkileşimli iyonosfer-termosfer modelleri ve amprik modeller farklı nötral yoğunluk klimatolojileri ve manyetik fırtınaya farklı tepkiler vermektedirler. Nötral yoğunluk üzerindeki manyetik fırtına etkilerinin klimatoloji üzerine bindiği gözlenmiştir. Sadece nötral yoğunluk maksimumu üzerine odaklanan bir hata tespit çalışması yanlış yönlendiricidir. Bu tarz bir çalışmada, klimatolojiyi daha yüksek, fakat fırtına etkisini daha az tahmin eden bir model, sonuç olarak başarılı olarak görülme riski taşımaktadır. Uydu sürüklemesinin gerçek zamanlı tahmini, fırtına zamanı etkilerin doğru nicelleştirilmesine ve tahmin edilmesine bağlıdır. Takiben, çalışmamızın bu aşamasında model klimatolojisi ile termosferin manyetik fırtınaya cevabını ayırmak için çeşitli teknikler uyguladık. Hem CHAMP verileri, hem model çıktıları için fırtına öncesinde tespit edilen manyetik aktivitesiz zamanlar göz önüne alınarak referans hatları oluşturulmuştur. Veriler bu referans hatları kullanılarak kaydırılmış ve manyetik fırtına kaynaklı değişimler ortaya çıkartılmıştır. Model performanslarında, sakin dönem klimatolojisinden farkı olan modeller için %113'e varan iyileşmeler kaydedilmiştir. Fizik temelli modellerin düşük KPli olaylar için en kötü, KP yükseldikçe ise daha iyi tahmin yapabildikleri gözlenmiştir. Manyetik fırtınanın kaynağının Koronal kütle atılımı (KKA, coronal mass ejection: CME) ya da eşdönümlü etkileşim bölgesi (EEB, corotating interaction region: CIR) olması model performansını etkilememektedir. Nötral yoğunluklar yeterli biçimde hesaplanabilmektedir. Amprik modeller klimatolojiyi tahmin etmekte başarılıdır. Bu nedenle fırtına-zamanı nötral yoğunlukları referans hattı kaydırmasından fazla etkilenmemektedir. Ancak, nötral yoğunluk maksimumuna yüksek yaklaşıklıklar gösterebilir dahi, cevap eğrilerinin gözlemlenen yoğunluk değişimlerinden hayli farklı oldukları görülmektedir. Uydu sürüklemesinin gerçek zamanlı hesaplamaları için, klimatolojinin ayrılması ve ensemble (toplu-model) yaklaşımının beraber kullanımlarını önermekteyiz. İlâveten, Joule ısınması ve nötral yoğunluk değişimleri için doğrusal regresyon kullanarak basit bir model oluşturulmuştur. Fizik bazlı modellerin JI tahminleri ve CHAMP nötral yoğunluk gözlemlerinin arasındaki bağlantıya bakılmıştır.

Çalışmamızın son kısmında, jeomanyetik olarak üretilmiş akımların aşağı-orta enlemlerdeki özelliklerini belirlemek amacıyla Türkiye'de kaydedilen elektrik ve manyetik alan ölçümleri incelenmiştir. Bozcaada, Çanakkale (coğrafi koordinatlar: 37.5°K, 106°D) bölgesinde bir elektrometre ve bir manyetometrenin de dahil olduğu bir manyetotellürik istasyon kurulmuştur. Manyetik hareketlilik esnasında yüksek elektrik alan ve manyetik alan değişimleri gösteren vakalar ileri inceleme için seçilmiştir. Manyetik aktivitenin etkisi manyetik alanın yatay bileşeninin türevlerinin

değişimi ve arkaplan manyetik ve elektrik alanlardan sapmasının bulunması yoluyla incelenmiştir. Manyetik alan verisinde S_q akımının etkisi, arkaplan salınımına kübik spline eğrileri oturtularak veriden çıkartılmıştır. KP ve Dst indisleri kullanılarak seçilen kuvvetli manyetik aktivite esnasında, manyetik alan bileşenleri ve türevlerinde ve elektrik alan bileşenlerinde yüksek frekanslı, kuvvetli dalgalanmalar tespit edilmiştir. Bulunan bu dalgalanmalar sakin bir günün manyetik alan ve elektrik alan salınımı ile karşılaştırılmıştır. Manyetik ve elektrik alan bileşenlerinin birbirleriyle olan yakın ilişkisi gösterilmiştir. Elektrik ve manyetik alan bileşenlerinde manyetik fırtına fazlarına göre iki farklı tipte değişim gözlenmiştir: başlangıç ve ani başlangıç fazına denk gelen salınımlar ve manyetik fırtına ana fazına denk gelen salınımlar. Başlangıç ve ani başlangıç fazlarında ortaya çıkan salınımların koronal kütle atılımı olayları nedeniyle artan dinamik basınca bağlı olarak meydana geldiği düşünülmüştür. Bütün olaylar, KKA nedeniyle güneşaltı manyetopozun sıkışmasına karşılık olarak yükselen manyetik ve elektrik alan değerleri sergilemiştir. Enlemlerimizde JOÜAların manyetik fırtına başlangıç ve ana fazıyla ilişkili olduğu gösterilmiştir.

Sonuç olarak, bu tez çalışmasında, manyetik olarak hareketli zamanlar için termosferik Joule ısınması ve termosferik nötral yoğunluk değişimlerini tahmin etmekteki güncel kapasitemizi analiz ettik. Avrasya bölgesinde ilk defaya mahsus olarak JOÜAları tespit etmek üzere elektrik ve manyetik alan değişimleri incelendi. Çalışmamız uzay havasının termosferik yüksekliklere ve yer seviyesine etkilerinin anlaşılmaları ve modellenmeleri konusundaki araştırmalara katkıda bulunmayı amaçlamıştır.



1. INTRODUCTION

Quoting from the US National Space Weather Program which started in 1994, space weather is defined as the “conditions on the Sun and in the solar wind, magnetosphere, ionosphere, and thermosphere that can influence the performance and reliability of space-borne and ground-based technological systems and can endanger human life or health.”. Most of the technological systems are vulnerable to solar activity related changes in the space environment (Arbesser-Rastburg and Jakowski, 2007; Bothmer and Daglis, 2007; Crosby, 2007; Daly et al., 2007; Lanzerotti, 2007; Reitz and Facius, 2007; Trivedi et al., 2007). The effects of space weather to the technological systems are briefly listed as “the disruption of satellite operations, communications, navigation, and electric power distribution grids”, which can cause a variety of socioeconomic losses (Pulkkinen, 2003). Consequently, space weather and its prediction gain more importance as we technologically advance. The giant budgets spent on the satellites and importance of their missions and programs dictate the prevention from possible damages due to space weather. Determining the limits of possible events and their consequences on Earth carries crucial importance. Using a data set which includes the change in the geomagnetic field’s horizontal component for the last 89 years, Kataoka (2013) gave extreme geomagnetic storm occurrence as 13% by means of a power law approach for solar cycle 24. A similar calculation relying on the maximum sunspot number for the solar cycle 24 yields a probability of 6%. Even though those seem to be very small numbers, the result of an extreme geomagnetic storm can be devastating for today’s technological infrastructure (Committee on the Societal and Economic Impacts of Severe Space Weather Events: A Workshop, and National Research Council, 2008). Schulte in den Bäumen et al. (2014) combined a physical model and a model for the global economy to estimate the impact on global economy in case of an extreme geomagnetic storm. They found that an event with similar magnitude to 1989 event can cause USD 2.4 to 3.4 billion damage to the global economy during the first year, only. The total damage would be around USD ~13 billion over the years (Kappenman, 2010). This impact would not just be limited with the countries in direct

encounter with the geomagnetic storm effects due to their geomagnetic location, but also countries depending on the global trade, but far from the impact area would feel the economical consequences indirectly (Schulte in den Bäumen et al., 2014). Following, Schrijver et al. (2015) lists the steps that require immediate attention and research as observation-based modeling throughout the heliosphere, reliable forecasts at least 12 hour ahead of the arrival of a coronal mass ejection (CME), characterizing the geospace response to variable solar wind conditions and utilizing a climatological model of space weather which includes the specifications of the extreme events.

Some of the long standing questions in space weather and its applications focus on the results of the interplay within the domains. Joule heating (JH), as an instant consequence of the magnetosphere-ionosphere-thermosphere (MIT) coupling is one of the mostly studied parameters. It is defined as the frictional heating arising from the relative motion of plasma and neutrals in the ionosphere (Vasyliunas and Song, 2005). Its accurate determination is extremely important in determining the heat balance in the upper atmosphere (Knipp et al., 2005; Zhu et al., 2005) and resulting thermospheric dynamics (Brekke, 1979; Balthazor et al., 1997; Sheng, 2014) as well as the partitioning of the solar wind power between different magnetospheric sinks (Lu et al., 1998; Tanskanen et al., 2002a; Turner et al., 2009). Joule heating leads to the expansion of the atmosphere causing higher mass densities in the upper altitudes, which in turn, increases the drag acting on the satellites. The difficulty in Joule heating studies lies in finding a reference level or model in the absence of global observations to calibrate and benchmark the models and their results against.

Another space weather consequence, which can be directly observed on Earth is the currents that are induced during geomagnetic disturbances in response to the variations in the ionospheric currents. These currents are called Geomagnetically Induced Currents (GICs). GICs can flow through any conducting substance or layer causing harm to technological infrastructure. The initial research on GICs focused on the sources and detection methods. Nowadays, the efforts are concentrating on the modeling of GICs and estimating the amount of possible damage on the infrastructure. However, no studies exist for the Eurasia region.

Our study falls in the category of characterizing the geospace response to variable solar wind conditions and deals with the space weather effects on the upper atmosphere and the ground, focusing on the Joule heating (JH), storm-time thermospheric neutral

density response and the implications of space weather on the ground, such as the geomagnetically induced currents (GIC). This is the first study that the magnetic and electric field variations that cause GICs have been investigated and reported in the Eurasia region.

1.1 Purpose of the Thesis

Following the recent advances in space weather studies, our study aims to focus on the several contemporary problems of the upper atmospheric Joule heating, its controlling parameters and its role on the upper atmosphere using a wide range of models and observations. One chapter of the thesis has also been assigned for the geomagnetically induced currents in order to demonstrate the space weather effects on the ground at our latitudes. Specifically, the questions that this thesis work will address are given as below:

1. On the variability of JH from the methods during geomagnetic disturbances:
 - a. Numerous empirical and numerical models of upper atmosphere, or MIT coupling models have been developed. How do these models compare against each other over the Joule heating?
 - b. Based on their assumptions, each model can provide an approach to study Joule heating. Is any of these models favorable to any other? Are there other ways to increase the reliability in the predictions of Joule heating?
 - c. Can we find new methods to obtain JH with higher reliability, which can be employed for the validation of space weather models at any point during the solar cycle?
 - d. What is the effect of neutral wind on JH?
2. On the assessment of the storm-time performances of the IT models in estimating the thermospheric neutral density:
 - a. How to extract the storm-time response from the models and data?
 - b. How to select appropriate metrics for the evaluation of the neutral density response from the models?
3. As a consequence of (1) and (2), can we define a relationship between Joule heating and storm-time thermospheric neutral density variations?

4. On the signatures of the geomagnetically induced currents (GICs) over midlatitudes:
 - a. What are the characteristics of electric and magnetic field variations over Turkey?
 - b. What are the sources of the electric and magnetic field disturbances over Turkey?

As a summary, this thesis study presents a comprehensive synthesis of the thermospheric, ionospheric and ground level aspects of the space weather using Joule heating and the magnetic and electric field variations on the ground for geomagnetically active times, i.e. when magnetospheric substorms and geomagnetic storms occur.

1.2 Structure of the Thesis

This thesis study addresses on four research problems: the upper atmospheric Joule heating (including the neutral wind effects on JH), the storm-time variations in thermospheric neutral density, the relation between JH and thermospheric neutral density and the geomagnetically induced currents over Turkey. Although each of these studies is developed in a self-consistent manner and complete in their own research-frame, because of the thesis format requirements, the thesis structure is organized such that the literature part, presented in Chapter 2, consists of the literature surveys of each research study, and is separate from the analysis and results belonging to each subject. The structure of the thesis is as follows: firstly, the basic concepts and terminology that are used throughout this study are introduced in subsections 1.3, 1.4 and 1.5. In Chapter 2, a thorough literature review on the subsections of the thesis are given. In Chapter 3, the observational data sources used in this study and their properties are described. Chapter 4 lists and familiarizes the reader with the state-of-the-art magnetohydrodynamic (MHD) and ionosphere-thermosphere (IT) models that were utilized in this study. Chapters 5 presents our work on Joule heating, a part of which was published in Space Weather journal (Eyiguler et al., 2018) and focuses on the JH variability and neutral wind effects on JH. In Chapter 6, the storm-time neutral density variations and the performances of the IT models are investigated and presented in detail. This part of our study was also submitted to Space Weather journal and is currently under review. In Chapter 7, using the methods employed in Chapter 6, the

correlation between JH and thermospheric neutral density is examined and a simple relation is derived. In Chapter 8, magnetic and electric field variations over Turkey during geomagnetic disturbances are demonstrated and possible sources of these variations are discussed. This part of our study was published in *Advances in Space Research* journal (Eyigüler and Kaymaz, 2017). Lastly, Chapter 9 summarizes and concludes the study along with our suggestions for future work.

1.3 Solar Wind-Magnetosphere Interaction on Average

The Sun dominates our whole solar system by emitting flares and continuously ejecting matter in the form of the solar wind, coronal mass ejections (CMEs) and high-speed streams. On average, solar wind has a speed of 450 km/s, 6.6 #/cc particles, temperature on the order of 10^5 K and a dynamic pressure of 2.67 nPa at 1 AU (Hundhausen, 1995). It is also shown that the average values of the solar wind properties change with respect to the solar cycle. The average velocity ranges from 388 ± 4 km/s to 459 ± 7 km/s and average of the density ranges from 8.5 ± 0.3 to 5.5 ± 0.2 #/cc for different solar cycles (Jian et al., 2011).

Magnetized planets and their magnetosphere behave differently under the variable solar conditions. Figure 1.1 shows the expanding solar wind plasma and interplanetary magnetic field in the form of Parker spiral, as well as the Earth's magnetosphere, which is compressed at the dayside by the solar wind dynamic pressure, and stretched in the nightside due to the tangential stress exerted by the solar wind.

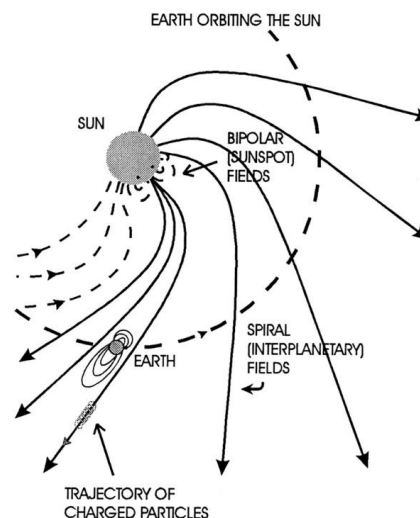


Figure 1.1 : Solar wind and the Earth's magnetosphere (Url-1).

Under the average conditions, as the solar wind approaches the Earth, it first meets the bow shock, at which the supersonic solar wind slows down to subsonic speeds. The bow shock is usually confined to 11-14 Earth radii (R_E) subsolar distance. Getting closer to the Earth, the magnetopause is marked as the boundary surface where the solar wind dynamic pressure and Earth's magnetic pressure equal to each other. Magnetopause is generally located about 9-11 R_E subsolar distance from the Earth (Lugaz et al., 2016). It separates the magnetospheric plasma residing in the magnetosphere from the solar wind plasma in the magnetosheath, which has a very turbulent nature. After passing the magnetopause, a charged particle behaves completely under the control of the Earth's magnetic field in the magnetosphere. The plasmasphere, which is populated with dense and cold plasma also exists within the magnetosphere. The tangential stress exerted by the solar wind leads to the elongated magnetotail and the open field lines are squeezed in the region of polar cusps (Russell, 2007). Figure 1.2a shows the magnetospheric environment and its surrounding as well as the current systems in the magnetosphere formed due to the interaction between the Earth and the interplanetary environment. The current systems in the magnetosphere result from the temporal variations in the magnetic field, Earth's rotation, and from the interaction of the Earth's magnetosphere with the upcoming solar wind (Jacobs, 1991).

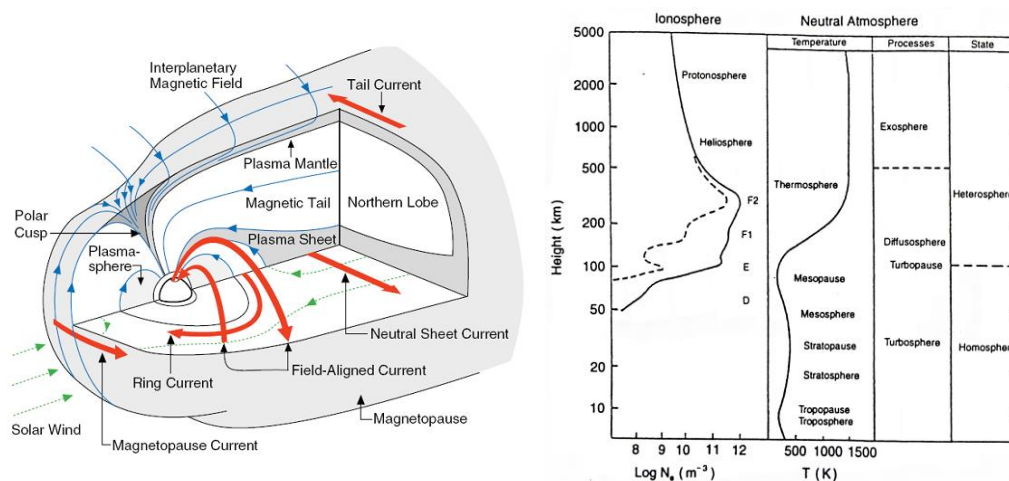


Figure 1.2 : a) Magnetosphere and the current systems (Russell, 2007) b) Layers of the atmosphere and their classifications (Dieminger et al., 1996).

The current closure completes in the ionosphere, which is the ionized layer of the atmosphere between 60-1000 km altitudes (Hargreaves, 1992). The magnetospheric currents are balanced via the field-aligned currents going downwards and upwards in the high-latitude ionosphere. Currents, horizontal and perpendicular to the electric

field are generated which are known as the Hall and Pedersen currents, respectively (Campbell, 2003). The solar wind-magnetosphere and ionosphere are strictly coupled with each other electrodynamically. However, the ionosphere also overlaps with the neutral atmospheric layers, thermosphere and mesosphere and hydrodynamically interacts with them. Figure 1.2b shows the layers of the neutral atmosphere, which overlap with the ionosphere.

1.4 Magnetosphere-Ionosphere-Thermosphere Coupling

The first observational evidence for the Magnetosphere-Ionosphere coupling was published by the Lockheed Palo Alto group who declared that the source of the Oxygen in the magnetospheric hot plasma can be the ions outflowing from the ionosphere (Moore et al., 2016).

Ionosphere constitutes the bottom part of the magnetospheric current system. High-latitude ionosphere is mainly where the magnetospheric current system closes over. Field-aligned currents form the bridge between the magnetosphere and the ionosphere as shown in Figures 1.2a, 1.3a and 1.3b.

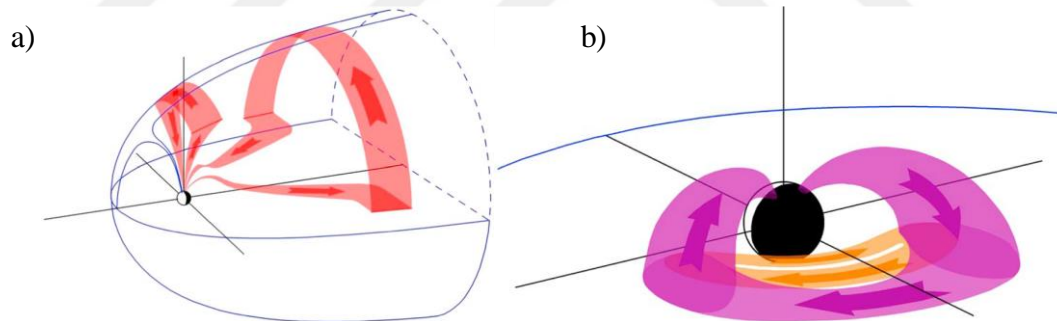


Figure 1.3 : a) Region-1 currents (shown in red) b) Region-2 currents and partial ring current (purple) and the banana current (orange) (Ganushkina et al., 2018).

The motion of the ions at the high-latitudes, which is termed as the ionospheric convection, is basically controlled by the solar wind-magnetosphere-ionosphere coupling as in Figure 1.4. Figure 1.4 displays the plasma velocity streamlines, which also are potential contours under southward (above) and northward (below) IMF B_z directions. The columns show the convection patterns for different IMF B_y conditions: $B_y < 0$, $B_y = 0$, $B_y > 0$. The solid circle shows the open-closed field line boundary. The dashed lines represent the regions connected to the reconnection sites at the magnetopause. For all B_y , the pattern consists of two cells when IMF B_z is southward

due to low-latitude reconnection. Anti-sunward flows dominate in the region of open field lines. Below the open-closed field line boundary, the flow is sunwards. The symmetry between the cells changes due to the tension IMF B_y applies for $B_y > 0$ and $B_y < 0$ conditions.

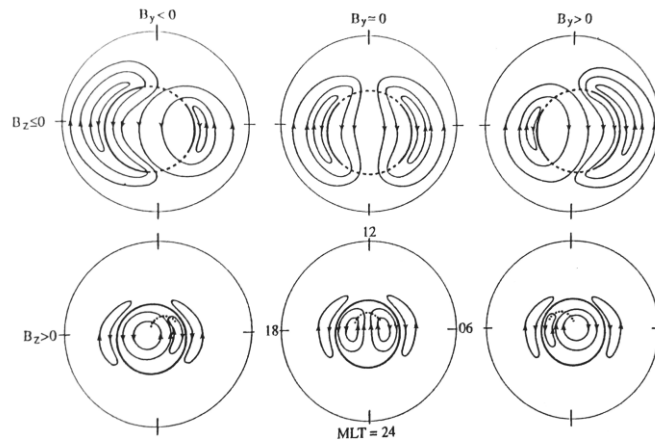


Figure 1.4 : Ionospheric convection driven by the solar wind (Cowley, 1996).

For B_z northward, the flows are restricted in a narrower region, and four cells form. The newly formed cells are due to the high-latitude cusp reconnection (Cowley, 1996). The scientific efforts to model and understand the ionosphere-magnetosphere coupling began with the desire to map the electrodynamic features of the ionosphere. The current understanding on the electrodynamics of the magnetosphere-ionosphere coupling is basically depicted in Figure 1.5.

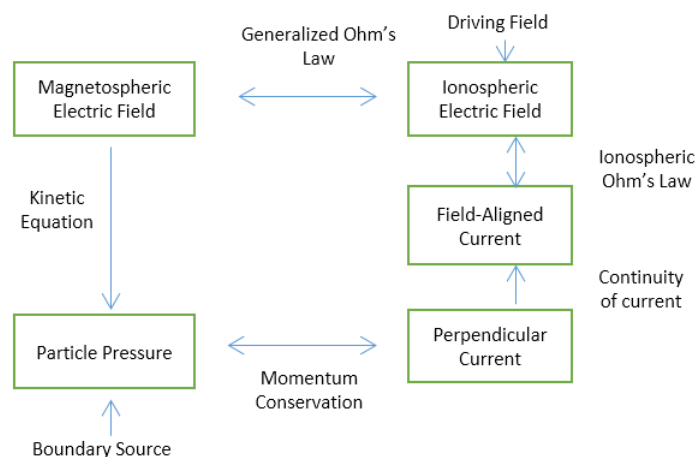


Figure 1.5 : Diagram showing the means of interaction and mechanisms in the ionosphere (reproduced from Kamide et al., 1993).

Nowadays, coupled geospace models are becoming increasingly employed to resolve the dynamics of the magnetosphere-ionosphere coupling and to enable space weather forecasts.

Figure 1.6 displays a representation of the processes when thermosphere is also introduced to the picture and shows the current understanding on the dynamics of the magnetosphere-ionosphere-thermosphere (IT) coupling. The main drivers of the system are absorption of the extreme UV radiation, JH by electrical currents, particle precipitation from the magnetosphere and dissipation of upward propagating waves (tides, planetary waves, gravity waves). Meanwhile the energy sinks are listed as the thermal conduction into the mesosphere, infrared cooling by CO₂, NO and O, and chemical reactions (Forbes, 2007).

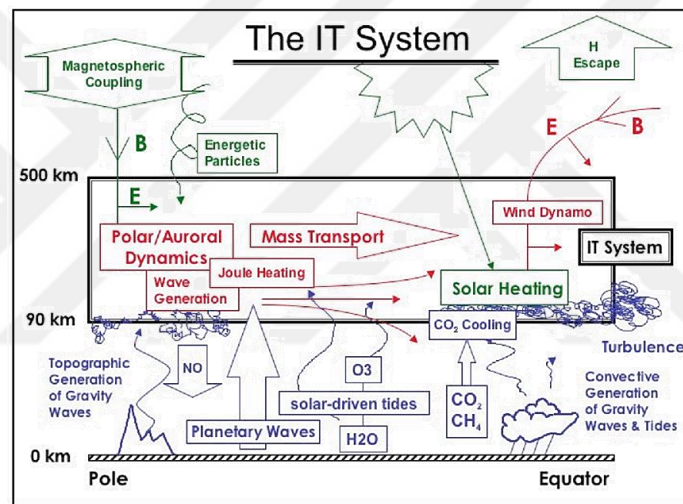


Figure 1.6 : Energy sources and sinks in the IT system (Forbes, 2007).

The interactions within the system amplify and are greatly modified during the geomagnetic disturbances, since the energy input is increased.

1.5 Geomagnetic Activity and Its Effects in the Near-Earth Space Environment

Geomagnetic storms and substorms are the geomagnetically active time periods that large changes in the Earth's magnetic field are observed. Geomagnetic storms affecting the global magnetosphere can last for days while substorms are events localized in the nightside magnetosphere with time scale of several hours. The effects of geomagnetic storms range from the space to ground. Figure 1.7 separates the effects into three regions such as the space, atmosphere and ground.

Geomagnetic storms and substorms have phases during which the incoming energy is stored, released and the conditions return to background levels. For geomagnetic storms the phases are; the initial phase followed by a sudden commencement, main phase and the recovery phase, whereas for substorms, the phases are named as the growth, expansion and recovery. The phases and strength of a geomagnetic storm or substorm are determined and measured by proxies known as geomagnetic indices. For geomagnetic storms, the disturbance storm time index (Dst) is favorable while auroral electrojet (AE) indice is employed for the substorms.

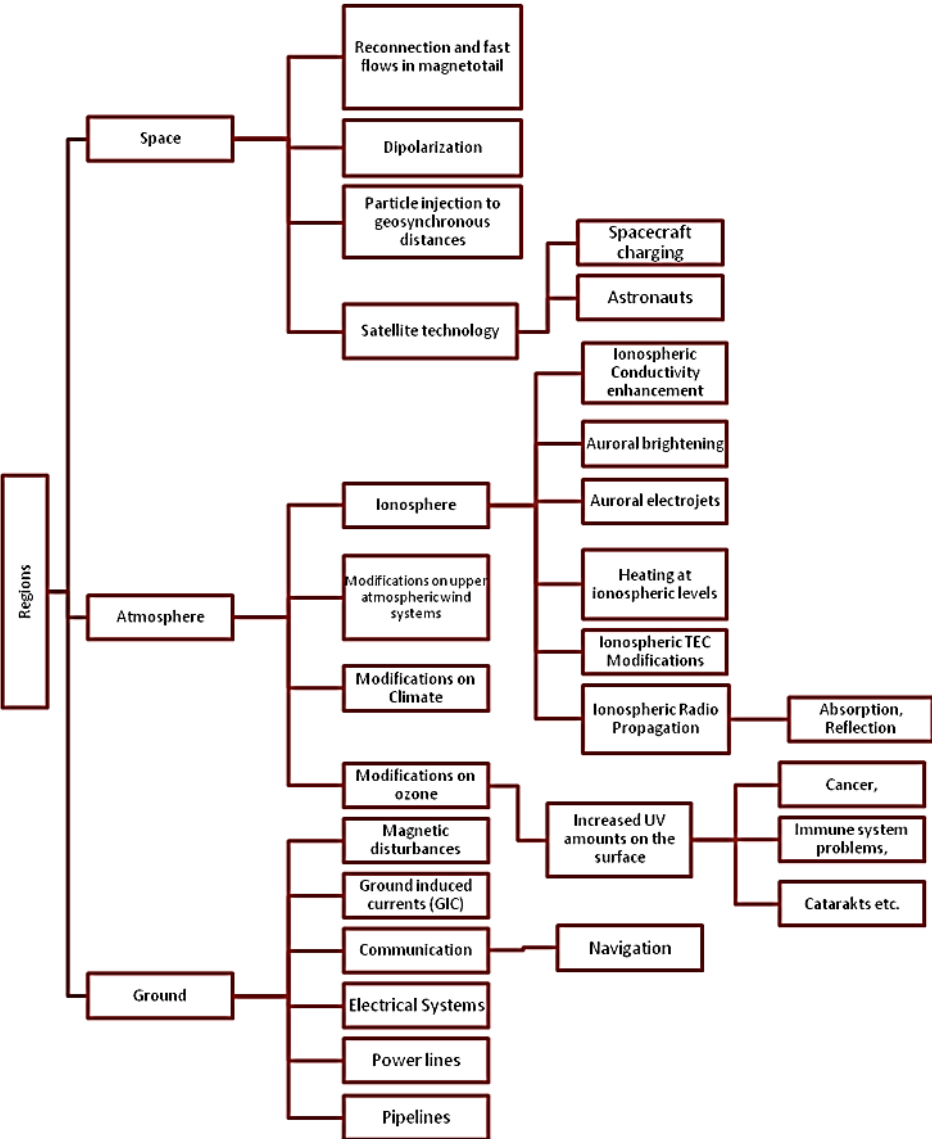


Figure 1.7 : Geomagnetic storm effects in space, Earth’s atmosphere and on the ground level.

The Dst indice is a proxy for the strength of the ring current, which amplifies during geomagnetic storms, but it is not as responsive to magnetospheric substorms. The Dst

increases in negative direction when the ring current starts to fill up. The intensified ring current's net effect on the equatorial magnetic field is a decrease approximated by the Dst. During the sudden commencement Dst shows an increase meaning that the dynamic pressure associated with the CME shock has hit the Earth's magnetosphere and pushed the magnetopause currents toward Earth. Consequently, the ring current starts to be filled up with more particles with a westward enhancement. Thus, on Earth, we measure a decrease in the magnetic field strength. During the recovery phase, the processes weaken, and magnetic field starts to return to its background, pre-storm-time magnitude as seen in Figure 1.8.

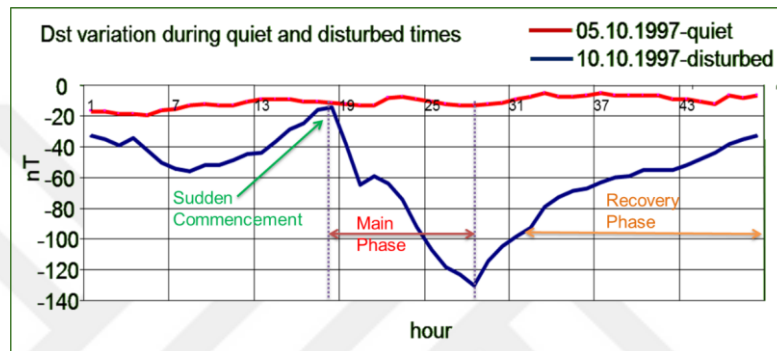


Figure 1.8 : Dst variation during geomagnetically active and disturbed intervals.

Another measure for the geomagnetic storm strength is the KP index, which is used by NOAA. KP gives information on the global geomagnetic activity and is calculated using 13 subauroral stations measuring the two horizontal field components of the magnetic field in 3 hour interval.

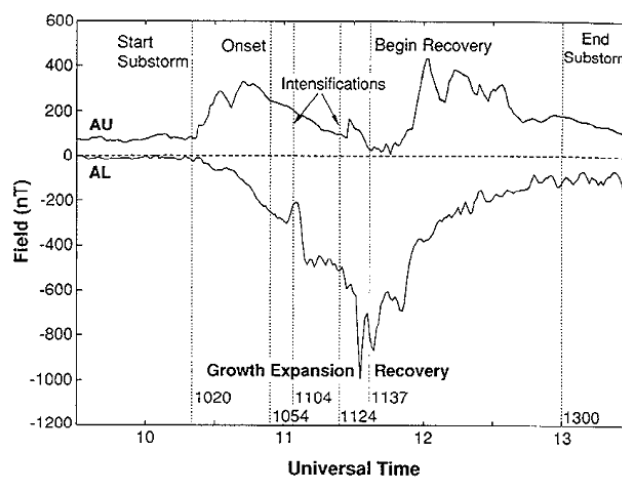


Figure 1.9 : The variation of the AU and AL components of the AE index during a substorm (McPherron, 1995).

Moreover, the total change in the magnetic field is obtained by using the AE index. AE represents the magnetic field disturbances at the auroral stations (Davis and Sugiura, 1966). The AE index comprises of auroral upper (AU) and auroral lower (AL) parts. The magnitude of the AE can be found by subtracting the AL from the AU. Figure 1.9 shows substorm phase identification with respect to the AE index.

For space weather prediction and the classification of events it is essential to know how these indices vary. Moreover, several relations between the indices and energy sinks were produced, some of which will be introduced in the consequent chapters.



2. LITERATURE REVIEW

In this chapter, we detail the previous studies in the literature on Joule heating (Section 2.1), Joule heating effects on neutral density (Section 2.2), thermospheric neutral density variations (Section 2.3) and geomagnetically induced currents (Section 2.4). Section 2.1 presents the JH calculation methods that were used in the previous studies and mentions the current efforts to find Joule heating. Section 2.2 describes the relation between JH and thermospheric neutral density and touches on the effects of JH, hence, neutral density on the technological systems. Section 2.3 introduces the factors that determine the variations in neutral density and how they are investigated and reports the current needs of the society. Lastly, section 2.4 showcases the sources of GICs that were previously detected and reported at different latitudes on Earth and explains the methods to determine the GICs.

2.1 Upper Atmospheric Joule Heating

In essence, JH can be calculated using three terms: the ionospheric Pedersen conductivity, ionospheric electric field, and the neutral wind generated electric field.

In the neutral wind frame, the local JH rate ($\vec{J} \cdot \vec{E}$) can be found by using

$$Q_j = \int_z \mathbf{J} \cdot \mathbf{E}' dz = \int_z \sigma_p(z) (\mathbf{E}_\perp + \mathbf{U}(z) \times \mathbf{B})^2 dz \quad (2.1)$$

as given in (Thayer et al., 1995; Wilson et al., 2006). In this equation, Q_j is the height-integrated JH rate at a specific point; \mathbf{E}' , the electric field in the frame of reference of the neutral gas, σ_p , \mathbf{E}_\perp , \mathbf{U} and \mathbf{B} are Pedersen conductivity, ionospheric electric field, neutral wind velocity, and ambient magnetic field, respectively (Thayer et al., 1995). None of these variables are simultaneously and globally available quantities. The electric field in Equation (2.1) may be obtained using ground magnetometer data (Kamide et al., 1981; Kamide et al., 1982) or from ground based radars such as Super Dual Auroral Radar Network (SuperDARN) (Greenwald et al., 1995; Ruohoniemi and Baker, 1998). The European Incoherent Scatter (EISCAT) radars can also provide

local electric fields in a narrow band (Aikio and Selkälä, 2009; Cai et al., 2014). The conductivities, neutral wind, and magnetic fields at JH heights are inferred from the models (Gjerloev and Hoffman, 2000; Baker et al., 2004; Zhang et al., 2005) or taken from indirect measurements (Aksnes et al., 2002; Sheng et al., 2014; Aikio et al., 2012; Anderson et al., 2013). The accuracy of calculating the JH rate depends upon the accuracy of these quantities involved in this equation. Previously, many studies neglected the effect of neutral wind on JH rates by assuming it has a small contribution at high latitudes (Kosch and Nielsen, 1995; Rodger et al., 2001). Another reason for neglecting the neutral wind is the difficulty of its characterization due to the lack of global and simultaneous observations (Deng and Ridley, 2007; Waters et al. 2004). the transfer of the electromagnetic energy equals to the height integral of the local JH rate at the point of interest and is usually calculated as given in Equation. (2.2) (McHarg et al., 2005; Aikio and Selkälä, 2009),

$$Q_j = \mathbf{J} \cdot \mathbf{E} = \mathbf{J} \cdot \mathbf{E}' = \Sigma_p \vec{E}_\perp^2 \quad (2.2)$$

Here, Σ_p is the height-integrated Pedersen conductivity (conductance) which can be obtained from a model in the same way as for Equation (2.1).

There are several statistical studies that utilize large amount of ground and space data. Assimilative mapping of the ionospheric electrodynamics (AMIE) technique, for example, constructs the parameters required in the calculation of the JH rate using radar, satellite and ground magnetometer data (Richmond and Kamide, 1988; Lu et al. 1998; Richmond et al., 1992). Historically, several relationships between the geomagnetic indices and JH were derived using sets of geomagnetic storm and substorm data. One of the indices that is widely employed to find the JH is the AE index, which is based on the change in the horizontal component of the ground magnetic field measurements (Davis and Siguira, 1966). AE can be calculated using different number of stations. However, the standard global AE index calculations rely on the geomagnetic field recordings at 12 high-latitude stations (AE₁₂), which are unevenly separated in geomagnetic longitude (MLong) along the auroral zone, between the geomagnetic latitudes (MLat) 60.44°N and 71.21°N in geomagnetic coordinates. AE₁₂ is provided directly by the World Data Center (WDC), Kyoto, Japan (<http://wdc.kugi.kyoto-u.ac.jp>) for public usage, which is an easy reachable data source for the quick-look JH calculations. The most commonly used relations between

the AE and JH are those from the works of Ahn et al. (1983), Ahn et al. (1989) and Richmond et al. (1990) due to the high correlation coefficients they found and the number of stations (12) involved in the calculations. In these studies, the relation between JH and AE are in the form

$$JH(GW) = aAE(nT) + b \quad (2.3)$$

where the coefficients a and b depend on the season and the number of AE stations and signify the hemispheric or global JH amount (Østgaard, 2002). Østgaard (2002) gave a detailed discussion of the previously determined JH-AE index relations and arrived at the conclusion that the coefficients based on AE_{12} by Ahn et al. (1983), Ahn et al. (1989) and Richmond (1990) are equally good and their seasonal dependence is weak. Because of the easy accessibility of AE index data, this method is useful for obtaining a preliminary and quick view of the JH rate. Likewise, Kallio et al. (2000) and Tanskanen et al. (2002b) used local IL index to provide JH during substorms. As in the case of AE, their empirical formula assumes a linear relationship between the IL and JH in the ionosphere following Ahn et al. (1983). Another study, which relates the JH with one of the geomagnetic indices is the Foster et al. (1983), in which ion drift velocity and particle precipitation data from AE-C (Atmospheric Explorer) spacecraft were used to obtain ionospheric electric fields and Pedersen conductances, respectively. They calculated JH using Equation (2.2) and binned the results according to KP index. Consequently, their results do not include neutral wind effects.

Chun et al. (1999) generated a set of hemispherically integrated JH rates using AMIE. Their study covers 40 days and includes geomagnetic storm periods from 1988 to 1997. They grouped the integrated JH rates according to the level of geomagnetic activity using the Polar Cap index (PC) which is a measure of transpolar ionospheric current strength (Stauning, 2013). Then, obtained a quadratic relationship between the hemispherically integrated JH and the PC index. The study by Knipp et al. (2005) added the Dst index to Chun et al. study and found a more reliable formula between the JH rates and geomagnetic indices. They derived four quadratic equations: one annual Equation. (2.4) and the other three (Equation (2.5), (2.6) and (2.7)), respectively, for winter (21 Oct-20 Feb), summer (21 Apr-20 Aug), and equinox (21 Oct-20 Apr and 21 Aug-20 Oct).

$$JH[GW] = 24.89 * PC + 3.41 * PC^2 + 0.41 * Dst + 0.0015 * Dst^2 \quad (2.4)$$

$$JH[GW] = 13.36 * PC + 5.08 * PC^2 + 0.47 * Dst + 0.0011 * Dst^2 \quad (2.5)$$

$$JH[GW] = 29.27 * PC + 8.18 * PC^2 - 0.04 * Dst + 0.0126 * Dst \quad (2.6)$$

$$JH[GW] = 29.14 * PC + 2.54 * PC^2 + 0.21 * Dst + 0.0023 * Dst^2 \quad (2.7)$$

Their correlation coefficients were higher than 74% for all periods (0.76, 0.84, 0.78 and 0.74, respectively). However, as the Dst index has an hourly cadence, these fits only provide a rough estimate of JH and there is considerable uncertainty due to the exclusion of electric field variability and neutral wind dynamics.

Thermospheric neutral wind modifies the ionosphere-thermosphere (IT) environment and the magnitude of the magnetosphere-ionosphere-thermosphere (MIT) coupling (Peymirat et al., 2002; Ridley et al. 2006). The previous studies on the neutral wind effect on Joule heating mostly focused on quantifying the amount of contribution by the neutral wind. Neutral wind is found to have both negative (Lu et al., 1995; Thayer et al., 1998) and positive contributions (Thayer et al., 1998) to the JH. Mainly three sources modify the neutral wind: the solar EUV heating, the diurnal tides through lower thermospheric waves and the magnetospheric effects, which include the Joule heating, particle precipitation and the ion-drag (Thayer and Killeen, 1991; Richmond et al., 2003; Kwak and Richmond, 2007; Kwak and Richmond, 2014; Dhadly et al. 2017). As a result, neutral wind patterns vary depending on the latitude, local time, universal time, day of the year, solar activity, geomagnetic activity, and IMF configuration (Wang et al., 2017; Dhadly et al. 2017). Additionally, some uncertainty always accompanies the measurements and the models of the IT so the exact amount of the effect of the neutral wind remains imprecise.

Since we do not have worldwide simultaneous measurements of the neutral wind, it is very difficult to form an exact climatology of the neutrals at the thermospheric heights. Moreover, available neutral wind measurements have some uncertainty associated with them. In studies, neutral wind is determined using optical airglow measurements, Fabry-Perot interferometers, radars (such as Arecibo i.e.), satellites (Richmond et al. 2003) and rockets with chemical release. The uncertainties range from 20 m/s (from satellites) to 100 m/s (from radars) for the measurements. Even for the same model,

the uncertainty ranges from minimum 5.6 m/s to maximum 156.4 m/s when the model is run with different auroral and ionospheric potential drivers (Liuzzo et al., 2014). Omission of several dependencies of neutral wind can change the neutral wind results. For example, Dhadly et al. (2017) have found HWM07 model is skewed towards summer conditions.

Thayer (1998) showed that the neutral wind can be considered in the calculations of JH by using the horizontal ionospheric current as given in Equation (2.8) below

$$Q_j = \int_{90 \text{ km}}^{z_{upper}} \frac{J(z)_{\perp}^2 \sigma_P(z)}{(\sigma_P(z) + \sigma_H(z))^2} dz \quad (2.8)$$

In Equation 2.8, J_{\perp} is the total horizontal ionospheric current, and σ_p and σ_H are the local Pedersen and Hall conductivities. The $\frac{(\sigma_P + \sigma_H)^2}{\sigma_P}$ term in Equation (2.8) is also known as the Cowling conductivity, σ_c . Using Equation (2.8), Thayer et al. (1998) showed that the neutral wind can both make positive and negative contribution to JH. They observed 40% reduction in height-integrated JH values for one event, whereas a 400% enhancement was detected for another event owing to the neutral wind. Lu et al. (1995) found a negative contribution of about 28% from the neutral wind using thermosphere-ionosphere global circulation model (TIGCM) simulation.

(Wang et al., 2004) demonstrated that if the magnetic field is only in vertical direction, Equation (7.3) can be written as in Equation (2.9) below.

$$Q_J = \sigma_P B^2 ((U_i - U_n)^2 + (V_i - V_n)^2) \quad (2.9)$$

Here, U denotes the neutral wind velocity (i: zonal, n: meridional) and V denotes the ion velocity (i: zonal, n: meridional), respectively.

On the other hand, Weimer (2005) empirical model offers a different approach that utilizes field-aligned currents and potential models together to calculate the total Poynting flux and Joule heating rate. Likewise, Olsson et al. (2004) carried out a statistical study on JH rate based on Poynting flux using electric and magnetic field data from Astrid-2 spacecraft. They obtained JH as a function of AE, KP, Epsilon and the solar wind kinetic energy flux. The most recent studies have included the use of the numerical models, such as magnetohydrodynamic (MHD) models of

magnetosphere-ionosphere interaction coupled with the physics-based ionosphere-thermosphere models to study JH. These models have been implemented to understand the two-way coupling between the magnetosphere and ionosphere domains. Palmroth et al. (2005) calculated JH via different methods to calibrate the Grand Unified Magnetosphere-Ionosphere Coupling Simulation-4 (GUMICS-4)'s solar wind transfer function which gives the ionospheric power consumption in the model. Li et al. (2011) ran Open Geospace General Circulation Model (OpenGGCM) to study several events with large Poynting flux values during northward IMF B_z intervals with large IMF B_y . They associated the Poynting flux hot spots to the cusp reconnection processes. Xi et al. (2015) tested Lyon-Fedder-Mobarry (LFM) model with flux conserving boundary conditions to match the upper boundary Poynting flux with hemispheric total JH under uniform conductance and electromagnetic energy conservation. They obtained promising results that are compatible with Richmond's Equipotential Boundary Poynting Flux theorem which states that topside Poynting flux values match the JH dissipated in the ionosphere only if they are bound by the same equipotential surfaces (Richmond, 2010). Additionally, the altitudinal distribution of JH and its impact on thermospheric dynamics were investigated using physics-based models of the ionosphere-thermosphere by several studies (Deng et al., 2011; Huang et al., 2012). Recently, Rastätter et al. (2016) carried out a study where they compared DMSP F15 Poynting flux with several empirical and physics-based models of the ionosphere-thermosphere for six geomagnetic storm events. They used Equation (2.2) to obtain JH from the models. Their study is the first to compare the JH of such variety of models with the DMSP Poynting flux. They found that all models gave different spatial distribution of JH. JH from coupled MHD models, including some runs of the Space Weather Modeling Framework / Block – Adaptive – Tree – Solarwind – Roe – Upwind - Scheme (SWMF/BATS-R-US, hereafter will be referred to as BATSRUS), were generally larger than the DMSP Poynting Flux. Since not any one method has shown superiority in the estimation of JH, the efforts in these studies help to find the most suitable approach for predicting JH and to improve the models that are involved in the calculation of JH rates.

2.2 Joule Heating Effects on Thermospheric Neutral Density

Bussy-Virat et al., (2018) reports that the largest source of errors for LEO satellite orbit determination comes from the thermospheric neutral density, which is largely enhanced by the JH during the geomagnetic storms (Zesta and Huang, 2016). JH causes the upwelling of the neutrals in the thermosphere resulting in the enhanced atmospheric drag on the satellites, thus becomes one of the main contributors in the drag force through the variations in thermospheric neutral density (Fedrizzi et al, 2012, Frey et al., 2014). Larger atmospheric drag reduces the life time of the satellites, increases orbit prediction errors and the probability of collisions between the objects existing in the LEO (Zesta and Huang, 2016; Prölss, 2011). The uncertainty in thermospheric neutral density, hence, the atmospheric drag, affects maneuver planning, re-entry predictions, collision avoidance and finding satellites with narrow field of view (Storz et al, 2005). The JH and particle heating comprise 20%-25% of the total thermospheric energy input (Zesta and Huang, 2016). All of the variations in the thermospheric energy input lead to associated variations in thermospheric neutral density. Thus, the knowledge of the timing and location of JH deposition which can be larger than the effect of solar EUV input in short time scales (Zesta and Huang, 2016), is crucial for the neutral density predictions. Consequently, several studies focused on the thermospheric response and lag times between the JH and thermospheric neutral density (Wilson et al., 2006; Oliveira et al., 2017 and references therein), as well as accurate estimation of JH (Rastätter et al., 2016; Palmroth et al, 2004). The time delays between the geomagnetic activity and thermospheric neutral density variations ranged from 1.5 hours to 6 hours and changed with respect to the latitude and magnetic sector (Taeusch et al., 1971; Burns and Killeen, 1992). In a recent study, Fedrizzi et al. (2012) derived a Joule heating index, which relates the neutral density variations to Joule heating by employing a physics-based ionosphere-thermosphere model (Coupled Thermosphere Ionosphere Plasmasphere electrodynamics-CTIPE). In their study, they first compared the neutral density data from CHAMP satellite with the CTIPE model estimations. They found that the standard deviation from the observations was about 0.21. Assuming that this is an acceptable amount of error, they utilized a shaping filter to directly relate the JH from the model to CHAMP neutral density estimations and derive a JH index. With a cross-correlation calculation, they demonstrated that the neutral density at the moment of observation is

related with the variations in the magnetospheric sources from 3 days ago. Their JH index displayed correlations of minimum 88% and maximum 95% with the CHAMP data of (Sutton, 2005).

2.3 Thermospheric Neutral Density Variations

In general, the sources of variations in thermospheric density can be decomposed into three main components: 1) the variations, which are governed by the solar irradiance (solar-cycle dependent, seasonal, diurnal) (Qian and Solomon, 2012) 2) the variations due to upward propagating tides and waves from the mesosphere (Sutton et al., 2007) and 3) the storm-time variations, which are largely influenced by the heat sources that come into play during geomagnetic activity, such as Joule heating (Fedrizzi et al., 2011; Kim et al., 2006), auroral particle precipitation (Deng et al., 2013) and heating due to small scale FACs (Lühr et al., 2004). Additionally, the storm-time thermospheric neutral density response is modulated by the thermospheric composition (Qian et al., 2009). In some geomagnetic storm cases, the damping of the thermospheric density by NO cooling is significantly stronger than expected. Those cases are classified as problem storms by Knipp et al. (2013) and it is shown that the thermosphere's response is strongly associated with the pre-storm properties of the solar wind. Different drivers of geomagnetic storms, such as the Coronal Mass Ejections (CME) and Corotating Interaction Regions (CIRs) cause different environmental responses in the thermosphere (McGranaghan et al., 2014). CIR and CME effects on thermospheric densities were investigated in several studies (Chen et al., 2014; Chen et al., 2012; McGranaghan et al., 2014; Lei et al., 2011; Thayer et al., 2008). Even though less geoeffective in terms of Dst magnitude, the total effect of CIR storms was found to be comparable to CME induced enhancements in thermospheric neutral density (Chen et al., 2014).

LEO satellite observations and empirical and physics-based models are employed in the investigations of thermospheric neutral density (Lathuillère et al., 2008; Sutton et al., 2006; Liu et al., 2005; Pardini et al., 2012; Codrescu et al., 2012; Deng et al., 2013; Solomon et al., 2011). Challenging Micro-Satellite Payload (CHAMP) and Gravity Recovery and Climate Experiment (GRACE) satellites are the most used satellites for the investigations of the neutral density and the associated atmospheric drag acting on satellites (Liu et al., 2011; Anderson et al., 2009; Picone et al., 2002; Bruinsma and

Forbes, 2010; Xu et al., 2011; Huang et al., 2011). In this kind of approach, the densities are calculated from the accelerometers on the spacecraft (Sutton, 2005).

However, in-situ measurements from satellites only provide the current state of the thermosphere. Hence, the empirical models involving semi-physical relations, which take geomagnetic and solar indices as input and the physics-based models of the ionosphere-thermosphere are employed to nowcast and forecast of the future state of the IT system in global scales. The nowcast and forecast of neutral density are necessities for early-action and response and orbit determination of the LEO spacecraft. The comparisons between the model and observations are made in different time scales: daily global mean (Solomon et al., 2011; Qian et al., 2008), orbit averaged (Bowman et al., 2008) and along the satellite track (Connor et al., 2016; Shim et al., 2012).

The community need at the current state is to be able to run the models for the real-time operations and the real-time calculations of atmospheric drag acting on the satellites. For this purpose, there is a need to assess the performances of the models and to specify the conditions when they perform satisfactorily and when they do not. Shim et al. (2011) compared the model results with the local measurements available from EISCAT radars for the ionospheric parameters NmF₂, hmF₂ and vertical drift with limited latitudinal coverage. Shim et al. (2012) focused on the space-borne measurements of the NmF₂, hmF₂, ionospheric electron density and thermospheric neutral density along the satellite track at the measurement locations. NmF₂ and hmF₂ from the models were compared with the observations from the Constellation Observing System for Meteorology, Ionosphere and Climate (COSMIC) while ionospheric electron density and thermospheric neutral density were compared using the measurements from Challenging Mini Satellite Payload (CHAMP). In both studies, root mean square error (RMSE), prediction efficiency (PE), ratio of (max-min) and ratio of maxima were employed to assess the model performances. They reported that the model performances depend on the metrics used and varied with latitude and geomagnetic levels. No models outperformed others in estimating the thermospheric and ionospheric parameters in all cases. Moreover, regarding the thermospheric neutral densities, models with high RMS yielded low prediction efficiencies. Additionally, storm-time PEs were higher than the quiet-time PEs. However, RMSE were largest during the geomagnetic storms due to the large variation in the neutral

densities, and PEs from the models did not show any systematic behavior dependent on geomagnetic activity.

2.4 Geomagnetically Induced Currents

Understanding the space weather is essential for our space-born and ground based technological systems as well as astronauts in orbit and air crews on polar flights. One of the most direct and observable consequences of space weather on the ground is the enhanced currents which are known to be Geomagnetically Induced Currents. These currents flow through Earth-grounded systems and units that are composed of electrically conducting components, modulate the electrical currents on our power systems, result in failures in city power grids, telecommunication systems, and lead to corrossions in railways and pipelines that are used for the transport of oil in long distances.

A latest Space Weather issue (24 March 2016) compiles all the studies of GICs up to date published in different journals. It gives an exclusive collection of GIC studies including the sources, latitude variations, storm-substorm relations, modelling, hazards on ground systems, and measurement systems. In this study, we present the measurements of GICs at our latitudes, 37.5°N MLAT (Magnetic LATitude), bring out their characteristics and discuss the possible causes for their occurrences. GICs and their effects at different latitudes were studied widely and established well (Araki, 1994; Araki et al. 2006; Curto et al. 2007, Rastogi et al. 1997, Tsunomura, 1998; Trivedi et al., 2007; Wik et al., 2008; Liu et al. 2014; Watari et al. 2009; Marshall et al. 2012; Torta et al. 2012; Torta et al. 2014; Barbosa et al., 2015; Matandirotya et al. 2015). Most of these studies used power grids to investigate GICs extensively, e.g. Wei et al. (2013) in North America, Boteler et al. (1998) in Canada, Viljanen and Pirjola (1994) in Finland, and Beamish et al. (2002) in UK-Scotland, Zhang et al. (2015) in China, Béland and Small (2004) in New Zealand, Pulkkinen et al. (2005) in Sweden. Depending on the latitude and strength of the magnetospheric activity, GIC magnitudes were found to vary from 10s of Amperes (A) to several hundreds of Amperes. Kappenman (2003) reported GICs on the order of 200 A in high latitude regions of US. Watari et al. (2009) estimated GICs in central Japan on the order of 45 A during 13 July 1982 storm that caused 796 nT change in the horizontal component

of the magnetic field. Trivedi et al. (2007) found GIC amplitudes of about 15 A in Brazil.

Mid- and low latitude GICs show similar signatures in general. Low latitude GICs or GICs at equatorial latitudes are dominated by the effects of the equatorial electrojet and superimposed on them are the effects from the magnetopause currents (Zhang et al., 2015). The main source of the large GICs occurring at the midlatitudes were found to be associated with the storm sudden commencement (SSC) or sudden impulse (SI) resulting from shocks in the solar wind (Marshall et al. 2012; Béland and Small 2004; Huttunen et al. 2008, Fiori et al. 2014). CMEs or CIRs (Corotating Interaction Regions) cause GICs as a result of the increased dynamic pressure at the subsolar magnetopause (Huttunen et al.2008; Fiori et al. 2014). Increased dynamic pressure creates magnetopause currents and gives rise to sharp increases in the magnetic field components measured on the ground. The sharp positive rise seen in Dst in response to the increase in magnetopause currents was named as Sudden Impulse (SI) and if this increase was followed by a main phase of the geomagnetic storm, then it was called storm sudden commencement (SSC). The effects of SSC and SIs in producing GICs were examined together in Fiori et al. (2014) under a generalized term “sudden commencement (SC)” to cover the effects of either SSC or SI. The similar terminology was also suggested by Joselyn and Tsurutani (1990) if the follow up main phase of the geomagnetic storm starts within the 24 hour after the sudden impulse was seen. While at lower and midlatitudes the driver of the GICs are mainly the increase in the magnetopause currents (Zhang et al. 2015; Fiori et al. 2014), at high latitudes, auroral currents (e.g. Viljanen, 1997; Viljanen and Tanskanen 2011; Fiori et al. 2014) and at equatorial and low-to-midlatitudes, equatorial electrojet contribute further on the effects of magnetopause currents (Carter et al. 2015; Zhang et al. 2015). Largest GICs at low and midlatitudes occurred during the main phase of the geomagnetic storms as associated with the intensification of the ring current (Zhang et al. 2015; Kappenmann 2006; Liu et al. 2009). However, GICs that occurred in response to SSCs were found to be stronger than those produced during the storm main phase (Zhang et al. 2015). The solar wind causes of GICs were studied in detail by Huttunen et al. (2008). They showed that the sheath and boundary layer regions of Interplanetary Coronal Mass Ejections (ICME) gave rise to stronger GIC variations than that of the ejecta. Fiori et al. (2014) grouped and compared the variations in the horizontal component of the

magnetic field whether resulting from CME or High Speed Streams (HSS). They demonstrated that the CMEs were the main driving source for the strong high latitude enhancements of the horizontal component of the magnetic field while weak or absence of high latitude enhancements in the horizontal component of the magnetic field are caused by both CMEs and HSS. These suggest that the shock in the solar wind velocity is a strong contributing factor to the stimulation of the strong ionospheric plasma convection flows within the auroral oval that give rise to geomagnetic disturbances on the ground levels (McPherron, 1991).

Viljanen et al. (2001) studied GICs by analyzing the variations in the time derivative of the horizontal magnetic field from 1982 to 2001 and showed that the strong GICs were associated with deviations larger than 1 nT/s in the time derivative of the horizontal magnetic field. The sudden increases in the time derivative of the magnetic field (dB/dt) in response to SCs were observed independent of the occurrence of the geomagnetic storm (Fiori et al., 2014; Zhang et al., 2015). In their study, any change in dB/dt larger than 1.67 nT/s induced GIC currents, however, variations above 3.33 nT/s resulted in strong GIC events, especially at high latitudes. This was attributed to the effects of the ionospheric plasma convection superimposed on the sudden commencement effects at the high latitudes (Fiori et al, 2014). As a continuation of their work, Viljanen et al. (2006) studied GICs larger than 1 nT/s for isolated (according to their terminology) substorms, namely $Dst > -40$ nT, and storm-time, $Dst < -40$ nT, substorm events using the time derivative of the horizontal magnetic field. They examined GIC occurrences in association with the ionospheric equivalent current systems and as a function of substorm phase. Their study showed that the maximum variation of time derivative of the horizontal magnetic field decreased with decreasing latitudes toward south in the north. Also in their study, the time of the maximum in the time derivative of the horizontal magnetic field peaked at lower latitudes for isolated events and occurred 5 min after the onset. The latitudinal distribution of the time derivative of the horizontal magnetic field was found to be scattered for storm-time substorms. The authors showed that the time derivative of the horizontal magnetic field displayed large east-west component (B_y) compared to north-south (B_x) component. They interpreted this as an indication of the smaller scale structures in the ionospheric current systems in addition to the rapid changes in the main electrojet. These affected the magnitude of the variations which were found to be larger for the storm-time

substorms than for isolated substorms. Furthermore, in their study using a large data base from 1983 to 2010, Viljanen and Tanskanen (2011) showed that the nighttime GICs inferred from the variations in the time derivative of the horizontal magnetic field were larger than those occurring during daytime. Their key finding was the presence of two maxima in the GIC occurrences in the auroral region; i.e. one around midnight and the other is around morning. They indicated that while the nighttime maximum in GIC occurrences was associated with the westward currents in the auroral electrojet, morning maximum was due to the east-west flowing currents in the ionosphere. The authors suggested a different cause for the GICs occurring in the morning, i.e. mechanisms other than or in addition to the ionospheric currents such as ULF waves. Similarly, Watari et al. (2009) reported GICs associated with ULF waves and Pc3 and Pc5 pulsations in midlatitudes in their study carried out in Japan (35.4° N).

Several methods were proposed for determining the GIC variations on the ground (Langlois et al. 1996; Boteler 1990). The most straightforward computation of GICs at a point on the ground requires knowledge of ground conductivity (Viljanen et al. 2004) and the geoelectric field through Ohm's law. Therefore, both the conductivity of the region and the measurements of geoelectric field are needed. However, determining the ground conductivity in different parts of the world is complicated as it depends on factors that are not easy to obtain using observations (Poll et al. 1989). Additionally, geoelectric field on the ground is also seldom directly measured quantity. In calculations of GIC studies, different approaches were used for geoelectric fields. In most of the GIC studies, the geoelectric fields on the ground were obtained from the electrical power grids. However, the grid parameters in many parts of the world are not easily known. The geomagnetic variations detected on the ground are also associated with variations in the electric field. Therefore, an alternative approach for assessing GICs at a point is to use the Faraday's induction law. Faraday's Law states that temporal variations in geomagnetic field produce variations in the geoelectric field. Therefore, GICs can be calculated by measuring the variations in these two parameters on the ground, namely the time rate of change of magnetic field and/or electric field directly. Many of the GIC studies were built on the geomagnetic field measurements rather than geoelectric fields because, compared to the electric field measurements, they are continuous, spatially cover wide ranges and long term, thus give a good opportunity to study GICs both temporally and spatially in a larger area.

Therefore, time derivatives of magnetic field were used in many studies to infer to the GIC variations in the absence of electric fields (Viljanen et al. 2001; 2006; Viljanen and Tanskanen 2011; Fiori et al. 2014; Zhang et al. 2015).



3. DATA

In this study, to depict the state of the ionosphere and thermosphere and to compare and validate the model estimations we utilized observational data from radars and LEO satellites. For the ionospheric electrodynamics part and the Joule heating study, we used the Super Dual Aural Radar Network data to obtain the electric fields. To determine the thermospheric neutral density variations during geomagnetic storms, Challenging Micro Satellite Payload (CHAMP) measurements were employed. The subsections 3.1 and 3.2 of this chapter present the properties of these data sets.

3.1 Super Dual Auroral Radar Network (SuperDARN)

SuperDARN is a result of an international collaboration between United States, France, United Kingdom, Canada, Japan, South Africa, Australia, China, Italy and Norway. It comprises of 11 radars in the northern hemisphere and 7 radars in the southern hemisphere (Chisham et al., 2007). Figure 3.5 shows the fields of view of SuperDARN radars in the northern and southern hemispheres.

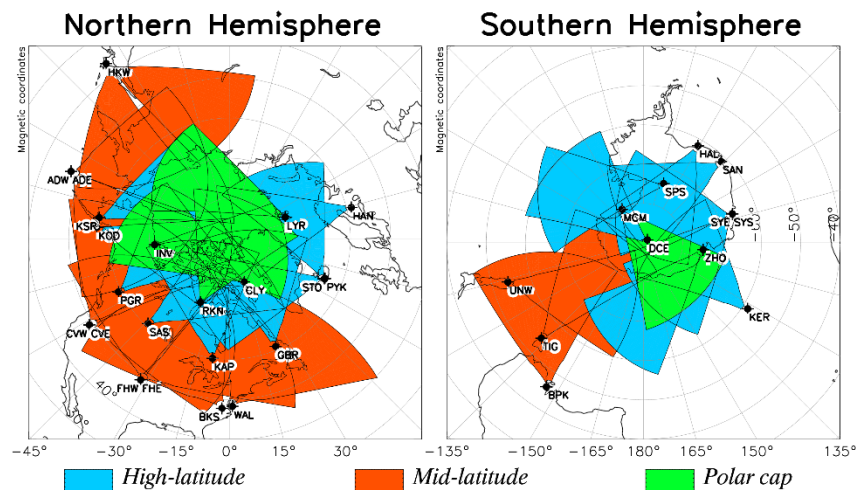


Figure 3.1 : The SuperDARN radar locations in a) Northern b) Southern hemispheres (Url-2).

Ionospheric irregularities in the E and F regions in the high-latitude region are monitored by use of high frequency (HF) and very high frequency (VHF) coherent-backscatter radars (Chisham et al., 2007; Greenwald et al., 1995). The primary research interests for the SuperDARN radars are:

1. To explore the structure and dynamics of the ionospheric convection
2. To measure the incoming energy from the MHD waves
3. To investigate the variations in the polar cap in response to the variable IMF conditions
4. To observe the plasma structures at high-latitudes, ionospheric irregularities and the gravity waves (Greenwald et al., 1995).

Using SuperDARN observations, the estimates of ionospheric electric fields can be obtained. To obtain the high-latitude potential pattern and the electric fields, velocity measurements from the radars are fitted to the convection pattern and the lacking points are filled with a weakly-sampled set of statistical velocity data that is keyed to the IMF (Ruohoniemi and Baker, 1998; Shepherd and Ruohoniemi, 2000).

3.2 Challenging Mini Satellite Payload (CHAMP)

CHAMP is a German satellite mission designed primarily to measure the Earth's gravity and magnetic field. Its secondary purposes include observing the atmosphere and ionosphere for weather prediction and space weather monitoring. CHAMP was managed by the Helmholtz-Zentrum Potsdam GFZ German Research Center for Geosciences, with its old name, GeoForschungsZentrum (GFZ). It was launched in 2000. The mission ended in September, 2010 with CHAMP's burning down during its entry to lower atmosphere. The orbital altitude started with 460 km and lowered to 300 km close to the end of the mission. It had an orbital period of 93.5 minutes and a near-circular orbit with a 83.7 inclination (Lu et al. 2017). In our work, we get use of the neutral density data derived from the accelerometer on CHAMP (Mehta et al., 2017; Sutton et al., 2007). The difference between the two data sets is the drag coefficients they use dependent on the geometry of the satellite. Mehta et al., 2017 provides the most recent calculations of thermospheric neutral density. Consequently its usage is more strongly supported.

4. MODELS

In our study, we utilize the state-of-the-art ionosphere-thermosphere models and coupled magnetohydrodynamic (MHD) models to study the variations of the parameters in the ionosphere and thermosphere. Coupled space weather and ionosphere-thermosphere models provide extensive opportunities to study the space weather chain and the extent and limits of the space weather effects in different domains. These models act as numerical laboratories. They fill the gap when there are not enough observations to study the global dynamics. In addition, they offer a framework to understand the system which ideas can be tested (Crowley, 2015; Ridley, 2003). However, the models still lack a perfect representation of the space environment and they need to be validated and calibrated according to the observations. The models that were used in this study are described in the following subsections.

4.1 Magnetohydrodynamic (MHD) Models: SWMF/BATSRUS

MHD approximation provides the macroscopic perspective for the dynamics of plasma environments. In MHD approach, the bulk motion of the plasma is studied. The plasma is considered as a fluid which is governed by the electromagnetic, pressure, viscosity, and gravity forces. Maxwell's equations are incorporated to the hydrodynamics approach to obtain the MHD equations. The ideal MHD does not contain the resistivity, viscosity, gravity, Coriolis (rotation), ionisation, radiation transport and thermal conduction terms. Plasma is solely driven by the magnetic pressure and tension. Thus, ideal MHD is only valid for the low frequency, large scale motions in which the scales are larger and slower than the scales that of the gyromotion of the particles.

In MHD models, ionosphere coupling is done by considering the ionosphere is a thin spherical shell. Furthermore, ionosphere completes the current closure within the magnetosphere via the field-aligned currents in between the magnetosphere and ionosphere domains. In most MHD models, the coupling is handled by use of a Poisson equation solution to the current continuity equation (Merkin and Lyon, 2010).

We used the Space Weather Modeling Framework / Block-Adaptive-Tree-Solarwind-Roe-Upwind-Scheme (SWMF-BATSRUS) model throughout this study. BATSRUS uses appropriately lagged ACE solar wind plasma and IMF as inputs for an ideal MHD environment. Roe's approximate Riemann solver (Roe, 1981) is utilized for the calculations. The ionosphere is coupled with the inner magnetosphere through the field-aligned currents. Ionospheric potentials are then solved from the FACs using the current continuity equation (De Zeeuw et al., 2004; Honkonen et al., 2013). The Ionospheric Electrodynamics (IE) module utilizes a statistical auroral conductivity model and returns the ionospheric parameters such as electrical potentials, electric fields, and conductances (Ridley et al, 2004; Toth et al., 2005).

4.2 Physics-based Models of the Ionosphere-Thermosphere

Physics based models of the ionosphere-thermosphere aim to provide the temporal evolution of the parameters in the ionosphere-thermosphere system. Within the physics-based models, the components self-consistently operate and communicate with each other to provide the state of the system. Self-consistency, here, means the the solutions satisfy all the equations in the system and momentum, energy and continuity equations are treated instantaneously (Fuller-Rowell and Rees, 1980). Models of the IT system employ the momentum, energy and continuity equations for each species separately. Below, we briefly describe the most used state-of-the-art IT models used in our study.

4.2.1 Thermosphere Ionosphere Electrodynamics General Circulation Model (TIEGCM)

The TIEGCM is developed at the National Center for Atmospheric Research High-Altitude Observatory (NCAR-HAO). For the neutrals, it solves the nonlinear, hydrodynamic, thermodynamic, momentum, energy and continuity equations and for ions, the ion continuity equation, as well as the ion and electron energy equations and the neutral wind dynamo (Qian et al., 2014). It has a long development history. The model started as a thermosphere general circulation model (Dickinson et al., 1981; Roble et al., 1982). The ionosphere was subsequently added by (Richmond et al., 1992) and self-consistency was achieved via the addition of electrodynamics effects. The TIEGCM can work with either of the Assimilative Mapping of Ionospheric

Electrodynamics (AMIE), Heelis et al. (1982) or Weimer (2005) ionospheric potentials. The model resolution is $5^{\circ}\times 5^{\circ}$ (latitude \times longitude) and the default time step is 2 minutes. For a detailed review and more information the reader is referred to (Qian et al., 2014).

4.2.2 Coupled Thermosphere Ionosphere Plasmasphere Electrodynamics (CTIPe)

To calculate the neutral winds, the neutral, ion and electron temperatures, mass mixing ratios, ion and electron densities and the electric potential in ionosphere-thermosphere, CTIPe model comprises of four main components, namely, the global thermosphere (Fuller-Rowell and Rees, 1980), the high-latitude ionosphere (Quegan, 1982; Quegan et al., 1982), the mid-low latitude ionosphere-plasmasphere (Bailey and J., 1983) and the global dynamo electric field (Millward et al., 2001; Richmond et al., 1992). Hemispheric power (itself or hemispheric power index), a model for high latitude potential pattern, F10.7, solar wind data and Earth's dipole tilt are required for the simulation to run (Codrescu et al., 2008). The output resolution is in $2^{\circ}\times 18^{\circ}\times 15$ (latitude \times longitude \times pressure levels). It solves the non-linear, first-principles equations of momentum, energy and continuity (Fuller-Rowell and Rees, 1980). NOAA-SWPC and CCMC/iSWA interface runs CTIPe for real-time total electron content estimations (Codrescu et al., 2012).

4.2.3 Global-Ionosphere-Thermosphere Model (GITM)

GITM is a coupled ionosphere-thermosphere model, which is developed by Ridley et al. (2006) from the University of Michigan. It differs from the other ionosphere-thermosphere models with its non-hydrostatic approximation. GITM solves the full momentum equation, so that non-hydrostatic effects are demonstrated and works in altitude rather than a pressure level based coordinate system (Deng et al., 2008). The GITM can be run with a temporal resolution as short as 2 seconds. The horizontal resolution is $2.5^{\circ}\times 5^{\circ}$ (latitude \times longitude) and the model extends from 90 km to 600 km.

4.3 Empirical Models of the Ionosphere and Thermosphere

Empirical models of the ionosphere and thermosphere provide the average state of the parameters in interest based on historical data. The empirical models were built to obtain a climatological view of the ionosphere/thermosphere. They are generally employed to validate the physics-based models when there is lack of data. In this work, we use the empirical models for model-model and model-data comparisons. The following subsections briefly describe the models used in this study.

4.3.1 Weimer model: Weimer05

Weimer-2005 (W05) model is an empirical model which uses the Dynamics Explorer-2 (DE-2) spacecraft data to calculate the Poynting flux from the field-aligned currents and electric potentials without the use of conductivities (Weimer, 2005). Under the quasi-static approximation, Poynting flux is assumed equivalent to the global Joule heating rate (Vanhamäki et al., 2012). It includes both the mechanical energy consumed by the neutral wind and the electromagnetic energy dissipated by the Joule heat (Palmroth et al., 2005). The model inputs are the solar wind parameters and dipole tilt angle of the simulated event. AL index is also an optional input to the model. We run the Weimer model from the CCMC interface with the AL option on.

4.3.2 International Reference Ionosphere-2012: IRI2012

International Reference Ionosphere (IRI) model is a product of the Committee on Space Research (COSPAR) and International Union of Radio Science (URSI). IRI was initiated as a result of the needs of the satellite operators and experiments in space as well as the studies of and applications on the radiowave propagation (Bilitza et al., 2014). The IRI is built on data from worldwide ionosondes, incoherent scatter radars (Jicamarca, Arecibo, Millstone Hill, Malvern, St. Santin), the ISIS and Alouette topside sounders and in-situ instruments on satellites and rockets. IRI is updated yearly. The latest version of the IRI is the IRI-2016 (Bilitza et al., 2017). The latest version provides the monthly mean of the ionospheric parameters: electron density, electron temperature, ion temperature, ion composition (O^+ , H^+ , He^+ , N^+ , NO^+ , O_2^+ , Cluster ions), equatorial vertical ion drift, vertical ionospheric electron, F1 probability, spread-F probability, auroral boundaries, effects of ionospheric storms on F and E peak

densities. For detailed information the reader is referred to (irimodel.org; Bilitza et al., 2014, Bilitza et al., 2017).

4.3.3 Mass Spectrometer and Incoherent Scatter Radar Exosphere (NRLMSISE-00)

The NRLMSISE-00 is the updated version of the MSIS model (Hedin, 1991). Its data comprises of satellite, rocket and incoherent scatter radar measurements. The model provides altitude profiles of temperature, number densities of species (He, O, N₂, O₂, Ar, H, and N), total mass density, and the number density of a high-altitude anomalous oxygen component of total mass density (Picone et al., 2002).

4.3.4 Jacchia-Bowman 2008: JB2008

Jacchia-Bowman 2008 model is the updated version of the Jacchia-Bowman 2006 (Jacchia and Bowman, 2006) and Jacchia model (Jacchia, 1970). The model uses data from Air Force from 1997-2007, HASUPERDARNM (High Accuracy Satellite Drag Model) densities from 2001 to 2005, CHAMP density values from 2001 to 2005 and GRACE accelerometer measurements from 2001 to 2005 (Bowman et al., 2008). The Air Force density values are derived from the drag analysis of satellites with perigee altitudes of 175 km to 1000 km. JB2008 provides the exospheric temperatures and thermospheric neutral density.

4.3.5 OVATION Prime

OVATION Prime (OP) is an empirical auroral precipitation model. The model specifies aurora in four types: monoenergetic and broadband aurora and electron and ion diffuse aurora (Newell et al., 2009; 2010). It can be run for historical times as well as for forecast purposes. The OVATION Prime model has the advantage of covering an entire solar cycle between January 1, 1988 to December 31, 1998 (Newell et al., 2009). The data for the post-noon and post-midnight sectors cover the years from 1992 to 1998 from the declining of the solar cycle 22 and the beginning of the solar cycle 23. Thus, seasonal variations are included reasonably well within the model.

4.4 Inputs to Models

In the previous subsections, the empirical and physics-based models of the ionosphere-thermosphere were described basically. In order to run the models, a user first needs to specify the initial state of the thermosphere and the ionosphere by inputting several parameters to the models. Table 4.1 presents the inputs to the empirical and physics-based models.

Table 4.1 : Inputs to the ionosphere-thermosphere models.

Model Name	Model Type	Model Inputs
NRLMSIS	Empirical	F10.7, daily Ap, 3 hourly ap
JB2008	Empirical	Dst, ap, F10.7, S10.7, M10.7, Y10.7
TIEGCM	Physics-based	F10.7, 81-day center averaged F10.7 (F107A), Hemispheric Power for usage with Weimer: IMF B_x , B_y , B_z , solar wind speed, for tides: GSWM
CTIPe	Physics-based	F10.7, ACE Level 2 solar wind data, Earth's dipole tilt angle, NOAA/POES hemispheric power data
GITM	Physics-based	F10.7, Solar irradiance, Hemispheric Power index, Weimer electric field, Fuller Rowell and Evans (1987) for auroral precipitation pattern, MSIS and IRI for the initial state of the thermosphere. For usage with Weimer: IMF B_x , B_y , B_z , solar wind speed, for tides: GSWM

Precise determination of the inputs to the models are important as the output of the models are strictly bound to the initial conditions of the ionosphere and thermosphere.

5. UPPER ATMOSPHERIC JOULE HEATING

As thoroughly explained in the literature survey in Chapter 2.1, upper atmospheric Joule heating can be calculated using various methods by either omitting or including the neutral wind effect. In this chapter, we present the methods, which were utilized to calculate the Joule heating in this study, in addition to their results for the selected cases.

Overall, we calculate the global JH using four methods: (1) empirical-statistical relations based on indices, (2) combinative methods without the neutral wind effect, (3) MHD and I-T model outputs by taking the neutral wind into account and (4) from empirical models.

Since several model outputs and, when available, observations were brought together to calculate the JH rate in some of the methods, their success depends strongly on the accuracy of the model assumptions and the measurements.

We describe the methods and introduce the selected events in the following subsections.

5.1 Selected Substorm Cases

On March 8, 2008, two successive substorms occurred from 11:00 UT to 21:00 UT in response to a Coronal Mass Ejection (CME) observed at 07:00 UT by Advanced Composition Explorer (ACE) with a speed of 400 km/s and density of 25 #/cm³ on the average. During the event interval, Interplanetary Magnetic Field (IMF) B_z turned southward twice and gave rise to a substorm. Both substorms were identified as isolated substorms according to the criteria defined by Kallio et al. (2000) and Tanskanen et al. (2002b) since Dst did not reach values lower than -40 nT and there were more than 3 hours between the expansion onsets (Liou et al., 2013). We note that the same events were studied by Wang et al. (2011) in the context of equivalent ionospheric currents.

Figure 5.1 presents the IMF and solar wind upstream data from ACE corresponding to the event interval. The first five panels are solar wind speed, density, IMF B_x, B_y, and B_z given in GSM coordinates. These data were propagated to the Earth's magnetopause based on the instantaneous solar wind speed and were obtained from the National Space Science Data Center (NSSDC) OMNIWeb (<http://nssdc.gsfc.nasa.gov/omniweb>).

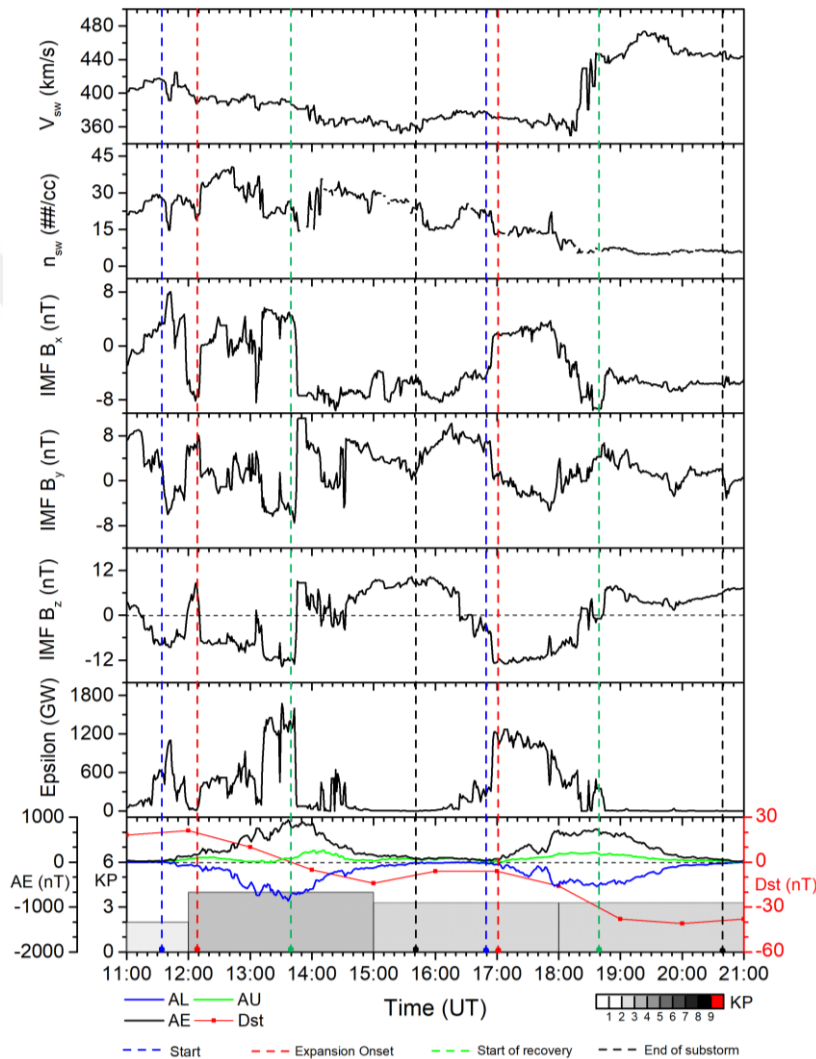


Figure 5.1 : Top five panels: IMF and solar wind upstream data in GSM coordinates from ACE spacecraft. Bottom two panels: Epsilon parameter and geomagnetic indices (AU/AL, AE, KP, Dst).

The last two panels in Figure 5.1, respectively, are, the solar wind power at the subsolar point of the magnetopause measured by Akasofu's Epsilon parameter (Epsilon in short) and geomagnetic indices AE/AU/AL, KP, and Dst. Epsilon is calculated using Equation (5.1) below, which was constructed by Perrault and Akasofu (1978)

$$\varepsilon = 4\pi/\mu_0 vB^2L^2 \sin^4(\theta/2). \quad (5.1)$$

In this equation, L ($\sim 7 \text{ Re}$) is the scale parameter, v is the solar wind speed, B is the IMF magnitude and θ is the clock angle given as $\tan(\theta) = B_y/B_z$.

We identified the boundaries of the substorm phases by examining the variations in the AL index. The start of an individual substorm is identified as the time when the variations in the AL index are greater than the mean of the variations prior to this time (the quiet time mean of AL). Following the methodology of Tanskanen (2009), the time of the expansion onset is marked as the time when at least a 100 nT decrease in AL is observed and the rate of decrease is greater than 80 nT in 15 min. We mark it as the start of the recovery phase when the AL index starts to return to the quiet time values. The end of the substorm is identified as the time when the AL reaches to its background levels. Based on this classification of the substorm phases, the dashed vertical lines from left to right as seen in Figure 1 identify the start of the Growth phase (SG, blue), the Expansion Onset (EO, red), the start of the Recovery phase (SR, green) and end of the substorm (ESS, black) respectively for both substorms. This representation is implemented in all figures throughout this thesis.

Accordingly, the first substorm starts at 11:37 ending at 15:40 UT lasting ~ 4 hours while the second substorm starts at 16:50 UT and ends at 20:40 UT lasting 3:50 hours. All data presented in Figure 1 are in 1-min resolution. Two moderate substorms correspond to the southward turnings of IMF B_z and cease when IMF B_z turns northward. When compared to the second substorm, IMF B_z fluctuations are seen to be slightly more during the first substorm. Since Epsilon follows the variations in the direction of IMF B_z , it shows faster variations during the first substorm and smoother, slower variations during the second substorm. Several intensifications in the AE index are seen in response to the variations in the IMF direction.

5.2 Indice-based Methods

In this study, we use the AE, KP and IL indices to calculate JH from geomagnetic indices. Each indice has different sets of coefficients, even though, all relations are in the form of linear equations.

For the AE index-based methods, we use two different sets of coefficients in equation (2.3). The first set of coefficients follows the work of Ahn et al. (1983). Since our two

substorm events occurred in March and the number of stations is appropriate for our study, we used $a_1=0.23$ and $b_1=0.0$. The second set of coefficients were given by (Olsson et al., 2004), which is independent of the season. In their work, $a_2=0.36$ and $b_2=-2.36$. This method is called as the Olsson method, hereafter. To display the lowest and highest JH estimates from statistical methods, IL and KP indices are also employed to calculate JH. The global Joule heating found by using IL index is called IL index method, or shortly IL and has a linear relationship similar to Equation (2.3). AE and IL methods represent the global Joule Heating over an area poleward of $\sim 60^\circ$ geomagnetic latitude. While AE stations are distributed among most of the MLT sectors but limited latitudinally, IL uses the IMAGE magnetometer stations, which are longitudinally restricted providing the best estimates between 16 UT-02 UT (Tanskanen et al., 2002) and latitudinally distributed from $\sim 56^\circ$ to $\sim 76^\circ$ N (Kauristie et al, 1997). In addition to the methods based on AE and IL, to give an overall picture, Foster et al. (1983) relation based on KP, which has 3 hours cadence is utilized and is named as the KP method. Similar to the AE and IL, the KP method assumes/displays a linear relationship between the KP and JH.

Table 5.1 : Summary of the methods for JH based on geomagnetic indices.

Method	Electric Field	Conductance	Joule Heating	Res (min)
AE	None	None	$a_1AE + b_1;$ ($a_1=0.23$ GW/nT, $b_1=0$)	2
Olsson	None	None	$a_2AE + b_2;$ ($a_2=0.36$ GW/nT, $b_2=2.76$)	2
IL	None	None	$cIL[nT] + d;$ ($c=0.3$ GW/nT, $d=0$)	2
KP	None	None	$4 + 20$ KP	180

5.3 New Combinative Methods

Six different combinations can be obtained for combinative methods depending on the source of the electric field and conductance data, which are needed to calculate JH rate as given in Equation (2.2) and Table 5.2. The name of the method is constituted by two uppercase characters: the first indicates the source of conductance, and the second represents the source of electric fields. Table 5.2 presents the methods and the data sources, which were utilized in JH calculations for the combinative methods.

Table 5.2 : Summary of the methods for JH without the neutral wind.

Method	Electric Field	Conductance	Joule Heating	Res (min)
IB	BCRCM	IRI	$\Sigma_p E_{\perp}^2$	2
IS	SuperDARN	IRI	$\Sigma_p E_{\perp}^2$	2
OIB	BCRCM	OP+IRI	$\Sigma_p E_{\perp}^2$	2
OIS	SuperDARN	OP+IRI	$\Sigma_p E_{\perp}^2$	2
BS	SuperDARN	BCRCM	$\Sigma_p E_{\perp}^2$	2
BB _{crfm}	BCRCM	BCRCM	$\Sigma_p E_{\perp}^2$	2
BB _{rcm}	BRCM	BRCM	$\Sigma_p E_{\perp}^2$	10

Since global, continuous and real-time observations of ionospheric conductances are not available, we used dayside conductances derived from International Reference Ionosphere Model (IRI2012), nightside conductances derived from OVATION Prime, and conductances from Ionospheric Electrodynamics (IE) module of the BATSRUS. Electric fields in Equation (2.2) were obtained using the SuperDARN radar chain and BATSRUS IE.

The estimates of ionospheric electric fields from SuperDARN are obtained by fitting velocity measurements from the radars with a sparsely-sampled set of statistical velocity data that is keyed to the IMF (Ruohoniemi and Baker, 1998; Shepherd and

Ruohoniemi, 2000). For March 8, 2008 events, the observations are mostly concentrated on the dayside spanning dawn, noon and dusk sectors. However, there is also some coverage in the nightside sector between 14:08 to 14:42 UT and 18:04 to 18:44 UT. Shaded areas in plots that depend on SuperDARN data indicate the time intervals when there is data in the nightside sector from SuperDARN. We use these time intervals to inspect the effect of data coverage on the JH calculated using the electric field obtained from SuperDARN.

BATSRUS uses appropriately lagged ACE solar wind plasma and IMF as inputs and couples the ionosphere with the magnetosphere through field-aligned currents (FACs). Ionospheric potentials are then solved from the FACs using the current continuity equation (De Zeeuw et al., 2004; Honkonen et al., 2013). The Ionospheric Electrodynamics (IE) module utilizes a statistical auroral conductivity model and returns the ionospheric parameters such as electrical potentials, electric fields, and conductances (Ridley et al, 2004; Toth et al., 2005). We run the BATSRUS model remotely on Community Coordinated Modelling Center (CCMC) computers (<http://ccmc.gsfc.nasa.gov>) with all its modules and updated dipole tilt. Two versions of the model were employed in our study: the first simulation results belong to a run with 10 min. resolution (Emine_Kalafatoglu_072709_1), which couples the BATSRUS and the Rice Convection Model (RCM). The second version is BATSRUS coupled with Comprehensive Ring Current Model (CRCM), which has 2 min. resolution (Emine_Kalafatoglu_022018_1). The RCM and CRCM are both ring current models that modify the plasma pressure distribution in the inner magnetosphere. Both models use the kinetic approach to model the ring current. However, the CRCM provides information on both the energy and pitch angle, enabling the investigation of the processes that lead to the scattering into the loss cone (Glocer et al., 2013). The two runs were used to bring out the differences between BATSRUS/RCM (BRCM) and BATSRUS/CRCM (BCRCM) in determination of JH rates. However, combinative methods were constructed using the CRCM outputs for the electric field and conductances. In Figure 5.1, the top five panels show the input to the models for the periods of our substorm events.

Conductances were obtained by combining two empirical models: International Reference Ionosphere-2012 (IRI2012) for the sunlit hemisphere and OVATION Prime derived conductances for the nightside auroral oval. However, the OP has a salt-and-pepper noise problem due to the heavy number of regression fits in the model as

indicated in (Newell et al., 2014). In our work, the overlapping of the salt-and-pepper noise in conductances and strong ionospheric electric fields may lead to unreliable, extreme JH values at the regions, which contain noise. Hence, the salt-and-pepper noise in the OP precipitation patterns were removed using MATLAB two-dimensional median filtering function (medfilt2) before the calculation of the conductances. Empirical relationships developed by Robinson et al. (1987) were employed to obtain the nightside conductances from the electron precipitation given by the OVATION Prime (OP) model. Proton precipitation and its effect on conductances were specified using the Galand & Richmond (2001) formulation. All calculations, except the index-based methods, were performed on a ($1^\circ \times 2^\circ$) (latitude \times longitude) spatial resolution. On the other hand, the conductances from IRI2012 (Bilitza et al., 2014) were first obtained in $10^\circ \times 15^\circ$ (lat \times long) resolution using the ionospheric conductivity model on WDC (Kyoto's web page: <http://wdc.kugi.kyoto-u.ac.jp/ionocond/sigcal/>). Following this, they were interpolated to the SuperDARN and BATSRUS electric field grid points. Global representation of the conductance pattern was obtained by adding the IRI conductances to the OP derived nightside conductances, spatially.

After preparing all quantities in the same resolution and at the same grid points, the local height-integrated JH rates were calculated by multiplying the conductances with the corresponding electric fields at the same grid locations. The local height-integrated JH rate at each latitude, longitude grid point was scaled by multiplying the resulting JH with the associated area of the grid spacing. Then, the summation of the scaled JH rates above 60° magnetic latitude was divided by the total area of the polar region ($>60^\circ$ latitudes) to obtain the globally averaged JH rates.

5.4 Methods with the Neutral Wind

The procedure for the calculation of JH with the neutral wind is similar for BB_{nw_crcm} and BB_{nw_rcm} , which use BATSRUS output of the Cowling conductance (determined from Pedersen and Hall conductances) and the ionospheric horizontal currents to calculate JH as described in Equation (2.4).

Weimer-2005 (W05) model is an empirical model which uses the Dynamics Explorer-2 (DE-2) spacecraft data to calculate the Poynting flux from the field-aligned currents and electric potentials without the use of conductivities (Weimer, 2005). Under the quasi-static approximation, Poynting flux is assumed equivalent to the global Joule

heating rate (Vanhamäki et al., 2012). It includes both the mechanical energy consumed by the neutral wind and the electromagnetic energy dissipated by the Joule heat (Palmroth et al., 2005). The model inputs are the solar wind parameters and dipole tilt angle of the simulated event. AL index is also an optional input to the model. We run the Weimer model from the CCMC interface with the AL option on. The simulation results can be reached from (Emine_Kalafatoglu_021218_IT_2).

Table 5.3 displays the methods to find the JH with the neutral wind from the W05 and BATSRUS.

Table 5.3 : Methods to determine the neutral wind contribution and the resultant Joule heating.

Method	Electric Field	Conductance	Joule Heating with neutral wind	Res (min)
BB _{nw_crcm}	J from BCRCM	$\sigma_c: \sigma_P, \sigma_H$ from BCRCM	$\int_{90 \text{ km}}^{z_{upper}} \frac{J(z)_{\perp}^2 \sigma_P(z)}{(\sigma_P(z) + \sigma_H(z))^2} dz$	2
BB _{nw_rcm}	J from BRCM	$\sigma_c: \sigma_P, \sigma_H$ from BRCM	$\int_{90 \text{ km}}^{z_{upper}} \frac{J(z)_{\perp}^2 \sigma_P(z)}{(\sigma_P(z) + \sigma_H(z))^2} dz$	10
W05	Electric and magnetic potentials from DE-2	-	$\vec{E} \times \Delta \vec{B} / \mu_0$	2

5.5 Detailed Analysis on March 8, 2008 Substorm Cases

In this section, we present our results in the following order: temporal variations (Section 5.5.1) and substorm phase dependence (Section 5.5.2), spatial variations (Section 5.5.3), magnetic local time and magnetic latitude dependences (Section 5.5.4) and the role of conductivity and electric fields (Section 5.5.5).

5.5.1 Temporal variations

Figure 5.2 presents Epsilon at the top, followed by JH rates estimated by different methods in GW. The plots in the panels are given in 2 min resolution in accordance with the resolution of the BCRCM output. However, KP method has a cadence of 3 hours because of the resolution of KP and BB_{rcm} and BB_{nw_rcm} are in 10 min resolution due to the resolution of the RCM run. In general, all methods except the index-based methods, display similar features and qualitative variations. Qualitative agreements demonstrate the effectiveness of the presented approach irrespective of the weaknesses in each parameter, which are transferred inherently from the sources used in the calculation of JH. At the same time, the figure provides a first-order quantification on the disagreements. Despite overall qualitative agreement, differences are noticeable in the timing of the JH peaks and the estimated magnitudes of JH. We note that the vertical scale in Figure 5.2 is different on the panel for IRI-based methods (panel 3) as the magnitudes of the estimated JH rates are much lower than those of the other methods.

Epsilon parameter in the first panel of Figure 5.2 is given to provide a reference for comparing the timing and general features of the JH variations. The timing of the activity onset and the time required to reach the maximum magnitude in JH are investigated in detail. The magnetosphere-ionosphere system is assumed to be directly driven by the variations in IMF. This is considered as a valid assumption as ionospheric convection is thought to respond within 10-15 minutes to the solar wind conditions (Cai et al., 2014). The panels from 2 to 4 in Figure 5.2 present the global JH rates obtained from the methods, which do not take the neutral wind into account, namely, the index-based methods (AE, Olsson, IL and KP), the IRI-conductance based methods (IB and IS), the OPI conductance based methods (OIB and OIS) and the BATSRUS conductance based methods (BB_{rcm} , BB_{crsm} and BS). The last panel presents the methods that include the neutral wind effect: the BB_{nw_rcm} , BB_{nw_crsm} and W05. The black solid lines represent JH power calculated based on IL, IB, OI, BB_{rcm} and BB_{crsm} , while the red solid lines represent power calculated from IS, OIS, BS and W05. The results that have lower resolution are plotted in grey: KP, BB_{rcm} and BB_{nw_rcm} . Grey shaded areas indicate the times when SuperDARN has data in the nightside sector.

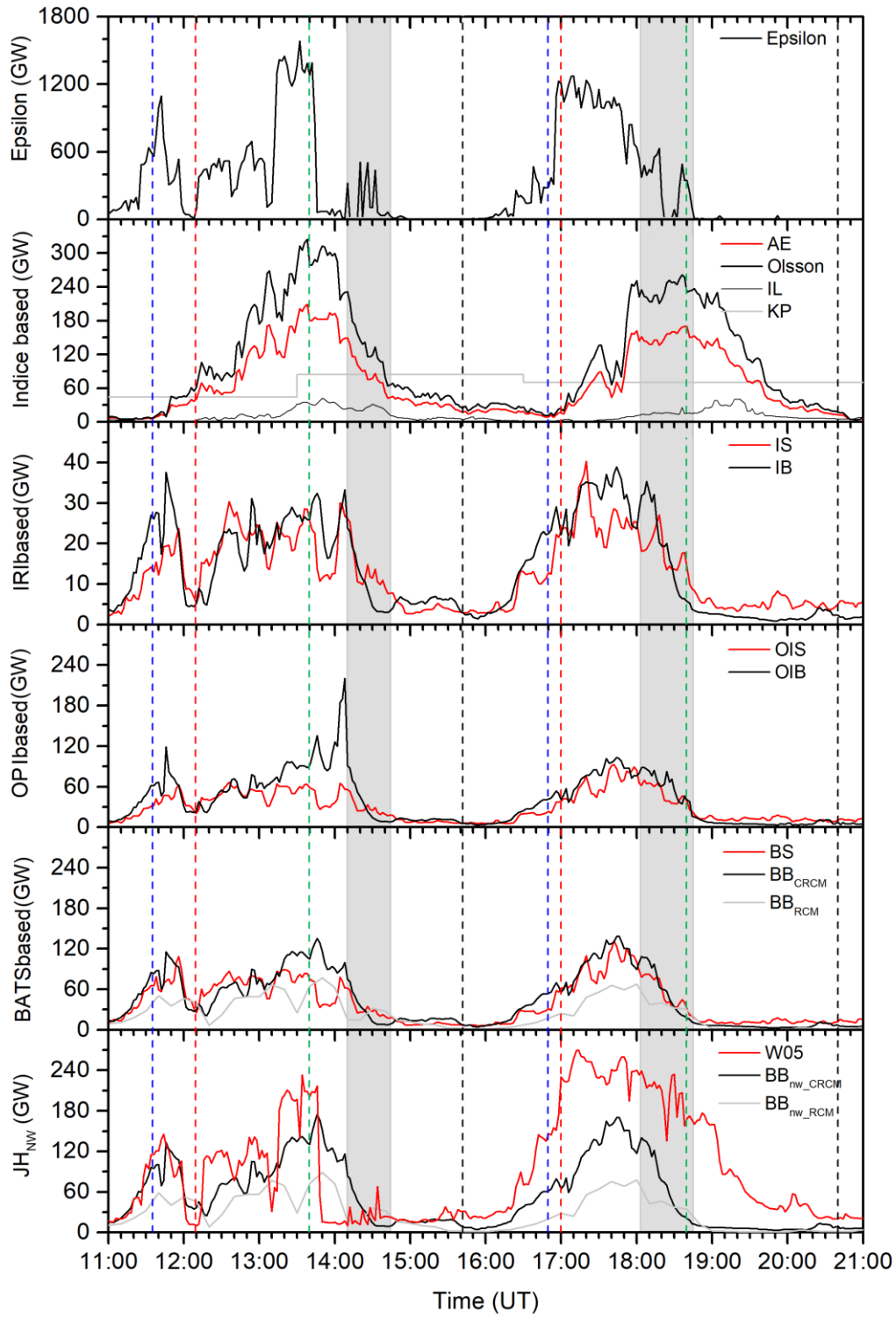


Figure 5.2 : Epsilon and Joule heating from the methods.

During both substorms, the variations in the AE-dependent methods (AE and Olsson) are smoother when compared with the variations in Epsilon and the other methods. The response of the AE-dependent methods to the first increase in Epsilon is found to be slower than the other methods around 40 to 50 min for the first and second substorm, respectively. The IL is seen to be even more delayed than the AE-dependent methods

during both substorms. This suggests that the overall auroral electrojet activity could not be captured very well by the local IL index during these substorm events. The KP method does not give a distinctive onset as it is a 3-hour index. Consequently, the JH variation from the KP method is independent of the substorm phases. On the other hand, JH rates from the other methods start to elevate right after the first increase in Epsilon. Except the index-based methods, all other methods seem to capture the variations in Epsilon and their temporal variations are seen to be in better agreement with Epsilon. The times of JH maxima estimated by the W05 are very close to the times of the Epsilon maxima for both substorms. However, during the recovery phase of the second substorm, as also seen in the AE, Olsson and IL methods, the rate of JH decrease in the W05 is slower than that of the combinative methods (BS, OIS, OIB, IS, IB) and BATSRUS model-based methods (BB_{crcm} and BB_{rcm}). The W05 continues to show high JH values when Epsilon has already decreased to pre-substorm levels. In case of the AE-based methods, the maxima are seen to be delayed up to 1.5 hour with respect to Epsilon. Time delays are also observed between the maxima of CRCM (BB_{crcm}) and RCM coupled BATSRUS (BB_{rcm}).

In Figure 5.2, the W05 and the methods that depend on AE (AE and Olsson) show the highest amount of JH. The IB, IS and index-based IL present the lowest estimates from the methods and their maxima are smaller than ~45 GW. The KP method estimates lie in between the AE and the IL methods with a maximum around 84 GW. The magnitude of JH from the IB and IS are 36% to 40% of the OPI-based OIB and OIS methods, respectively. The differences between the OIB and IB and the OIS and IS are only due to the addition of the nightside conductances. Even though observed later than the maxima in the KP, the OIS maxima during the second substorm (92 GW) is the closest to the KP method. The BB_{crcm} is always higher than the combinative methods OIS, OIB, IS and IB except the OIB maxima during the first substorm's recovery phase at 14:08 UT reaching up to ~220 GW. Although, the BB_{crcm} and BS differ towards the end of the expansion phase of the first substorm, they are basically the same during the second substorm. In general, the OIB and BS give higher JH than the OIS. The differences between the OIS and OIB and the BB_{crcm} and BS are found to be smaller when there is data in the nightside sector from SuperDARN. The BB_{rcm} predicts roughly the half of the JH that the BB_{crcm} produces throughout the substorm duration. The $BB_{\text{nw_crcm}}$ and $BB_{\text{nw_rcm}}$, which include the neutral wind effects, are always larger

than the BB_{rcm} and BB_{rcm} , which do not take the neutral wind into account. The AE-dependent methods (AE and Olsson) and the $BB_{\text{nw_rcm}}$ are the closest methods to the W05 during both substorms.

The qualitative and quantitative comparisons of Figure 5.2 indicate that the IL, the KP, and the IRI based methods show large differences from the other methods in the estimation of JH rates because the IL does not capture the global variations, the KP gives only an average estimate of JH because of its low resolution, and the IRI-based methods do not include a global representation of the conductivities. Therefore, hereafter, the analysis on the KP, IL and the IRI-based methods will not be further detailed.

5.5.2 Substorm phase dependence

In Figure 5.3, the dependence of JH rates on the substorm phases is investigated. Averaged (Figure 5.3a) and integrated (Figure 5.3b) JH rates for growth, expansion and recovery phases are shown for each method, except the KP, IL and IRI-based methods. The top and bottom panels are for the first and second substorm, respectively. First row illustrates the results for the first substorm and the second row gives the results for the second substorm. In Column (a), different colors indicate the results from the different methods used in this study: red, orange, yellow, light green, green, pink, lilac, grey, blue and cyan for BS, OIB, OIS, BB_{rcm} , BB_{rcm} , $BB_{\text{nw_rcm}}$, $BB_{\text{nw_rcm}}$, W05, AE and Olsson in the order seen in the figure. The letter G, E and R refer to the substorm phases as Growth, Expansion and Recovery. In Column (b), different colors indicate the different phases of the substorms; grey for growth, dark grey for expansion, and light grey for recovery phase. In all panels, the values seen on the column bars indicate JH rates, which are out of the scale given in the figure.

In Figure 5.3, column a, the W05 and AE-based methods (AE and Olsson) generally estimate the highest average Joule heating rates, during the expansion and recovery phases of the both substorms. The AE-based methods have the lowest JH rates during the growth phase whereas the W05 give the highest JH rates. The W05 estimates are ~ 2.8 times that of the closest method ($BB_{\text{nw_rcm}}$) during the growth phase of the second substorm as the W05 JH rates increased more rapidly and to higher levels than the other methods. In the figure, the OIS generally gives lower JH than the OIB indicating that the BCRCM electric fields are slightly higher than those provided by the

SuperDARN. In addition, the BS estimates are always higher than the OIS implying that the BCRCM conductances are constantly higher than the OPI conductances. It is also noticeable that the BB_{nw_crcm} and BB_{nw_rcm} are larger than the BB_{crcm} and BB_{rcm} at all times. This is due to the neutral wind effect, which contributes positively during these substorm cases.

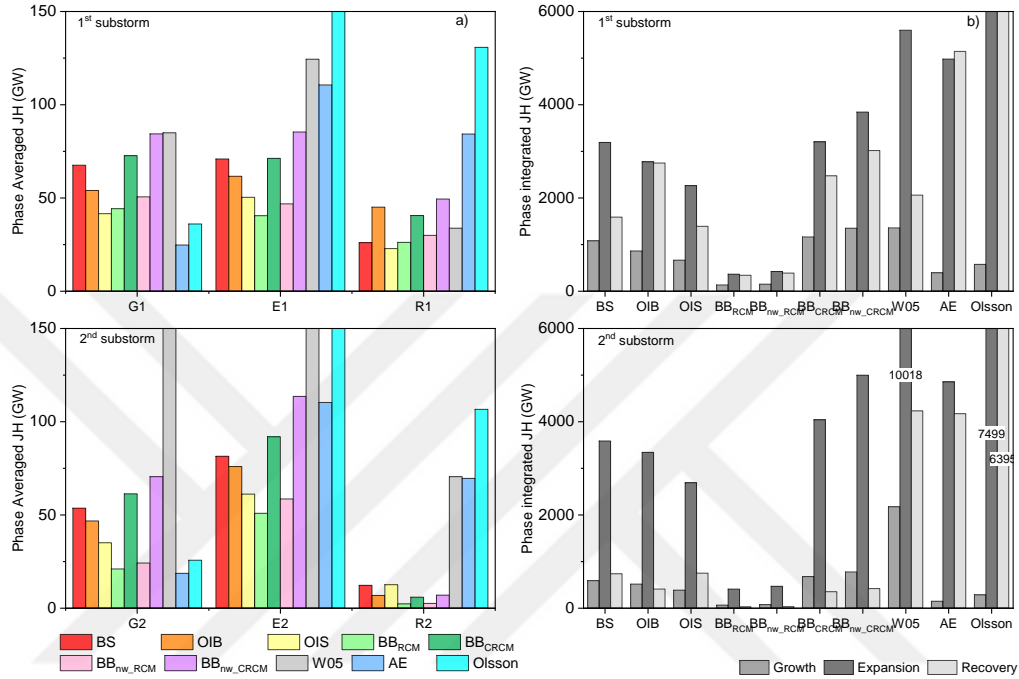


Figure 5.3 : JH from the Methods a) averaged over the substorm phases b) integrated over the substorm phases.

The figure clearly shows that the neutral winds increase Joule heating rates, which brings BB_{nw_crcm} predictions closer to those of the W05. The average JH produced by the BRCM (BB_{rcm} and BB_{nw_rcm}) runs remain lower than BCRCM produced JH rates (BB_{crcm} and BB_{nw_crcm}) throughout both substorms. There is not a pattern in the ordering of the methods by magnitude during the growth or recovery phases. On the other hand, during the expansion phase of both substorms, the JH from the methods can be sorted from the highest to the lowest as, the highest W05 and Olsson, followed by $AE > BB_{nw_crcm} > BB_{crcm} > BS > OIB > OIS > BB_{nw_rcm} > BB_{rcm}$. The AE-based methods give higher JH averages during the recovery phases of both substorms as their recovery are slower than the other methods. As a result, the differences between the AE-based methods and the others maximize during the recovery phases of the substorms. Similarly, W05 keeps estimating higher JH rates during the recovery phase of the second substorm. Phase-integrated JH rates in Figure 3, column b, show that all

methods give the highest JH during the expansion phase, moderate JH during the recovery, and the lowest JH during the growth phase. These figures indicate that there is considerable amount of JH from the statistical-empirical methods during the recovery phase, especially, in the case of the second substorm.

5.5.3 Spatial distribution

Figure 5.4 depicts a snapshot of the ionospheric potentials, spatial distribution of Pedersen conductances, ionospheric electric fields and JH rates for each data source and method above 60° magnetic latitude at 18:20 UT in geomagnetic coordinates. The time was chosen such that it is during the expansion phase when the energy deposition is high and there is data in the midnight sector from SuperDARN. Scales for ionospheric potentials, electric field, conductance and JH are represented with color bars below the figures. Maximum and minimum values and the location of the peak value in terms of MLT and magnetic latitude are given on the top right corner of each panel. Figure 5.4, the first row shows the ionospheric potentials generated by the BRCM, BCRCM, SuperDARN and W05 at 18:20 UT. The ionospheric potential pattern is equivalent to the high-latitude convection pattern. From the gradient of the electric potential, the equipotential contours are $\mathbf{E} \times \mathbf{B}$ drift trajectories representing the convection streamlines. The BCRCM, SuperDARN and W05 agree on the position of the convection patterns (ionospheric potentials) with respect to the noon-midnight meridian. However, BRCM does not show the same positioning; the convection cells are aligned along the noon-midnight meridian. It is shown that the W05 model produces stronger convection cells. Its CPCP (124 kV) is twice as large as the BCRCM, which provides the lowest CPCP (61.2 kV) among the models at 18:20 UT. Figure shows that at 18:20 UT, the SuperDARN, BRCM and BCRCM estimates are very close to each other (~60 kV). Consequently, the second row, E_{\perp}^2 from W05 displays the highest values. BCRCM and W05 show a similar cell throughout dusk sector expanding like a tongue towards post-noon sector. Moreover, BCRCM shows a weak cell in the post-midnight sector, which overlaps with the W05 cell that covers much of the post-midnight sector and expands towards the dawn till 09 MLT. In both cases, the BCRCM cells are ~6° poleward of the W05. BRCM provides much weaker electric field values, which are concentrated in the dusk and midnight sectors and does not demonstrate any cells in the dawn sector.

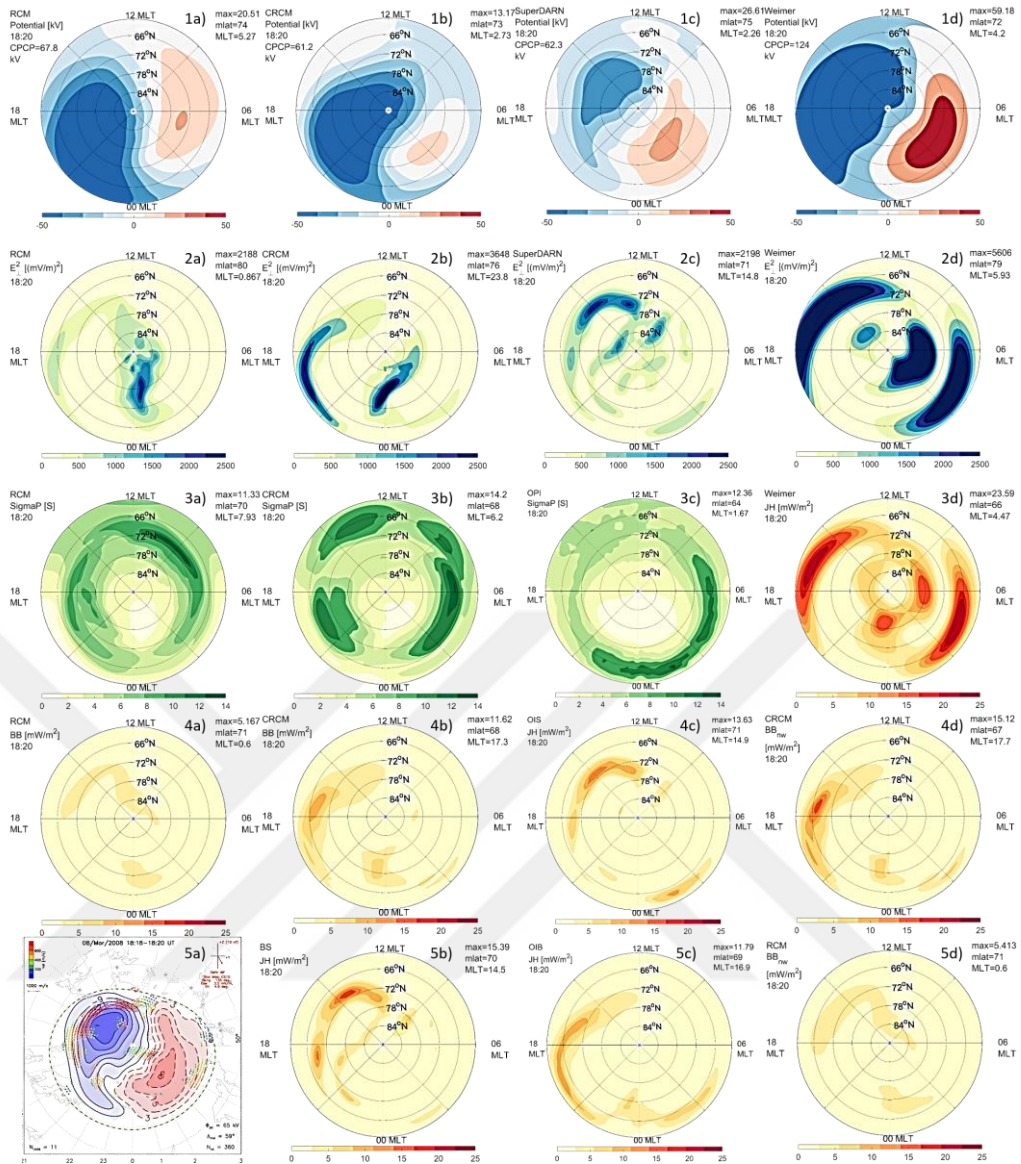


Figure 5.4 : Spatial distribution of JH and associated parameters at 18:20 UT.

Nevertheless, the strong electric field produced by BATSRUS in the midnight sector expanding equatorward from the pole till the 66°N MLat does not exist in the SuperDARN and W05. The enhancements in the electric field patterns at the nightside are found poleward of 72°N MLat in the SuperDARN and W05. On the other hand, SuperDARN electric field shows detailed structure in the dusk, noon and post-midnight sectors and does not show much enhancement in the pre-morning sector (03-06 MLT). Even though the W05 provides less structure in all sectors, the locations of the electric field structures provided by the SuperDARN mostly agree with the W05 except the pre-morning sector. However, the electric field pattern between 15 and 18 MLT in the SuperDARN is located poleward of the W05, between 66°N and 72°N MLat. The structures in the SuperDARN are weaker and narrower than the W05. The

enhancements in the BRCM, BCRCM, SuperDARN and W05 during the substorm cycle are consistently found at the same locations for each of these.

Figure 5.4, first three columns on the third row (3a, 3b, 3c) present the Pedersen conductances from BRCM, BCRCM and OPI. It is seen that the BCRCM generated conductances are overall much higher than the BRCM generated conductances. The conductances in the post-midnight sector in BCRCM are found slightly more equatorward than the BRCM. Most of the regions with enhanced conductances are similar in the OPI and BCRCM. However, the BCRCM shows higher conductances than OPI in general, except the post-midnight sector where OPI provides higher values. The post and pre-noon sector conductances displayed in the BCRCM are not that strong in the OPI, either. There is a ~ 3 S difference in the noon sector between the OPI and BCRCM provided conductances. Besides, the BCRCM shows much lower conductances around 00 MLT where the OPI provides the highest conductances.

Figure 5.4, 4a (BB_{rcm}), 4b (BB_{crcm}), 4c (OIS), 5b (BS) and 5c (OIB) present the JH from the combinative methods and BATSRUS model. Figure 5.4.4a presents the coverage and the number of observation points from the SuperDARN at 18:20 UT. As seen from (5.4.4a), there is slight data in the pre-midnight and post-midnight sectors, and well-defined dawn and dusk cells at 18:20 UT from SuperDARN. BB_{crcm} exhibits larger values than the BB_{rcm} in all sectors. The maximum JH rates are observed in the dusk sector between 14 MLT and 17.3 MLT in all methods, except the BB_{rcm} . The BB_{crcm} has a secondary maximum at the midnight sector whereas the methods that depend on the OPI show their secondary maxima at the post-midnight. The methods, which were constructed using the SuperDARN electric fields (BS and OIS) provide JH within a narrower band, while the BB_{crcm} and OIB, which use the BATSRUS electric field pattern present wider areas of increased JH in the dusk sector. The BS values are larger than the OIS in all sectors except in the post-midnight sector. When compared with the BB_{crcm} , for the OIB, the usage of the OPI conductances leads to a wider and more equatorward JH pattern, which expands towards the pre-morning from the midnight sector. The JH patterns closely follow the electric field patterns that are used to calculate the Joule heating rates. The locations of JH rates in the OIS and BS overlap with the locations of electric fields that are found in SuperDARN whereas the locations of the JH rates in the OIB and BB_{crcm} agree with the locations of the strong electric fields from the BCRCM.

Figure 5.4, 3d (W05), 4d (BB_{nw_crcm}) and 5d (BB_{nw_rcm}) demonstrate the JH values when the neutral wind effect is included. Weimer model gives the highest and widest JH pattern among the three methods. BB_{nw_rcm} is smaller than the BB_{nw_crcm} in all sectors. The midnight enhancement is apparent in both BB_{nw_crcm} and W05 in addition to the dusk cell. Even though weaker, BB_{nw_rcm} indicates JH in the post-midnight/pre-dawn sector similar to W05. The midnight cell is slightly equatorward whereas the dusk cell is poleward to some extent in BB_{nw_crcm} than the W05. The fourth cell in the inner part of dawn sector that is found in W05 is not present in BB_{nw_crcm} .

The spatial distributions of the parameters at other times (movies in supporting information: Movie S1 to Movie S12) also result in similar structures.

5.5.4 MLT and Magnetic latitude dependence

Figures 5.5a and 5.5b illustrate the dependence of the maximum JH rate on MLT (left) and magnetic latitude (in the middle), respectively. Figure 5c gives the distribution of maximum among the MLT and MLat. In the figure, top two panels are the JH rates from the BB_{crcm} and BS and the bottom two panels are those from the OIS and OIB. Panels in this figure display the MLT and magnetic latitude corresponding to the maximum JH rate at each 2 min interval. Magnetic local time sectors are defined such that 03-09 MLT is dawn, 09-15 MLT is noon, 15-21 MLT is dusk, and 21-03 MLT is the midnight sector. Filled dots represent the maximum JH rates. Color bar on the right indicates the magnitude of the JH rate. Dashed lines depict the substorm phases as in Figures 5.1 and 5.2. Grey shaded areas indicate the times when SuperDARN had data in the nightside sector.

Figure 5.5 shows that the JH maxima are distributed from $62^{\circ}N$ to $89^{\circ}N$ magnetic latitudes (MLat) in the methods that use BATSRUS electric field (BB_{crcm} -5.5.1a and OIB-5.5.4a). However, the locations of the maxima from the methods that use SuperDARN (BS-5.5.2a and OIS-5.5.3a) are concentrated in a narrower band of magnetic latitudes between $62^{\circ}N$ and $81^{\circ}N$. The maxima in the BS and OIS do not retreat as poleward as the OIB and BB_{crcm} during the recovery phases of the substorms. The substorm-related equatorward progression of the JH is clearly visible in all plots (5.5.1a, 5.5.2a, 5.5.3a, 5.5.4a).

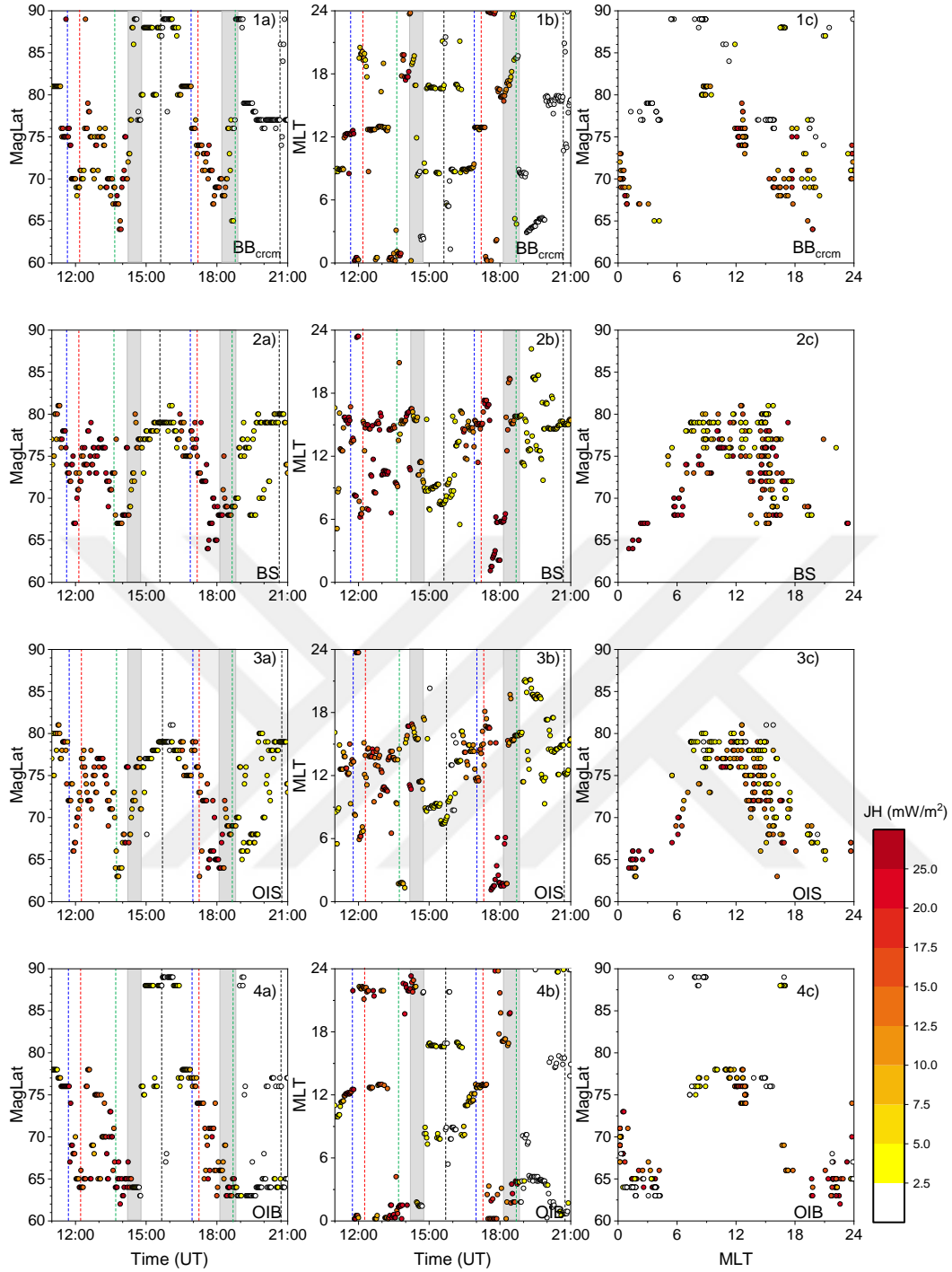


Figure 5.5 : Variation in maximum Joule heating with a) MLT, b) Magnetic Latitude (MLat) and c) the distribution of JH maxima in MLT vs MLat.

JH maxima from all methods are found more equatorward with the expansion onset and more poleward with the beginning of the recovery. The BS gives the most maxima at ~ 9 MLT and at ~ 15 MLT (5.5.2c) whereas for the OIS (5.5.3c), most are found ~ 14.5 MLT. Additionally, the OIS and BS provide some maxima around the post-midnight during the second substorm's expansion phase (5.5.3b). The BB_{crcm} (5.5.1c)

and OIB (5.5.4c) give most maxima in midnight and noon sectors, but overall, maxima are distributed across all MLTs. The BB_{crsm} also shows maxima in the dusk sector during the second substorm's expansion phase (5.5.1b and 5.5.1c).

In Figure 5.6, we further examine the magnetic local time sector dependence of methods and show the results. The Joule heating in the panels is the total within the magnetic local time sectors. For Figure 5.6a, the green, red, blue and black lines indicate the dawn, noon, dusk, and midnight sectors, respectively. For Figure 5.6b, the red, green, black and blue lines correspond to OIB, OIS, BS and BB_{crsm} . Note that the scales for OIB in Figure 5.6a and midnight sector in Figure 5.6b are different than the other panels: 0-120 GW. The other panel scales are 0-50 GW. Grey shaded areas indicate the times when SuperDARN had data in the nightside sector.

Each panel in Figure 5.6a compares the JH estimates from a particular method in different magnetic local time sectors. It is seen that during the quiet interval preceding the substorms, JH is larger in the noon sector for all methods. With the substorm onset, JH from different methods starts to increase in all sectors. The increases are found mainly in the midnight sector for the OIB; noon and dusk sectors for the OIS and BS and midnight and dusk sectors for the BB_{crsm} . The OIS and BS also show enhancements in the midnight and dawn sectors during the second substorm's expansion phase.

Each panel in Figure 5.6b compares each method against the others for a particular magnetic local time sector indicated on the vertical axis. In this figure, the vertical axis in each panel is the sectoral sum of the JH within the associated MLT sector estimated by the methods shown in different colors. It is observed that all methods give the same order of magnitude estimates for JH in each sector. The OIS method estimates are generally the lowest in all sectors. On the other hand, the BB_{crsm} estimates are generally the highest at the midnight sector, except the OIB peak at 14:08 UT. The BS and BB_{crsm} exhibit the highest values at the dusk sector.

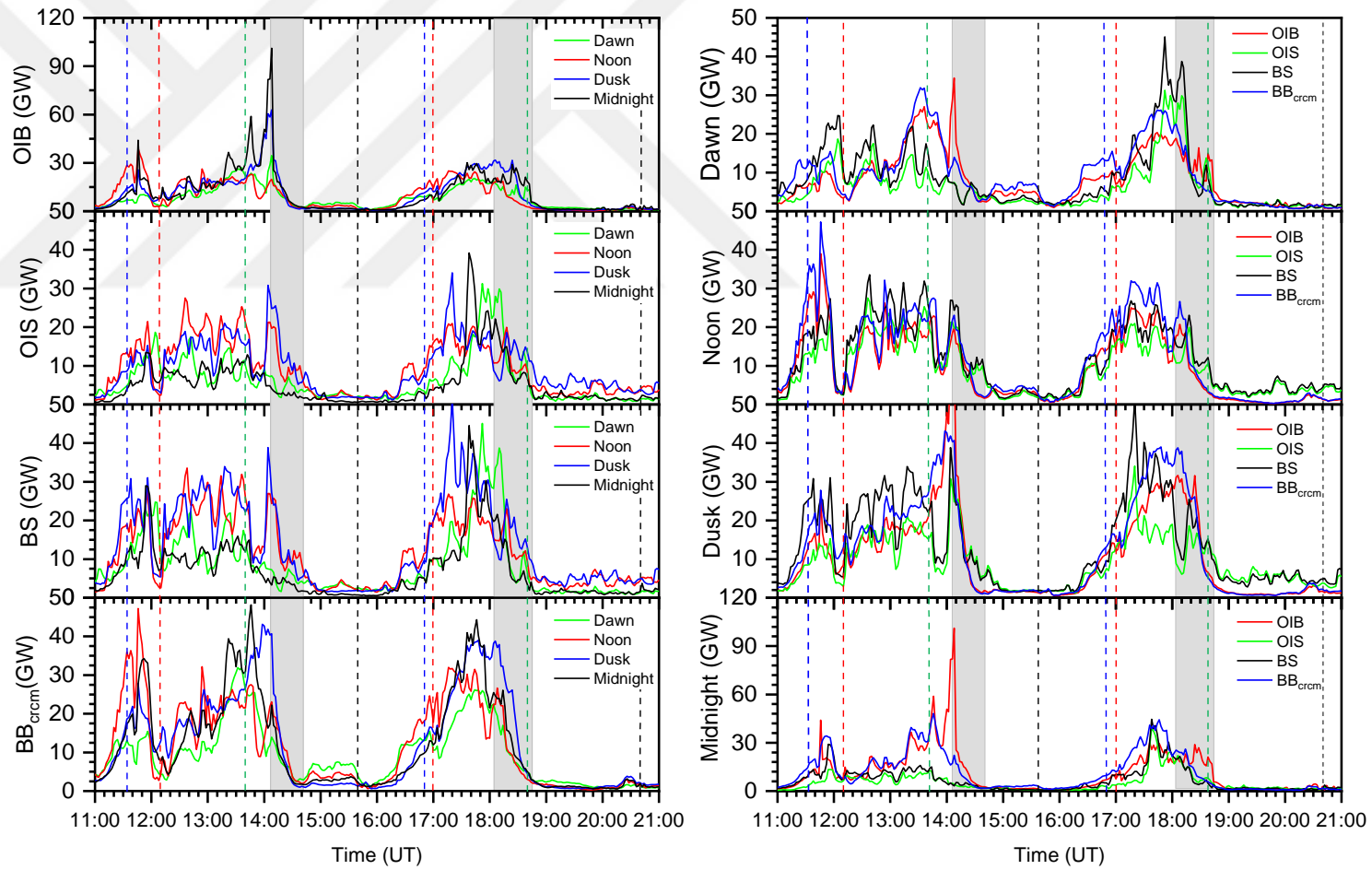


Figure 5.6 : Magnetic sector dependence of JH. a) evaluation with respect to methods (OIB, OIS, BS, BB_{crcm}) b) evaluation with respect to the magnetic local time sectors.

5.5.5 Role of conductance and electric fields

Differences between the methods presented in the previous sections make it essential to evaluate the electric fields and conductances from SuperDARN, BATSRUS and OPI in order to comprehend the results on JH rates. In the top two panels of Figure 5.7, we compare the methods BB_{crcm} , BS, OIB, OIS, OS and IS in order to understand the effects of Pedersen conductances and electric field. In the figure, from top to bottom: Left: contribution of IS and OS to the JH from OIS: %IS (red), %OS (blue) and the OS/IS ratio (black). Ratios: OIS/IS (green), BB_{crcm}/BS (blue), BB_{crcm}/OIB (black) and BB_{crcm}/OIS (red); Ionospheric Pedersen conductance from OP (red, thin), IRI (dashed, black), OPI (red, thick), BCRCM (black, thick) and BRCM (grey); Cross Polar Cap Potentials from W05 (red), SuperDARN (black, thick), BCRCM (black, thin) and BRCM (grey); at the bottom number of observation points for SuperDARN, color scale on the right. Grey shaded areas indicate the times when SuperDARN has data in the nightside sector. We study the differences in JH rates from the methods by taking ratios as shown in the first and second panels. In the first panel of Figure 5.7, the %IS shows the effect of the dayside conductances, the %OS, the effect of the nightside conductances and the OS/IS shows the ratio between the two. The partitioning of JH (OIS) due to the dayside and nightside conductances is found by calculating the percentage of contribution from each method using ($\%IS = IS/OIS * 100$ and $\%OS = OS/OIS * 100$). The panel indicates that during the substorms, JH obtained by using the nightside conductances (%OS) contributes 74% of the total JH (12:10 UT) at the maximum and can be as large as 2.81 times JH obtained by using only the dayside conductances (OS/IS). The minimum contribution from the nightside conductances, which is about 31% of the OIS, occurs at 16:26 UT during the quiet time preceding the second substorm's growth phase. On average, during the substorms, the JH due to the nightside conductances are around 60% of the total JH. Table 5.4 displays the JH due to the dayside and nightside conductances on average in percentage.

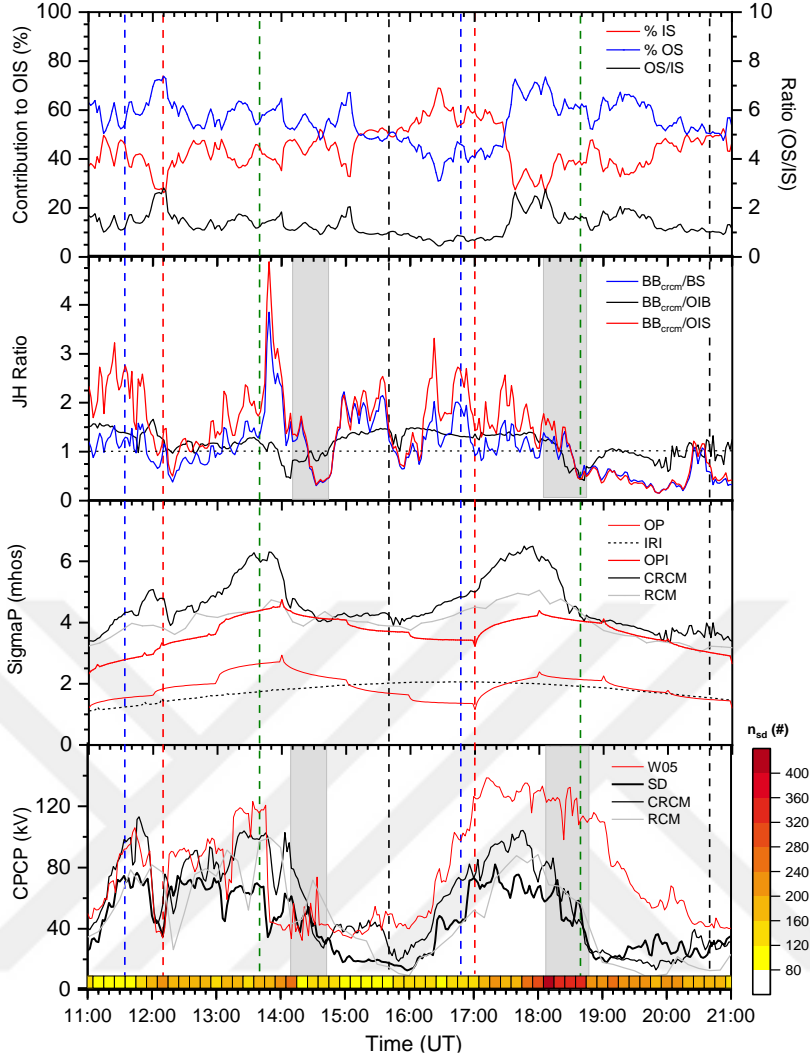


Figure 5.7 : Comparison of JH, Pedersen conductance and CPCP.

Table 5.4 : The amount of JH due to the dayside and nightside conductances (%).

Mean (%)		$\frac{IS}{OIS}$	$\frac{OS}{OIS}$	$\frac{IB}{OIB}$	$\frac{OB}{OIB}$
First substorm	G	43	56	42	58
	E	44	55	44	56
	R	40	60	40	60
	F	42	57	42	58
Second substorm	G	27	73	23	77
	E	39	61	31	67
	R	45	55	36	64
	F	37	63	30	69
Both substorms		40	60	36	64

In the second panel, we present the ratios BB_{crcm}/OIS , BB_{crcm}/OIB and BB_{crcm}/BS . The BB_{crcm}/BS shows the effect of electric fields, the BB_{crcm}/OIB , the effect of conductances and the BB_{crcm}/OIS indicate the effect of different sources, i.e. physical mechanisms or measurements that are used in the calculation of JH. It is found that the

$BB_{\text{cr cm}}/OIS$ ratio varies between 0.3 and 4.8. Most of the time the $BB_{\text{cr cm}}$ is larger than the OIS by about a factor of 1.5. On average, best agreements between the $BB_{\text{cr cm}}$ and the OIS were seen during the expansion phase of both substorms. The highest discrepancies were found during the recovery phase of the first substorm when the $BB_{\text{cr cm}}$ is greater than OIS, reaching to a factor of 4.8. The $BB_{\text{cr cm}}/BS$ shows the same tendencies as the $BB_{\text{cr cm}}/OIS$ throughout the event intervals. This suggests that the differences between the $BB_{\text{cr cm}}$ and the OIS are due to the different electric field patterns that are used rather than the conductances. Consequently, the $BB_{\text{cr cm}}$ to OIB ratio remains mostly steady, within a factor of 0.45-1.65 during both substorms and shows the best agreement is between the OIB and the $BB_{\text{cr cm}}$ among the methods. In the $BB_{\text{cr cm}}$, the change of conductance pattern from the BATSUS conductances to OPI conductances leads to a maximum 10% increase in JH with respect to the OIB. Table 5.5 demonstrates the average ratios of JH obtained from the methods with respect to substorm phases.

Table 5.5 : Average ratios of JH obtained from the methods with respect to substorm phases (G: growth, E: expansion, R: recovery, F: full interval).

Mean		$\frac{BB_{\text{cr cm}}}{BB_{\text{rcm}}}$	$\frac{BB_{\text{cr cm}}}{BS}$	$\frac{BB_{\text{cr cm}}}{OIS}$	$\frac{BB_{\text{cr cm}}}{OIB}$	$\frac{OIB}{OIS}$	$\frac{OIS}{IS}$
First substorm	G	1.6	1.1	1.7	1.4	1.3	3.0
	E	2.2	1.0	1.4	1.1	1.2	2.5
	R	2.4	1.6	1.8	1.1	1.7	2.3
	F	2.1	1.2	1.6	1.2	1.4	2.6
Second substorm	G	2.7	1.4	2.0	1.3	1.6	1.7
	E	1.9	1.1	1.5	1.2	1.3	2.6
	R	4.3	0.5	0.5	0.9	0.5	2.4
	F	2.9	1.0	1.3	1.1	1.1	2.3
Both substorms		2.5	1.1	1.5	1.2	1.3	2.4

The $BB_{\text{cr cm}}/BS$ and the $BB_{\text{cr cm}}/OIS$ ratios tend to approach to 1 during the intervals when SuperDARN has data from the nightside as seen from Table 5.6.

Table 5.6 : Average ratios of JH: $BB_{\text{cr cm}}/BS$ and $BB_{\text{cr cm}}/OIS$ when SuperDARN has data in the midnight sector.

mean	$BB_{\text{cr cm}}/BS$	$BB_{\text{cr cm}}/OIS$	Substorm phase
14:08-14:42	0.89	0.95	Recovery
18:04-18:44	0.95	1.04	Expansion

The second panel displays the difference in the globally averaged Pedersen conductances of the OP, IRI, OPI, BATSRUS/CRCM and BRCM. IRI is used to obtain the dayside empirical Pedersen conductance values. It shows a very smooth variation in conductance, which is not much different from the quiet time level. The OP provides the conductances due to the electron and ion precipitation from the magnetosphere into the ionosphere. It displays step-wise changes at the beginning of each hour. Then the conductance slowly and monotonously increases or decreases till the next hour. The variations in the OP are in accordance with the phase of the substorms. The conductances are the smallest during the quiet times, increase during the expansion and decrease during the recovery phases. The OPI is the method that gives the conductances by merging the IRI and OP conductances. The order of magnitude of the OPI and BRCM conductances are found to agree well. The difference between the two increases during the growth and expansion phases and decreases during the recovery phases of the substorms. However, the BCRCM demonstrates the highest conductance values and shows a stronger enhancement during the substorms. On the other hand, the BCRCM conductances are very close to the OPI and BRCM during the recovery phase despite the large difference during the expansion phases. The difference in conductances from OPI and BATSRUS range from 0.5 S to 2.2 S and is higher during the expansion phases of both substorms. The mean difference is 0.85 S with a standard deviation of 0.65 S. Both the BCRCM and BRCM conductances start to increase before the OPI enhances during the second substorm.

In the third panel of Figure 7, cross polar cap potentials (CPCP) from the W05, SuperDARN, BCRCM and BRCM are shown. CPCP provides the information regarding the strength and variability of the electric fields. Both substorms exhibit CPCP disturbances of moderate geomagnetic level. Overall, the CPCP from SuperDARN and the BRCM agree reasonably well. However, the BCRCM and W05 are generally higher than SuperDARN and BRCM. Although the estimates of W05 and BCRCM are very close to each other during the first substorm, W05 gives much higher values than the others during the second substorm. SuperDARN CPCP are slightly smaller than those of BRCM during both substorm. The number of SuperDARN observation points are given at the bottom of Figure 7. During the expansion and recovery phases, the numbers were rather high, exceeding 200 and reaching 420 during the expansion phase of the second substorm. An examination of

the data coverage shows the data mostly come from the dawn, dusk, and noon sectors with some contribution from the midnight sector during the time intervals shaded in grey. During the other time intervals, the observations come mostly from the dawn, dusk, and noon sectors.

5.5.6 Role of the neutral wind

In this section, we investigated the neutral wind contribution to the JH rate during substorms using ionospheric electrodynamics parameters. The effect of the neutral wind on JH (JH_{nw_crcm} and JH_{nw_rcm}) is calculated by subtracting the results of Equation (2.4) from those of by Equation (2.3) using BCRCM and BRCM outputs. Figure 5.8 demonstrates the effect of the neutral wind on the spatial distribution of JH at 18:20 UT. The first row presents the JH from BCRCM whereas the second row presents JH from the BRCM with neutral wind, without neutral wind and the effect of neutral wind, respectively, from left to right. The scales are shown at the bottom and maximum and

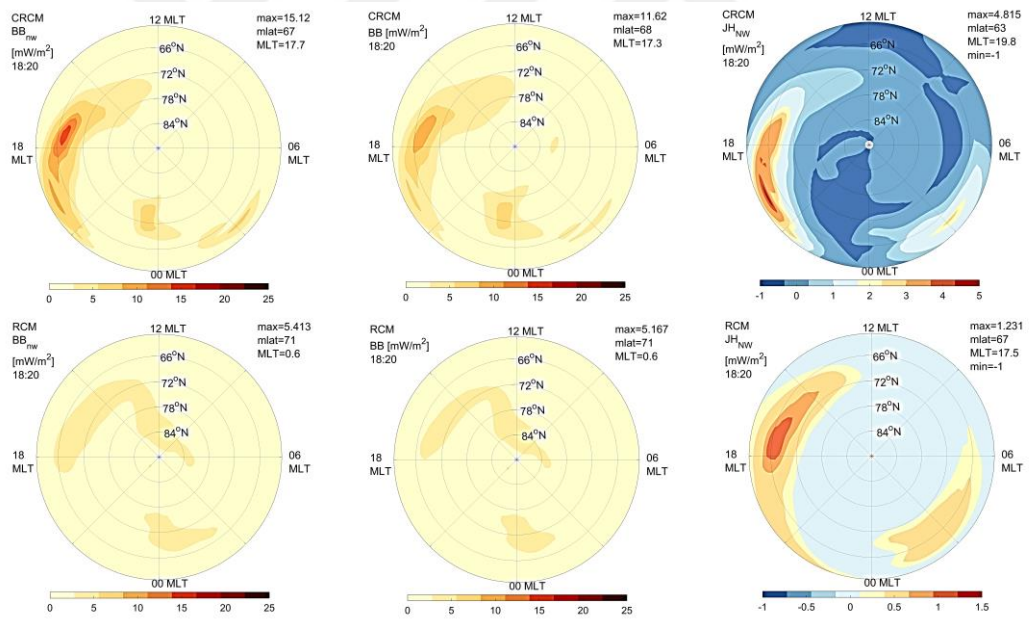


Figure 5.8 : JH with neutral wind, without neutral wind and neutral wind effect. Top: BCRCM, bottom: BRCM results.

minimum JH values are shown in the upper right corner of each graph as in Figure 5.4. Figure 5.8 reveals that at 18:20UT, the neutral wind contribution from the RCM is positive everywhere in the polar cap meanwhile CRCM neutral wind values show negative effects at the noon and postnoon sectors between 66° and 71° N in addition to the negative values at the midnight sector extending southward from the pole. The

region of positive contribution from the RCM and CRCM are found at similar locations in the predawn and dusk sectors. However, the highest values from JH_{nw_crcm} is concentrated in early dusk (15-18 MLT), whereas the highest values from JH_{nw_rcm} are found mainly between 18 and 21 MLT. The region of positive contribution from the RCM and CRCM are found at similar locations.

Figure 5.9 compares the temporal variation of JH_{nw_crcm} and JH_{nw_rcm} . In Figure 5.9, it is seen that JH_{nw_crcm} was always larger than JH_{nw_rcm} for these substorm cases. The neutral wind contribution is also found to be larger in the BCRCM than the BRCM.

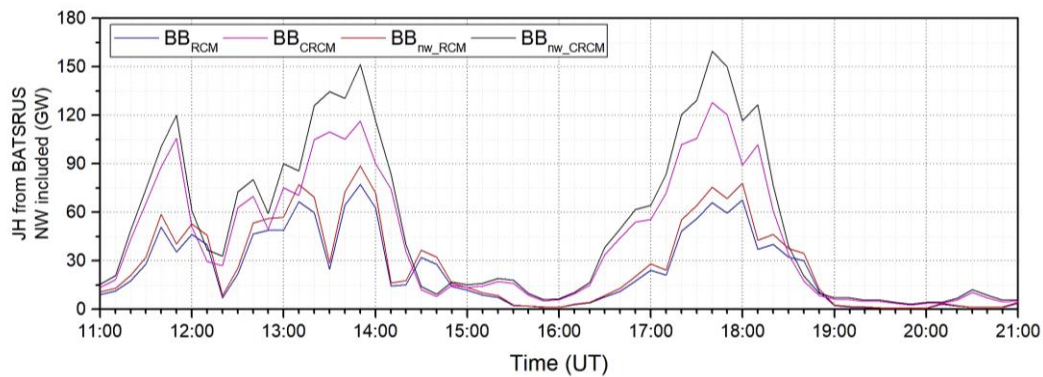


Figure 5.9 : Joule heating from BCRCM and BRCM with and without the neutral wind.

Figure 5.10 details the neutral wind contribution from the BCRCM. The first panel in Figure 5.10 depicts the contribution of the neutral wind (NW) to the overall JH rate in GW (black) and in percentage (red). On the average, the neutral wind is found to contribute positively and comprises ~15% of the total JH. The neutral winds enhanced the global JH by a maximum 40 GW, which is 27% of the total JH at 13:50 UT, right after the expansion phase of the first substorm.

Besides the peak after the expansion phase of the first substorm, the contribution in percentage from the neutral wind doesn't vary much with time (i.e., with the phase of the substorm), particularly during the second substorm. The second panel in Figure 5.10 demonstrates how the NW contribution is distributed according to the magnetic local time sectors. The highest NW contribution occurred in the dusk sector (blue) throughout the substorm events. The JH due to the neutral wind in the dawn (green) and midnight (black) sectors are similar in magnitude but are smaller than the values in the dusk sector.

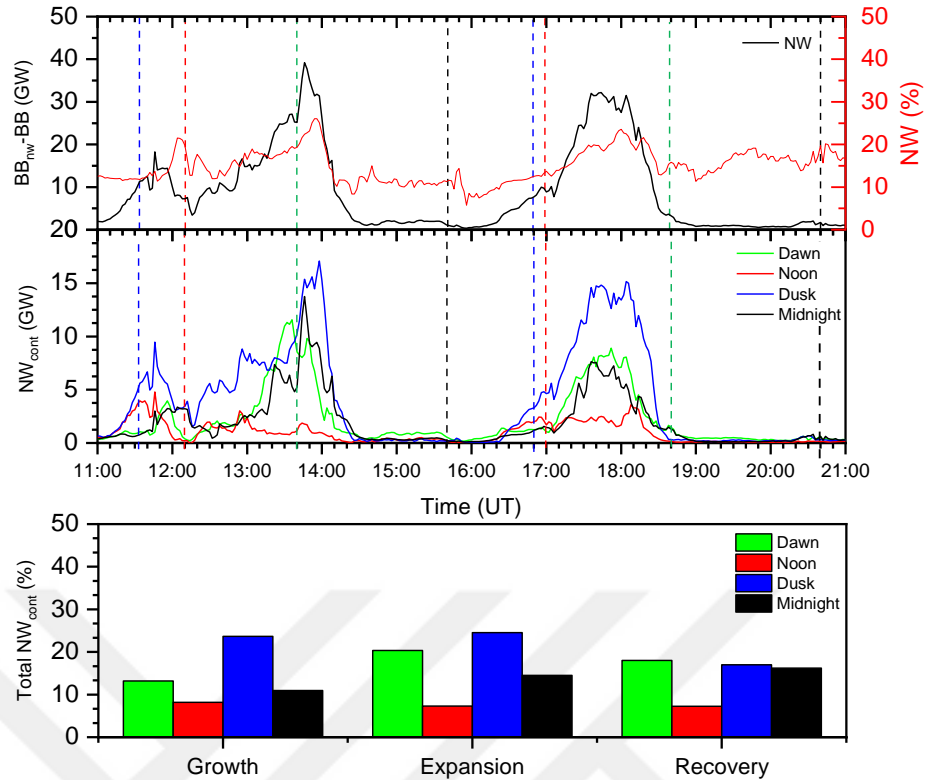


Figure 5.10 : Neutral wind contribution to JH for March 8, 2008 substorms.

The neutral wind contribution to JH in the noon sector (red) does not seem to vary drastically according to the substorm phases. Rather, it stays nearly constant around 1.75 GW. Examination of the spatial distribution of the NW contribution shows that the NW mainly decreased the JH in large part of the noon sector. Consequently, the total effect of the neutral wind at the noon sector remains positive, but at very low levels. The third panel in Figure 5.10 depicts the differences according to the substorm phases. We find that the highest contributions from the neutral wind to JH are from the dawn (20%) and dusk (25%) sectors during the expansion phases of the substorms. The smallest contribution from the neutral wind was from the noon sector at all substorm phases.

5.6 Discussion on Joule Heating Variability

Several studies compared JH rates using MHD models, proxy methods, AMIE mapping techniques, spacecraft observations of Poynting flux, electric and conductivity measurements from radars as well as the ground magnetic field observations (Zhang et al, 2005; Raeder et al., 2001; Wiltberger et al., 2004; Palmroth et al., 2005; Ahn et al., 1983; Lu et al., 1995; Gary et al., 1994; Waters et al., 2004).

Among these, our approach is the closest to the Palmroth et al. (2005) study. In their work, three methodologies were applied to compare the magnitudes and temporal characteristics of JH obtained from the GUMICS-4 MHD model with those from the AE proxy method, the AMIE climatology, and combined observations of electric fields from SuperDARN and conductances extracted from the UV and X-ray imager on the Polar spacecraft (s/c) and hereafter referred to as the SP method. Their substorm event and ours occurred in the same month, March 1998 and 2008, respectively. Palmroth et al. (2005) compared the GUMICS-4 MHD model JH rates with those of the SP method and found that the temporal variations in GUMICS-4 JH are similar to those from the SP, but there is a slight delay between each other. Their SP data has 10 minutes resolution due to the procedure used in deriving the Pedersen conductances. In our study, similar time shift exists between the variations and onsets of the BB_{rcm} and the methods that use the SuperDARN electric field (BS and OIS) as seen in Figure 5.2. Figure 5.11 presents the comparisons of the JH estimations from different combinative methods, which use BCRCM and BRCM outputs in 10 minute resolution. Time delays are also observed between the maxima of CRCM (BB_{crcm}) and RCM coupled BATSRUS (BB_{rcm}). The first panel shows the IRI-based methods, IS_{crcm} , IS_{rcm} , IB_{crcm} , IB_{rcm} , the second panel: OPI, SuperDARN, BATSRUS-CRCM (BCRCM) and BATSRUS-RCM (BRCM) based methods: OIS, BS_{crcm} , BS_{rcm} , BB_{rcm} , BB_{crcm} and the third panel, comparisons between the methods when BRCM is shifted 10 and 20 min: OIS, BB_{crcm} , BB_{rcm_20min} , BB_{rcm_10min} . The subscript RCM denotes the methods, which use BRCM output for conductances or electric fields. The subscript CRCM denotes the methods, which use BCRCM output for conductances or electric fields. As seen, there is a 20 min. difference between the maxima of BB_{crcm} and BB_{rcm} during the second substorm. However, the onsets and variations of the BB_{crcm} , BS and OIS are somewhat synchronous (Figure 5.2 and Figure 5.11). The BB_{rcm} exhibits weaker and slower JH enhancements and decreases slowly and to lower levels of JH with respect to the BB_{crcm} .

The most underlining result of Palmroth et al. (2005) study is the quantitative difference between the GUMICS-4 MHD model and SP based JH. Throughout the substorm interval, GUMICS-4 gives consistently lower JH by a factor of 10 than that of the SP and AE-based JH. They attribute the lower JH values from GUMICS-4 to the lower CPCP and weaker Region 2 currents in the model. In our study, BB_{crcm} and

OIS agree qualitatively well and $BB_{\text{crcm}}/\text{OIS}$ is 1.5 on the average (Figure 5.7, Table 5.4). Palmroth et al. (2005) discussed and concluded that the temporal evolution of GUMICS-4 is well correlated with the JH rates from the AE proxy method throughout their substorm events despite the differences in the order of magnitudes.

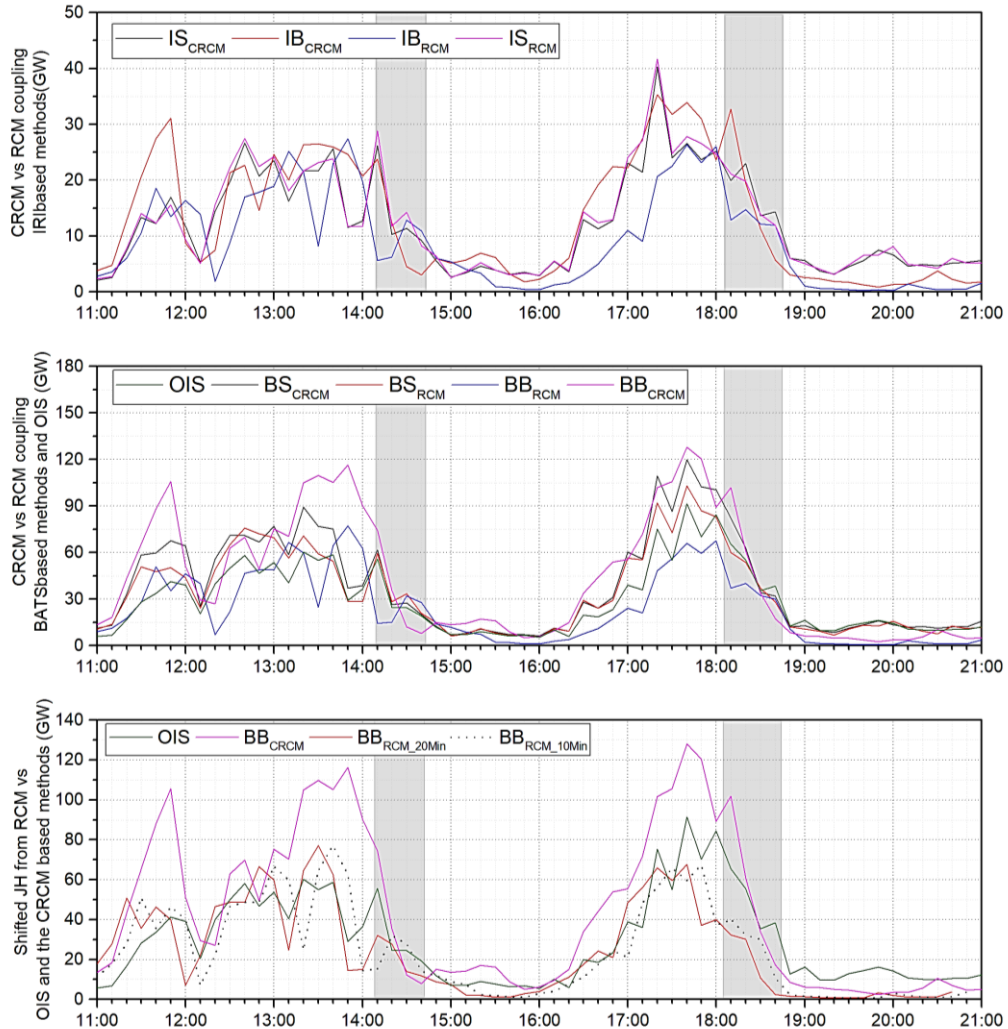


Figure 5.11 : Comparisons of the JH estimations from different combinative methods which use BCRCM and BRCM outputs.

Palmroth et al., 2005’s main goal was to calibrate the JH results from the GUMICS-4 MHD model using the existing data sets and methods. However, they first had to determine which model would be valid to calibrate GUMICS-4 MHD simulation with. JH studies include several difficulties, which make it hard to assess because of the uncertainties in the methods and decide which model is closer to reality.

Recently, Gordeev et al. (2013; 2015) proposed a framework for validating the MHD model performances. The first step is to select a set of global variables, which represent

the characteristics of the system. Secondly, they suggest comparing the MHD results for the selected variables with statistical empirical relations rather than against satellite measurements. Satellite measurements may include localized structures, which cannot be captured by the MHD models as the MHD models represent the large-scale structures better. Thirdly, the model runs should be prepared such that the input consists of average statistical distribution of the solar wind parameters. In the case of Joule heating, the variables that should be selected for the assessment of the validity of a method should be the variables that are used to estimate the JH. Those variables are the electric field, conductances and neutral wind. The CPCP can also be used instead of electric fields as it is a direct measure of the strength of the electric fields. In this work, one of our aims is to obtain JH variability from different methods given the disadvantages of each method that come from their own restrictions. These disadvantages can also give us opportunity to study the variations in JH under the diverse conditions inherited in the variables of JH and thus help us to construct the limits. From this perspective, it is also important to determine how much the estimates would deviate from the empirical models if a dynamic environment is simulated with the physics-based MHD models. Hence, we do not use the average solar wind properties. Instead, the dynamic solar wind, which gives rise to the substorms, is input to the models. We present the deficiencies of each method and try to assess the effect of each parameter involved in the calculation of JH by using combinative methods for the selected substorm cases. These results from the combinative methods are compared with the empirical model estimations.

In Figure 5.2, Olsson (Olsson et al., 2004), AE and IL (Ahn et al., 1983) and W05 (Weimer, 2005) from the empirical statistical methods and BB_{nw_crcm} and BB_{nw_rcm} from the model results include the neutral wind effects. KP method (Foster et al., 1983), BB_{crcm} , BB_{rcm} , OIS and the other combinative methods (BS and OIB) do not include the neutral wind effects to JH. W05 uses DE-2 data during 1981-1983 and Olsson method uses 6 months data from 1999 from the Astrid-2 satellite. Additionally, Ahn et al.'s (1983) method data is from 1978. This means that the three methods were constructed using solar maximum time recordings. However, the KP method (Foster et al., 1983) uses AE-C data from 1974 to 1978, belonging to solar minimum conditions and employs equation. 2.2 to calculate JH as in BB_{crcm} , BB_{rcm} , OIS, OIB and BS. Even though it has 3 hours cadence, the KP method still gives information

about the level of the expected average amount of JH. The events of March 8, 2008, which are studied in this work occurred during the solar minimum. Thus, even though not accurate enough in terms of the temporal variation, it is more reasonable and realistic to compare the magnitude of JH from the methods with those of the KP method.

It is seen that the index-based methods show a broad range of results for the two substorms. Olsson method always displays the highest JH magnitudes and the IL provides the smallest and the most delayed JH both in terms of substorm onset and timing of the JH maximum. In the classical view of the substorms, the delay between the substorm onset in the ionosphere and the changes in IMF B_z is associated with the response time of the ionosphere to the magnetospheric loading-unloading processes of the energy (Kallio, 2000). It is straightforward that the JH rates obtained from the AE method have the same variations as the AE index due to the linear relationship in Eq. (3). Consequently, Olsson and the AE method have a time lag of 40-50 min from the activity onset at the Epsilon for the first and second substorm, respectively. However, W05, as an empirical model, does not show a lag between the start of the energy deposition to the magnetosphere and JH increase in the ionosphere with respect to the Epsilon during both substorms. Rather, it suggests a directly driven process. The timings of the maxima in W05 are also nearly synchronous with the maxima in Epsilon (2 to 4 min. lag in first and second substorms, respectively). On the other hand, the W05 becomes as delayed as AE during the recovery phase of the second substorm, showing a slower decrease in JH magnitudes. For the first substorm, the end of the energy transfer as indicated by the Epsilon is at 14:35 UT. Following this, Epsilon stays at levels close to zero. Additionally, by 14:35 UT, AE is found to have already completed its fast recovery and it is in the slow recovery phase. However, during the second substorm, even after the Epsilon returns to quiet levels, AE and AL index show a very slow recovery to the quiet-time values. In our case, W05 model includes both the solar wind input and the variations in AL. Thus, it responds to the variations in Epsilon nearly concurrently during the first substorm and is also affected by the slower recovery of the AL index (westward electrojet) during the second substorm. Olsson method is also dependent on the AE index. Hence, it provides the same timings as the AE method. The magnitude of JH from the Olsson method exceeds the W05 during the first substorm and the response curve is different than the W05. On the other hand,

during the second substorm, despite the 50 min. shift with regard to W05, the shape of the response curve is nearly the same as the W05 method and the magnitudes match with the W05.

The OIS is constructed using the OVATION Prime+IRI conductances and SuperDARN electric fields. OVATION Prime is an empirical model for the auroral precipitation and IRI is an empirical model for the ionospheric parameters. SuperDARN electric fields, while driven by the instant solar wind conditions, approach to a statistical model when there is lack of data from the nightside. Thus, the electric field variations can also be assumed to be provided by an empirical model, which is expected to be closer to reality especially when there is enough data. Consequently, when using dynamic solar wind input, we argue that OIS would be sufficient to use as a method to calculate JH. Additionally, JH magnitudes estimated by the OIS are very close to the KP method estimations, confirming its validity for its usage for the comparisons with other methods. Moreover, the spatial distribution of the conductance pattern, OPI, which is one of the main components in the calculation of JH, agrees with the previous studies in the literature. Table 1 of (Gjerloev and Hoffman, 2000) lists the expected magnitude and location of the maximum Hall and Pedersen conductances during geomagnetically active periods from six models. From the table, it is seen that for an event with similar AE and KP to the events in this study, the maximum of the Pedersen conductance in the post-midnight sector is expected to be around 13 S and is generally located at around 64° MLat and between 0 to 5 MLT. In the pre-midnight sector, maxima are mostly found from 21 to 23 MLT and are about 12 S between 69° -74° MLat. The OPI captures both maxima in the midnight sector with similar magnitudes and locations to the ones listed previously in the literature. The maxima are located around 64° to 66° MLat and in between 21-23 MLT and at ~2 MLT with a magnitude of 13 to 15 S.

In Figure 5.2, the qualitative agreements between the BB_{rcm} and OIS variations (no time delays between the two) suggests the BB_{rcm} response is more reliable than the BB_{rcm} and the BB_{rcm} results are promising despite the magnitude difference from the OIS and the KP method. Even though, BB_{rcm} , in terms of magnitude seems to agree with OIS better in Figure 5.2, an investigation of the spatial distribution of the Pedersen conductances and electric field indicate they do not agree on the spatial distribution of the JH and the parameters that construct the JH (Figure 5.4). With more coverage and

data in the midnight sector by SuperDARN, the BB_{crim} and OIS methods approach to each other and their ratio varies between 0.95 and 1.04 (Table 5.6).

However, (Gjerloev et al, 2018) has put forward a new technique for the SuperDARN convection patterns, which gives far less dynamic response from the ionosphere to the changing conditions in the solar wind. The variations in the OIS are basically controlled by the variations in the ionospheric electric field. Thus, for comparisons with the BB_{crim} and BB_{rcm}, knowledge of the electric field in precision is required to know which pattern is more reliable. In this study, we use the technique by (Ruohoniemi and Greenwald, 1996) to derive SuperDARN convection maps. Thus, it is expected that we see more variations in the electric fields than those that would be estimated by the (Gordeev et al., 2018). Moreover, considering the qualitative variations in CPCP, which are consistent between W05 and OIS (Figure 5.7), we assume the OIS gives reasonable estimates.

During the expansion and recovery phases of the selected substorms, the number of observations at the SuperDARN was rather high, exceeding 200 and reaching 420 during the expansion phase of the second substorm. An examination of the data coverage shows the data mostly comes from the dawn, dusk, and noon sectors with some contribution from the midnight sector at the time of the first substorms recovery phase and the second substorms expansion phase. However, at other times, the data coverage was more limited with the dawn, noon and dusk sectors. The generous coverage across the dayside is favorable for constraining the solution for the global electric field pattern as the dayside throat region is then well mapped (Shepherd et al., 2002). Consequently, we expect that the SuperDARN results are reliable in respect of the global pattern but lack detail in the midnight sector at times other than 14:08 to 14:42 UT and 18:04 to 18:44 UT. Between 14:08 to 14:42 UT and 18:04 to 18:44 UT we expect the electric field and potential patterns to be more reliable since some of the observations exist in the midnight sector.

Wang et al. (2008) compared the CPCP between BRCM with DMSP and showed that the model underestimated the CPCP around 50% in the winter hemisphere and overestimated 50% in the summer hemisphere. On average, the model estimated the peak potentials $\sim 1.6^\circ$ MLat and peak of the FACs to be $\sim 4^\circ$ MLat poleward of the peaks in DMSP. They argued that the poleward locations of the peaks point out to a polar cap boundary more poleward than observed by the satellites during the storm periods,

which might be a result of the inner boundary of the model. The model was unable to capture the equatorward part of the high-latitude FACs, which are affected by the plasma sheet and ring current. In our study, the CPCP from the RCM and SuperDARN have the same order of magnitudes despite the 10 min lag of BRCM. It is found that the different choice of inner magnetospheric configuration in the MHD model changes the resultant ionospheric variations largely on quantitative and qualitative scale. BCRCM shows much larger CPCP than BRCM. The BCRCM predicts higher values than the SuperDARN, however, when there is data in the nightside, the difference between the SuperDARN and BCRCM decreases. SuperDARN may be underestimating the magnitude of electric fields when there is less data coming from the nightside. The W05 estimates are higher even during the quiet times preceding the substorms. The qualitative agreement between the W05, SuperDARN and BCRCM supports that the three models are capturing the essence of the variations in the ionosphere.

BCRCM and BRCM Pedersen conductances also differ from each other (Figure 5.4). While, BRCM does not produce the physics in the midnight sector so that underestimates the Pedersen conductances in post and pre-midnight sectors, the BCRCM gives adequate maxima at the locations found in the literature. However, with respect to the OPI, there is a clear overestimation by the BCRCM in all sectors except midnight, during the expansion phases of both substorms. In the BCRCM, the CRCM controls the amount of electrons lost in the loss cone as well as the inner magnetosphere-ionosphere coupling by the FACs. (Glocer et al. 2013) reported that the ion flux could be overestimated by the model if the model has less O⁺ on the boundary. It is possible that the overestimation of Pedersen conductances leads to the magnitude differences that are observed between the BCRCM and the OIS.

Aikio and Selkälä (2009) studied the statistical properties of the JH rate, electric field, and conductance in the high-latitude ionosphere using EISCAT radar measurements between March 6 and April 6, 2006 (declining phase of the solar cycle). They demonstrated that all these parameters show a clear MLT dependence on the KP index. For high KP, Aikio and Selkälä showed that the highest JH rates occur when both electric fields and conductances increase between 03-05 MLT in the morning sector. In the evening sector, a smaller maximum of JH occurs at 18 MLT while the minimum JH rates are found at night (23 MLT). The location and magnitudes of JH in W05

model agrees with the findings of Aikio and Selkälä (2009). However, the other methods show weaker JH in the dawn sector and close to the post-midnight as the SuperDARN, BRCM and BCRCM do not produce the electric field patterns in the dawn as strong as the W05. Even though the conductances provided by the BCRCM and OPI are high in the dawn, the electric field shows a counter-effect on JH magnitudes. Despite much of the dawn electric field is missing, all methods agree on a secondary maximum at 03 MLT. In these particular event cases, as seen from Figure 4, at 18:20 UT, the highest JH from the methods are found around 15 to 18 MLT, as high electric fields and high conductances are co-located and overlapped in the dusk sector. As the post-midnight conductances are lower in the BRCM and BCRCM, the BS method provides lower JH than the OIS in the post-midnight. The OIB reveals a more equatorward and expanded JH pattern at the dawn than the OIS, and larger cells in midnight and post-midnight sectors as the BCRCM electric field pattern is wider and higher than the SuperDARN in these sectors. Besides, in their study, Foster et al. (1983) found the highest JH in regions near noon, dawn and dusk in the dayside sector offering a horse-shoe shaped distribution. Those are the regions where strong electric field is co-located with high conductances. During the spring, JH maxima were found between 13-16 MLT. Fujii et al. (1999), using 28 days EISCAT 1 mode I data during 1989 and 1991, reported maxima at dawn and dusk sectors (04-08 MLT and 12-16 MLT or 16-20 MLT), which are co-located with electric field maxima. In addition to Fujii et al., Olsson et al., (2004) found maxima between 14-18 MLT between latitudes 60° - 70° and among 08-12 MLT between 70° - 80° MLat. In Baker et al.'s study (2004) study, which involves SuperDARN and a conductance model, enhanced JH was found inside the regions of weak aurora and strong electric fields and on the dusk side, close to the Region-1 currents. In Figure 5.5 of our study, distribution of the JH maxima shows that the highest values from the OIS and BS are generally found in the dusk and noon sectors, too. However, especially the OIB shows some spread in the midnight sector. This is because the BCRCM electric field pattern presents values, which are co-located with the post-midnight maxima seen in the OPI. Likewise, the peak in the OIB during the first substorm's recovery phase is created by the co-location of strong electric fields and conductances in the midnight sector (Figure 5.2, Figure 5.6).

The role of the electric field variability in the calculation of the JH rate was studied in detail by many in the literature (e.g. Aikio and Selkälä 2009; Codrescu et al., 1995;

Deng and Ridley, 2007). Yigit et al. (2011) demonstrated that increasing grid resolution helps to resolve the variations in the electric potential and gives better agreement with the AMIE results. Emery et al. (1999), using TIEGCM and AMIE, reported an increase by a factor of 1.5 in the summer hemisphere and 2.5 in the winter hemisphere for the adjustment of JH values to match the observations. Zhang et al. (2005) calculated JH using combined empirical models such as the Hardy et al. (1987) model for the conductances, Weimer (2001) for the electric field, HWM93 model for the neutral winds and IGRF for the magnetic field. Their model (Combined Empirical Joule Heating model: CEJH) gave consistent results with AMIE. However, CEJH model estimations were higher than AMIE during strongly disturbed conditions and lower during less-disturbed conditions. They suggested that the absence of a saturation function for the polar cap potentials may be the reason for this difference. In our study, we find that all the combinative methods are on the same order with Foster et al., (1983) study, which was also constructed using solar minimum data and JH from the combinative methods and MHD-model show the same temporal variations. A complete, unified version of global magnetosphere-ionosphere-thermosphere including the electric field variations does not currently exist. In addition to the individual effects of the Pedersen conductances and electric fields, their relative variations are also found to be important in determination of the JH rates (Aikio and Selkälä, 2009). Out-of-phase variations between electric fields and conductances are observed especially in short temporal scales and within small-scale, localized structures in the ionosphere resulting in lower JH rates. In our study, the effect of the electric field pattern is found to be stronger than the effect of conductances in determining the spatial distribution of JH. The differences in the spatial distribution of the JH from the methods are found to be mainly caused by the different spatial distribution of the electric fields. Especially, when there is data coming from the nightside, the performance of the OIS improves. It is encouraging to see that the OIS and BB_{crim} magnitudes agree well during these intervals (Table 5.4 and Table 5.5). The differences in between the methods can be considered as a result of the small-scale variations in the electric fields.

In addition, the methods BB_{nw_crim} and W05 which include the neutral wind effect demonstrate similar locations of enhanced JH. However, JH rates from W05 are very high with respect to the BB_{crim}. The two methods best agree during the first substorm's

expansion phase. At other times, $BBnw_crcm$ is half of the W05. Their onsets agree for both substorms, however, the recovery phase variations differ greatly from each other. Figure 5.8 indicates at the maximum, a 27% neutral wind effect on the JH rates in the dusk sector. The OIS does not include any neutral wind effects. However, adding a 27% difference to the OIS to account for the effect of the neutral wind for these events will not make the magnitudes of JH by the OIS close enough to the W05 and Olsson predictions. As Olsson and the W05 were both constructed using solar maximum data, this leads us to consider that they overestimate the JH dissipation in the ionosphere during the solar minimum.





6. NEUTRAL DENSITY VARIABILITY

In the previous chapter, we investigated the variability of JH during substorms and compared the methods with each other for two substorm cases during solar minimum. In the following chapters, we investigate the role of JH on the neutral density variation (Chapter.7) and the neutral density variability (Chapter 6) during selected geomagnetic storms. To investigate the role of JH on the neutral density variability during geomagnetic storms, first, methods to extract the storm-time response of the thermosphere were constructed. Then they were applied to neutral density from models and observations.

In this chapter, we introduce the baseline shifting methods and select the most efficient method to extract the storm-time response. Six events with KP ranging from 5 to 8+ are investigated using the physics-based and empirical models of the ionosphere-thermosphere. Table 6.1 presents the year and Julian date of the events with geomagnetic storm start and end times and the maximum values of geomagnetic indices along with the solar wind drivers for the events. In the table, an interval is defined as quiet when $KP < 3$ - and the neutral density variation in CHAMP is less than or equal to $1.25 \times 10^{-13} \text{ kg/m}^3$ in two consecutive passages of the spacecraft without a decreasing or increasing trend. We define it as the start of the storm when the increase in CHAMP neutral density is more than $1.25 \times 10^{-13} \text{ kg/m}^3$ and there is an increasing trend in two consecutive passages. The end of the storm is marked as the time when CHAMP neutral densities return to quiet-time average neutral density level. The threshold, $1.25 \times 10^{-13} \text{ kg/m}^3$, was selected by inspecting the orbit-averaged neutral density variations on quiet day cases (2007-79, 2007-190, 2007-341) in (Shim et al., 2012) (see Figure 6.1). In this figure, 2007-341 is represented with: green line with circle; 2007-79 red line with plus; 2007-190, blue line with asterisk. It is apparent that the maximum variation in global thermospheric neutral densities is around $\pm 1.22 \times 10^{-13} \text{ kg/m}^3$.

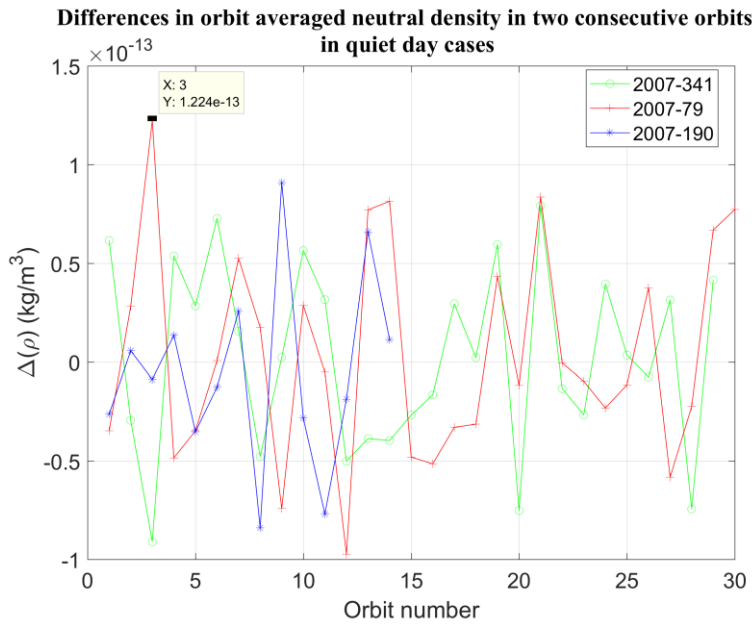


Figure 6.1 : Differences in orbit-averaged neutral densities in two consecutive orbits on quiet day cases.

The variation of the KP and Dst geomagnetic indices during the events is shown in Figure 6.2.

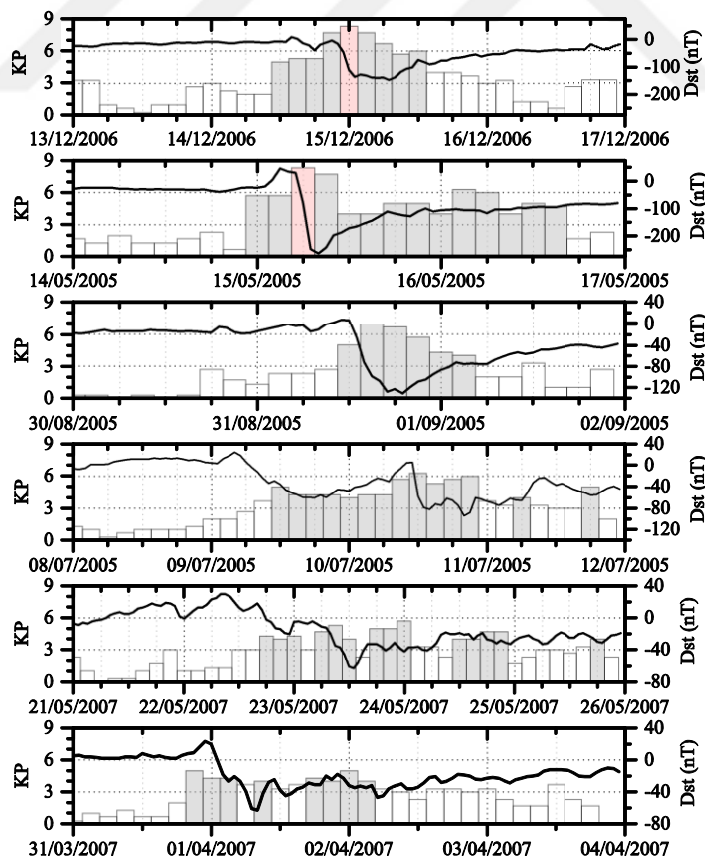


Figure 6.2 : KP and Dst variations during the GEM-CEDAR storm intervals.

Table 6.1 : GEM-CEDAR Challenge events. Table shows the maximum values of geomagnetic and solar indices (KP_{max}, F10.7, Dst_{max}, HP_{max}), solar wind sources of the events and quiet and disturbed intervals.

Event	KP _{max}	F10.7	Dst _{max} (nT)	HP _{max} (GW)	Driver	Quiet Interval	Disturbed Interval
2005-135	8+	103,3	-247	1225	CME	May 14, 04:30-May 15, 02:30	May 15, 04:00 - May 16, 23:59
2006-348	8+	84,86	-159	504	CME	December 13, 15:00- December 14, 14:00	December 14, 14:00- December 16, 12:00
2005-243	7	83,1	-122	260	HSS	August 30, 06:00- August 30, 23:59	August 31, 07:30-September 1, 23:59
2005-190	6+	100,8	-92	238	HSS	July 8, 09:30-July 9, 06:30:00	July 09, 07:00- July 12, 00:00
2007-142	5+	71,8	-49	197	HSS	May 21, 08:20-May 22 07:30	May 22, 08:30- May 25, 23:59
2007-091	5	71,16	-63	286	HSS	March 31, 03:00-March 31, 20:30	March 31, 23:00 -April 3, 23:59

Four of the events are due to a high speed stream and two of the events are due to a CME. The HSS events last longer, however their Dst and KP are less than the CME events.

Two empirical and three physics-based models are employed in this study. The empirical models are Naval Research Laboratory Mass Spectrometer and Incoherent Scatter Extended (NRLMSISE-00, will be referred to as MSIS, hereafter) (Picone et al., 2002) and Jacchia-Bowman-2008 (JB2008) (Bowman et al., 2008), whereas the physics-based models are Thermosphere-Ionosphere-Electrodynamics General Circulation Model (TIEGCM) (Richmond et al., 1992), Coupled Thermosphere Ionosphere Plasmasphere electrodynamics (CTIPe) (Millward et al., 2001; Codrescu et al., 2008) and GITM (Ridley et al., 2006). For each run and model, the initial parameters and model input are the same. The corresponding runs at the Community Coordinated Modeling Center (CCMC) can be found in Table 6.2.

Table 6.2 : Model runs at the CCMC for each event.

Event	Simulation IDs in CCMC Runs on Request System	Model Name and Version	Resolution (lat × long)
2006-348	Emine_Kalafatoglu_110113_IT_1	TIEGCM 1.95	2.5° × 5°
	Emine_Kalafatoglu_112613_IT_1	GITM 2.0	2.5° × 5°
	JaSoon_Shim_061114_IT_1	CTIPe	2° × 18°
2005-135	Emine_Kalafatoglu_050714_IT_2	TIEGCM 1.95	2.5° × 5°
	Emine_Kalafatoglu_051314_IT_1	GITM 2.0	2.5° × 5°
	Emine_Kalafatoglu_070314_IT_3	CTIPe	2° × 18°
2005-243	Emine_Kalafatoglu_050814_IT_1	TIEGCM 1.95	2.5° × 5°
	Emine_Kalafatoglu_051414_IT_1	GITM 2.0	2.5° × 5°
	JaSoon_Shim_061114_IT_2	CTIPe	2° × 18°
2005-190	Emine_Kalafatoglu_050714_IT_4	TIEGCM 1.95	2.5° × 5°
	Emine_Kalafatoglu_051314_IT_2	GITM 2.0	2.5° × 5°
	JaSoon_Shim_061114_IT_3	CTIPe	2° × 18°
2007-142	Emine_Kalafatoglu_050914_IT_3	TIEGCM 1.95	2.5° × 5°
	Emine_Kalafatoglu_051314_IT_3	GITM 2.0	2.5° × 5°
	Emine_Kalafatoglu_070714_IT_1	CTIPe	2° × 18°
2007-091	Emine_Kalafatoglu_050914_IT_2	TIEGCM 1.95	2.5° × 5°
	Emine_Kalafatoglu_051514_IT_2	GITM 2.0	2.5° × 5°
	Emine_Kalafatoglu_070714_IT_2	CTIPe	2° × 18°

Weimer-2005 (Weimer, 2005) is selected as the high-latitude driver for each model for consistency. Details on the models and standard configurations for the runs can be found in (Shim et al., 2011; Shim et al., 2012).

Our approach for assessing the storm-time model performances consists of three steps, such as orbit averaging, baseline shifting and assessment of the results. In the

following sections, we describe the tools designed for each step. The codes were written in MATLAB and are in transition to Python language.

6.1 Orbit Averaging Tool (OAT)

The orbit averaging tool (OAT) is used for taking orbital averages of thermospheric neutral density from CHAMP and models. Comparisons along the track involve local time effects, small-scale structures, and diurnal and seasonal variations (Qian and Solomon, 2012; Liu et al., 2005; Lühr et al., 2004; Kwak et al., 2009), which make it hard to specify the reason behind the difference in model estimations and observations. Figure 6.3 presents the CHAMP satellite orbital parameters X, Y, Z, latitude and longitude. The satellite passes from different local time regions making the direct evaluation and interpretation of the global environmental response more difficult.

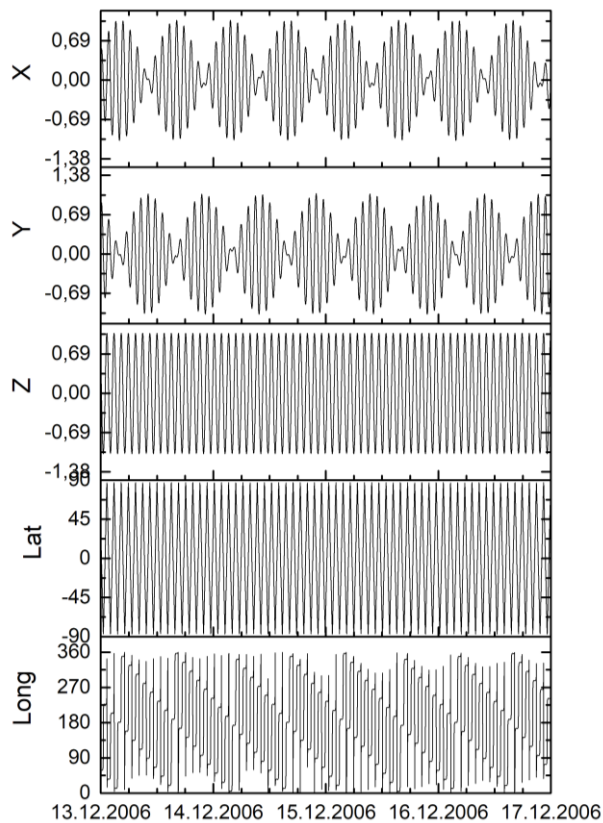


Figure 6.3 : CHAMP satellite daily orbital parameters.

Figure 6.4 shows how the neutral density varies along the satellite track. The increases and decreases in neutral density, nearly like a sinusoidal wave are due to the diurnal variation of the neutral density.

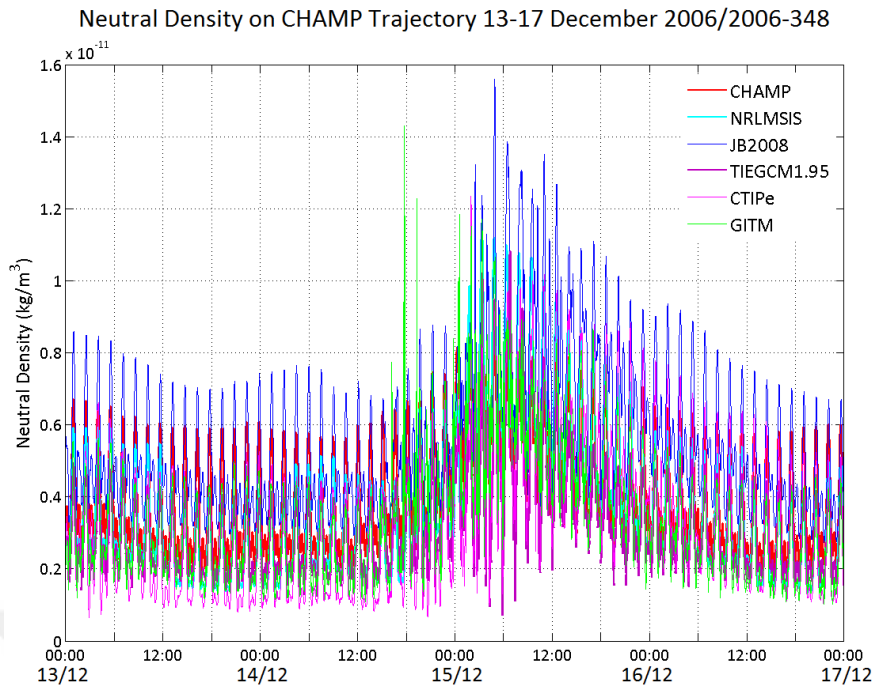


Figure 6.4 : Neutral density estimates from different models and the observations from CHAMP during the December 13, 2006 storm.

The storm effects start to appear after December 14, 2006, 12 UT as a superposition to the diurnal variations at the background. The total response is the result of season, solar cycle, local time, pre-storm conditions, storm intensity and storm duration (Suresh, 2016). On the other hand, orbit-averaging smooths out the abovementioned effects and provides a measure of the global response to the geomagnetic storm. The tool works with CHAMP ephemeris data. First, the beginning and end times of each orbit are determined: an orbit starts at the highest latitude in the northern hemisphere, crosses the highest latitude in the southern hemisphere and ends at the highest latitude in the northern hemisphere, that is, when a new orbit start is marked. One orbit lasts approximately 92 minutes. There are typically ~15 orbits in a day. After determining the orbit start and end times according to the locations of CHAMP (latitude), orbital averages are calculated for neutral density estimates from each model and CHAMP observations. An example of orbit averaged densities along the CHAMP orbit are shown in Figure 6.5. The daily variations are smoothed out and it is seen that the globally averaged neutral densities vary around the same level during quiet intervals.

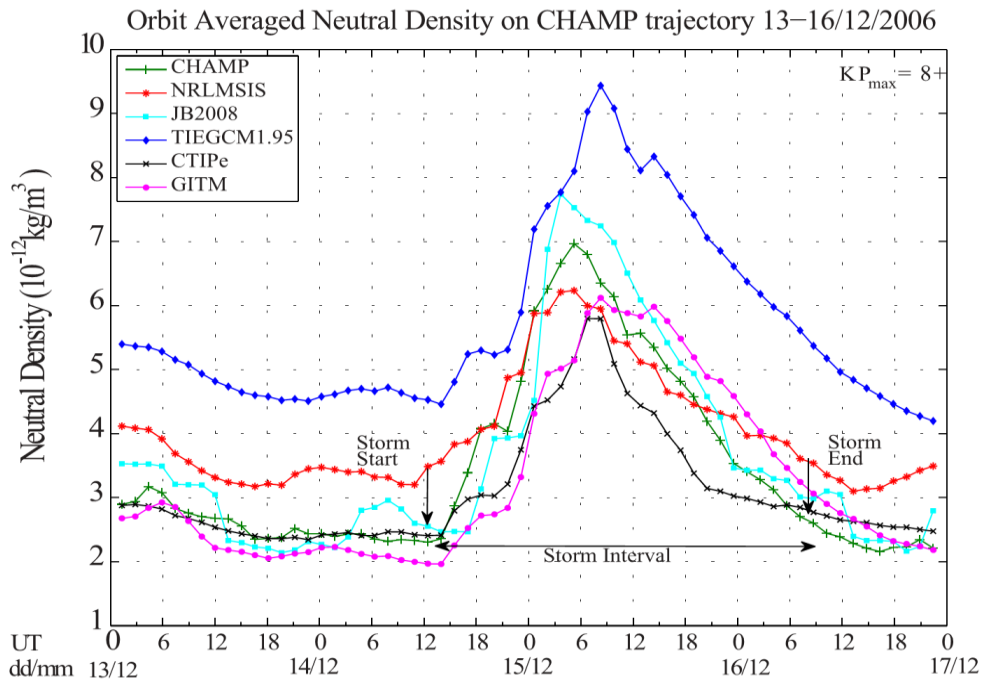


Figure 6.5 : Orbit-averaged neutral densities from the models and CHAMP as a product of the OAT.

6.2 Baseline Shifting Tool (BAST)

The baseline shifting tool (BAST) takes the orbit-averaged neutral densities in and shifts the data to the selected baseline. Table 2 presents the baseline shifts that are applied to the thermospheric neutral density. Subscript indice “n” represents the orbit number during the entire event, “i” represents the quiet time orbit number. ρ_q : quiet time neutral density from the model or CHAMP, ρ_{qC} : CHAMP observations during the selected quiet-time interval and ρ_{qm} : neutral density estimations from the model for the selected quiet-time interval. Δ and \times show that subtraction and multiplication is performed to shift the data. Overbars denote the mean.

Two baseline levels are selected: CHAMP level and zero level. Shift1 (S1), Shift3 (S3), Shift4 (S4) and Shift6 (S6) shift the data to CHAMP level using the quiet-time neutral density values. S1 and S4 use the quiet-time difference between CHAMP and the models, whereas S3 and S6 employ the quiet-time ratio between CHAMP and models. Shifting the data to CHAMP level removes the bias between the model and observed values. However, the shifted data still inherently includes the natural quiet-time variation of the thermosphere on a quiet day. In Shift2 (S2) and Shift5 (S5), the data are shifted to zero level, so that all the variations on a quiet-day are removed from

the model and observations. Consequently, only the storm-time variations are revealed. The second approach is more useful in characterizing the effects that are due to the geomagnetic storm.

Table 6.3 : Baseline shifts. ρ_{old} is the original orbit-averaged time series whereas ρ_{new} is the baseline shifted time series.

Shifts	Difference between the orbit averaged values	Shifting parameter	New estimates after the removal of the climatology	Quiet-time variation level (baseline)
Shift1 (S1)	$\Delta\rho_{1,i}=\rho_{qC,i} - \rho_{qm,i}$	$S_1=\overline{\Delta\rho_1}$	$\rho_{new,n}=\rho_{old,n}-S_1$	CHAMP level
Shift2 (S2)	$\Delta\rho_{2,i}=\rho_{q,i}$	$S_2=\overline{\Delta\rho_2}$	$\rho_{new,n}=\rho_{old,n}-S_2$	Zero level
Shift3 (S3)	$\times_{1,i}=\rho_{qC,i}/\rho_{qm,i}$	$S_3=\overline{\times_{1,i}}$	$\rho_{new,n}=\rho_{old,n}\times S_3$	CHAMP level
Shift4 (S4)	$\Delta\rho_{4,i}=\rho_{qC,i} - \rho_{qm,i}$	$S_{4,i}=\Delta\rho_{4,i}$	$\rho_{new,n}=\rho_{old,n}-S_{4,n}$	CHAMP level
Shift5 (S5)	$\Delta\rho_{5,i}=\rho_{q,i}$	$S_{5,i}=\Delta\rho_{5,i}$	$\rho_{new,n}=\rho_{old,n}-S_{5,n}$	Zero level
Shift6 (S6)	$\times_{2,i}=\rho_{qC,i}/\rho_{qm,i}$	$S_{6,i}=\times_{2,i}$	$\rho_{new,n}=\rho_{old,n}\times S_{6,n}$	CHAMP level

To shift the baseline to zero level and to extract the storm-time response of the thermosphere from the total thermospheric variation as in S2 and S5, it is important to determine the quiet day variations accurately. Accordingly, BAST requires the time intervals for the quiet and storm periods as input. The storm-time changes in the thermosphere are thought to be superimposed upon the quiet day levels. Thus, to be able to extract the storm-time response, first we have to estimate the quiet day variations (will be referred to as the background variations, hereafter) and assume the remaining changes in the thermospheric neutral density are due to the geomagnetic storm. For this purpose, it is essential to know what the variations on the day of the geomagnetic storm would have been unless there was a geomagnetic storm. As a result, the methods, which are generally used for time series forecasting purposes can

be used to estimate the background variations. The choice of the method depends on the mechanisms that cause the variations in the data and the time-scales that we are concerned with. The thermosphere varies in diurnal, seasonal and semi-annual time scales along with the solar and geomagnetic activity dependent variations (Zesta and Huang, 2016). In our study, we are mostly concerned with days-lasting events, which can occur at any time during the solar cycle. Hence, taking yearly or multi-year averages as in the case of climatology method would smooth out most of the seasonal, semi-annual and solar cycle dependent variations that influence the variations on a quiet day. This can lead to the underestimation of the actual variation on a quiet day. Consequently, using long-time statistics would not fit to today's scenario as accurately as we want due to the averaging that is involved in the process. Thus, methods requiring long-time data, like the trend method are also omitted. On the other hand, the analog method finds a day in the past with same or similar conditions and assumes that the present day will behave the same. However, it is also difficult to apply the analog method in the applications of space weather, as finding a perfect analog with the same solar wind conditions (similar IMF, V_{sw} , ρ_{sw}), geomagnetic indices and solar flux is nearly impossible. Another way to estimate the quiet day variations is to run the physics-based and empirical models of the ionosphere-thermosphere (IT). The IT models take the indices as inputs, which determine the level of activity on a quiet-day, ranging from the F10.7 (closely related to number of sunspots), F10.7A (81-day center averaged F10.7), daily A_p , hourly a_p , hemispheric power index to the Dst. The physics-based models of the IT also need the solar wind data to specify the ionospheric convection. In this case, the specification of the indices and the solar wind plays an important part in running the models and specifying the background level from the models. Hence, first the inputs to the models need to be determined accurately. To the authors knowledge, currently, there is no common consensus on what to use for the quiet-time levels of the indices and the solar wind properties. In addition, running the IT models introduce other uncertainties, which are unquantified at the moment. Therefore, for our purposes, we exclude running the IT models to determine and remove the storm-time background variations. However, an example of baseline shift using a climatological run is shown in Figure 6.6. The TIEGCM model is run for the same interval, December 13-December 17, in year 2007. During the interval, KP was at very low levels. However, the solar wind parameters and F10.7 were slightly

different. Consequently, subtraction of the two runs from each other led to the underestimation of quiet-day variations in TIEGCM (Figure 6.6-Panel 2).

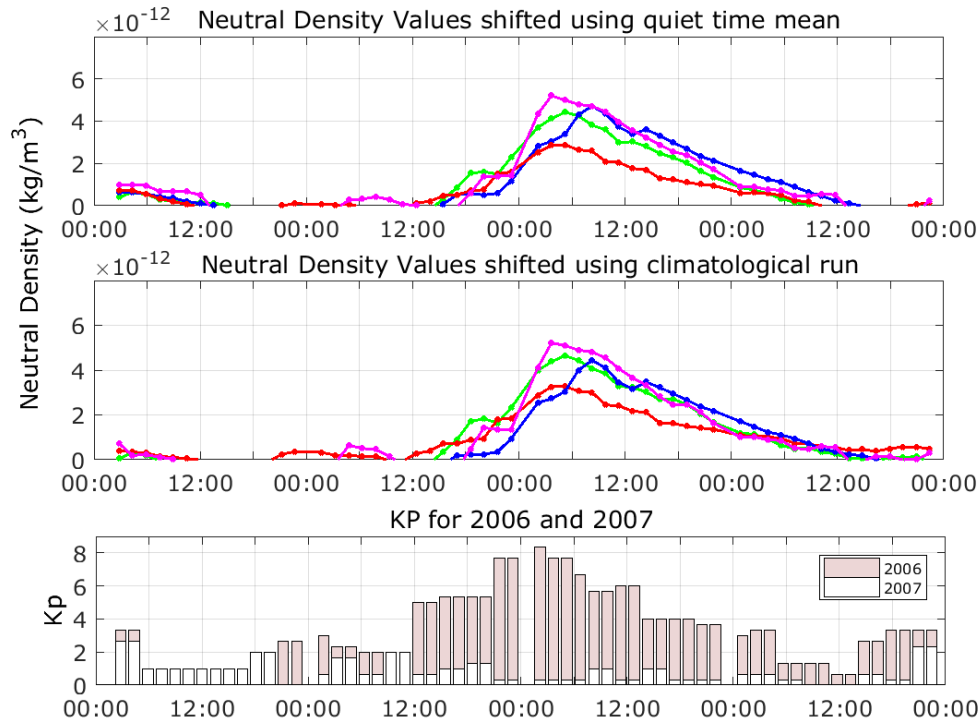


Figure 6.6 : An example of climatological baseline shift for 2006-348 event.

On the other hand, one of the quickest approaches in forecasting a time series is the persistent method, which proves handy when patterns change very little and features on the map move slowly. This is what we expect from the thermospheric variations on a quiet day without a geomagnetic storm. In this method, it is assumed that the following day would behave the same as the day before. Accordingly, the persistent method is valid when short-range forecasts are needed. Consequently, to reproduce the quiet time variations we employ the persistent method to estimate the background variations that the storm effects are superimposed on. It is assumed that the thermospheric neutral density variations on the day with the geomagnetic storm would have varied around the same baseline that it did on the observed quiet interval preceding the geomagnetic storm.

S1, S2 and S3 use a quick and dirty approach. The shifting parameters are calculated using only the quiet-time averages of data. First, for each model and CHAMP, neutral density averages during the quiet interval on the day prior to the geomagnetic storm are found. Following, the baseline shifts are applied. In S1, the mean difference between the model and CHAMP during the quiet time are subtracted from the whole

interval, so that the remaining data fluctuate around the CHAMP level during the quiet time. In S2, the quiet-time averages of each model and CHAMP are subtracted from themselves. As a result, quiet time variations vary around the zero level and the neutral density enhancement due to the storm are found. In S3, mean quiet-time ratio is calculated and whole interval is divided to this ratio.

S4, S5 involve point-to-point subtraction and S6 involves taking point to point ratios, respectively. For point-to-point applications, a new time series is needed, which displays variations similar to the quiet time during the storm interval. For this purpose, time series are reproduced using the quiet-time neutral density values at each orbit by assuming that the orbit averaged neutral density would stay the same if there is no geomagnetic activity as in the persistent method. As, we deal with orbit averages, which give the global response, this is a meaningful assumption. Emmert and Picone (2011) found the trend in density data is -1.94% per decade. Similarly, Qian et al. (2006) report -1.7% between the years 1970 and 2000. Hence, the long-time trend is very small to affect the daily tendency of thermospheric variations. The global averages should stay and vary around the same level if there is no heat and energy input to the thermosphere system. Figure 6.1 shows, in 2007, for quiet days, the background variations fluctuated around the same level, supporting this approach. Hence, for the baseline shift, first a quiet time interval is selected on the day preceding the geomagnetic storm. Then, using the selected quiet time interval, the quiet-time values for the disturbed intervals are duplicated for the disturbed interval in a sequential sense. Event though, the altitude, latitude and longitudes change with every orbit of the spacecraft on the following days, the changes in neutral density due to the location of the spacecraft are assumed to be small compared to the large fluctuations because of the geomagnetic storm (Qian and Solomon, 2012). Finally, the newly generated quiet time series are subtracted from the whole selected interval point-to-point. After the subtraction, the remaining variations in the neutral density are due to the geomagnetic storm in effect. In (Shim et al., 2015) a previous version of this approach was employed, in which the day preceding the geomagnetic storm was selected as the quiet time interval. In that case, some high-latitude variations when KP was higher than 2 and less than 3, which typically correspond to substorm conditions in the high-latitudes led to the overestimation of the quiet-time neutral densities, leading to smaller enhancements in computed storm-time changes for S2 and S5. Our current approach makes the calculations of quiet-time neutral densities as accurate as

possible. We estimate the errors to be as high as the selected threshold: $\pm 1.25 \times 10^{-13}$ kg/m³, which is about 5% to 7% of the quiet-time neutral density of the selected events. Shift amounts for S1 and S2 are displayed in Table 6.4.

Table 6.4 : Shift amounts for S1 and S2 (kg/m³).

Event	Model	ρ_{avg}	$\Delta\rho$
2005-135	SV2.3	2,92E-12	4,55E-13
	MSIS	3,53E-12	1,06E-12
	JB2008	2,95E-12	4,83E-13
	TIEGCM	4,11E-12	1,64E-12
	CTIPe	3,01E-12	5,44E-13
	GITM	2,54E-12	7,02E-14
	M2017	2,47E-12	0
2006-348	SV2.3	2,40E-12	3,72E-13
	MSIS	3,32E-12	1,30E-12
	JB2008	2,46E-12	4,31E-13
	TIEGCM	4,61E-12	2,58E-12
	CTIPe	2,41E-12	3,86E-13
	GITM	2,11E-12	8,02E-14
	M2017	2,03E-12	0
2005-243	SV2.3	2,56E-12	4,45E-13
	MSIS	2,30E-12	1,81E-13
	JB2008	2,30E-12	1,77E-13
	TIEGCM	3,45E-12	1,33E-12
	CTIPe	2,95E-12	8,29E-13
	GITM	2,89E-12	7,71E-13
	M2017	2,12E-12	0
2005-190	SV2.3	2,67E-12	4,30E-13
	MSIS	2,68E-12	4,36E-13
	JB2008	2,63E-12	3,93E-13
	TIEGCM	4,47E-12	2,23E-12
	CTIPe	2,78E-12	5,42E-13
	GITM	2,47E-12	2,26E-13
	M2017	2,24E-12	0
2007-142	SV2.3	1,78E-12	2,95E-13
	MSIS	2,44E-12	9,58E-13
	JB2008	2,19E-12	7,03E-13
	TIEGCM	3,28E-12	1,80E-12
	CTIPe	2,01E-12	5,27E-13
	GITM	1,65E-12	1,66E-13
	M2017	1,48E-12	0
2007-91	SV2.3	2,04E-12	3,57E-13
	MSIS	2,30E-12	6,12E-13
	JB2008	1,98E-12	2,89E-13
	TIEGCM	3,09E-12	1,40E-12
	CTIPe	1,76E-12	7,66E-14
	GITM	1,69E-12	8,03E-15
	M2017	1,69E-12	0

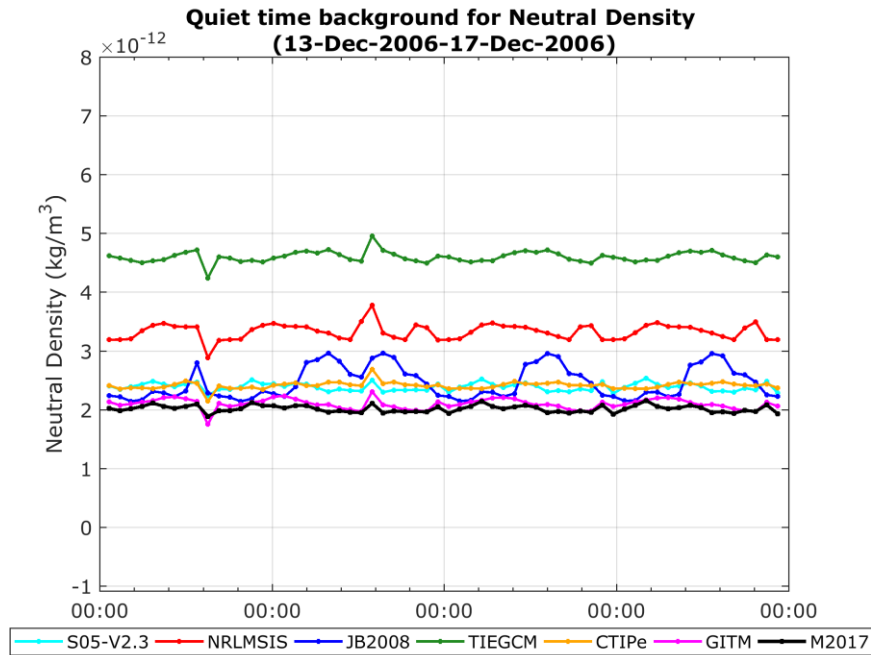


Figure 6.7 : Generated background series for 2006-348 event.

The background series that were generated for each event for the shifts S4, S5, and S6 are given in Figure A1 to A5 in Appendice. Figure 6.7 displays an example for 2006-348 event.

6.3 Performance Assessment Tool (PAT)

Storm-time model performances are evaluated after shifting the baseline of the model and observations. Model performances are measured with respect to the newly derived CHAMP thermospheric neutral density data by Mehta et al. (2017). Mehta et al. (2017) calculated the density estimates by taking a more complicated geometry into account and using the most recent advances in the modeling of gas-surface interactions and the modeling of physical C_D . They reported differences up to 20% for some cases from the neutral density estimates of Sutton (2005), which were widely used in the previous studies in the literature. Therefore, we also include Sutton (2005), named as SV2.3 hereafter to the assessment, and show the differences between Mehta et al. (2017), empirical and physics-based models and SV2.3 for each of the individual GEM-CEDAR challenge events. Mehta et al. (2017) is similarly referred to as M2017, hereafter.

Performance Assessment Tool (PAT) includes seven metrics and calculate the skill scores that are used to measure the model performances during individual events.

Those are: ratio between the model maximum and CHAMP maximum (Ratio_{\max}), ratio between the model mean and CHAMP mean ($\text{Ratio}_{\text{avg}}$), time delay between the peak of the model and peak of the CHAMP observation (TD), mean absolute error (MAE), normalized root mean square error (NRMSE), prediction efficiency (PE) and integrated density change (IDC). Equations from (6.1) to (6.7) show the definitions of the metrics. The subscripts i and t represent the orbit number and time, respectively. All calculations are based on the storm-time variations after performing the baseline shifts.

$$\text{Ratio}_{\max} = \frac{\rho_{\text{model},\max}}{\rho_{\text{CHAMP},\max}} \quad (6.1)$$

$$\text{Ratio}_{\text{avg}} = \frac{\rho_{\text{model},\text{avg}}}{\rho_{\text{CHAMP},\text{avg}}} \quad (6.2)$$

$$\text{TD} = t_{\text{model},\max} - t_{\text{CHAMP},\max} \quad (6.3)$$

$$\text{MAE} = \frac{\sum(\rho_{\text{CHAMP},i} - \rho_{\text{model},i})}{N} \quad (6.4)$$

$$\text{NRMSE} = \frac{1}{N} \sqrt{\sum \frac{(\rho_{\text{CHAMP},i} - \rho_{\text{model},i})^2}{(\rho_{\text{CHAMP},\max} - \rho_{\text{CHAMP},\min})}} \quad (6.5)$$

$$\text{PE} = 1 - \text{RMS}_{\text{model}} / \text{RMS}_{\text{ref}} = 1 - \frac{\sqrt{\sum(\rho_{\text{CHAMP},i} - \rho_{\text{model},i})^2}}{\sqrt{\sum(\rho_{\text{CHAMP},i} - \bar{\rho}_{\text{CHAMP},i})^2}} \quad (6.6)$$

$$\text{IDC} = \sum_i \left(\sum_t \rho_{\text{CHAMP},t} - \sum_t \rho_{\text{baseline},t} \right)_i \quad (6.7)$$

Among the metrics, the IDC works with the orbit and storm-time integrated neutral densities. Meanwhile, other metrics use the orbit-averaged neutral densities. The perfect score for the ratios (Ratio_{\max} , $\text{Ratio}_{\text{avg}}$) is 1, whereas TD should be zero, meaning there is no lag between the peak of the model and the time of the maximum from CHAMP. Determining the TD for less intense events is different from determining the TD for intense events. In intense events, the maximum of the neutral density is distinguishable, whereas in less intense events, there may be numerous local maxima. Consequently, we first mark the timing of the maximum neutral density from

M2017, then detect the timing of the closest local maxima from the models. MAE gives the average distance between the observation and model estimations. Values approaching to zero indicate better agreement between the model and observations. Furthermore, MAE gives a dimensioned skill score, that is, it has the same units with the neutral density (kg/m^3). On the other hand, ratios, NRMSE and PE are dimensionless. PE varies between 1 and negative infinity. PE equals to 1 indicates perfect agreement between the model and observations whereas PE=0 means the model errors are in the same order with the variations of the observations. Negative PE values show that the observed mean is a better estimate for forecasts than the model (Shim et al., 2012). The NRMSE, is the normalized version of RMSE. The NRMSE gives errors in percentage. RMSE, consequently, NRMSE, vary with the variability of error magnitudes and the mean absolute error (Wilmott and Matsuura, 2005). When interpreted together with the MAE, NRMSE provides information on the variability of error magnitudes.

6.4 Characteristics of the Thermospheric Neutral Density from the Models

Before the Shifts

Figure 6.8 shows the non-shifted storm-time maximum neutral density on the left, storm-time average neutral density from the models and CHAMP, in the middle, and the timing difference between the maximum in M2017 and models with respect to the events on the right. In the figure, the circles denote CHAMP neutral density estimations: orange, SV2.3 and dot-centered black, M2017. The triangles and the diamond show the model estimations: red, right-triangle: MSIS; blue, left-triangle: JB2008; green, up-triangle: TIEGCM; cyan, down-triangle: CTIPe; pink, diamond: GITM. X-label is the events listed from severe ($KP > 8$) to weak ($KP = 5$) starting from left to right, according to the NOAA classification based on KP values. M2017 represents the updated neutral densities by Mehta et al., (2017) and SV2.3 is the old neutral density estimates from CHAMP satellite accelerometer observations from (Sutton, 2005).

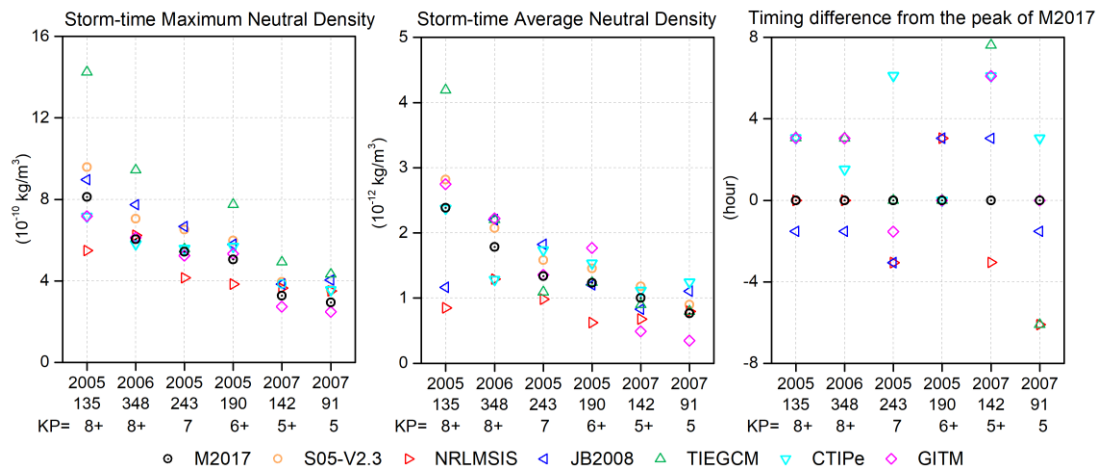


Figure 6.8 : From left to right: storm-time maximum in neutral density, storm-time average neutral density, timing difference between the peak of models and M2017 (without shift).

As evident from the plot, the storm-time maximum and average neutral densities from M2017 display a decreasing trend with weaker geomagnetic storms. Even though SV2.3 always shows higher values than M2017, it follows the same trend in neutral densities. For the neutral density maximum, all models show the same tendency as in CHAMP observations, except the 2005-243 event, which is due to an HSS. TIEGCM and JB2008 overestimate the neutral density peak in each event, whereas GITM slightly underestimates in HSS storms (2005-243, 2007-142 and 2007-91) and 2005-135. On the other hand, it is very close, but slightly overestimates M2017 in 2006-348 and 2005-190. MSIS neutral density maxima are higher than M2017 for events with $KP < 6$, but lower than M2017 for events with $KP > 6$, except the 2006-348 event. Despite being lower than M2017 in 2005-135, CTIPe is slightly lower than M2017 for events $KP > 8$, and higher than M2017 for events with $KP < 8$. Overall, CTIPe and GITM are the two models that generally show the closest neutral density maxima to M2017. These patterns in the modeled neutral density maxima change in the average neutral densities. A model overestimating the neutral density maxima can give a lower average than the M2017 or vice versa for the same events such as JB2008 and GITM for 2005-135, TIEGCM for the 2005-243 and MSIS for the 2006-348 and 2007-142. MSIS underestimates in all events except the 2007-91. JB2008 shows a somewhat random behavior and does not display a trend. Its behavior is independent of KP levels and solar wind drivers of the events. TIEGCM, and GITM display the decreasing trend also for the neutral density averages, except the 2005-243 event as in neutral density

maxima case. None of the models are found to be consistently closer to M2017 in terms of neutral density average before the baseline shifts.

Timing differences between the models and M2017 also change with respect to event. Interestingly, most of the models performed the best in capturing the timing of maximum in 2005-190 event, which is due to a CME during an HSS. The variations in timing differences seem to be random. The timing difference between the maxima of M2017 and the models are found to be between ± 7.5 hours.

6.5 Demonstration of the Methods: A Case Example

Figure 6.9 shows 2006-348 event as an example, which is classified as ‘severe’ according to the NOAA geomagnetic storm scale based on KP. The selected quiet time for the event is between 13/12/2006 15:00 UT and 14/12/2006 14:00 as shown in Table 6.1. The original time series from the model and observations are displayed in top-left corner, and the generated background series are in the bottom left. The background series are generated using the persistent method as explained in Section 6.2 by using the quiet-time neutral density estimations from the models on the day preceding the geomagnetic storm and sequentially reproducing them. It is seen that most of the models overestimate the neutral densities during the quiet-time interval. Appropriately, the shifts remove the bias from the models, so that we can compare the storm-time variations directly between the model and CHAMP observations. S4, S5 and S6 change the response curve of the models due to the point-to-point subtraction and multiplication. Especially the models, which display large fluctuations during the quiet-time as in JB2008 case are greatly modified in case of S4, S5 and S6. Models, other than the JB2008, show very little variations from their original temporal behavior as their fluctuations are very small during the quiet-time. In S1, S2, and S3, the models with climatology closer to M2017 change only slightly as the quiet-time averages are used and only one quantity is subtracted from the whole series. As seen, S4 and S6 match the climatology of the models and M2017 one-to one during the time preceding the geomagnetic storm. After S5, orbit-averaged densities from the models become zero during the quiet-time.

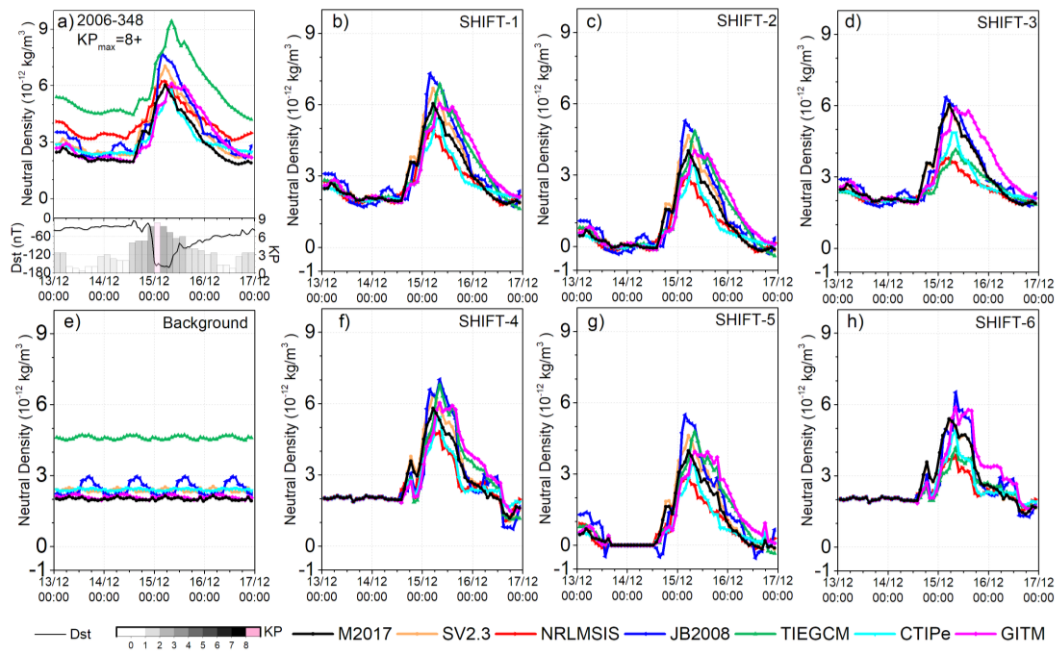


Figure 6.9 : An example event: 2006-348. First row, from left to right: a) top: Neutral density from the model and observations without shift; below: KP and Dst indices, neutral density estimations from the models and M2017 after b) S1, c) S2, d) S3. Second row, from left to right: e) Background series for the persistent method, neutral density estimations from the methods and M2017 after f) S4, g) S5, h) S6.

Before the baseline shifting procedure, MSIS is one of the best performing models with a maximum close to the M2017 for the 2006-348 event. However, with the removal of its bias, it is found that it actually underestimates the neutral density enhancement due to the geomagnetic storm. In the case of TIEGCM, the model overestimates the quiet-time neutral density so much that, the neutral density maximum and average during the storm are the highest among the models. Consequently, the resulting differences between the model and observation are the highest. On the other hand, shifting the baseline to CHAMP levels indicate that despite the bias in the model, quiet-time variations from the TIEGCM actually are modeled fairly-well and the storm-time response is closer to the observations than they are before the shift. These cases demonstrate the usefulness of the shifts in determining the actual storm-time response from the models. The variation of the thermospheric neutral density during the other events before and after the baseline shifting procedure and the generated background series are shown in Figures A1 to Figure A5 in the Appendix.

6.6 Evaluation of the Model Performances

Figure 6.10 presents the ratio of maximum neutral density (left column) and ratio of average neutral density (middle column) from each model to M2017. O denotes the original skill scores whereas S1 to S6 represents the shifts from Shift1 to Shift6. Red symbols represent the severe events with high KP; blue denotes strong event with $KP=7$; cyan is for $7 > KP > 6$; and green color is for weak events with KP around 5. Circle represents the event 2005-135; square, 2006-348; up-triangle, 2005-243; down-triangle, 2005-190; cross, 2007-142; plus, 2007-91.

SV-2.3 exhibits the best agreement with M2017 for all events after the baseline shifting. S3 and S6 yield the best results among the shifts and lead to one-to-one match between the M2017 and SV2.3 for all events. Perfect agreement within the two estimates that depend on CHAMP accelerometer observations are obtained after the shifting process. This means that M2017 and SV2.3 are different by a constant factor in each event. Employing average values as in S3 or point-to-point subtraction as in S6 does not seem to make a difference in the results. S3 and S6 work equally well. For the empirical and physics-based models, S1 and S4 produce the closest ratios to 1 among the shifts for both the ratio of maximum and ratio of average neutral densities. S2 and S5 cause the ratios to be more spread for all events and models. For all models, except the JB2008, using S3 and S6 lead to underestimation, whereas for JB2008, taking ratios lead to an overestimation in neutral density. For MSIS, CTIPe and GITM baseline shifting causes the ratios to diverge from 1 for some events, whereas for TIEGCM and JB2008 the shifts cause performance enhancement in capturing the maximum in M2017. Additionally, in TIEGCM, the 2005-135 event shows a distinct behavior and captures the maximum in M2017 better after S3 and S6. MSIS and GITM are found to underestimate the maximum in M2017 generally, after the shifts. On the other hand, JB2008 is found to constantly overestimate the peak except the event 2007-142. TIEGCM demonstrates higher maximum and averages than M2017 in severe cases ($KP > 8$) and underestimate the maximum in M2017 in event 2005-243. The ratio between the TIEGCM and M2017 is improved for events with $KP < 7$. On the contrary, CTIPe overestimates for events with $KP < 7$ and underestimates in with $KP \geq 7$. As a result, there is a clear dependency on the storm strength in the selected cases for TIEGCM and CTIPe.

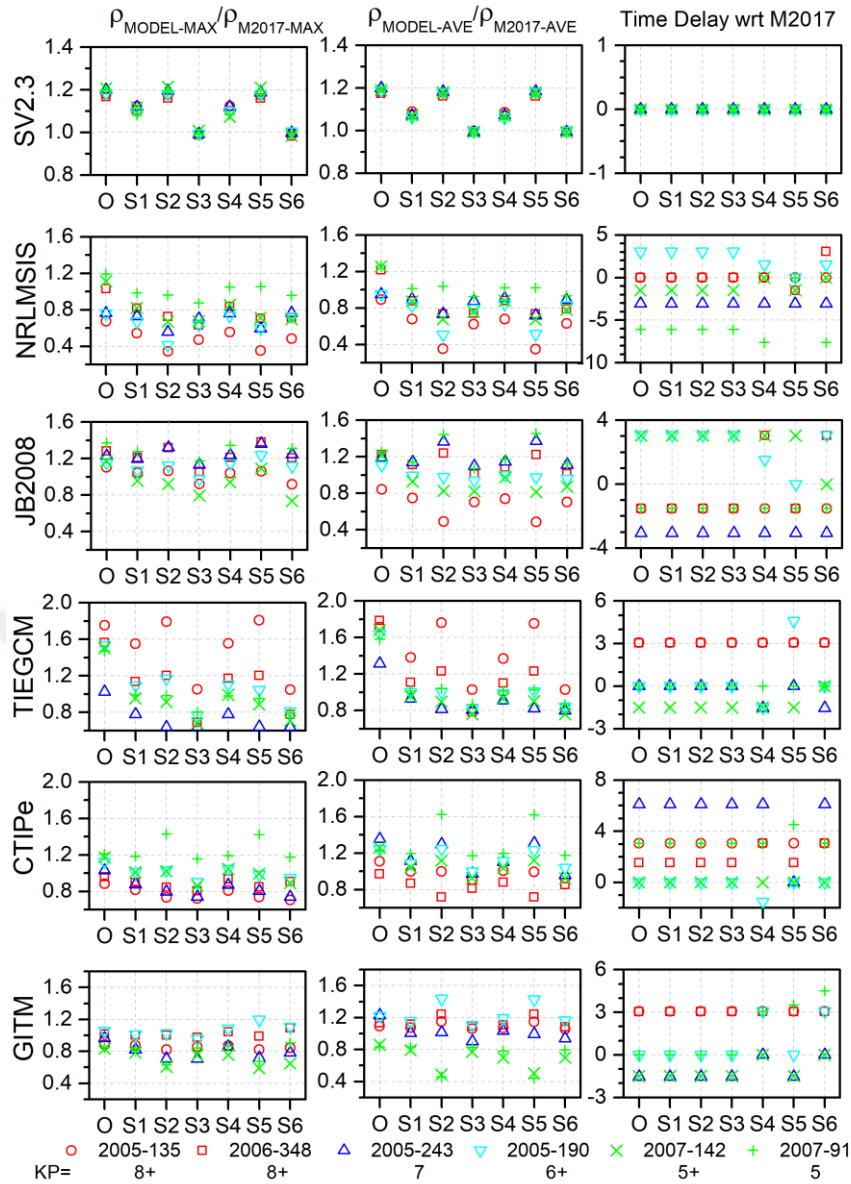


Figure 6.10 : Skill scores. From left to right: storm-time ratio of maximum neutral density of the models to M2017, storm-time ratio of average neutral density from the models to M2017, timing difference between the peak of models and M2017. From top to bottom: SV2.3, MSIS, JB2008, TIEGCM, CTIPe, GITM.

The same conclusions mostly hold true for the ratio with neutral density averages; only the amount of underestimation or overestimation changes. However, a model overestimating the neutral density maximum may underestimate the average density as in JB2008 case for the 2006-348 event. Moreover, a model underestimating the neutral density maximum may overestimate the average density as in CTIPe for the event 2005-243 and GITM as in events with $KP \geq 7$.

Timing differences between the maximum in M2017 and the models are shown on the right column in Figure 6.10. S1, S2 and S3 do not change the lags between the model

maximum and M2017. This is natural as only a constant value is used for the baseline shifts. However, S4, S5 and S6 lead to delays and early or on-time predictions changing the timing of the maximum from the models. There is not a pattern in the change of timings from the models. The timings change randomly with respect to event and models.

Figure 6.11 reveals the changes from the quiet-time values of the neutral density maximum (top panel) and averages (middle panel) from the models in percentage. Results of S2 are on the left and results of S5 are on the right column. The symbol and colors are the same as Figure 6.4. The percentages are calculated as $\% \text{Change} = 100 \times ((\text{storm} - \text{quiet}) / \text{quiet})$. Time and orbit-integrated density change (IDC) is shown in the bottom panel. The percentage change from the background variations and the IDC are calculated around the zero-baseline level when all climatology is removed. Accordingly, S2 and S5 are used in the calculations of percentage change and the IDC.

In M2017, the change in neutral density maximum due to the geomagnetic storm is found to be nearly as twice as the change in neutral density average for the observations and models for all events. The change in neutral density maximum ranges from 200% to 90% and the change in neutral density average range from 100% to 45%. The percentage change for the neutral density maximum and averages, which are calculated by means of S2 and S5 are nearly the same as each other for all models and events. Both the change in maximum and average of the observations (M2017 and SV2.3) show a decreasing trend with geomagnetic storm intensity in terms of KP. TIEGCM and CTIPe estimate the closest percentages to M2017 for events with $KP \leq 7$. CTIPe also performs reasonably well for events with $KP \geq 7$.

Contrary to the case in percentage change, IDC calculated by S2 and S5 indicate different values. IDC estimations by means of S2 are generally higher than the estimations after S5. Point to point subtraction leads to lower neutral density values. Geomagnetic storms with less KP, which are due to HSSs (2007-142, 2005-190) display IDCs as large as the events due to CMEs (2005-135, 2006-348). There is not any model, which is consistently closer to the IDC from M2017.

In IDC based on S2, MSIS is closer to M2017 more times than the other models (4 of the 6 selected cases: 2006-348, 2005-243, 2007-142, 2007-91). TIEGCM

overestimates in all events. Similar to TIEGCM, JB2008 and CTIPe are higher than the M2017, except the 2005-135 and 2005-243 event, respectively. GITM shows a distinction between $KP \geq 6+$ and $KP < 6+$ events: it over predicts the IDC in events with $KP \geq 6+$ and under predicts for events with $KP < 6+$. Even though some of the models approach to M2017 in terms of IDC in S5, GITM persists to show this distinction according to the KP level, except the 2005-243 event, where it performs the best in both S2 and S5. In S5, MSIS diverges from M2017 values, whereas TIEGCM demonstrates very close estimations to M2017 in 4 of the 6 selected cases. JB2008 results remain mainly the same with respect to M2017 between S2 and S5. However, the values get closer to M2017 in 2006-348 and 2005-190 cases.

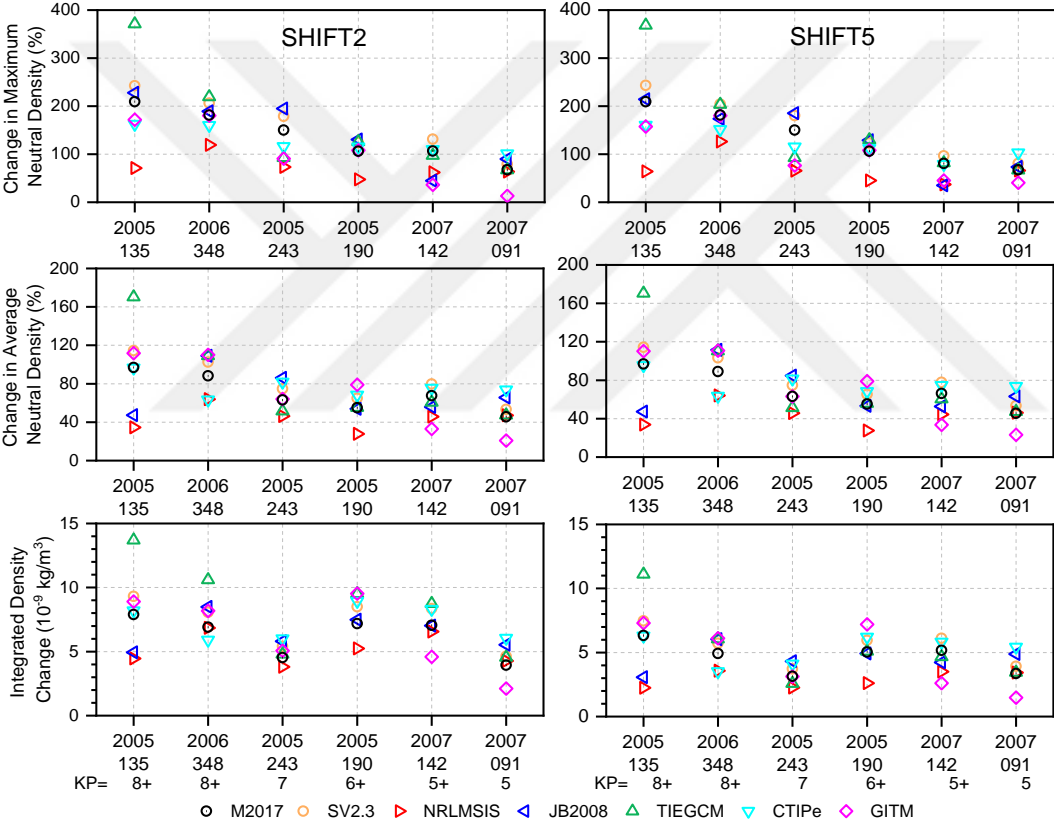


Figure 6.11 : From top to bottom: storm-time orbit and time integrated neutral density, storm-time change in maximum neutral density, storm-time change in mean neutral density.

Figure 6.12 presents the skill scores from the models, such as the mean absolute error (MAE), normalized root mean square error (NRMSE) and prediction efficiency (PE). MAE and NRMSE are negatively-oriented skill scores, meanwhile PE is positively-oriented. This means that, lower values of MAE and NRMSE are more desirable

whereas PE closer to one shows the perfect agreement between the models and M2017, in our case.

From Figure 6.12, the effect of baseline shifts on the storm-time performance of the models can be distinguished. It is found that generally, the calculated errors after the baseline shifts are on the same order. This shows that the results depending on the shifts are consistent with each other and the actual errors are successfully approximated. In the figure, baseline shifts are found to reduce the errors (MAE, NRMSE and PE) for the TIEGCM and SV2.3 for all cases. Additionally, as in the case of the ratios, S5.V2.3 errors are more efficiently reduced using the shifts S3 and S6 compared to the other shifts. The errors in TIEGCM increase with the intensity of the geomagnetic storm. After removing the climatology via the baseline shifts, the errors in CTIPe and JB2008 are also found to decrease except the 2006-348 and 2005-135 events, respectively. The events with the most errors in CTIPe model are found to be the problem cases, which Knipp et al., (2013) listed (2005-190, 2005-243 and 2005-135). JB2008 errors do not seem to depend on either KP levels or solar wind drivers of the events. They rather change randomly. GITM shows a reduction in error for events with $KP \geq 6+$ and growth in errors for the events with $KP < 6$ after the baseline shifts. On the contrary, the model errors increase for MSIS for events with $KP \geq 6+$, except the 2005-135 event, and decrease for events with $KP < 6$ after the removal of the climatology.

The MAE provides information on the amount of mean error in dimensioned units (kg/m³, in the case of thermospheric neutral density). MAE is found to be high for strong events and low for weak events after the baseline shifts (except for GITM in 2005-243 and CTIPe in 2006-348), which is consistent with the findings of (Shim et al., 2012). Moreover, the behavior of RMSE is the same with MAE in all cases and models and the amount of error grows with respect to event intensity. This is due to the scale of the event. The amount of error increases because of the large temporal variability of the thermospheric neutral density in geomagnetic storms. Normalization shows the errors are actually around the same magnitudes in terms of percentage for the events. Consequently, in the middle column, normalized root mean square error provides the errors in percentage. A high MAE may account for a low NRMSE based on the variation of the thermospheric neutral density during the event. However, the changes in MAE and NRMSE after the shifts are consistent with each other. An

increase in MAE after the shift, with respect to the original time series without shift, mirrors itself as an increase in NRMSE with respect to the original time series, as well. Thus, basically, the MAE and NRMSE provide the same information on the change in errors. However, NRMSE gives the additional information that how much this error accounts for from the perspective of the variability of the thermospheric neutral density based on the event. The NRMSE from the models are confined between 60% to 10% after the shifts. Before the shift, TIEGCM has the maximum NRMSE with ~125% for the event 2007-91. The shifts revealed that its actual storm-time performance to be on the order of ~12% (S1, S2, S4, S5) to ~33% (S3, S6) for the same event. In contrast, MSIS has a minimum error around ~25%, which increases to ~37% (S1, S2, S4, S5) to ~41% (S3, S6) for the event 2005-135. In addition to these, except the SV2.3 and TIEGCM in 2005-135 event, it is observed in the NRMSE that S3 and S6 introduce slightly higher errors compared to the other shifts in all events. The 2005-135 is an exceptional case as can be seen from MAE, RMSE, NRMSE and PE of the TIEGCM. Interestingly, only for TIEGCM among the other empirical and physics-based models of the IT and solely in this event, baseline removal via ratios (S3 and S6) reduces the error more than the shifts based on subtraction. In this case, the storm-time variation is so high and strong that it is compensated by taking ratios. However, we argue that this is not the true performance of the model. The model actually overestimates the storm-time variation, and the reduced error via ratios is probably artificial as storm effects are generally additions to the background. Methods based on ratios (S3 and S6) in other events, give rise to the underestimation of the average and maximum values of the neutral density from TIEGCM (Figures 6.6 and 6.9, Figures A1 to A5). Despite, the shifts S3 and S6 reduce the errors more than the other shifts for the SV2.3, since neutral density are derived from the accelerometer on spacecraft and the error can be multiplied during this process. The PE on the right column shows the same variations with the NRMSE according to the event. The PE increases when the NRMSE increases and vice versa. The original PE of TIEGCM in negative direction is so low that the scales are compressed. PE results after the shifts S1 to S6 are shown in another frame inside the PE panel for TIEGCM with scaled y-axis due to the very low PE in original estimations. However, after the shifts, there is a clear improvement in skill scores, which can be seen from the frame interior to the figure.

Lastly, all shifts and all events in terms of MAE, NRMSE, and PE show that the shifts S3 and S6 work perfectly for the SV2.3 and the errors are on the order of $\sim 1\%$, with a maximum of $\sim 2.5\%$.

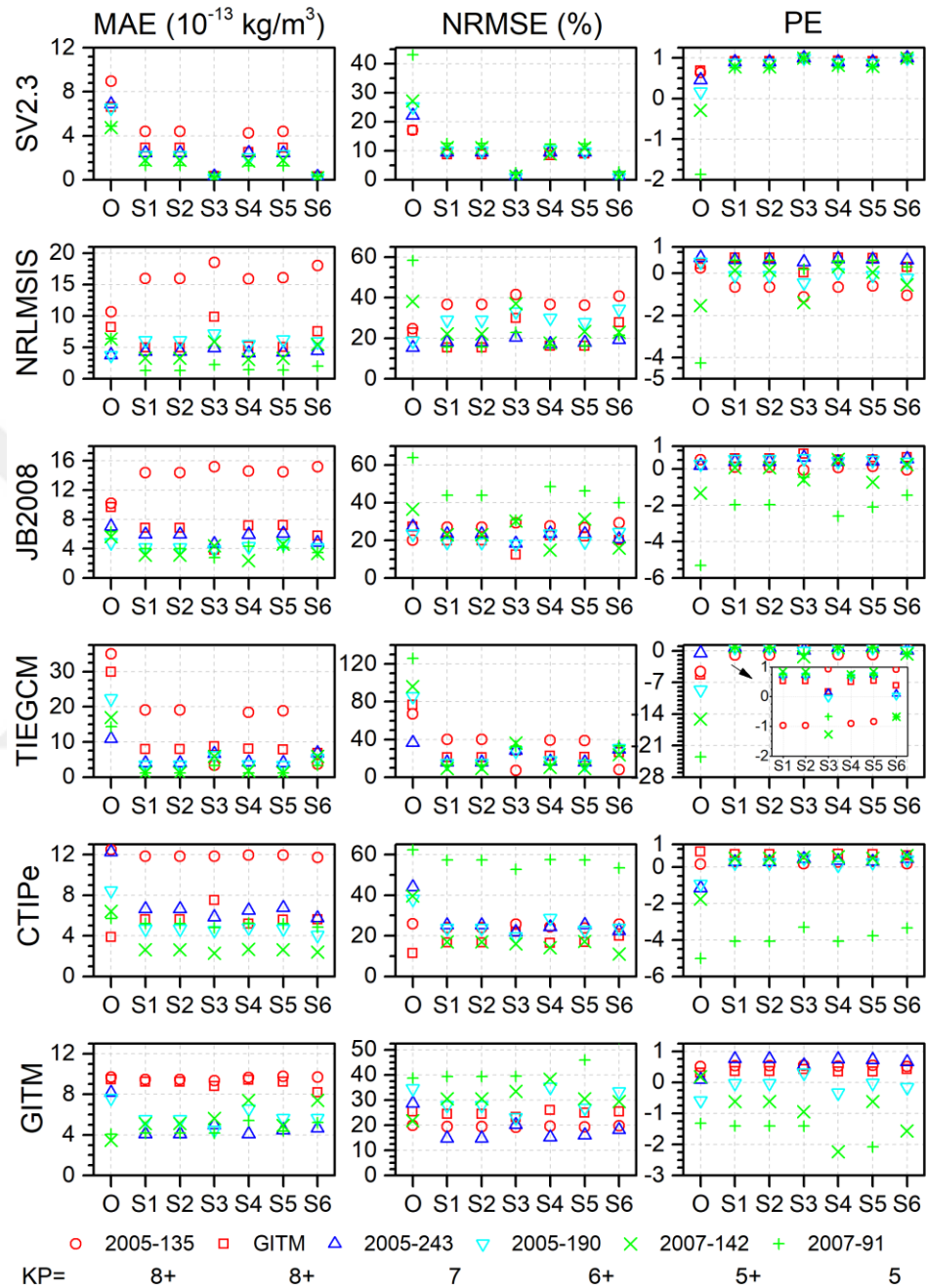


Figure 6.12 : Skill scores: From left to right: MAE, NRMSE, PE. KP scales, axis labels, colors and symbols are the same as Figure 6.10.

6.7 Discussion on the Performances of the Methods

In this study, in order to evaluate the storm-time performance of the models, we employed baseline shifts to remove the climatology and selected metrics to quantify the errors from the models. It is shown that it is critical to define quiet-time references in determining the actual storm-time performances. Six approaches were developed to remove the effects of climatology from the storm-time performances of the models. The model data was shifted to either CHAMP levels or zero level by using averages or point-to-point subtraction or multiplication. The quiet-time interval is determined by inspecting the CHAMP neutral density variations on the day preceding the geomagnetic storm. Quick and dirty methods (S1, S2 and S3) use the quiet-time average of the neutral density. Shift1 (S1) and Shift3 (S3) employ the quiet time average difference and quiet time average ratio between the model and observation and shift the data to CHAMP levels. Shift2 (S2) uses the quiet-time average and shifts the data to zero level by subtracting the whole climatology. Shift4 (S4), Shift5 (S5) and Shift6 (S6) also use the difference between model and CHAMP observations, i.e., difference from zero and quiet time ratio between the model and observation, respectively. However, for S4, S5 and S6, persistent method is employed to generate the background series so that the methods are applied point-to-point.

For the storm-time performance assessment of the models, generally S1, S2, S4 and S5 are found to work equally well. The choice of different baseline levels (shifting the models to the level of CHAMP observations or shifting observations and models to zero level by removing all the climatology) and using either a quick and dirty or persistent approach does not change the amount of error associated with a model. The storm-time errors of the models are found to be on the same order after S1, S2, S4 and S5 in all selected cases. Besides, S3 and S6 increase the variability of the errors from the models when compared to the other shifts. This is due to the fact that the storm-time effects are generally superimposed upon the background (climatological) variations and their nature is not multiplicative. Hence, modifying the original time series using ratios does not work as efficiently as the subtraction process for the empirical and physics-based models. On the other hand, the shifts S3 and S6 work the best for SV2.3 as the difference between the M2017 and SV2.3 is the modeling of the C_d factor, which is a coefficient in the drag equation. Hence, when neutral density is derived from accelerometer data, systematic error and bias can be multiplied, so it is

reasonable to divide to remove them. This follows that the findings of the past model validation studies which used SV2.3 can be re-evaluated and calibrated using the S3 or S6. It is found that the nature of the climatology determines the choice of the baseline shift. For models, which show unexpected, decreasing trend, we advise using S1 and S2, which employ only the quiet-time average differences and values to shift the model estimations to the selected baseline, as S4 and S5 may lead to unphysical variations in model estimations as illustrated in GITM for weak events (Figure A5 and Figure a6).

We also investigated if there is a pattern in models, which leads to constant overestimation or underestimation from the models. It is found that, TIEGCM is more successful in low KP events, and its success rate decreases with the intensity of the storm. GITM shows a reduction in error for events with $KP \geq 6+$ and increase in errors for the events with $KP < 6$. On the contrary, the model errors increase for MSIS for events with $KP \geq 6+$, except the 2005-135 event, and decrease for events with $KP < 6$. JB2008 shows somewhat random errors for the selected cases. Three of the six events selected in this study were listed as problem storms by (Knipp et al., 2013). We find that, CTIpe has the most difficulties in these cases (2005-190, 2005-243 and 2005-135). Figures A2, A3, and A4 show that the CTIpe is slow to recover the neutral densities, thus the errors are due to the overestimation of the neutral densities. $Ratio_{avg}$ in Figure 6.10 also supports this conclusion. On the other hand, for these storms, the range of errors from the models are between 13% to 40% and do not greatly differ from the other cases. Thus, we do not see any distinction among model performances with respect to the solar wind drivers of the events, but find differences based on KP for some of the models (MSIS, TIEGCM, GITM). In some events and models, the shifts reduce the errors due to climatology in evaluating the storm-time performances up to 113% (TIEGCM-2007-91: 125% to 12%) whereas in some events, they increase the errors by 13% (MSIS-2005-135: 12% to 25%).

Furthermore, it is possible to estimate integrated neutral density change (IDC) during the storm via S2 and S5, which shift the baseline to zero level. IDC is important as drag has a cumulative effect on orbit determination and prediction (Emmert et al., 2017). For the evaluations in drag calculations, we suggest using the upper limits for IDC that are calculated after S2 and S5 to stay on the safe side.

The second part of this study involves the metrics to quantify the errors. Six metrics are employed for this purpose: the ratio between the model maximum and CHAMP

maximum (Ratio_{\max}), ratio between the model mean and CHAMP mean ($\text{Ratio}_{\text{avg}}$), time delay between the peak of the model and peak of the CHAMP observation (TD), mean absolute error (MAE), normalized root mean square error (NRMSE), prediction efficiency (PE) and integrated density change (IDC). It is found that Ratio_{\max} and $\text{Ratio}_{\text{avg}}$ may not be consistent with each other even after the baseline shifting procedure. A model overestimating the ratio of maximum may predict the $\text{Ratio}_{\text{avg}}$ well. This is due to the shape of the response curve and is controlled by how fast the growth and decay rates of the neutral density are within the model. Thus, neither the neutral density maximum nor the neutral density average is definitive in model performance assessment when used alone. In this study, consistency is achieved between the skill scores MAE, RMSE, NRMSE and PE after the baseline shifts. (Chai et al., 2014) suggests using several metrics together as each of them points out a different aspect of the error properties of a model; especially in studies involving the assessment of more than one model when the error distribution becomes important. Consequently, we suggest using MAE, NRMSE and PE together for the neutral density evaluations. MAE will provide the mean amount of error, NRMSE, the error percentage with regard to the event and PE will provide how efficient the model is in capturing the variability and mean of the neutral density observations.

7. ON THE RELATION BETWEEN JOULE HEATING AND NEUTRAL DENSITY

Neutral density estimations from the empirical and physics-based models of the IT were investigated in the previous chapter. Baseline shifting techniques were used to eliminate the effects of the pre-storm time interval and to remove the bias between the model estimations and CHAMP observations. These techniques can further be used to explore the relation between JH and neutral density during geomagnetic storms. In this chapter, we employ the baseline shifting techniques to construct simple relations between the JH and thermospheric neutral density from the IT models.

In a previous study, (Fedrizzi et al., 2012) employed a shaping filter to JH time series to match the JH from CTIPe model with neutral density observed by CHAMP. Using CTIPe model, they created a Joule heating index, which is directly related to the neutral density change in the thermospheric altitudes from CHAMP satellite. In our work, we investigate the correlation between the JH from the IT models, CTIPe and TIEGCM, and neutral density from the same IT models and CHAMP observations.

Previous work on the relation between JH and neutral density revealed that the neutral density variations in thermospheric altitudes follow the variations in JH with a time lag. This time lag varies between 1.5 hours and 6 hours depending on the event (Oliveira et al., 2017). Consequently, to find the correlation between the JH and neutral density, first, the JH and neutral density have to be superposed. For this purpose, we first apply a cross-correlation between the neutral density and JH and find two time lags:

1. Time lag between the JH and neutral density estimations from the model
2. Time lag between the JH from the model and CHAMP neutral density estimations of (Mehta et al. 2017)

After JH data is temporally shifted according to these two time lags above, we investigate the relation between JH and neutral density in three ways:

1. Over the entire data using instantaneous stormtime JH and neutral density

2. Event-based separate investigations based on stormtime variations in JH and neutral density
3. Integrating JH and neutral density over entire events

In all calculations, baseline shifts described in Section 5.4 are employed to find the neutral density change associated with the Joule heating. However, values of JH and neutral density integrated over the satellite orbit are used instead of the orbit-averaged values. We prefer the Shift2 (S2) as it is simple but as efficient as the other shifts. In S2, the reference level for the modeled neutral density is the zero level. Hence, S2 is useful in removing the bias and climatology from the models, so that effects due to previous days are eliminated.

The success of the fits are measured using the residual sum of squares and the correlation coefficient. Equation 7.1 gives how residual sum of squares is calculated. y_i is the observed thermospheric density and $f(x_i)$ is the thermospheric density predicted using the regression fits.

$$RSSE = \sum_{i=1}^n (y_i - f(x_i))^2 \quad (7.1)$$

$$r = \frac{n(\sum xy) - (\sum x)(\sum y)}{\sqrt{[n\sum x^2 - (\sum x)^2][n\sum y^2 - (\sum y)^2]}} \quad (7.2)$$

Equation 7.2 shows the equation for Pearson's correlation coefficient. x is JH from the model and y is the predicted thermospheric neutral density from either the model or CHAMP.

7.1 Relation between the Instantaneous JH and Neutral Density

Figure 7.1 presents the JH and neutral density variations during the same event presented in Chapter 6.5: i.e. the 2006-348 event. On the left, original time series with no time shift is displayed. In the middle, shifted time series and on the right, time lags between the models and CHAMP neutral density are shown. For the 2006-348 event, the time delays between the model JH and neutral densities range from 2 hours to 5 hours. Figure 7.1b illustrates that the neutral densities are shifted to the JH maximum using the time lags found by the cross-correlation analysis based on Figure 7.1a.

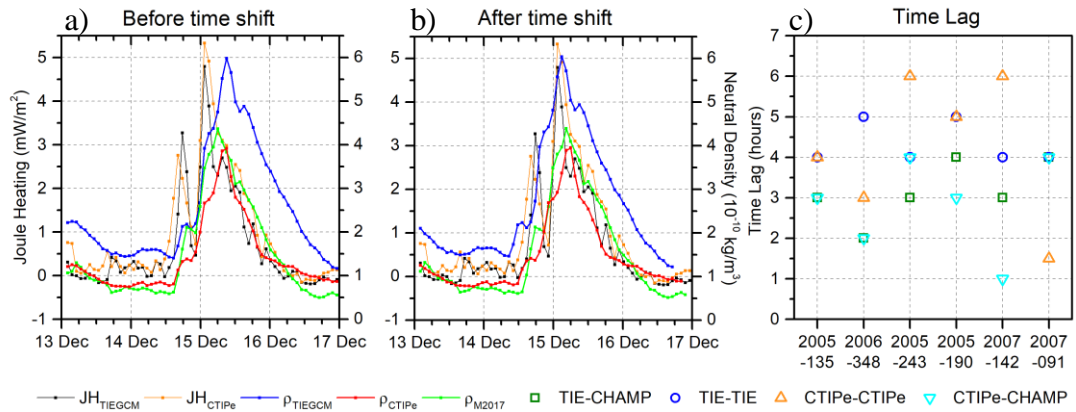


Figure 7.1 : Temporal variation of neutral density from CHAMP, TIEGCM and CTIPe and superposed JH from TIEGCM and CTIPe (2006-348) a) before the time shift, b) after the time shift c) time delays.

The time lags found by the same way for all 6 events studied in the previous chapter are presented in Figure 7.1c. The figure indicates that the time lags between the Joule heating and the neutral density vary from 1 to 7 hours between the models. Time series after the time shifts for the other 5 events can be found in the appendice section.

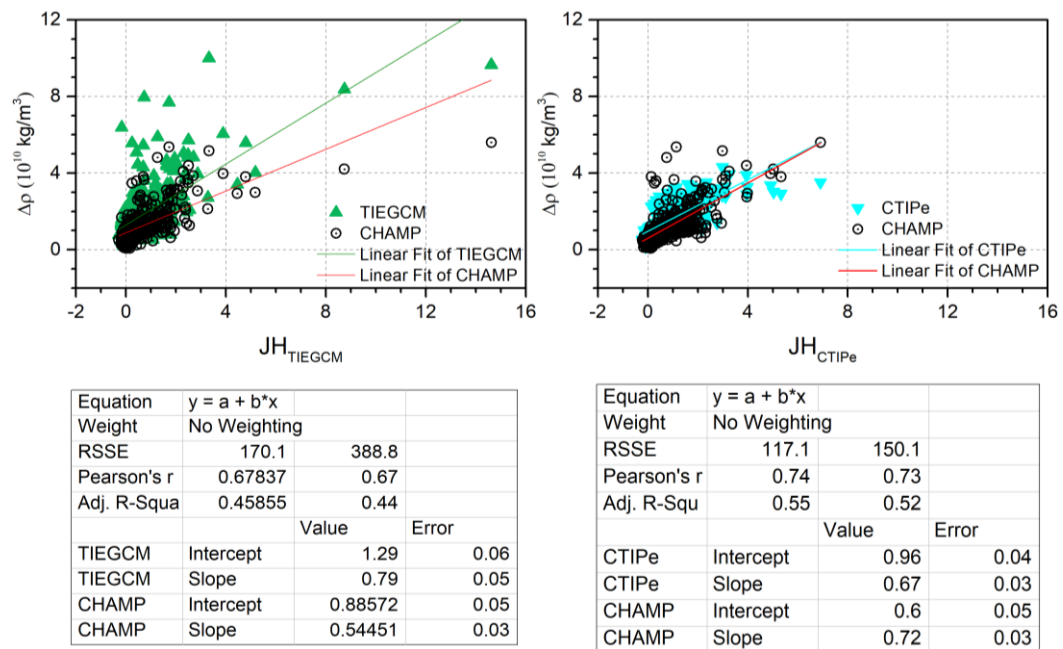


Figure 7.2 : Correlation between the JH from the models and neutral density estimations a) TIEGCM and CHAMP b) CTIPe and CHAMP.

In Figure 7.2, we present the relation between model JH and neutral densities from the models and CHAMP. The left panel and the table below give the correlation between TIEGCM JH and neutral density from TIEGCM and CHAMP, whereas the right panel and the table below it display the correlation between JH from CTIPe and neutral

density from CHAMP and CTIPe. The black points denote the CHAMP measurements, green upward triangle, TIEGCM and cyan, downward triangle the CTIPe model results. The points are instantaneous neutral density values plotted versus predicted JH from the models and include the storm time data of all events. It is found that the correlations between the model JH and model neutral densities are slightly higher than the correlations between the model JH and CHAMP observations for both models. CTIPe model is better in terms of residual sum of squares and displays higher correlation coefficient (0.73) between model estimated JH and neutral density from CHAMP than the TIEGCM estimated JH and neutral density from CHAMP (0.67).

7.2 Storm-time Relation Between the JH and Neutral Density

Figure 7.3 displays the relations between storm-time JH and storm-time neutral density from the models and CHAMP. In each panel green, upward triangles denote the storm-time TIEGCM neutral densities, cyan, downward triangles denote the CTIPe neutral densities and black dots denote the CHAMP measurements. The green solid lines represent the regression between TIEGCM JH and TIEGCM neutral density, solid cyan lines represent the regression between CTIPe JH and CTIPe neutral density and black solid lines represent the regression between model JH and CHAMP neutral density. From top to bottom events are plotted according to the severity of the geomagnetic storm from the strongest to the weakest based on KP scale.

The slope and intercept, residual sum of squares and R values for the regression lines for each event and model are listed in Table 7.1. The regressions display more meaningful relations for the 2006-348 and 2005-243 events, since $R \geq 0.80$ for these events for both models. However, for other events, R changes between 0.30 to 0.63 at the most. Both models show the worst performance for the low KP, HSS events. Root sum square is found to be lower for the HSS events. However, this is due to the small amount of variation in neutral density during the HSS events. Since it is not normalized, the RSSE does not give the performance of the models in percentage and should be compared within the models for each event. The slope and intercept of the regressions are also very different from event to event. This is due to the differences in response of the JH and neutral density to the varying interplanetary magnetic field directions.

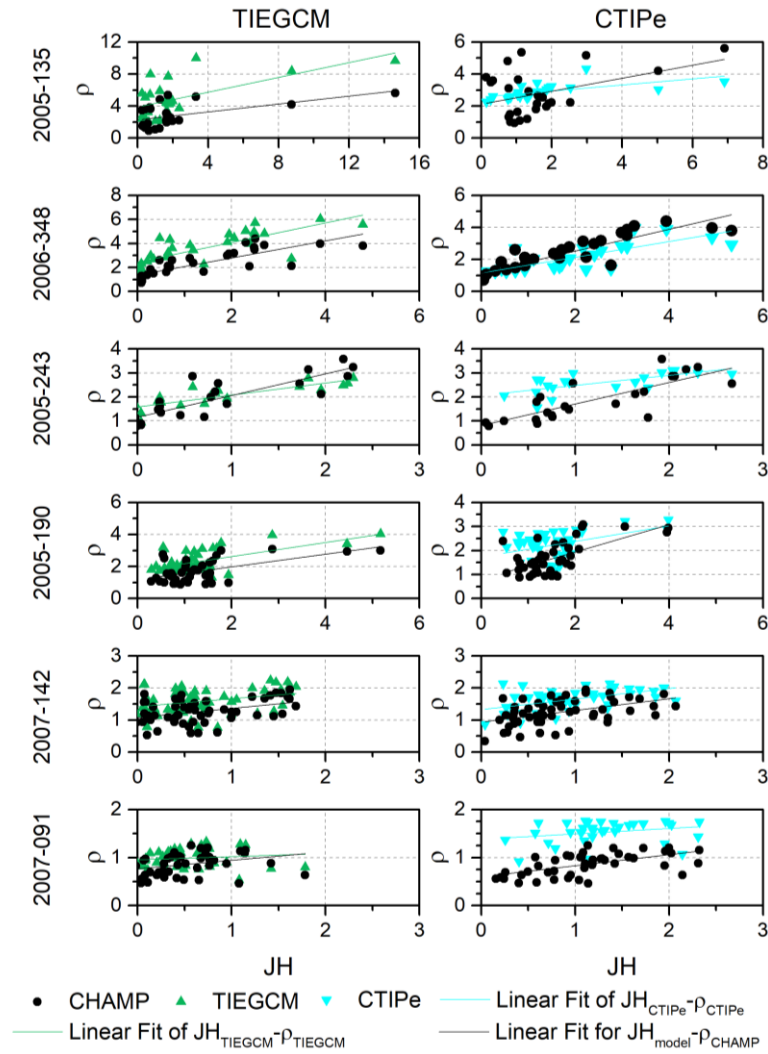


Figure 7.3 : Storm-time correlation between the JH and neutral density for all events.

Table 7.1 : Properties of the correlation between model JH and CHAMP neutral density.

Storm-time Correlations		a (Slope)	b (Intercept)	RSSE	R
2005-135	TIEGCM-CHAMP	2,26	0,24	35,68	0,53
	CTIPe-CHAMP	2,11	0,40	41,03	0,42
2006-348	TIEGCM-CHAMP	1,35	0,71	12,53	0,82
	CTIPe-CHAMP	1,14	0,68	7,62	0,89
2005-243	TIEGCM-CHAMP	1,15	0,90	4,24	0,87
	CTIPe-CHAMP	0,80	0,89	5,55	0,80
2005-190	TIEGCM-CHAMP	1,17	0,39	12,51	0,56
	CTIPe-CHAMP	0,79	0,56	11,01	0,63
2007-142	TIEGCM-CHAMP	1,07	0,28	5,85	0,40
	CTIPe-CHAMP	0,93	0,36	6,54	0,47
2007-091	TIEGCM-CHAMP	0,76	0,17	2,08	0,30
	CTIPe-CHAMP	0,60	0,23	1,54	0,57

TIEGCM performs slightly better for the high KP events, whereas CTIPe performs slightly better for the low KP events in this data set. However, it is hard to draw any general conclusions from 6 events.

7.3 Relation Between the Integrated JH and Neutral Density

Lastly, we look for a relation between the integrated JH and integrated neutral densities for the seven GEM-CEDAR events listed in Section 5.4. For this purpose, we calculate the total Joule heating and integrated density change as in Equations 7.3 and 7.4.

$$JH_{total} = \int Q_j(t)dt \quad (7.3)$$

$$\Sigma\rho_{event} = \int \rho(t)dt \quad (7.4)$$

After finding the integrated values, a linear relationship is obtained by utilizing the linear regression method between the storm-time integrated density change and the total Joule heating. Figure 7.4 shows the results.

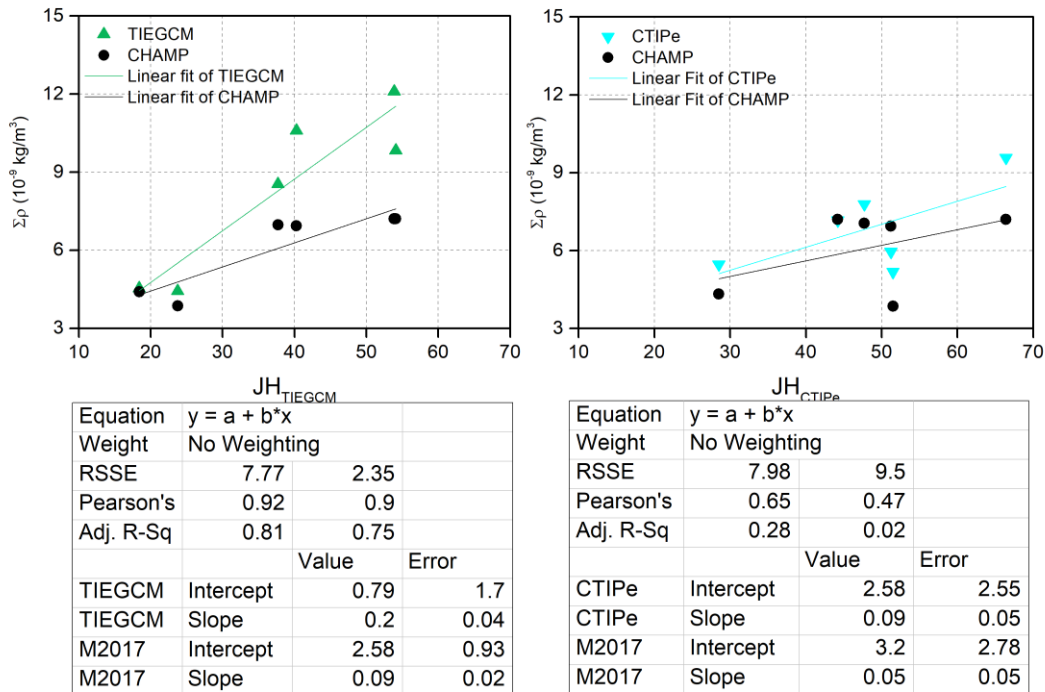


Figure 7.4 : Integrated storm-time neutral density response from models and CHAMP for GEM-CEDAR events vs. integrated JH from IT models. From left to right: a) TIEGCM and CHAMP b) CTIPe and CHAMP.

Interestingly, TIEGCM model gives better correlation between the total JH from the model and the total neutral density from CHAMP. The correlation coefficient shows an extremely high relation on the order of 0.9. On the other hand, CTIPe correlation coefficient remains at low levels around 0.47 for the integrated density and JH. This correlation coefficient is very low compared to the correlation coefficients found by Fedrizzi et al. (2012).

7.4 Discussion on the relation between JH and neutral density

In this chapter, we showed the relations between JH from the models and thermospheric neutral density from the models and space borne measurements. We found that the relations can be as low as 0.3 (TIEGCM-CHAMP/2007-91) and as high as 0.89 (CTIPe-CHAMP/2006-348). The relations are highly variable and change based on the event. The success rate of the fits decrease with decreasing event intensity and is less for the events due to high speed streams.



8. FIELD WORK

This chapter has been assigned to study the space weather effects on the ground. Geomagnetically induced currents (GICs) are the most direct and world wide consequences of the near Earth space environment that are observed on the ground magnetic stations. These currents are detected at various levels at different latitudes over the globe. In this chapter, we examine the variations in geomagnetic and geoelectric field over Turkey during geomagnetic activity and investigate the possible sources in association with the geomagnetically induced currents. This study is the first that presents the direct measurements of the geoelectric field and the geomagnetic field variations in connection with GICs in the Eurasia region.

8.1 Magnetotelluric Measurements in Bozcaada

To monitor the geoelectric and geomagnetic field variations at mid-latitudes, over Turkey, a magnetotelluric measurement system was setup in Bozcaada, Çanakkale, Turkey. In Figure 8.1, panel a indicates the location of the measurement system in the island of Bozcaada, panel b depicts a sketch of the instrumental set up in the field and panel c shows the components of the measurement system.

As panel a shows, Bozcaada is the third largest island of Turkey in the northeastern part of the Aegean Sea about 6 km away from the mainland Anatolia. It constitutes Bozcaada district of Çanakkale province which is shown in light green on the map. The geographic and geomagnetic coordinates of the station are (39.50°N, 26.02°E) and (37.5°N, 106.1°E), respectively. Hereafter, throughout the study, we will use the geomagnetic coordinates for Bozcaada. Bozcaada has a size of 40 km² and the population is small of about 2500 and mainly occupied with farming. The soil in Bozcaada is adequate for grape, crop, pulse, and fruit growth and the area was being used mainly for farming purposes during its historical development and still so. It is the soil's electrical conductivity here that concerns us as we use electrical measurements at a certain depth below the surface to infer to the underground geomagnetic currents. The electrical conductivity of the soil in the area is associated

with the basic ingredients of the soil that allow the farming. In several places nearby Bozcaada region, the electrical conductivity of the soil was found to be small changing from 0.030 dS/m to 0.49 dS/m on the surface resulting from the salinity and basic natural minerals in the soil (Şeker et al., 2009; Parlak et al., 2008). It is anticipated that the electrical conductivity will change with the depth. However, unfortunately we were not able to find any source that give detailed information on the soil electrical conductivity mapping.

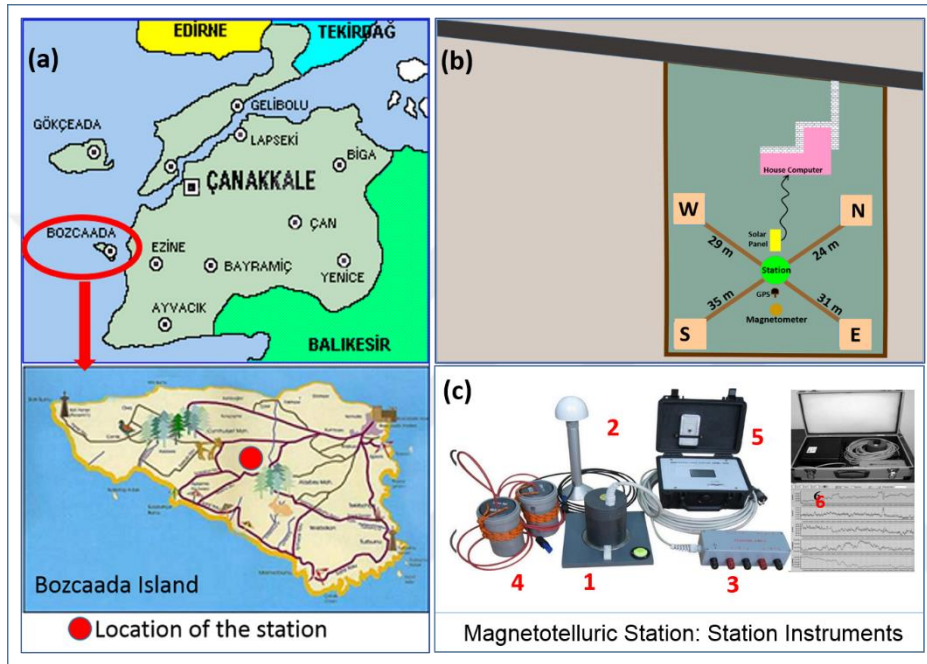


Figure 8.1 : (a) A map of the region and island Bozcaada, Çanakkale, Turkey, where the instruments were installed. (b) Plan of the instrumental set up in the field. (c) Instruments that came with magnetotelluric station; (1) Magnetometer, (2) GPS receiver, (3) Electrometer, (4) Electrodes, (5) Station, (6) An example of raw data.

In this study, we use Laboratory for ElectroMagnetic Innovation (LEMI)'s Long-period Magnetotelluric Station (LEMI-417) which consists of one electrometer and four electrodes to measure the geoelectric field, a magnetometer, and LEMI-417 electronic unit that allows acquisition, processing and storage of the measured data in the internal memory and their transmission to the computer via RS-232 (or RS-422) interface (see Figure 8.1c). The magnetometer is based on the fluxgate principles. Additionally, built-in GPS receiver provides satellite synchronization of the internal clock and the coordinates of the MTS location. Detailed technical specifications for the instruments can be found at (www.lemisensors.com). The magnetotelluric currents consist of both the natural electrical currents flowing within the Earth and the electrical currents originating externally from the ionosphere and/or magnetosphere. They are

produced on the ground through the electromagnetic induction by the time-varying geomagnetic fields or whenever a conducting body moves across the Earth's permanent geomagnetic field (Lanzerotti and Gregori, 1986). LEMI-417 was designed for the measurement of natural magnetic and electric field components and their variations in laboratory and field conditions (<http://www.isr.lviv.ua/lemi417.htm>; Korepanov, 2011). The LEMI-417 electronic unit records the absolute measurements of the magnetic field in three directions, i.e. B_x , B_y , B_z , and electric field in two directions, i.e. E_x and E_y , and the resolution is 1 second. The magnetic field and electric field components are measured in a coordinate system such that x-axis points to magnetic north and is positive northward; y-axis points to magnetic east and is positive eastward; and z-axis points down toward the center of the Earth's and is positive downward. Accordingly, B_x and E_x are the north-south and B_y and E_y are the east-west components of the magnetic and electric field in this coordinate system. Magnetic and electric field data are recorded in nT and $\mu\text{V/m}$, respectively. We convert the electric field data to mV/km throughout this paper to be consistent with the previous GIC studies in the literature. In addition, LEMI-417 measures the subsurface temperature at the location of the magnetometer and electrometer. Temperature measurements are necessary to check the efficiency and the stability of the system. The raw data are stored automatically in the memory card and later transferred into the computer via internet. Measurements started in Sept 2013 and the system operates since then.

All LEMI-417 components seen in Figure 1c were placed in a small, local farm area on a hill located in the middle of the island with dimensions of about 100x100 m. The magnetometer, electrometer with four channels, and the LEMI417 electronic unit were buried under the ground at about 80 cm depth in the middle of the field as seen in Figure 8.1b. Four Cu-CuSO₄ electrodes were arranged in the field such that the electrodes were separated by 60m in the east-west direction and by 59m in north-south direction and placed at the same soil depth as the magnetometer. The placement of electrodes in the north-south and east west is indicated in Figure 8.1b. The surroundings are electrically quite, i.e. away from the electrical power lines, busy local motorways and streets, and any other large systems and buildings that may generate large amounts of electricity that will affect our electricity measurements at about 80 cm below the soil surface. Also shown in Figure 8.1b, are the GPS antenna and the solar panel, placed nearby the measurement unit to power the whole system.

8.2 Event Selection and Data Preparation

For the geomagnetically induced currents over Turkey, we mainly focus on the variations observed in the horizontal components of the magnetic (B_x , B_y) and electric (E_x , E_y) fields measured by LEMI-417, i.e. north-south and east-west components, and the time derivatives of the horizontal magnetic field components, i.e. dB_x/dt and dB_y/dt , and compare and discuss their variability during the geomagnetic disturbances. At any particular period, the north-south (E_x) and east-west (E_y) electric field components are linearly related to the north-south (B_x) and east-west (B_y) magnetic field components through the equations given below:

$$E_x = ZB_y \quad (8.1)$$

$$E_y = -ZB_x \quad (8.2)$$

In these equations, Z is the estimates of the characteristic impedance which is related to the conductivity of the surface. This relationship is valid under certain conditions, that is when the electromagnetic fields are plane waves at the earth's surface and that the earth consists of parallel layers (Naidu, 2012).

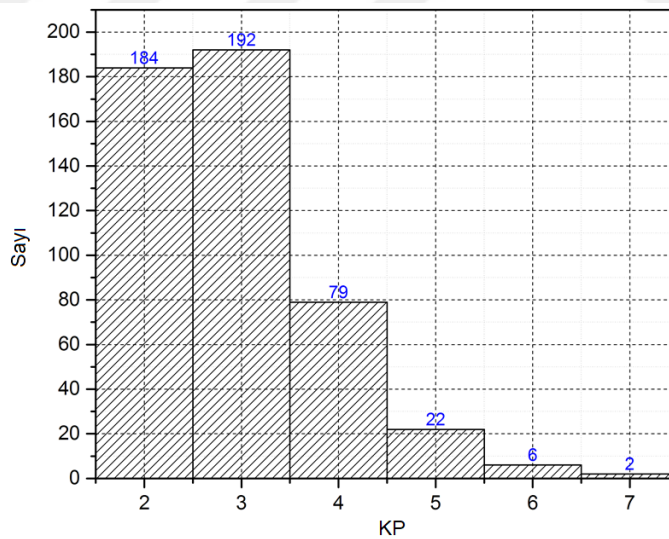


Figure 8.2 : Number of events between September 2013 and September 2014 according to KP index.

In order to study the magnetic and electric field variations during geomagnetic activity, we selected three geomagnetic disturbance events by examining the geomagnetic indices, KP, Dst and AE, from World Data Center (WDC) for Geomagnetism, Kyoto's web site (<http://wdc.kugi.kyoto-u.ac.jp/>). Figure 8.2 shows the number of events

binned according to the KP level. We focus on the $KP > 5$ events, which are classified as geomagnetic storms according to the NOAA KP scale. There were 30 events which fit to this criterion between September 2013 and September 2014. We selected three events from this database for detailed investigations. Two of these events consist of geomagnetic storms together with magnetospheric substorms while one of them is a non-storm sudden commencement event. As our station is located at midlatitudes, in our search of geomagnetic disturbances, we especially paid attention that the KP index was larger than 5 and Dst indicated sudden commencement, which is typically around 20-30 nT, within the selected time interval. We also added AE index variations along with KP and Dst corresponding to our cases. KP index is a three-hour magnetic index, and Dst and AE index are available in hourly and minute resolution. Following Gonzalez et al. (1994), one of our selected intervals (April 20, 2014) corresponds to typical substorm activity, while the other two (Oct 8, 2013 and June 8, 2014) correspond to moderate and weak geomagnetic storms, respectively. We also determined a geomagnetically quiet day as a reference in order to refer to the variations during geomagnetically disturbed times. All three indices were obtained from the website of WDC for Geomagnetism, Kyoto. Once the geomagnetic activity intervals were determined, we examined the corresponding features in our ground magnetic and electric field measurements at these intervals after removing the noise using wavelets and the background variations using the best curve fits. Time variations of the indices were plotted at the bottom of each figure in the next section where we present the data for the selected cases while Table 8.1 below presents the events selected to be studied in this part of our work and their corresponding maximum KP, Dst and AE index.

Table 8.1 : Selected events and corresponding maximum KP, Dst and AE index during the period of ground level fluctuations.

Case No	Event Date	Storm Scale	Dst (nT)		KP	AE (nT)
			SC _{max}	Dst _{min}		
0	October 6, 2013	Quiet	3	-5	1+	166
1	April 20, 2014	Typical	28	-1	5	922
2	October 8, 2013	Moderate	22	-62	6-	1415
3	June 8, 2014	Weak	30	-35	6+	1780

In addition to the geomagnetic indices, we searched for the correlation between our magnetic and electric field measurements and the structures such as CMEs or

Interplanetary Coronal Mass Ejection, High Speed Streams (HSS), and Interplanetary Shock Structures (ISS) in the solar wind plasma and Interplanetary Magnetic Field (IMF). For this purpose, we used IMF and plasma data, i.e. density, velocity, temperature, dynamic pressure, measured by MFI and SWE instruments at ACE spacecraft located at the Lagrangian point L1. To correctly associate the features, the solar wind and IMF were advected to the Earth's bow shock by taking the solar wind transit time from L1 point to the shock into account. The resolution of the IMF and plasma data are 16 secs and 64 secs as measured at ACE and the data were obtained from NASA's CDAWeb (Coordinated Data Analysis Web) public data resources (<https://cdaweb.sci.gsfc.nasa.gov/>). The presence of the solar wind structures including CME corresponding to our events are determined by examining the total magnetic field and its components, especially IMF B_z component, density, velocity, temperature, and dynamic pressure variations.

Figure 8.3 presents the magnetic field and electric field variations recorded on October 6, 2013 as an example of the quiet day when there are no magnetic storms and magnetospheric substorms. We use KP, Dst and AE indices to identify the geomagnetic activity intervals. While AE index is a good indicator for auroral disturbances and identifies the presence of magnetospheric substorms, KP and Dst are used to determine the global geomagnetic activity level and to indicate the presence of the magnetic storms, respectively. The terminology used by Viljanen (2001, 2006) was adopted to refer to the storm-time substorms when Dst falls below -40 nT, i.e. Dst < -40 nT, and isolated substorms when Dst > -40 nT. In our study, we use the term sudden commencement (SC) simply to refer to both the sharp rise in Dst and the follow up initial phase of the geomagnetic storm. The last panel in the figure shows the geomagnetic activity level with KP index (white to black bar plots) on the left scale, and Dst (red) and AE (black) indices on the right. KP index for this day ranged from 0 to 1+ while Dst varied between ± 5 nT. AE exceeded 100 nT very briefly at about 13:30 UT but generally showed small variations between 0 nT and 166 nT. All three indicate that there is no magnetic storm or substorm and thus the day is geomagnetically quiet. The dashed black line gives "0 nT" level for Dst and AE indices. ACE magnetic field and solar wind plasma data (not shown here) also do not indicate any major solar storms or CME events in the solar wind corresponding to this day. Therefore, the day is quiet in terms of solar activity as well. From top to bottom,

other panels in Figure 8.3 are the magnetic field components in the order of B_x , B_y , and B_z in nT and the electric field components (E_x and E_y) in mV/km plotted for October 6, 2013.

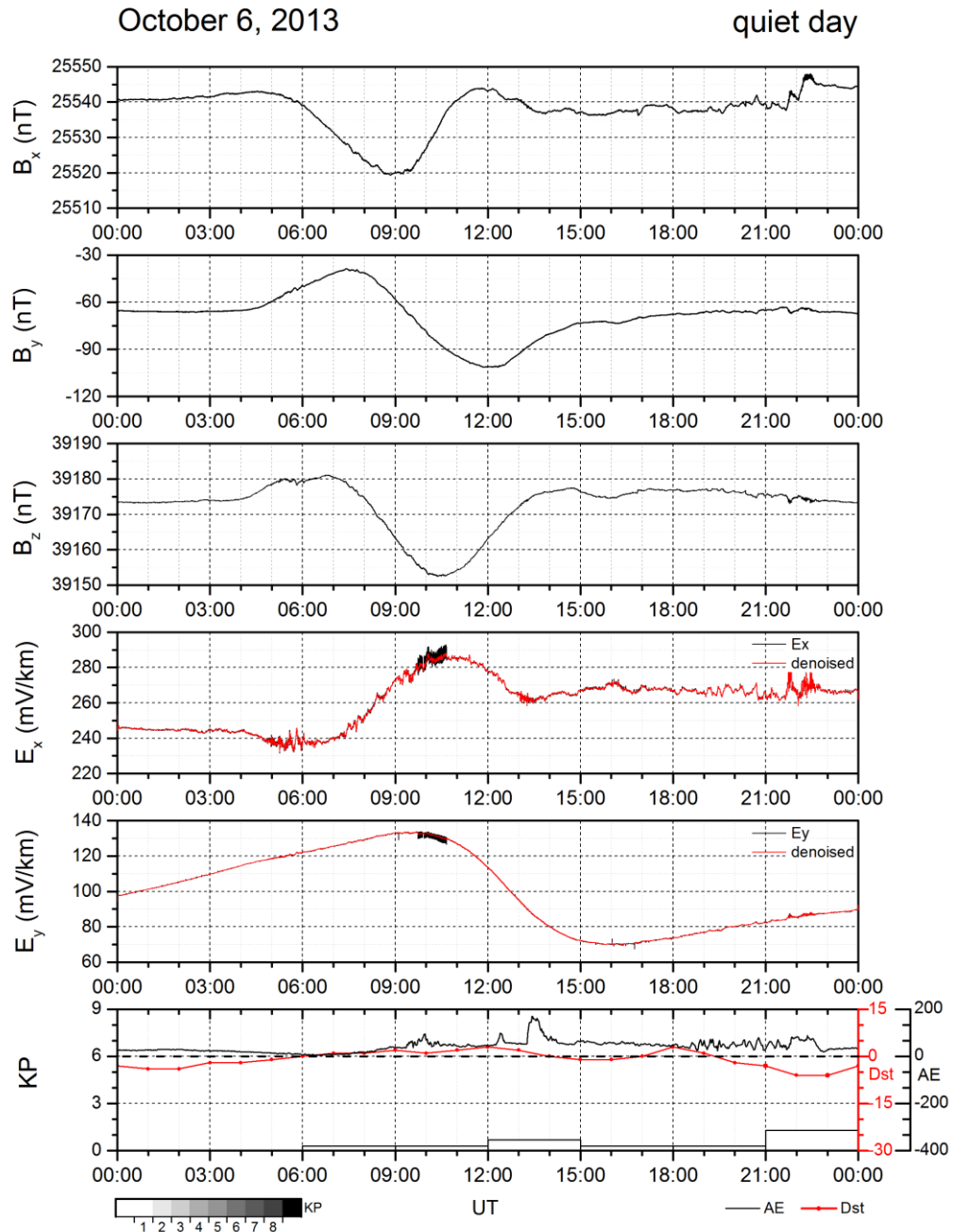


Figure 8.3 : Example of variations in B_x , B_y , B_z , E_x and E_y from top to bottom for a quiet day: October 6, 2013. The last panel gives the geomagnetic activity indices: KP on the left, Dst and AE on the right.

In Figure 8.3, we see that all three components of the magnetic field, but especially B_y and B_z components, are very smooth and illustrate a daily pattern associated with the background Sq (Solar quiet) currents in the ionosphere (Sutcliffe, 2000). A relatively

typical, small amplitude, larger scale wavy variations of a quiet day are apparent in the afternoon after 12:00 UT, especially in B_x and B_z components. Also apparent are the fluctuations in the form of very small ripples seen at around 06:00 UT in B_z component while they appear at about 07:30 UT in B_x and extend till about 09:30 UT in the morning. Contrary to B_x and B_z , we notice that B_y component of the field in the figure does not show any discernible variations at these times. A nearly sinusoidal daily pattern in the magnetic field components is clear, presenting the apparent daily trend of the field variations. In the figure, while a large scale, sinusoidal variation during the day is obvious in the electric field measurements, we see higher frequency wavy variations compared to those of the magnetic field components, in especially E_x component. E_y component presents less wavy, smoother variations compared to E_x except for the tiny fluctuations which are observable after 15:00 UT. Additionally, the wavy variations with relatively shorter durations and lasting for about one to two hours were observed in E_x component at about 06:00 UT, 13:00 UT and 22:00 UT. However, none of these fluctuations, or the short-duration features correspond to any geomagnetic disturbance in the magnetic indices given in the last panel of Figure 8.3. We see that Dst is near 0 nT, 2 nT, and -5 nT while AE is also near 0 nT, 160 nT, and 66 nT, respectively at the time of these variations in E_x component. Similarly, ACE data do not show any unusual structures in the solar wind or any solar activity such as CME presence in the interplanetary medium. As a result, these variations are quite different than the variations corresponding to the geomagnetically active days given in the further sections of the study. In fact, except the small wavy variations at 06:00, 13:00 and 22:00 UT, which will be investigated in depth in the near future, typical quiet day variations of E_x and E_y in our search present similar features. E_x is always more structured and wavier than E_y and a periodic sinusoidal feature is obvious in both components during the day. Therefore, we accept this case as the representative of the quiet day variations of both magnetic and electric field components and compare the features observed during the geomagnetically active days with these observed on quiet days.

In addition to the fluctuations mentioned above, other apparent tiny variations with relatively high frequency but constant amplitude were detected above the background daily variations of E_x and E_y as displayed in black in Figure 8.3. These were seen around 9:45 UT and 10:45 UT and are the noise caused by the solar panel located

nearby the measurement unit. Sometimes, they occurred near the sun rise from 06:00 UT to 09:00 UT in the morning and at other times, they were observed in the afternoon when the solar panel was charging. Their duration usually lasts about an hour. Also seen overlapped on E_y , are the tiny sharp spikes which are noticeable between 15:00 UT and 16:00 UT. These were found to be associated with the lightning events occurring locally in the region and will be studied separately in another study.

The red curves overlaid on E_x and E_y in Figure 8.3 show electric field components after the noise was removed. After a close examination of the variations in E_x and E_y components in our data set, we applied discrete wavelet transform technique to remove the noise. Discrete wavelet transform is a technique in which the original signal is decomposed into several levels using wavelets. Wavelets are localized waves limited in time and frequency. They can be shrunk into smaller time scales or they can be expanded in time using the scale parameter in their formula. As they also depend on time, they can also be shifted in time accordingly. This property of the wavelets allows the user to define the abrupt and local changes in the signal. As a result, they are more efficient and flexible than the Fourier transform techniques when handling non-stationary data. They were also proven to be highly robust in noise removal and powerful in reconstructing the original signal back in time domain (Kumar and Foufoula-Georgiou, 1997). One of the advantages that we experienced about the discrete wavelet transform is that, after decomposing the data using the selected wavelet family, the user can keep more information from the original signal and remove the noise sufficiently by modifying the coefficients and selecting appropriate thresholds. In our case, we basically wanted to remove the high frequency variations that appear periodically in our electric field data created by the solar panel, especially during the sunrise and sunset but also some other times when the solar panel recharges itself. For this purpose, we found Daubechies family-2 (Daubechies, 1992) removes the noise we defined among the several other wavelet forms that we tried such as Haar (Stanković and Falkowski, 2003) and symlets (Cohen et al., 1992) using the MATLAB wavelet toolbox. We determined the thresholds required by this technique by visually selecting the noisy intervals that will be removed (e.g. during the sunrise and sunset) and then used three levels of decomposition for the analysis. In the resulting denoised signal, we found that the method successfully removed the unwanted noise as seen in

Figure 8.3. Daubechies wavelets are also one of the most used wavelets in geophysical applications (Duka et al., 2012; Mendes et al., 2010).

8.3 Case Examples

In this section we present our detailed investigations on the three selected events.

Figure 8.4 presents our first event that corresponds to a geomagnetically disturbed day. The magnetic field components, electric field components and the magnetic indices are given in respect from top to bottom. As in the previous figure, the red curves in the electric field panels describe the denoised electric field data using the wavelet technique described above. This event occurred on April 20, 2014 and is a sudden commencement event demonstrating an example of a geomagnetic disturbance corresponding to a pressure pulse in the solar wind (see Figure 8.10). The pressure pulse compresses the magnetosphere at the subsolar magnetopause that cause an increase in Dst to 28 nT at about 12:00 UT. At the same time, KP shows a peak of 5. Even though the magnetosphere was compressed, this compression did not produce any geomagnetic storms during this day, and also following day when Dst stayed positive and small. AE varied in between 100 and 300 nT from 12:00 UT to 15:00 UT at the time when Dst and KP reached their peaks, but then increased to values above 500 nT after 15:00 UT. AE was low before 12:00 UT varying around 50 nT. These indicate that the case is also an isolated substorm according to the description in Viljanen et al. (2006). In the first five panels in Figure 6.32, we see that the magnetic and electric fields started to fluctuate at 11:00 UT when KP raised to 4-, Dst became slightly positive, and AE enhanced to 100 nT. The fluctuations became finer after 13:00 UT and continued until Dst leveled off towards zero. The fluctuations appeared throughout the sudden commencement phase. These fluctuations were seen to be superimposed on the background magnetic and electric fields and lasted for two hours during this event. One-to-one matching between the fluctuations in the magnetic and electric fields and the magnetic indices is remarkable and indicates a strong correlation on their causes. In addition to the fluctuations, a marked increase in the magnitude of the magnetic field components was detected. With respect to the background variations, an increase of about 40 nT in the magnitudes of both B_x and B_y and about 10 nT in B_z was observed. These deviations in the horizontal component of the magnetic field at midlatitudes show good agreement with those given in the literature

(e.g. Kono, 2007). In panels 4 and 5, high fluctuations in electric field components on the order of 10 mV/km to 100 mV/km were detected.

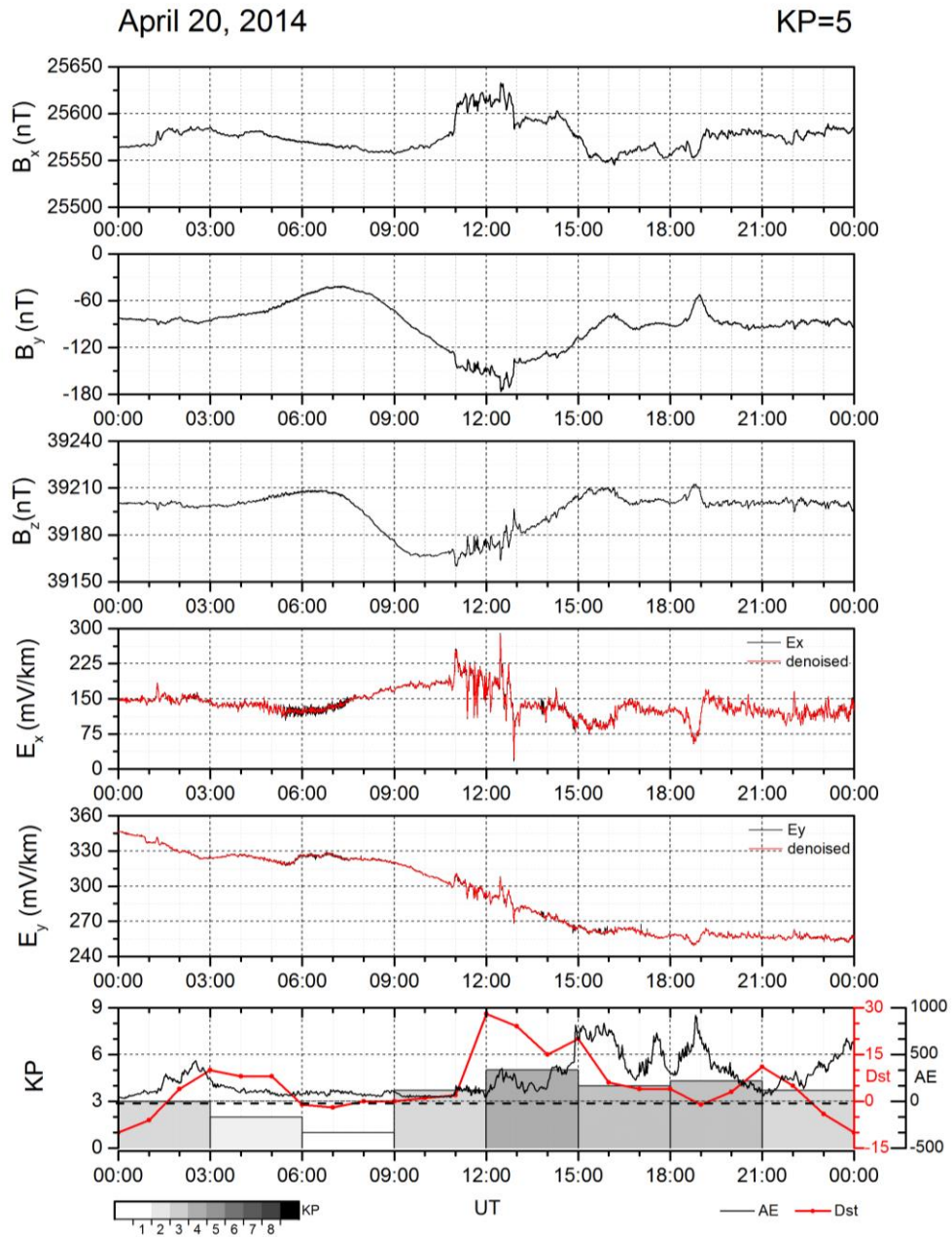


Figure 8.4 : Magnetic and electric field measurements for April 20, 2014, a sudden commencement event with substorm scale geomagnetic activity. From top to bottom: variations in B_x , B_y , B_z , E_x and E_y , and geomagnetic activity indices: KP on the left, Dst and AE on the right.

In Figure 8.5, we present an expanded time interval from 09:00 to 16:00 UT and compare the time derivatives of horizontal magnetic field components (dB/dt) with the variations in the horizontal component of electric field, E_x and E_y . In the figure, the panels on the left and from top to bottom were given in the order of north-south

component of the magnetic field, the time derivative of the north-south component of the magnetic field (dB_x/dt), the east-west component of the electric field, E_y , and the magnetic activity indices KP and Dst. Clearly these variations lasting from 11:00 to 13:00 UT in all panels are seen to be coherent with each other. The fluctuations in the magnetic and electric field components started with a rise in Dst at 11:00 UT when KP showed 4- and AE increased slightly from its background of 50 nT to 100 nT. When sudden commencement appeared in Dst at 28 nT at 12:00 UT, KP reached its peak and AE started to increase slowly at the same time. Fluctuations in magnetic and electric field measurements continued until 13:00 UT. They ended at 13:00 UT, however small amplitude variations continued until 16:00 UT as Dst decreased. During this time interval, from 12:00 to 13:00 UT, KP stayed at 5 and AE showed variations around 300 nT. AE increase continued after the high fluctuations ceased in B_x , dB_x/dt , and E_y . In the second panel, we can see that the time variations of B_x (north-south) component varied between -0.5 and +0.5 nT/sec.

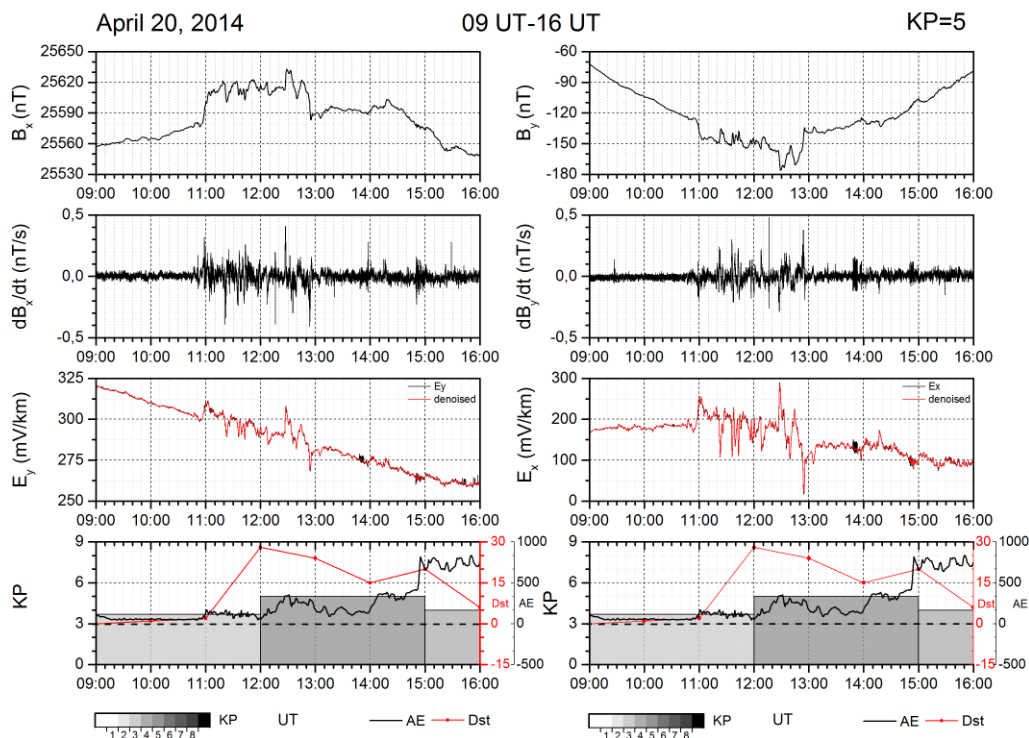


Figure 8.5 : North-south and east-west components of the magnetic field (top panels), dB/dt (second panels), associated electric field variations (third panels) during the geomagnetic activity and geomagnetic activity indices on April 20, 2014. From the top, B_x , dB_x/dt , E_y , and activity indices (KP, Dst and AE) are on the left panels, and B_y , dB_y/dt , E_x and activity indices (KP, Dst and AE) are on the right panels.

Clearly these variations in dB_x/dt were seen to be correlated with the variations in the east-west component of the electric field. Electric field (E_y) fluctuations were seen to change in between ± 20 mV/km from maximum to minimum. This agreement between the magnetic field, electric field, and the magnetic indices indicates that these ground level variations have a common cause related to the geomagnetic disturbance initiated with the strong sudden commencement. Therefore, we interpret these coherent variations observed in the magnetic and electric field components measured in Bozcaada as a result of GICs occurring in response to the dayside compression. Right panels in Figure 8.5 illustrate the similar high fluctuations in B_y , dB_y/dt , and E_x components. Here too, the high fluctuations corresponding to the magnetospheric disturbance are very clear.

The variations in the magnetic field components and their derivatives and their identification with the GICs were reported in several studies as resulting from auroral electrojets at the high latitudes (Viljanen et al. 2001, 2006; Pulkkinen et al., 2003; Viljanen and Tanskanen 2011), sudden compression of the magnetosphere on the dayside associated with the interplanetary shocks (sudden commencement) (Zhang et al., 2015; Fiori et al., 2014; Kappenman, 2003; Pulkkinen et al. 2003), ULF waves (Viljanen et al. 2001; Kataoka and Pulkkinen, 2008; Watari et al. 2009; Viljanen and Tanskanen, 2011), sudden impulses (Marshall et al., 2012), and others. For example, Viljanen et al. (2001; 2011) found two peaks in GIC occurrences at latitudes poleward of 55°N ; one at midnight and the other at morning hours. They associated the maximum at midnight with the auroral currents which are stronger during the substorms while the morning maximum which lasts longer was interpreted as the result of the pulsation activity increasing during the morning hours. Viljanen et al. (2001, 2006) also noted on a third maxima within 10 to 15 MLT sector that occur at the most northern stations (75°N) in the arctic region. In our case, the sharp change in B_x and B_y occurs at 11:00 UT that corresponds to the local time at 14:00 LT as it is 3 hours ahead of UT in April. This is very different than the occurrence time that Viljanen et al. (2001) found for ULF waves at their latitudes. At the time of our event, AE shows values reaching 800 nT. However, being in the mid latitudes, we consider our station away from the direct effects of the auroral currents flowing stronger above 55° . Both the timing of the sharp increase in north-south and east-west components of the magnetic field (B_x and B_y) and the start of the high fluctuations in the electric field and

time derivatives of the magnetic field clearly correspond to the sharp increase in the sudden commencement. Therefore, we attribute these changes mainly to the increased magnetopause currents in response to the increased solar wind dynamic pressure.

In Figure 8.6, we quantify the deviations from the background magnetic field and denoised electric field by removing the diurnal trend. The trend in magnetic field components was removed by considering the magnetic field we measure on the ground is the sum of the main field and the perturbations from magnetospheric and ionospheric currents (Pirjola, 2002), that may include one or more of the currents such as auroral currents, field aligned currents, magnetopause currents, ring currents, and geomagnetic tail currents. As the Earth's main field is very slowly changing at a specific location, we assume that it is constant on the selected days and the larger scale, diurnal variations are due to the Sq variations superimposed on the main field. We applied cubic spline method on the magnetic field data recorded on the previous quiet day to determine a simple model of the quiet day magnetic field variations. Following this, Sq related variations during the magnetically active days were eliminated by subtracting the magnetic field modelled by using cubic spline method from the magnetic field data of the disturbed day. After removing the large scale Sq variations, the method exposes the variations resulting from the smaller scale magnetospheric or ionospheric currents for further study. For the events presented throughout this part of our work, the deviations from the quiet day were determined as described.

Top panels in Figure 8.6 illustrate the result when the Sq variations were removed from the magnetic field data. Panels clearly show that with respect to the quiet day, B_x component on the ground increased first sharply by more than 20 nT and then fluctuated around 30 nT at this level. The maximum was seen to be 43 nT. B_y component, on the other hand, varied between -23 nT and 15 nT. In general, the fluctuations were around the level of -5 nT until 12:30 UT after when the larger fluctuations were recorded. The event was characterized by a sharp increase and decrease that correspond to the sudden commencement in both components. Bottom panels in Figure 8.6 exhibit the magnitude of the deviations in the horizontal component of the electric field. Similar to the trend removal process in magnetic field components, the deviations for the electric field components from the quiet day background were established by subtracting the electric field data simply from the

model fit applied to the electric field data in Figure 8.6. As before, the cubic spline fit was used for this process.

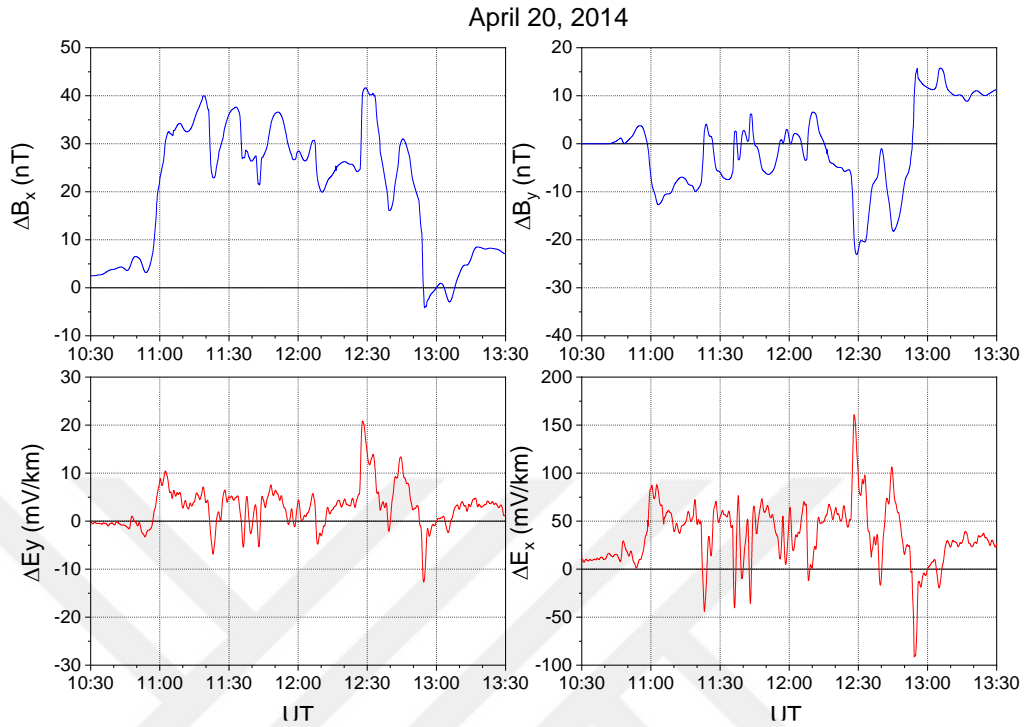


Figure 8.6 : Magnetic field deviations from the background, ΔB_x (left) and ΔB_y (right). (Bottom): Electric field deviations from the best fit curves for electric field components given in Figure 8.4, ΔE_y (left) and ΔE_x (right).

In these panels, we can see that E_x varied in the range of -40 to 75mV/km. First, E_x sharply raised to 75mV/km and then fluctuated around 55-60mV/km with a maximum at 160mV/km. E_y , on the other hand, showed smaller deviations on the order of 5-10mV/km with a maximum of 20mV/km for this event. Time derivative of magnetic field data changed from +0.5 to -0.5nT/sec (Figure 4). These variations are smaller than those reported in Viljanen et al (2001, 2006) at high latitudes northward of 55°N and in Turnbull et al. (2009) study which was for latitudes above 50°N. As our measurements were taken at a much lower magnetic latitude (MLAT), 37.5°N versus 55°N, the response of magnetic and electric fields at our latitudes is anticipated to be different than those seen at higher latitudes. The main cause of GIC variations at high latitudes was given as the overhead auroral currents (Viljanen et al. 2001, Pulkkinen, 2003). Latitudinal differences in the magnitude of the fluctuations and their occurrence times suggest different causes for the GICs at our latitudes.

Figure 8.7 compares the north-south components of the magnetic field with the east-west components of the electric field from 10:30 UT to 13:30 UT during the interval

when the sudden commencement was seen. B_x and E_y were presented together because the east-west directed ionospheric currents drive north-south magnetic field and east-west electric fields. In the figure, the top panel indicates that B_x and E_y components vary in the same manner, namely, during the fluctuations as one increases, the other increases too, and vice versa. On the other hand, the bottom panel indicates that B_y and E_x show inverse relation while they fluctuate. In other words, while one increases the other decreases and vice versa. During our events, AE index (100-300 nT) indicates a weak-to-moderate magnetospheric substorm after especially 15:00 UT. Moderately weak substorm event together with the time of the substorm, and the fact that the ground disturbances started by a strong sudden commencement with Dst close to 30 nT suggest the magnetopause currents resulting from the dayside compression as the dominant source and rather than the effects of the auroral currents.

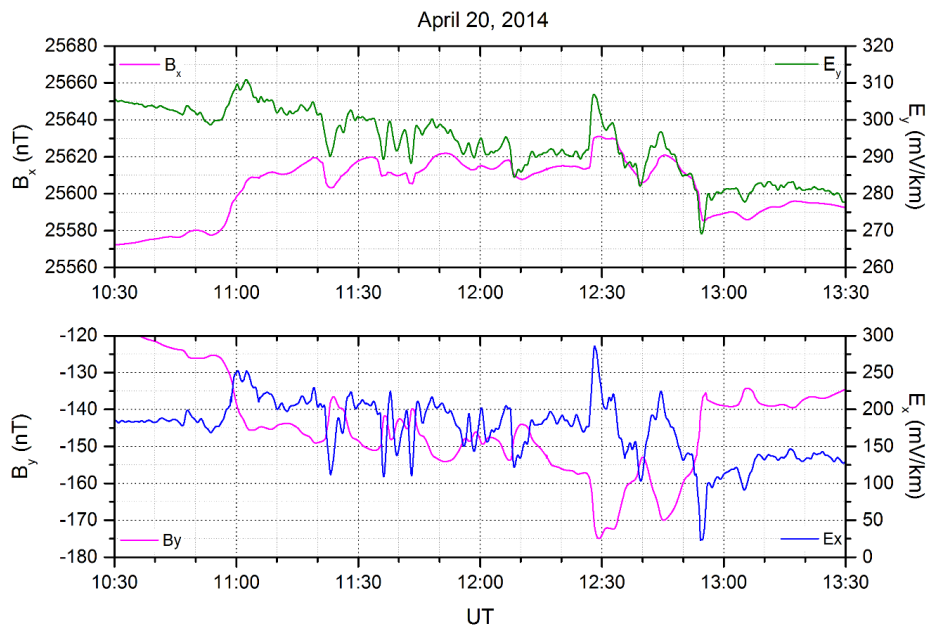


Figure 8.7 : Magnetic field and electric field variations during the April 20, 2014 sudden commencement event for an expanded interval. On the top: the variations between north-south component of magnetic field, B_x (left), and east west component of electric field, E_y (right). On the bottom: the variations between the east-west component of magnetic field, B_y (left), and north-south component of electric field, E_x (right).

Figure 8.8 was produced to illustrate and compare the north-south and east-west component of the electric field during the geomagnetic storm period from 10:30 to 13:30 UT. interval. Figure specifies the range of variations in E_x and E_y and indicates that the fluctuations in E_x are much higher than those in E_y . While E_y varies in the range of 30 mV/km, i.e. from 270 mV/km to 300 mV/km during the day, E_x has a range of

variation of about 60 mV/km until 12:30 UT and after 265 mV/km (from 20 to 285mV/km). E_x is seen to exhibit larger scale of variability. Deviations from the background E_x vary around 60-70 mV/km with a maximum and minimum at -100 and 150 mV/km, respectively. The variations in electric field components can result from either the variations in the electrical conductivity of the soil or due to the external variations that cause changes in the geomagnetic field. In this case, because of the fact that we see the large differences between E_x and E_y corresponding to the geomagnetic storm periods, and in the absence of the soil conductivity measurements at Bozcaada, we attribute these differences to the geomagnetic effects.

Figure 8.9 displays the one to one correspondence between the horizontal geoelectric component and the time rate of change in the horizontal geomagnetic field during this event.

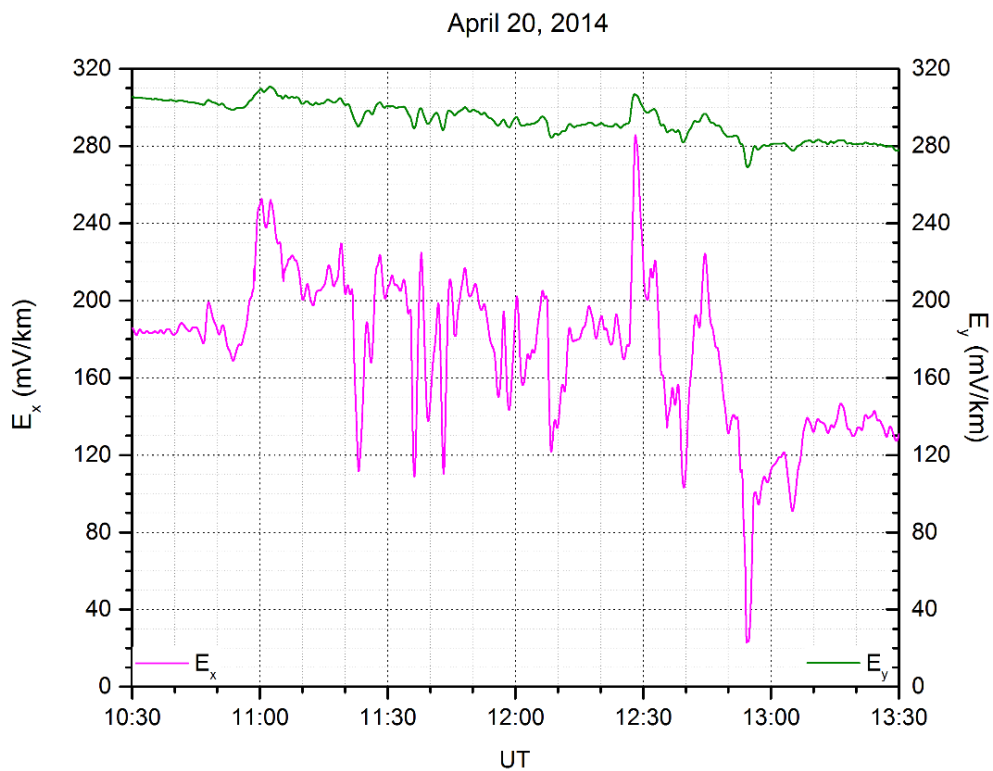


Figure 8.8 : Electric field variations in the east-west (E_y) and north-south (E_x) components during the April 20, 2014 sudden commencement event for the expanded period.

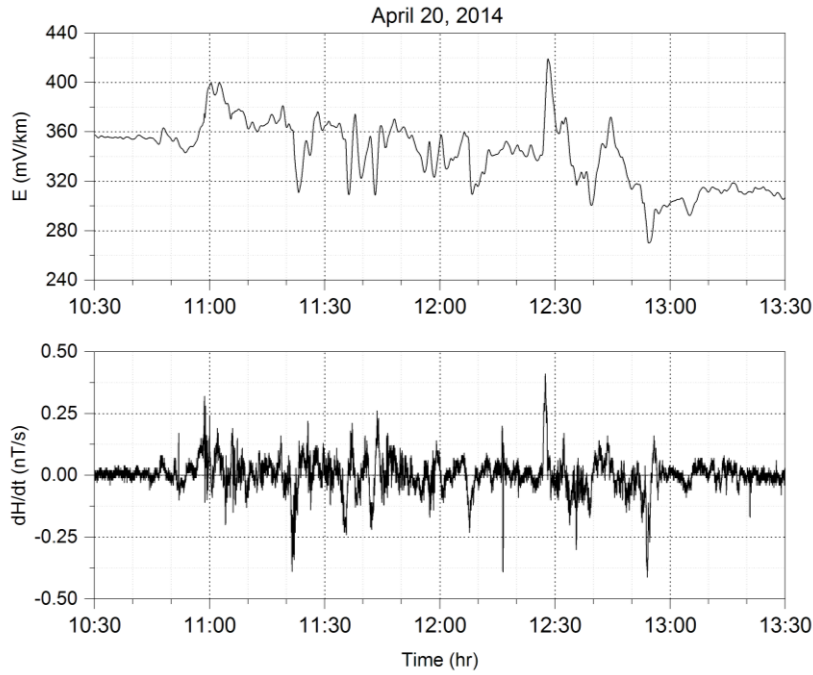


Figure 8.9 : Variations of the horizontal component of geoelectric field and the derivative of the horizontal component of the geomagnetic field for April, 20, 2014 event.

In order to investigate further on the causes of these fluctuations recorded at our station, we plotted the solar wind density and IMF data during the time period when the high fluctuations in the magnetic and electric fields were present in Figures 8.4 to 8.9. Figure 8.10 shows solar wind plasma and IMF together with magnitude of the horizontal components of the magnetic field (H) and electric field (E) where $H = \sqrt{B_x^2 + B_y^2}$ and $E = \sqrt{E_x^2 + E_y^2}$. Instead of showing either (B_x with E_y) or (B_y with E_x), we simply used H and E in this panel in order to show total variations in the horizontal components. We used this panel only to show if the structures observed in the solar wind were related to the fluctuations that we measured on the ground. First five panels from top to bottom are interplanetary magnetic field (IMF), density, velocity, temperature, and dynamic pressure of the solar wind from 09:00 UT to 16:00 UT while the last panel displays H (left, blue) and E (left, red) together with auroral activity index AE (right, light gray). Also in the first panel, total IMF is shown in black while z-component of the interplanetary magnetic field (IMF B_z) is indicated in red on the y-axis. In Figure 8.10, we see that all solar wind parameters increase very sharply at 11:00 UT and vary strongly after this time. Figure clearly indicates the presence of a CME event. The shock related to the CME event is seen at 11:00 UT which is the time that the strong fluctuations in our magnetic and electric field data started.

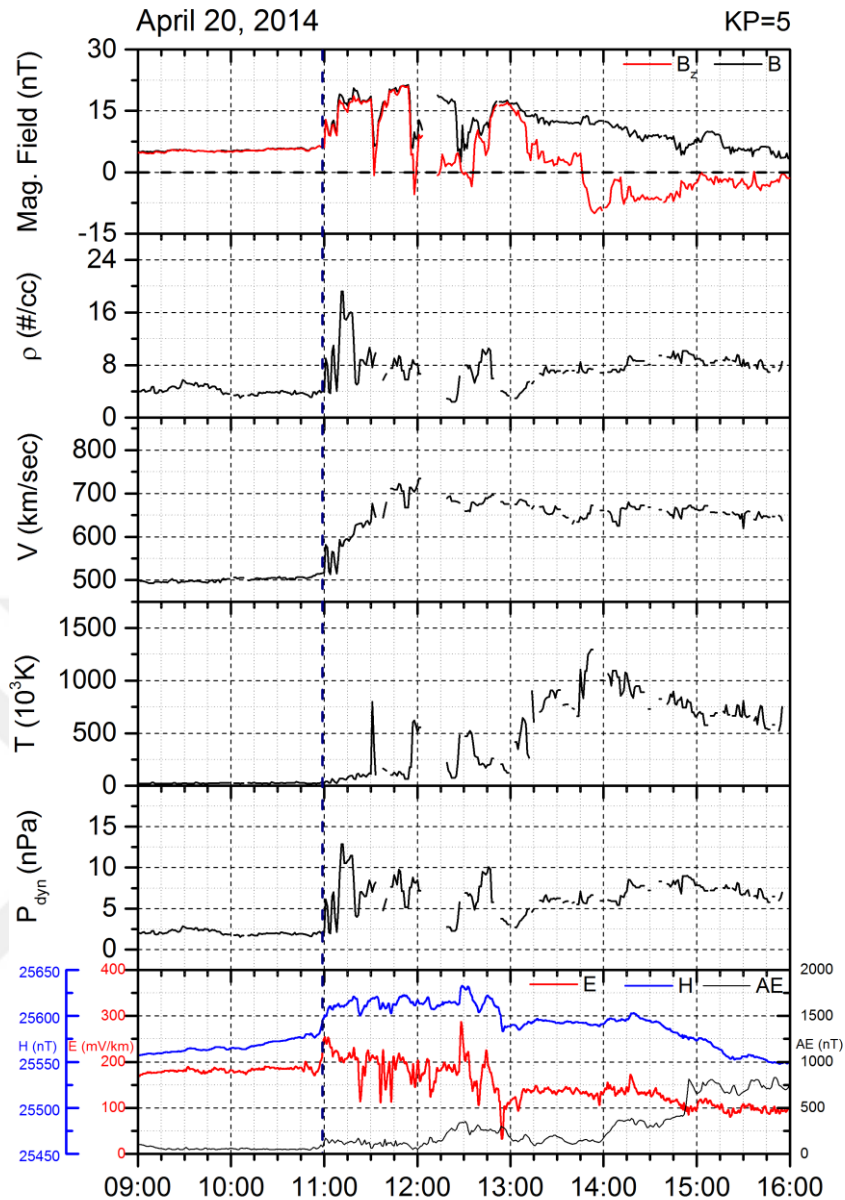


Figure 8.10 : IMF and solar wind parameters for April 20, 2014 event. From top to bottom: Interplanetary magnetic field (IMF B, IMF Bz), solar wind density, solar wind velocity, solar wind temperature, solar wind dynamic pressure, and horizontal components of the electric field and magnetic field given along with the AE index.

At 11:00 UT, solar wind density increases from 8 #/cm³ to about 10 to 20#/cm³ beyond the shock, while velocity increases sharply from 500 km/sec to 570 km/sec after the shock but it keeps increasing afterwards within the CME sheet until about 12:00 UT. As a result of density and velocity increases at the CME shock, the dynamic pressure increases from about 3 nPa to 5 to 13 nPa after the shock. Dynamic pressure indicates a very strong CME shock which is expected to have consequences when it hits the Earth. In addition, both the total magnetic field is seen to increase from 5 nT to about 20 nT behind the shock and the temperature is also seen increasing from 10.000 K to

50.000 K just after the shock but enhanced up to 1×10^6 K at about 14:00 UT. IMF B_z in the total IMF panel is positive but sharply increased at the shock to about 15 nT. It stayed northward throughout the CME sheet and turned southward at 13:45 UT after when AE enhanced slowly up to 750 nT marking the occurrence of the auroral substorm. The sudden commencement was seen at 11:00 UT which meant that the CME shock started to push the magnetosphere on the dayside subsolar magnetopause. The magnetosphere was compressed as the dynamic pressure of the CME stayed high. The sudden commencement reached its peak at 12:00 UT. The magnetosphere stayed compressed for couple of hours until 19:00 UT and during this time Dst was high and positive indicating the compression. Taken together, these observations indicated that the magnetic and electric field variations we measured on the ground were driven by the sudden commencement which was a result of the CME and magnetosphere interaction. Although it was a strong CME, the interaction did not produce any magnetic storm and thus our event remained as a sudden commencement followed by a weak-to-moderate isolated substorm.

The main points derived from these observations recorded in Bozcaada on April 20, 2014 can be reviewed as below:

We observed fast and large fluctuations in the horizontal components of the magnetic and electric field at our Bozcaada station that correspond to a geomagnetic event with strong Dst, moderately high KP and weak-to-moderate AE.

The geomagnetic disturbance and the ground fluctuations of magnetic and electric fields correspond to sharp increases in solar wind density, velocity, temperature and dynamic pressure as well as the total magnetic field.

The fast and large amplitude fluctuations appear following a sharp jump in the magnetic and electric field components that occur in response to the magnetospheric compression on the dayside. Magnetospheric compression was caused by the increased solar wind dynamic pressure owing to the presence of a CME in the solar wind. Fluctuations in both magnetic and electric field components started with a sharp jump at the time of the sudden commencement in Dst following the compression. They continued at the elevated state throughout the sudden commencement. They were seen to be superimposed on the smooth daily background variations.

This event corresponds to substorm scale activity according to the terminology used by Gonzalez et al. (1994), together with a strong sudden commencement which did not lead to a main phase. As a result, geomagnetic storms were not observed. During the event Dst did not become negative. Throughout the event period when fluctuations on the ground magnetic and electric field were observed, Dst was larger than -40 nT, KP was 5, and AE was around 100 to 300 nT. The peak of KP coincided with the sudden commencement signature in Dst.

As a result of (1), (2), and (3), we think that the source of the ground fluctuations, thus GICs at Bozcada station is the increased magnetopause currents during the compression. Considering the presence of a weak-to-moderate substorm, the latitude of our station, and the time of the ground fluctuations indicate the effects from the auroral currents can be ignored on the presence of GICs observed at Bozcaada for this event.

During the event, it was shown that the north-south component of the magnetic field varied in the same manner as in the east-west component of the electric field. When B_x increases E_y decreases and vice versa. In the case of east-west components of the fields, B_y varied opposite to E_x , or vice versa.

During the event, the magnitude of the north-south component of the electric field (E_x) showed larger fluctuations than those of the east-west component of the electric field (E_y).

The time derivatives of the horizontal magnetic field exhibited similar type of fast fluctuations as in the horizontal electric fields. According to Faraday's Law, magnetic field or electric field measurements can be used to determine the size of the GIC currents. These observations validate the relation.

The magnitude of the time derivative of magnetic field showed fluctuations between ± 0.5 nT/sec in both B_x and B_y components. The fluctuations were slightly higher for dB_x/dt than for dB_y/dt .

These ground fluctuations observed in the magnetic and electric fields started at 11:00 UT and lasted for two hours until 13:00 UT. The corresponding Local Time (LT) for their appearance was from 14:00 LT to 16:00 LT in the afternoon.

Our next two examples are the events recorded during storm-time substorm activity. That is, their occurrence corresponds to a geomagnetic storm accompanied by a

succession of magnetospheric substorms. Figure 8.11 yields 3-days stretch of the magnetic and electric field components from October 8, 2013 to October 11, 2013. In October, the local times at Bozcaada are still 3 hours ahead of the UT times. As in the previous figures, the last panel gives the magnetospheric activity based on KP (left), Dst (right, red) and AE (right, black). KP showed a maximum of 6. This event was characterized as a moderate geomagnetic storm as Dst decreased to -62 nT at 02:00 UT on October 9, 2013 (05:00 LT in the morning). The event started with a slight increase in Dst beginning at 15:00 UT and reached 15 nT at 18:00 UT after a steady rise on October 8, 2013. Its peak, 22 nT, occurred sharply at 21:00 UT when KP peak was observed. AE index stayed low below 100 nT until 18:00 UT and reached its peak, 1378 nT, at 21:25 UT. Two consecutive substorm activities, one on October 8, 2013 with AE peak at 21:00 UT that coincided with the sudden commencement, and the other at 08:05 UT on the next day with a maximum AE of 1268 nT, occurred during the main phase of the geomagnetic storm. Dst started decreasing at 21:00 UT, became negative at 22:00 UT (around local midnight) on October 8, 2013, and then dropped to -61 nT at 01:00 UT, peaking at -62 nT at 02:00 UT on October 9, 2013. The magnetospheric compression started at about 15:00 UT on October 8, 2013 as indicated by the occurrence of sudden commencement and lasted 8 hours. This was followed by the main phase of the magnetic storm beginning at 22:00 UT and lasting until 02:00 UT on the next day. The recovery phase started at 02:00 UT and continued until October 9, 2013, 22:00 UT. KP stayed at about 5 to 6- for about 15 hours during the storm's main and recovery phases.

First five panels in Figure 8.11 display that the large fluctuations in all magnetic field and electric field components on the ground increased significantly from 19:00 UT on October 8, 2013 to 07:00 UT in the next day, October 9, 2013. The period of high fluctuations coincides with the time of the increase in KP and the maximum in Dst and sudden commencement. The large fluctuations in this event lasted 11 hours. Although the magnetosphere is moderately active, it is clear that the corresponding magnetospheric disturbances drive these high fluctuations measured on the ground in Bozcaada. In fact, it is possible to distinguish the magnetic and electric field fluctuations as those corresponding to the first substorm and those to the second. During the entire event, B_x increased by about 60 nT and B_y decreased by about 40 nT

with respect to the daily background variations. B_z component, on the other hand, did not indicate any significant deviation but fluctuated strongly during the storm interval.

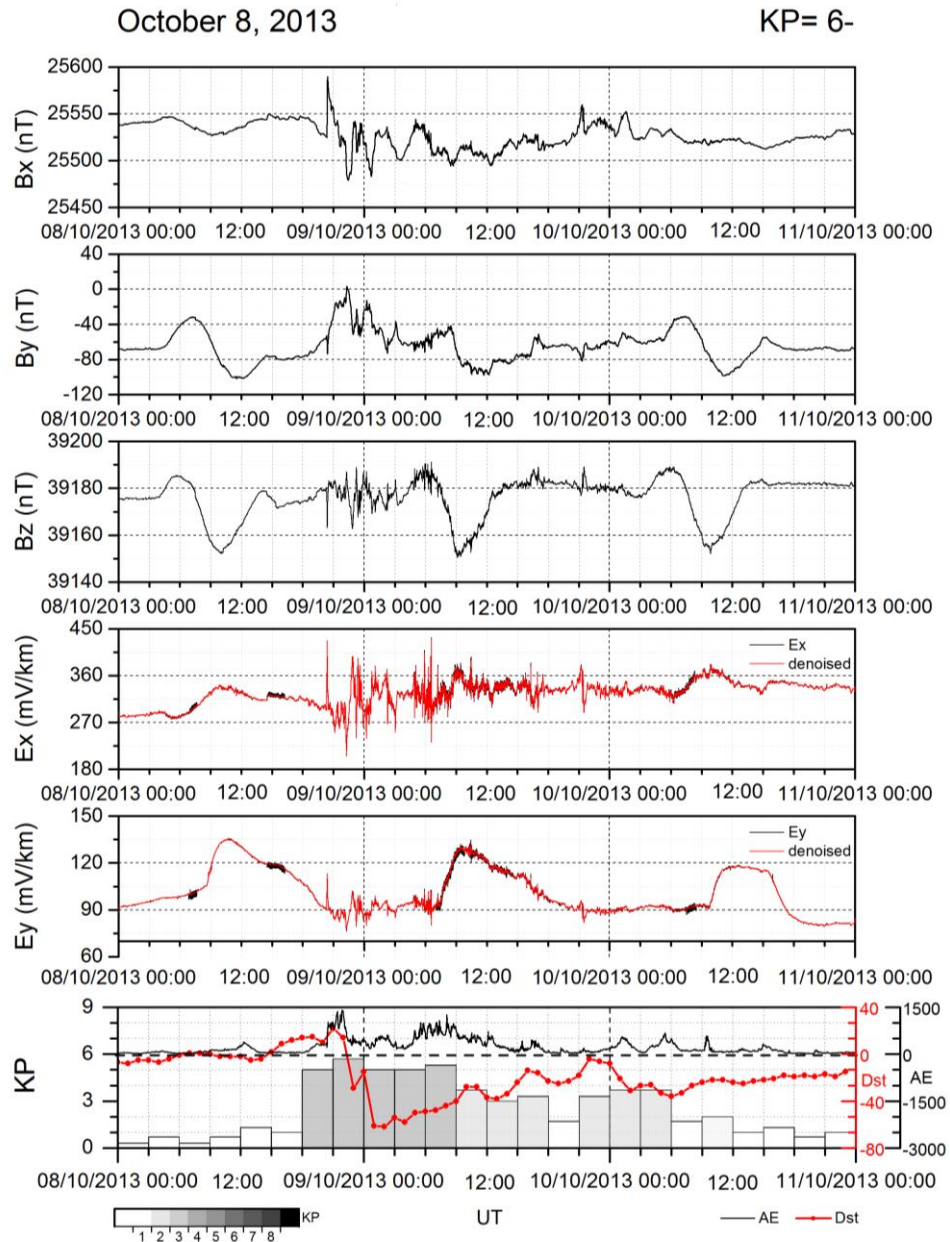


Figure 8.11 : Magnetic and electric field measurements extending from October 8 to 11, 2013 during weak-to-moderately disturbed geomagnetic activity. From top to bottom: variations in B_x , B_y , B_z , E_x and E_y , and geomagnetic activity indices: KP on the left, Dst and AE on the right.

In panels 3 and 4, electric field components, E_x and E_y , displayed high fluctuations varying from 10 mV/km to 100 mV/km that accompany the variations in the magnetic field panels. On the days preceding and following the magnetic storm day (October 9, 2013), no high fluctuations in both magnetic and electric field were detected. Both

magnetic and electric field data presented relatively smooth variations during the non-storm days which are similar to the quiet reference day given in Figure 5.10.

In Figure 8.12, we present the expanded time interval from 12:00 UT on October 8, 2013 to 18:00 UT on October 9, 2013.

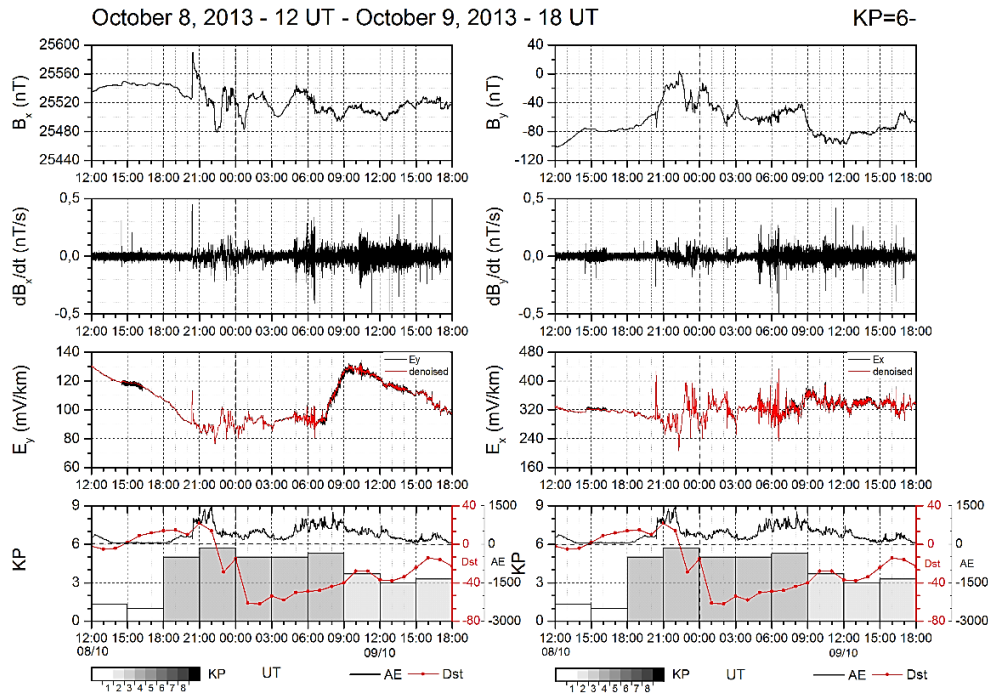


Figure 8.12 : North-south and east-west components of the magnetic field (top panels), dB/dt (second panels), and associated electric field variations (third panels) during the geomagnetic activity on October 8, 2013. From the top, B_x , dB_x/dt , E_y , and activity indices (KP, Dst and AE) are on the left panels, and B_y , dB_y/dt , E_x and activity indices (KP, Dst and AE) are on the right panels.

The panels from top to bottom are given as in Figure 8.4. On the left, the figure compares the time derivative of north-south component of the magnetic field (dB_x/dt) with the horizontal component of the electric field, E_y , and on the right, the time derivative of east-west component of the magnetic field (dB_y/dt) with the north-south component of the electric field, E_x . Figure provides the details about the agreements / disagreements between the high fluctuations in the magnetic and electric field components seen from 19:00 to 07:30 UT with the magnetospheric disturbances as observed in KP and Dst. Here it is clearer that the first group of fluctuations occurs corresponding to the sudden commencement and maximum AE, indicating the start of the first magnetospheric substorm, while the second group of high fluctuations starts at the AE peak at 05:00 UT, i.e. the time of the second magnetospheric storm. Electric

field deviations were found to be within 20mV/km from maximum to minimum. Variations in the second panel that gives the time derivative of B_x (north-south) component change between -0.5 and +0.5 nT/sec, similar to those seen in Figure 8.4. These agreements among the north-south component of magnetic field, east-west component of the electric field, and the time derivatives demonstrate the presence of the geomagnetic currents at these latitudes. While throughout the entire storm/substorm period, the magnetic and electric fields fluctuate, the highest fluctuations were seen at the start of the magnetospheric substorms, i.e. 20:00 UT and 05:00 UT that correspond to near local midnight and the early morning hours. Among several drivers of the ground variations of the electric and magnetic fields, ionospheric currents caused by auroral activity are the strongest sources at high latitudes. The magnitude of the fluctuations seen above our station are less when compared to those found in high latitudes. Therefore, the possibility that they are caused by the high latitude current systems is low.

Removing the daily Sq quiet day variations as described in the previous events (Figure 6.41) showed deviations on the order of ± 60 nT for B_x component and between 75 and -40 nT for B_y component. Similarly, as described in the previous sections, the subtraction from the best curve fit applied for electric field components indicated deviations on the order of 125 mV/km to -90 mV/km for E_x and 25 mV/km to -13 mV/km for E_y components.

In order to correlate with the solar wind structures and IMF, Figure 8.14 presents the ACE magnetic field and solar wind plasma data. The panels from top to bottom are the same as in Figure 6.38 showing the total magnetic field (left in black) and IMF B_z (right in red), density, velocity, temperature and dynamic pressure at L1 point for one day starting from 16:00 UT on October 8, 2013. Added in the last panel are the horizontal components of the magnetic (left in blue) and electric (left in red) fields at Bozcaada and AE index on the right in gray.

We can see very clear signatures of a CME structure in the solar wind at the time of ground observations. The CME shock was detected at about 20:25 UT when we first observed the fluctuations in the magnetic and electric field measurements in the last panel.

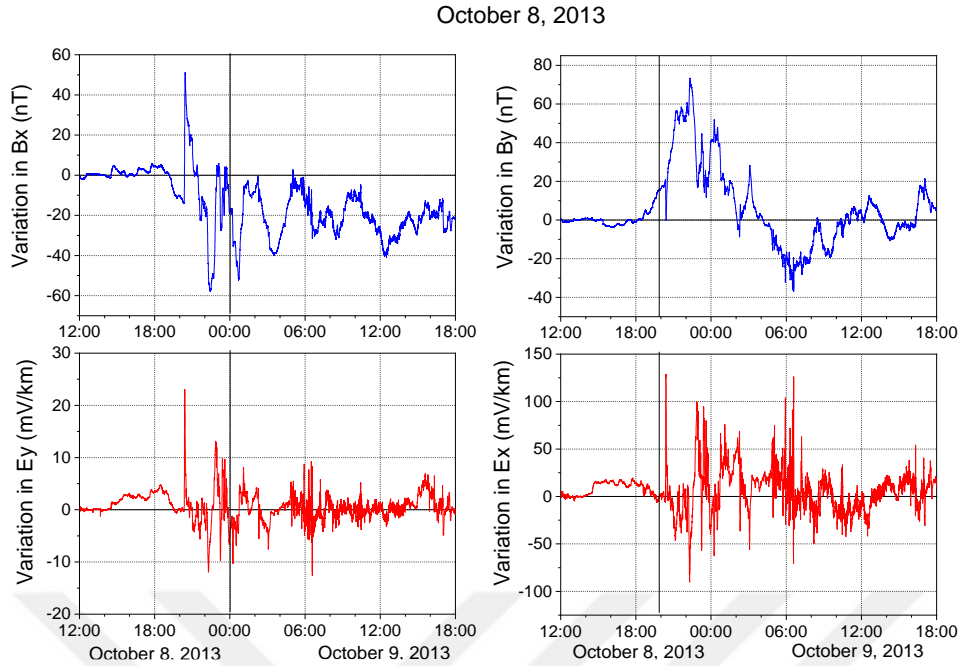


Figure 8.13 : Electric field variations in the east-west (E_y) and north-south (E_x) components during the October 8, 2013 sudden commencement event for an expanded interval.

All the solar wind parameters, the total magnetic field, density, velocity, temperature and dynamic pressure show sharp increases at the time of the shock. We did not have density data from ACE prior to the shock; therefore, the dynamic pressure was not calculated. However, all other parameters prior to the shock indicate a typical solar wind. Therefore, we assume an average dynamic pressure on the order of 1 nPa and increased to about 15 nPa after the shock. Both the solar wind density and dynamic pressure indicate sharp increases seen twice during the interval of ground fluctuations. One is the shock at 20:00 UT on October 8, 2013 that resulted in an increase in AE indicating presence of magnetospheric substorms and another increase was recorded on October 9, 2013 at 04:30 UT causing a second increase in AE and indicating the second substorm. IMF B_z was very low prior to the first shock but turned slightly southward at the shock and started to fluctuate sharply between ± 15 nT after the shock until the maximum was reached in the solar wind dynamic pressure. At this time and after, the fluctuations became larger between ± 30 nT which implied presence of magnetospheric substorms near Earth distances. IMF B_z ceased to its background zero levels after the CME passage. These measurements indicate that the variations observed on the ground are due to both increases in the dynamic pressure.

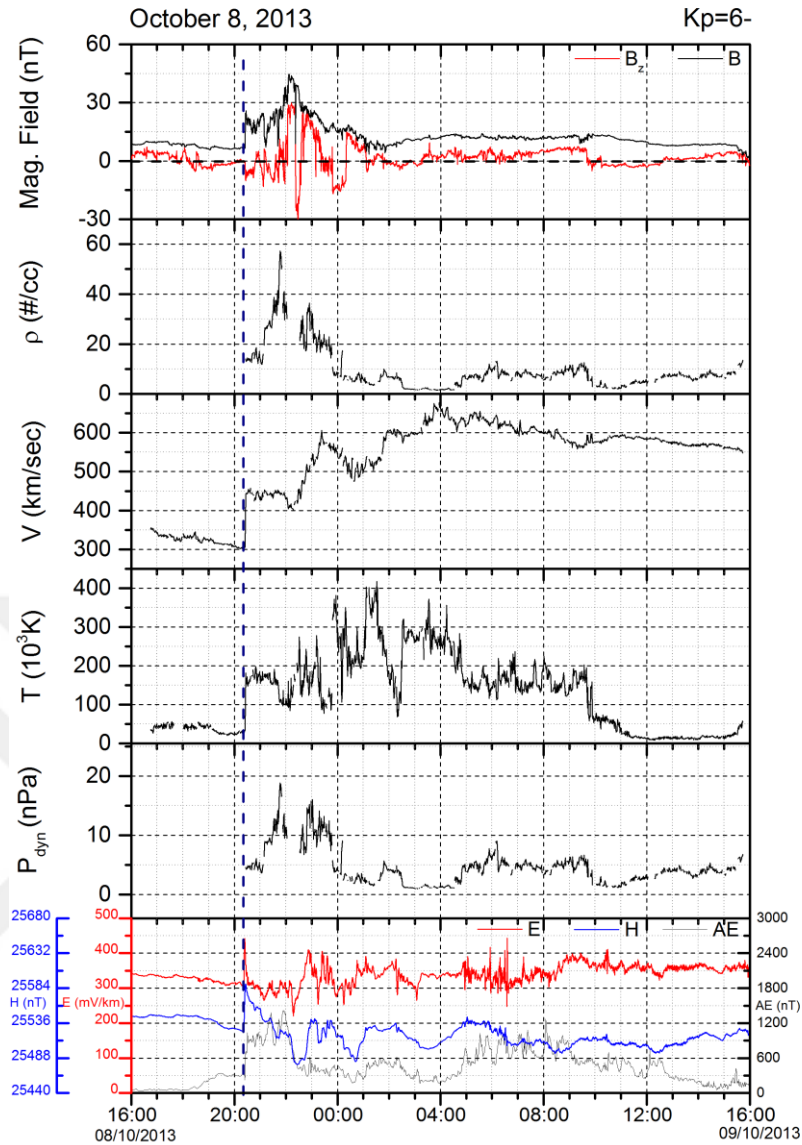


Figure 8.14 : IMF and solar wind parameters for October 8, 2013 event. From top to bottom: Interplanetary magnetic field (IMF B, IMF B_z), solar wind density, solar wind velocity, solar wind temperature, solar wind dynamic pressure, and horizontal components of the electric field and magnetic field given along with the AE index.

In this event, our ground observations of magnetic and electric field correspond to a geomagnetic storm. As in the previous example, we attribute the variations during the sudden commencement to the increased magnetopause currents resulting from the compression at the dayside magnetopause. In addition to the magnetopause currents, the ground variations during the main phase of the geomagnetic storms are also associated with the variations in ring current affecting Dst. Therefore, we think that the most likely contributor to the variations during the main phase of the geomagnetic storm is the ring current (Hamilton et. al., 1988). Strong increases in ring current were found to be associated with an enhanced, growing near Earth geomagnetic tail current

during the geomagnetic storms which can cause strong deviations in the magnetic fields on the ground, and causing depressions in Dst (Alexeev et al., 1996; Lopez, et al., 2015). Together with the ring current, strong geomagnetic tail currents may contribute in driving the variations that we observe at our station. However, the separation of these sources needs a detailed analysis that we consider for future study.

We review the characteristics of October 8, 2013 event as below:

This was an example of a case with both sudden commencement and two consecutive magnetospheric substorms taking place during a geomagnetic storm.

Fast and large amplitude fluctuations in magnetic and electric field components started at 20:00 UT (October 8, 2013) prior to the main phase during the sudden commencement and ended at 07:00 UT (October 9, 2013) which lasted about 10 hours corresponding to the initial, main and the recovery phases of the magnetic storm.

Deviations from the daily background pattern given in Figure 6.39 started at about 15:00 UT on October 8, 2013 before the peak of the sudden commencement reached when Dst started to rise. This compression was observed as a sharp jump of about 40 nT in B_x component of the field. The initial phase of the storm that covers the sudden commencement lasted for about 5 hours and ended 21:00 UT.

High fluctuations in dB_x/dt and dB_y/dt corresponded to the large variations in E_y and E_x respectively.

The magnitude of fluctuations in dB_x/dt and dB_y/dt varied between ± 0.5 nT/sec.

The fluctuations and deviations from the background were larger in E_x than those in E_y . Deviations for E_x can be larger than 90 mV/km while they are smaller for E_y on the order of 10 mV/km.

Event corresponds to a CME shock in the solar wind at the time of the high fluctuations which were detected on the ground magnetic and electric field measurements.

Possible drivers of these ground variations are the magnetopause currents during sudden commencement phase while during the main phase, in addition to the magnetopause currents, the ring current, with likely contributions from the near Earth tail currents are considered because of their effects on Dst during the geomagnetic storm main phase.

Figure 8.15 presents the last example of the ground observations of electric and magnetic fields in Bozcaada during the geomagnetic disturbances. The geomagnetic storm occurred on June 8, 2014.

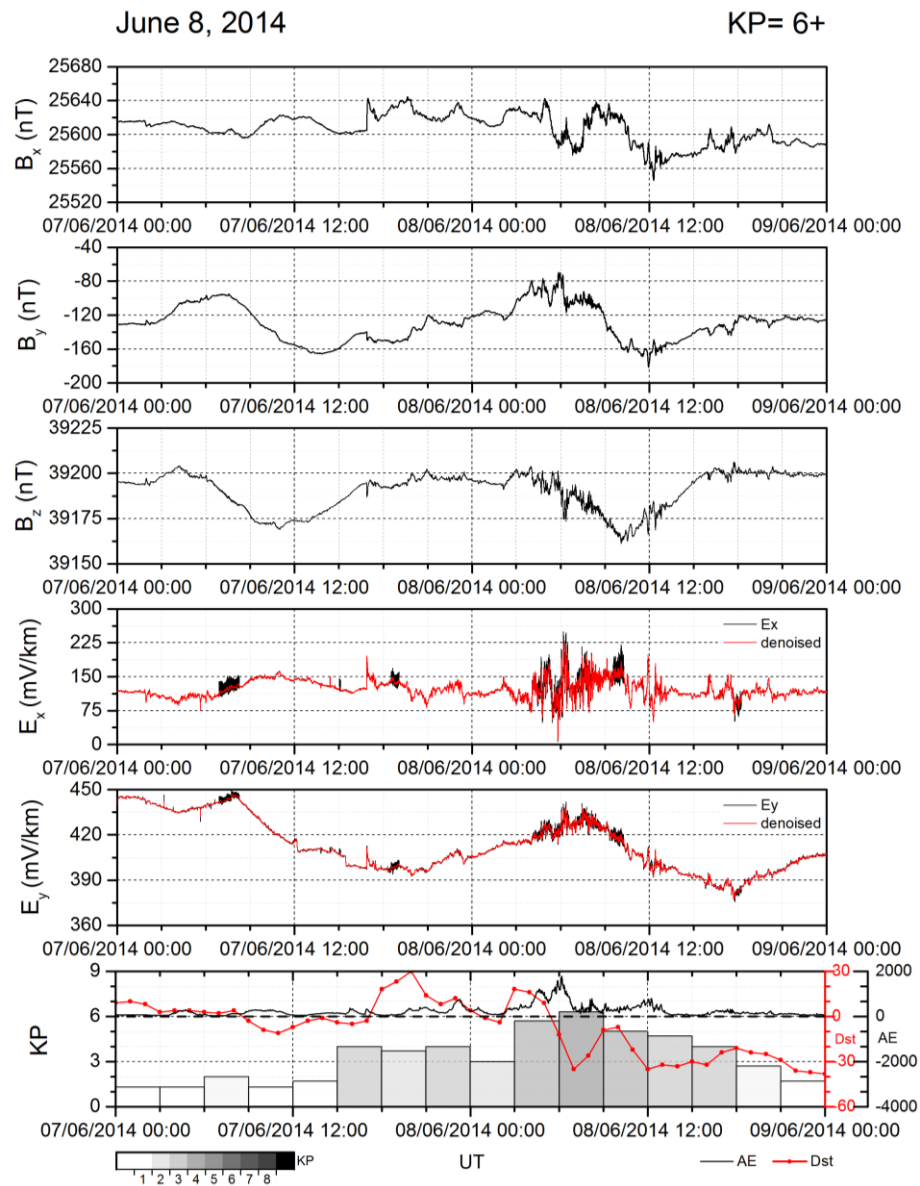


Figure 8.15 : Magnetic and electric field measurements from June 7 to June 9, 2014 during a weak geomagnetic storm. From top to bottom: variations in B_x , B_y , B_z , E_x and E_y , and geomagnetic activity indices: KP on the left, Dst and AE on the right.

Maximum KP, Dst and AE index during the entire event period were 6+, -35 nT, and 1780 nT respectively. There are two sudden commencements seen during this time interval at 17:30 UT on June 7 and at 03:00 UT on June 8, respectively. KP was at 4 when the first sudden commencement with Dst = 30 nT was initiated. At this time, AE was less than 100 nT. The first sudden commencement lasted for about 8 hours and ended at 01:00 UT on June 8. The second sudden commencement was triggered at

02:00 UT on June 8, and continued for about 3 hours until 05:00 UT. In between the two sudden commencements, there was a very slight divergence below zero. At the time of second commencement, D_{st} reached 22nT. KP was higher and varied between 6- and 6+. At the start of the second sudden commencement at 02:00 UT, AE started to increase slowly first to 600 nT and then reached its maximum, about 1780 nT, at 06:00 UT. The maximum of KP and AE occurred at the same time at 06:00 UT when Dst became negative indicating the start of the main phase of the geomagnetic storm. At the same time, a magnetospheric substorm was also initiated as seen from the peak of the AE.

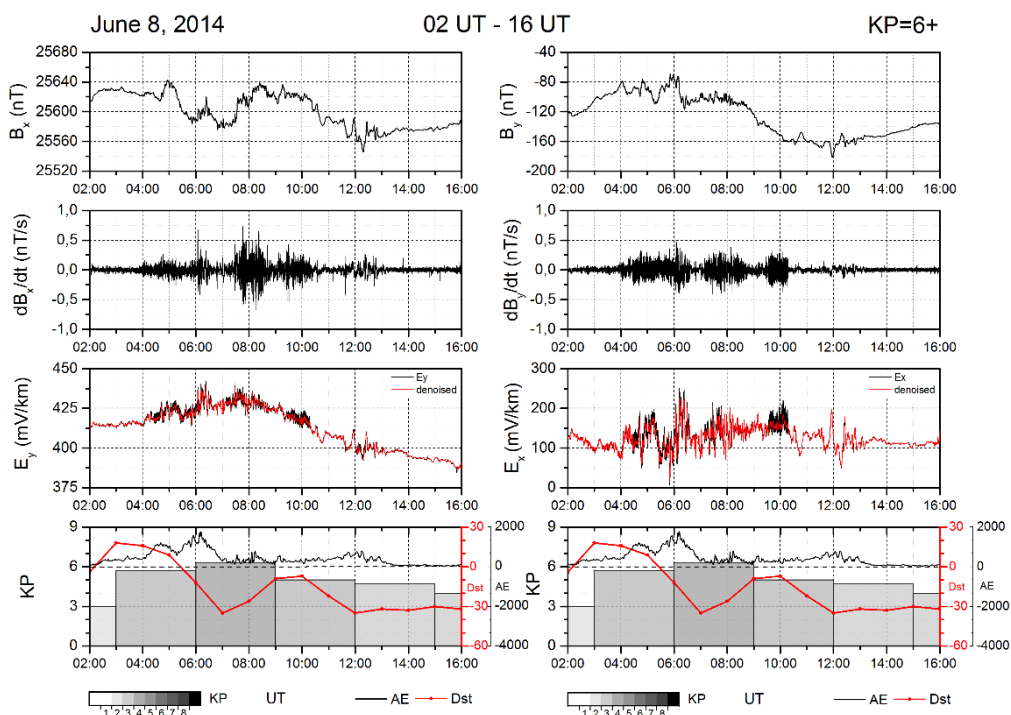


Figure 8.16 : North-south and east-west components of the magnetic field (top panels), dB/dt (second panels), and associated electric field variations (third panels) during the geomagnetic activity on June 8, 2014. From the top, B_x , dB_x/dt , E_y , and activity indices (KP, Dst and AE) are on the left panels, and B_y , dB_y/dt , E_x and activity indices (KP, Dst and AE) are on the right panels.

Examining magnetic and electric field panels indicates two types of variations as well. One corresponding to the initiation of the first sudden commencement when AE was less than 100 nT and KP was around 4, and the other corresponding to the magnetic storm/magnetospheric substorm when AE and KP peaked at 1780 nT and 6+, respectively. During the first sudden commencement interval, when Dst reached 30nT, a spiky jump in electric field components, E_x and E_y , and a fairly sharp increase in B_x

and decrease in B_y , similar to the previous cases, were observed. The magnitude of these variations was small when compared to those shown in previous cases. The fluctuations that occurred during the sudden commencement intervals and during the main phase of the magnetic storm are seen to be in different character. Main phase fluctuations are large amplitude variations while the sudden commencement fluctuations are spiky and small amplitude wavy fluctuations. Main phase fluctuations started at the time when both the magnetospheric substorms started, i.e. at the peak of AE and KP. During this time, AE and KP were both lower in magnitude but Dst became stronger, i.e. more negative as one of the characteristics of the main phase of the magnetic storm. The compression by the solar wind was evident in both magnetic and electric field components starting at about 17:30 UT in June 7, 2014 and ending at 05:30 UT on June 8, 2014.

Figure 8.16 gives the expanded interval covering the second sudden commencement and main phase of the magnetic storm from 02:00 UT to 16:00 UT on June 8, 2014 when KP is the highest at 6+, AE has its peak at 1780 nT, and Dst becomes negative.

As in previous events, the range of E_x variations is larger than those of E_y . Figure 8.16 presents the variations of the components for this event. E_y variations were found to be between 380 mV/km and 440 mV/km, while E_x component changed from 50mV/km to 150mV/km. Time derivatives of the magnetic field (dB_x/dt and dB_y/dt) showed larger variations than ± 0.5 nT/sec at several instances. We removed Sq quiet day variations as described in the previous events. Deviations from the background quiet day for this event were found to be on the order of 40 to -75 nT for B_x component, and between 33 and -26 nT for B_y component as seen in Figure 8.17. We subtracted the daily background variations from electric field components using a best curve fit as in the previous events. The electric field departures from the background were found to be on the order of 120 mV/km to -95 mV/km for E_x and 13 mV/km to -10 mV/km for E_y components.

June 8, 2014

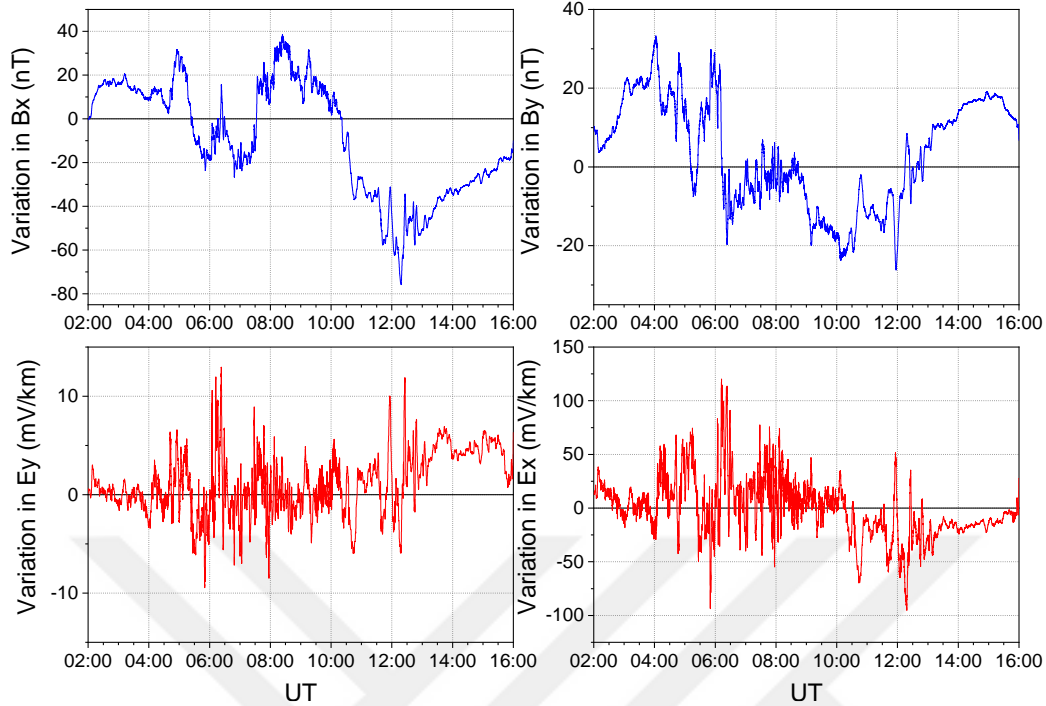


Figure 8.17 : Magnetic field deviations from the background, ΔB_x (left) and ΔB_y (right). (Bottom): Electric field deviations from the best fit curves for electric field components given in Figure 8.13, ΔE_y (left) and ΔE_x (right).

Figure 8.18 gives the solar wind plasma and IMF variations corresponding to this event. The panels are given in the same format as in Figure 8.10 and Figure 8.14. A strong shock related to a CME event in the solar wind occurred at about 17:00 UT when all solar wind plasma parameters and IMF increased sharply. The shock produced the first sudden commencement in Dst at about 17:30 UT and initiated the first spiky jumps followed by finer fluctuations in our ground magnetic and electric field measurements. A second large increase in solar wind dynamic pressure occurred at about 02:30 UT when total magnetic field, density, velocity and temperature also showed a second increase. The small timing differences between the solar wind plasma measurements and Dst result from the resolution of Dst index which is in hourly resolution while the solar wind data presented are in minute. A second sudden commencement was seen in Dst in response to the second increase in dynamic pressure. This second increase in dynamic pressure led to the initiation of the main phase of the magnetic storm and the start of the magnetospheric substorm. During this time, AE increased slightly at first but later, it reached its peak indicating the occurrence of the magnetospheric substorm. IMF B_z component showed a sharp

positive increase at the shock time and then varied between north and south with magnitudes from ± 10 nT. Strong southward IMF B_z on the order of about -20 nT was seen at the start of the fluctuations at 04:00 UT. Thereafter, it varied strongly north and south between -10 nT and 20 nT. Also, there seen to be a third increase in dynamic pressure at 07:00 UT which occurred during the main phase of the magnetic storm. Corresponding fluctuations were found in the ground magnetic and electric field data at 07:00 UT. Similar to the second event, this event, too is a geomagnetic storm event. The likely sources for the variations we observe at our ground station are due to the magnetopause compression during the sudden commencement phase of the geomagnetic storm and during the main phase of the storm, the variations in Dst indicate the ring current with likely contributions from the near Earth geomagnetic tail currents which enhance during the main phase.

In the following, we describe the general features of the June 8, 2014 event:

In this event, there were two sudden commencements, one magnetospheric substorm and one magnetic storm.

In the solar wind, a CME related shock caused all solar wind plasma and magnetic field parameters increased compared to the pre-shock values. There was also a second shock that corresponded to the CME pause where all solar wind parameters showed a second increase and varying southward IMF B_z .

All magnetic indices showed increased variations in response to the changes in the solar wind plasma and magnetic field. Dst and KP increased as response to the first compression and the first sudden commencement was seen during this time. During second compression, a second sudden commencement was seen and both KP and AE reached their peak at this time. Main phase of the storm began and magnetospheric substorm was recorded.

On the ground, examination of magnetic and electric field variations showed two types of fluctuations in response to the variations in the solar wind. Those corresponding to the sudden commencement and those to the main phase of the magnetic storm. In response to the sudden commencement interval which is the initial phase of a magnetic storm, fluctuations were characterized by a spiky jump or sharp dip like features followed by finer variations in the magnetic field and electric field. The main phase

fluctuations, on the other hand, presented large amplitude fluctuations with higher frequencies.

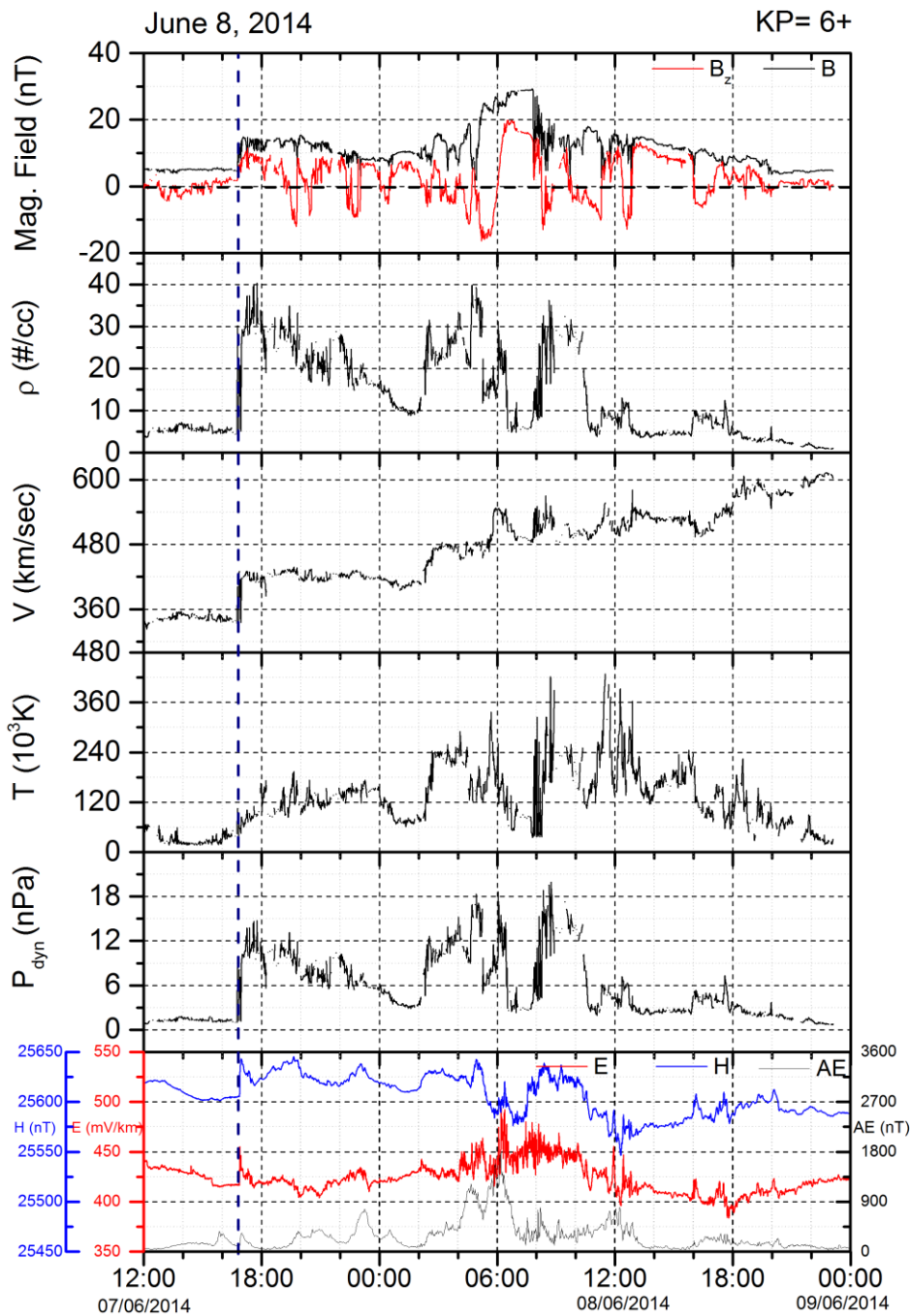


Figure 8.18 : IMF and solar wind parameters for June 8, 2014 event. From top to bottom: Interplanetary magnetic field (IMF B , IMF B_z), solar wind density, solar wind velocity, solar wind temperature, solar wind dynamic pressure, and horizontal components of the electric field and magnetic field given along with the AE index.

Fluctuations that occurred during the initial phase of the storm including the sudden commencement started at about 16:30 UT. They continued for 12 hours as the

magnetosphere was being compressed starting from 16:30 UT (June 7) to 04:30 UT (June 8, 2014).

The fluctuations during the main phase of the storm started at 04:30 UT (June 8, 2014) until the end of the storm.

High fluctuations in dB_x/dt and dB_y/dt corresponded to the high fluctuations in E_y and E_x respectively.

The fluctuation levels in dB_x/dt and dB_y/dt varied between 1 and -1 nT/sec.

The magnitude of the deviations from a magnetically quiet day varied between 40 nT and -75 nT for B_x , while those for B_y were between 33 and -25 nT.

Level of fluctuations or the deviations from the background were found to be larger in E_x than in E_y . Deviations for E_x varied between +125 mV/km and -90 mV/km while those for E_y varied on the orders of 10 mV/km.

Similar to the second event, likely drivers for these ground variations are considered as the magnetopause currents during the sudden commencement and ring current with effects from the near Earth tail currents during the main phase.

8.4 Discussion on the Geomagnetically Induced Currents at Mid-Latitudes

We presented the ground magnetic and electric field measurements as associated with moderate geomagnetic activity over Bozcaada, Çanakkale, Turkey using magnetotelluric methods. During geomagnetic activity, ionospheric currents due to the electric fields caused by the electrons from the magnetosphere flow into the ground and produce disturbances on the measured electric field and magnetic field data through the ground connections of the electrical power networks. These electrical currents on the ground are called geomagnetically induced currents (GICs). We associate these fluctuations observed in the electric field and magnetic field measurements recorded in Bozcaada during different levels of geomagnetic activity as GICs. We studied the characteristic features of the electric field and magnetic field fluctuations caused by the GICs at our latitudes, $\lambda_{\text{geomagnetic}} = 37.5^\circ\text{N}$. We examined their occurrence times, duration, structure, and possible sources. In the absence of electric field measurements, these currents were examined using the time derivatives of magnetic fields (Viljanen et al. 2001, Zhang et al. 2015, Fiori et al. 2014). In this

study, using magnetotelluric methods, we measured magnetic field and electric field concurrently and calculated the time derivatives of magnetic field and evaluated the variations detected as associated with three selected events which all involve one sudden commencement and at least one magnetospheric substorm. The magnetic and electric fields and the time derivatives of the horizontal component of the magnetic field presented large fluctuations during our events when compared to those recorded in a magnetically quiet day when there were no storms/substorms. Fluctuations superimposed on the quiet time daily variations were found to be on the order of 100s mV/km in case of E_x and on the order of 20s in case of E_y . Magnetic field disturbances varied around 20 nT and 40 nT for B_x and B_y , respectively. These fluctuations were present both during the sudden commencement phase of the geomagnetic activity and also during the main phase of the geomagnetic storm. Their characteristics during the initial phase, that includes the sudden commencement, were found to be different than those of the main phase of the geomagnetic storm. In the absence of the main phase, i.e. when only sudden commencement was present, the fluctuations were found to be generally larger, and started with a sharp, spiky rise or drop in the both components of the magnetic and electric field. The follow up high amplitude fluctuations were seen if there was a proceeding magnetic storm manifesting with a main phase. The magnitude of the fluctuations during the main phase of the geomagnetic storm were larger than those of the initial phase, i.e. sudden commencement phase only. However, the sharp rise/drop at the time of the sudden commencement remained as a stable feature and defined one of the characteristics of the sudden commencement type of GICs at our station. Table 6.3 below summarizes and quantifies the average characteristics of the fluctuations seen in the ground electric and magnetic fields associated with the magnetic storm and/or magnetospheric substorms at the time of the maximum dB_x/dt and dB_y/dt . Duration-1 refers to the duration of the sudden commencement while Duration-1 is for the main phase of the magnetic storm. SC: Sudden Commencement, MP: Main Phase of the magnetic storm. UT: Universal Time and LT: Local Time where $LT=UT+3$.

Table 8.2 indicates that E_x was the component that was affected from the geomagnetic activity the most when compared to the E_y . As seen, the magnitude of the E_y fluctuations are smaller than the magnitude of the E_x fluctuations. This indicates that on the ground, the magnetospheric effects are stronger in the north-south component

of electric field, E_x , than the that of the east-west component, E_y . Even though distribution of the soil's conductivity with depth in Bozcaada is another source of the variations of the ground electric fields, the fact that we did not see similar fluctuations in the quiet day electric fields, examined by scanning through many more examples of the magnetically quiet days, other than the one presented here, makes us to consider that these variations recorded during the geomagnetic storm and magnetospheric substorms have a magnetospheric source. In the near future, we plan to investigate the soil's conductivity distribution using impedance tensor given in Equations 8.1 and 8.2 when we collect enough electric and magnetic field measurements in Bozcaada. In the absence of the conductivity distribution and based on the examination of one-year of electric field data measured, we infer that these differences in the magnitudes of E_x and E_y result from the magnetospheric effects, and eventually related to the solar wind structures like CME shocks.

Table 8.2 : Average characteristics of magnetic and electric field fluctuations measured at Bozcaada station at the time of the maximum time derivative of magnetic field components during geomagnetic disturbances.

Events	Apr. 20, 2014	Oct. 8, 2013	June 8, 2014
Storm type	SC only, No MP	Storm	Storm
Start time-UT(LT) with SC	11:00 (13:00)	20:00 (23:00)	17:00 (20:00)
Start time-UT(LT) with MP	None	22:00 (01:00)	04:00 (07:00)
dB_x/dt (nT/s)	0.40	0.45	0.72
dB_y/dt (nT/s)	0.48	0.26	0.40
ΔE_x (mV)	160.93	128.72	75.51
ΔE_y (mV)	18	23.04	7.01
ΔB_x (nT)	41.63	50.98	25.83
ΔB_y (nT)	23	73.31	8
Dst SC (nT)	28	22	30
Dst MP (nT)	None	-62	-35
Duration-1	11:00-13:00	15:00-22:30	16:30-05:30
	2 hours	7.5 hours	13 hours
Duration-2	none	22:30-04:00	05:30-13:00
		5.5 hr	>7.5* hr

*: This storm main phase continues the next day. The number here was given based on Figure 8.16.

Comparing the deviations in magnetic field components at the time of the maximum time derivative of the field components showed that B_x component presented larger deviations than those of B_y component. Another feature that was notable in our measurements was the coherency in the variations of B_x and E_y , and B_y and E_x . We showed that B_x and E_y exhibit similar variations such that when one increased during the magnetospheric activity, the other one increased too, and vice versa. On the other hand, B_y and E_x showed an opposite variation in that one increased while the other one decreased during the geomagnetic storms.

Close examination of dB/dt variations showed that the magnitude of the dB/dt fluctuations during the geomagnetic storms was lower, on the order of ± 0.5 nT/sec, compared to the GICs inferred from the time derivative of the horizontal magnetic field (e.g. Viljanen et al. 2001, 2006; Fiori et al. 2014, Doumbia et al. 2017) and direct measurements of GICs (e.g. Pulkkinen et al., 2003). However, in our cases, compared to the background variations in magnetic and electric field data, observed fluctuations were easily detectable during the high KP and Dst events. Two of our events occurred during the storm-time substorms, i.e. geomagnetic storm with magnetospheric substorms, while one of them was a moderately weak isolated substorm or a geomagnetic disturbance with a strong sudden commencement only. In the absence of the geomagnetic storm, increased solar wind dynamic pressure at the time of the event produced strong sudden commencement that resulted in the fluctuations we observed on the ground as GICs. Since our location is away from the high latitude enhancement of the GIC currents resulting from the magnetospheric substorms and considering the occurrence time of these fluctuations we interpreted the magnetic and electric field signatures as the consequences of the large scale magnetopause currents increased during the solar wind compression. A sharp increase in all components of the magnetic field and electric field was recorded in response to the sudden compression at the dayside magnetopause corresponding to the increase in solar wind dynamic pressure. An initial sharp boxlike, or a sharp spiky jump together with relatively low amplitude, tiny fluctuations superimposed on the background fields were identified during the sudden commencement period of all events presented. In the presence of the main phase of the magnetic storm, this enhancement was followed by high fluctuations. If the main phase of the magnetic storm was not present, then the magnetic and electric field fluctuations ceased toward the background values indicating that GICs

diminished. This was the case in our first event, April 20, 2014 when there was no main phase in the geomagnetic activity. This event corresponded to an extremely large solar wind dynamic pressure that increased from 2 nPa to 10 nPa and caused the jump in Dst seen during the sudden commencement phase. The second-high dynamic pressure was seen corresponding to June 7, 2014 event. This compression was moderate with dynamic pressure increasing from 2 nPa to 6 nPa and creating a weak geomagnetic storm with Dst around -35 nT. The last event on October 8, 2013 corresponded to the smallest increase in dynamic pressure among the three events, and resulted in a moderate magnetic storm.

Table 8.3 : Solar wind plasma and IMF data at the CME shock corresponding to the large amplitude ground level magnetic and electric field fluctuations at the time of the sudden commencement or the magnetospheric compression.

Parameters	April 20, 2014			October 8, 2013			June 8, 2014		
	Pre-shock	At the shock	Max after shock	Pre-shock	At the shock	Max after shock	Pre-shock	At the shock	Max after shock
IMF B_{tot} [nT]	7	13	21	8	20	45	5	15	29
IMF B_z [nT]	6	12	20	0	-10	-30	1.8	5	20
V [km/s]	510	582	734	300	450	670	350	430	600
n [#/cm ³]	4	10	20	5*	14	58	5	25	40
T [Kx10 ⁴]	2.5	4	80	2	18	48	2	15	20
P _{dyn} [nPa]	2	7	13	1.2*	5	18	1	10,	20
Dst [nT]	SC: 28		MP: - -	SC: 22		MP: -62	SC: 28		MP: -35
KP		5			6-			6+	

*: No data from ACE spacecraft. Typical solar wind dynamic pressure and density were assumed to be 1.2 nPa and 5 #/cm³ prior to the shock.

GICs that occurred during the sudden commencement have a different character than those occurred during storm main phase. The magnitudes of the sudden commencement GICs were seen to be larger but the level of fluctuations was lower when compared to the main phase GICs. Main phase GICs were high level rapid fluctuations in the components of magnetic and electric field and lasted longer than sudden commencement GICs. However, this feature depends on the duration of the sudden commencement at the magnetopause. Table 8.3 presents the solar wind plasma and IMF parameters at the first CME shock. In the Table, SC: Sudden Commencement, MP: Main Phase.

Pulkkinen et al. (2003) reported on the coherency of GICs as response to the sudden commencement in their investigation of GIC drivers in April 2000 geomagnetic storm. They found that main phase GICs occurred more frequently around 06:00-07:00 UT. In our events, sudden commencement time GICs occurred at 11:00, 20:00 and 17:00 UT (i.e. 14:00, 23:00 and 20:00 LT) while the main phase GICs were observed at 22:00 and 04:00 UT (i.e. 01:00 and 07:00 LT). The storm-time substorm events caused GICs in the early (01:00 LT) and late morning (07:00 LT) and two of the sudden commencement GICs occurred at local midnight (23:00 and 20:00 LT). Our statistics do not allow us to ascertain this point at this time in this event based study. Other than ionospheric currents, ULF waves can also drive GICs as pointed out in Viljanen et al. (2001, 2006). Midnight maximum in Viljanen et al. (2001) was found to be associated with the westward flowing auroral currents while morning maximum was suggested to be associated with eastward flowing ionospheric currents resulting from other smaller scale structures. In our isolated storm event when there was only sudden commencement without a storm, the apparent reason for the occurrence of the GICs at our station (37.5°N MLAT) is the magnetopause currents resulting from the interaction between CME related interplanetary shock and the magnetosphere at the magnetopause. In fact, all three of our events correspond to a strong shock in the solar wind associated with a CME. The timings of the CME shock occurrences, the time of the compression at the magnetopause and the ground based magnetic and electric field fluctuations all coincide and thus identify the source clearly. Extremely large dynamic pressures with a maximum varying around 15 nPa were attributed as a cause for these high frequency and large amplitude ground magnetic and electric field fluctuations.

9. CONCLUSION AND FUTURE RESEARCH

9.1 Thesis Summary and Conclusions

In this thesis study, we presented a comprehensive study on the thermospheric, ionospheric and ground level aspects of the space weather using Joule heating, thermospheric neutral density and the magnetic and electric field variations on the ground for geomagnetically active times.

In Chapter 5, we studied the variability of JH from different methods during two consecutive substorm events using four different approaches: 1) index-based methods, 2) an MHD model, 3) combinative methods that couple the conductivity and electric field from different sources, 4) a solar wind-driven empirical model that includes the effect of AL. New combinative methods were introduced to extract the role of the conductances and electric field on JH. One of the new methods to calculate Joule heating rates was constructed by combining OVATION Prime+IRI models for the height-integrated conductances and SuperDARN for the electric fields. The OIS was found to be representative enough for the global Joule heating rates in the ionosphere as it shows the same order of magnitude estimates with the (Foster et al., 1983) method, which depends on the KP and its spatial distribution agrees with the previous studies in the literature. Other combinative methods have shown that the spatial distribution of the Joule heating pattern resembles the electric field pattern. All methods, except the AE index dependent Olsson method, displayed increased Joule heating levels during the expansion phase and less amount of Joule heating in the recovery phase. Different recovery times were found during the recovery phase. AE index-based methods, especially the Olsson method during the first substorm, showed still abundant Joule heating during the recovery phase and the slowest recovery times.

Moreover, in Chapter 5, SWMF-BATSRUS MHD model coupled with RCM and CRCM modules was used in various combinative methods to investigate the Joule heating in the upper atmosphere. In previous studies, MHD models were compared for specific parameters and the results revealed that all MHD models are performing better

on the dayside and their performances decrease from the dayside to the nightside (Honkonen et al., 2013). Gordeev et al. (2017) showed that the substorm cycle was not modeled well-enough by the BATSRUS model. Wang et al. (2008) also showed that the BATSRUS/RCM performs better in capturing the well-defined FAC sheets on the dayside, however, fails to capture the localized multiple FACs in the nightside, which cover a wide range of latitudes. We find that BATSRUS/RCM fails to reproduce the nightside Pedersen conductance patterns. However, BATSRUS/CRCM predictions are highly adequate in describing the conductance distribution and the overall JH. The global patterns of JH produced by BATSRUS/CRCM are similar to W05 when neutral wind effects are included. Without the neutral wind, it still shows the qualitative agreement with the OIS, but quantitatively, its JH predictions are 1.5 times that of the OIS estimates for JH rates. These confirm that the specification of the inner boundary and the composition of the inner magnetosphere in SWMF/BATSRUS plays a major part in the production of the Pedersen conductances and ionospheric convection patterns.

On the other hand, Olsson et al (2004) and W05 models both overestimate the JH with respect to other methods used in this study. The Foster et al. (1983) method, despite having low temporal resolution, agrees with the combinative methods on the magnitude of JH rates. This suggests that there is a need for an empirical model which represents all solar conditions including data from one complete solar cycle, thus covering both solar minimum and solar maximum conditions. W05 and Olsson et al. (2004) inherently contain the effect of the conductances on JH. However, the data included in the models are restricted to the solar maximum years. The OIS has the advantage that it can be used during both solar minimum and solar maximum conditions with relatively high confidence levels. The OIS at least provides the average estimate of JH by combining the empirical conductance and statistical and data-filled electric field patterns. The performance of the OIS improves when SuperDARN has more data in the nightside sector so that the substorm time variations in the ionosphere can be simulated more realistically.

In Chapter 5, we also showed that the JH due to the nightside conductances constitute 60 to 70% of the total JH while the dayside conductances constitute to the 27-45% of the total JH (Table 5.4). Hence, we see that not only the nightside conductances, but

also the dayside conductances play a significant role in the accurate determination of the magnitude of resultant JH.

Joule heating leads to the expansion of the upper atmosphere and higher amount of neutrals in lower altitudes. Consequently, for LEO satellites, the accuracy of neutral density estimations is important in the calculations of satellite drag. In Chapter 6 of our study, we follow the systematic assessment of IT models by (Shim et al., 2012) and use the same set of geomagnetic storms in GEM-CEDAR challenge. This study shows, the models of the I-T present variable errors depending on the event studied. None of the models perform perfectly for all cases. We show that baseline shifting is useful in assessing the storm-time model performance when models have bias against the data during the quiet-time. Removal of the baseline allows for the detection of actual storm-time response and performances from the models. It is also shown that the discrepancies between the model and observations are different during the quiet-time and during the geomagnetic storm due to the mechanisms in effect. Thus, we emphasize that quiet-time climatology and storm-time performances of the models should be evaluated separately, and after baseline shifts, especially for the models with quiet-time bias. Additionally, we recommend using mean absolute error, normalized root mean square error and prediction efficiency together for the performance assessment of the models as each metric provides different aspects of the error. On the contrary, using only the ratio of average and ratio of maximum for performance assessment of a model are not suggested. A model capturing the average may not be estimating the maxima well, meaning that those metrics provide limited performance measures.

In Chapter 7, we showed that a relation between JH and thermospheric neutral density can be found by using the baseline shifting procedures. This part of the study was carried out using the JH and neutral density results from the TIEGCM and CTIPe models. Both models presented a time lag between JH and neutral density from the models and CHAMP observations varying between 1 to 7 hours, which agrees with the previous studies in the literature. Even though this is a preliminary analysis, the results showed that, for the CME events in this study, CTIPe model performed better than the TIEGCM according to the residual sum squares and Pearson's R. However, TIEGCM was better in some of the individual events.

In Chapter 8, we presented the measurements of magnetic electric fields recorded in Bozcaada, Çanakkale (37.5 °N, 106°E) in order to study the variations in GIC occurrences in our region for the space weather effects on the ground level. We showed that compared to those found in earlier studies, although small in magnitude, the GICs were detectable at our latitudes. Using direct measurements of magnetic and electric field, we determined the characteristics of GIC fluctuations during geomagnetically disturbed times. One of the differences between this study and those in the literature is that the variations in magnetic and electric field components were used to interpret GIC fluctuations as opposed to the total variation of the horizontal component of the magnetic field and its time derivatives. In addition, it is the first time that the electric field measurements were presented together with the time derivatives of magnetic field. We selected three cases corresponding to geomagnetically active days and characterized and organized the fluctuations according to the geomagnetic activity phases. We found that GICs occur during the sudden commencement phase of the geomagnetic storm together with the main phase, identified as SSC storms, or during the sudden commencement only, i.e. without a follow up main phase of a geomagnetic storm, called sudden impulse (SI) or sudden commencement events. The characteristics of these GIC fluctuations and their magnitudes reported in this part of our work were found to be similar to those of SSC and SI given in the literature. GICs corresponding to the sudden commencement phase are shorter in durations than those of main phase GICs and depend on the compression of the solar wind. They are seen as sharp jumps or drops and the magnitude of fluctuations that follow is lower at the elevated/decreased level. Main phase GICs, on the other hand, present large amplitude high frequency wavy variations compared to those of sudden commencement GICs. These variations suggest that the effect of magnetopause currents are stronger in our latitudes than the effects from the auroral or ionospheric currents seen at high latitudes or from the effects from equatorial electrojets seen at the low equatorial latitudes. The magnitude of dB/dt variations are on the order of 0.5 nT/s for both dB_x/dt and dB_y/dt . This is about the half of the observed at high latitudes. However, decrease in magnitude is expected as one goes away south from the high latitudes of northern hemisphere. The occurrence of all three GIC events correspond to a CME and its related shock in the solar wind. This emphasizes that the presence of GICs during sudden commencement are due to the magnetopause currents resulting from the CME compression at the subsolar magnetopause as associated with a strong dynamic

pressure. For those seen during the main phase, when Dst is negative, on the other hand, the ring current and the near Earth tail currents as associated with the geomagnetic storm appears to be the possible driver at our latitudes rather than the high latitude auroral electrojets. Taken together these preliminary results indicate that the magnetopause currents owing to the dayside compression, geomagnetic storm associated ring current with likely effects from the near Earth tail currents, and although not discussed, possibly the ULF waves are the contributing factors on the occurrence of GICs in our region. A separation of these drivers need a more comprehensive analysis.

9.2 Future Work and Recommendations

In this study, we developed methods of combining datasets to estimate JH and applied them to a case study of two substorms. The study revealed wide variation in the magnitude of JH rates but greater consistency in terms of variations between growth, expansion, and recovery phases, and still greater consistency when the datasets are more realistic (BATSRUS, SuperDARN). Future study will implement these methods to examine a wider set of events throughout a solar cycle.

For satellite drag calculations, the accuracy of neutral density estimations is important. The uncertainty in thermospheric neutral density in an event can be represented well by using an ensemble of models and iterating the results. Murray (2018) demonstrated the usefulness of ensembles in space weather forecasting to determine the uncertainty and (Knipp, 2016) reported the studies, which use the ensemble method for space weather forecasting. We want to point out that multi-model ensemble forecasts can be of great use and is a candidate for future work to consider for the community especially for the integrated density change, maximum and average neutral density which are found to be highly variable among the models and are important in satellite drag calculations and for real-time operations.

Additionally, in this study, for the first time in Eurasia region, we started to record long-time measurements of the geoelectric and geomagnetic field together. However, for the successful modelling and prediction of the space weather events, worldwide continuous observations of GICs are needed. The more we know about the latitudinal distributions and variations of the GICs, the more it will help scientist to improve more accurate models for their predictions. Among the few studies at midlatitudes, this study

in our region is the first of its kind and forms a base for a large statistical study on the properties of GICs and their sources in our region. This will in turn close an important observational gap for global space weather predictions. Currently the continuous simultaneous measurements of magnetic and electric field are carried out carefully to build up a good data base. The planned future work on GICs include the modelling of the currents at our latitudes and finding the links between the electricity failures at Bozcaada and electric and magnetic field variations measured at the magnetotelluric stations.



REFERENCES

- Ahn, B. H., Akasofu, S. I., and Kamide, Y.** (1983). The Joule heat production rate and the particle energy injection rate as a function of the geomagnetic indices AE and AL. *Journal of Geophysical Research: Space Physics*, 88 (A8), 6275-6287.
- Ahn, B. H., Kroehl, H. W., Kamide, Y., and Gorney, D. J.** (1989). Estimation of ionospheric electrodynamic parameters using ionospheric conductance deduced from bremsstrahlung X ray image data. *Journal of Geophysical Research: Space Physics*, 94 (A3), 2565-2586.
- Aikio, A. T., and Selkälä, A.** (2009). Statistical properties of Joule heating rate, electric field and conductances at high latitudes. *Annales Geophysicae*, 27 (7), 2661–2673. <http://doi.org/10.5194/angeo-27-2661-2009>.
- Aikio, A. T., Cai, L., and Nygrén, T.** (2012). Statistical distribution of height-integrated energy exchange rates in the ionosphere. *Journal of Geophysical Research: Space Physics*, 117 (October), 1–14. <http://doi.org/10.1029/2012JA018078>.
- Aksnes, A., Stadsnes, J., Bjordal, J., Østgaard, N., Vondrak, R. R., Detrick, D. L., ..., and Chenette, D.** (2002). Instantaneous ionospheric global conductance maps during an isolated substorm. *Annales Geophysicae*, 20 (8), 1181–1191. <http://doi.org/10.5194/angeo-20-1181-2002>.
- Alexeev, I.I., Belenkaya, E.S., Kalegaev, V. V., Feldstein, Y.I., and Grafe, A.**, (1996). Magnetic storms and magnetotail currents. *Journal of Geophysical Research: Space Physics* 101, 7737–7747. doi:10.1029/95JA03509.
- Anderson, C., Kosch, M. J., Nicolls, M. J., and Conde, M.** (2013). Ion–neutral coupling in Earth's thermosphere, estimated from concurrent radar and optical observations above Alaska. *Journal of Atmospheric and Solar-Terrestrial Physics*, 105, 313-324.
- Anderson, R. L., Born, G. H., and Forbes, J. M.** (2009). Sensitivity of Orbit Predictions to Density Variability. *Journal of Spacecraft and Rockets*, 46 (6), 1214–1230. <https://doi.org/10.2514/1.42138>.
- Araki, T.** (1994). A Physical Model of the Geomagnetic Sudden Commencement. In Engebretson, M.J., Takahashi, K., Scholer, M. (Eds.), *Solar Wind Sources of Magnetospheric Ultra-Low-Frequency Waves*. American Geophysical Union, pp. 183–200. doi:10.1029/GM081p0183.

- Araki, T., Keika, K., Kamei, T., Yang, H., and Alex, S.** (2006). Nighttime enhancement of the amplitude of geomagnetic sudden commencements and its dependence on IMF-B_z. *Earth, Planets and Space*, 58, 45–50. doi:10.1186/BF03351912.
- Arbesser-Rastburg, B., and Jakowski, N.**(2007). *Effects on satellite navigation, in Space Weather- Physics and Effects*, pp. 383–402, Springer Berlin Heidelberg, Berlin, Heidelberg.
- Bailey, G. J.** (1983). The effect of a meridional E× B drift on the thermal plasma at L= 1.4. *Planetary and Space Science*, 31 (4), 389-409.
- Baker, J. B. H., Zhang, Y., Greenwald, R. a., Paxton, L. J., and Morrison, D.** (2004). Height-integrated Joule and auroral particle heating in the night side high latitude thermosphere. *Geophysical Research Letters*, 31, 0–3. <http://doi.org/10.1029/2004GL019535>.
- Balthazor, R. L., Moffett, R. J., and Millward, G. H.** (1997). A study of the Joule and Lorentz inputs in the production of atmospheric gravity waves in the upper thermosphere. *Annales Geophysicae*, 15 (6), 779–785. <http://doi.org/10.5194/angeo-15-779-1997>.
- Barbosa, C., Alves, L., Caraballo, R., Hartmann, G.A., Papa, A.R.R., and Pirjola, R.J.** (2015). Analysis of geomagnetically induced currents at a low-latitude region over the solar cycles 23 and 24: comparison between measurements and calculations. *Journal of Space Weather and Climate*, 5, A35. doi:10.1051/swsc/2015036.
- Beamish, D., Clark, T.D.G., Clarke, E., and Thomson, A.W.P.** (2002). Geomagnetically induced currents in the UK: Geomagnetic variations and surface electric fields. *Journal of Atmospheric and Solar-Terrestrial Physics*, 64 (16), 1779–1792. doi:10.1016/S1364-6826(02)00127-X.
- Béland, J., and Small, K.** (2004). *Space Weather Effects on Power Transmission Systems: The Cases of Hydro-Québec and Transpower New Zealand Ltd.* In *Effects of Space Weather on Technology Infrastructure*. Kluwer Academic Publishers, Dordrecht, pp. 287–299. doi:10.1007/1-4020-2754-0_15.
- Bilitza, D., Altadill, D., Zhang, Y., Mertens, C., Truhlik, V., Richards, P., ..., and Reinisch, B.** (2014). The International Reference Ionosphere 2012 – a model of international collaboration. *Journal of Space Weather and Space Climate*, 4, A07. <http://doi.org/10.1051/swsc/2014004>.
- Boteler, D. H.** (1990). Prediction of extreme disturbances with application to geomagnetic effects on pipelines and power systems, *Solar Terrestrial Predictions Proceedings, 1*, pp. 53-68.
- Boteler, D.H., Pirjola, R.J., and Nevanlinna, H.** (1998). The effects of geomagnetic disturbances on electrical systems at the Earth's surface. *Advances in Space Research*, 22, 17–27. doi:10.1016/S0273-1177(97)01096-X.

- Bothmer, V., and Daglis, I. A.** (2007). *Space Weather- Physics and Effects*, Springer Science & Business Media, Berlin, Heidelberg.
- Bowman, B. R., Tobiska, W. K., Marcos, F. A., Huang, C. Y., Lin, C. S., and Burke, W. J.** (2008, August). A new empirical thermospheric density model JB2008 using new solar and geomagnetic indices. In *AIAA/AAS Astrodynamics specialist conference and exhibit* (p. 6438).
- Brekke, A.** (1979). On the relative importance of Joule heating and the Lorentz force in generating atmospheric gravity waves and infrasound waves in the auroral electrojets. *Journal of Atmospheric and Terrestrial Physics*, 41 (5), 475-479.
- Bruinsma, S. L., and Forbes, J. M.** (2010). Anomalous behavior of the thermosphere during solar minimum observed by CHAMP and GRACE. *Journal of Geophysical Research: Space Physics*, 115 (11), 1–8. <https://doi.org/10.1029/2010JA015605>.
- Bussy-Virat, C. D., Ridley, A. J., and Getchius, J. W.** (2018). Effects of Uncertainties in the Atmospheric Density on the Probability of Collision Between Space Objects. *Space Weather*, 16, 519–537. <https://doi.org/10.1029/2017SW001705>.
- Cai, L., Aikio, A. T., and Nygrén, T.** (2014). Solar wind effect on Joule heating in the high-latitude ionosphere. *Journal of Geophysical Research A: Space Physics*, 119 (12), 10440–10455. <http://doi.org/10.1002/2014JA020269>.
- Carter, B.A., Yizengaw, E., Pradipta, R., Halford, A.J., Norman, R., and Zhang, K.** (2015). Interplanetary shocks and the resulting geomagnetically induced currents at the equator. *Geophysical Research Letters*, 42 (16), 6554-6559. doi:10.1002/2015GL065060.
- Chai, T., and Draxler, R. R.** (2014). Root mean square error (RMSE) or mean absolute error (MAE)? – Arguments against avoiding RMSE in the literature, *Geoscientific Model Development*, 7 (3), 1247–1250. <https://doi.org/10.5194/gmd-7-1247-2014>.
- Chen, G., Xu, J., Wang, W., and Burns, A. G.** (2014). A comparison of the effects of CIR- and CME-induced geomagnetic activity on thermospheric densities and spacecraft orbits: Statistical studies. *Journal of Geophysical Research: Space Physics*, 119 (9), 7928–7939. <https://doi.org/10.1002/2014JA019831>.
- Chen, G., Xu, J., Wang, W., Lei, J., and Burns, A. G.** (2012). A comparison of the effects of CIR- and CME-induced geomagnetic activity on thermospheric densities and spacecraft orbits: Case studies. *Journal of Geophysical Research: Space Physics*, 117 (A8). <https://doi.org/10.1029/2012JA017782>.
- Chisham, G., Lester, M., Milan, S. E., Freeman, M. P., Bristow, W. A., Grocott, A., ..., and Greenwald, R. A.** (2007). A decade of the Super Dual

Auroral Radar Network (SuperDARN): Scientific achievements, new techniques and future directions. *Surveys in geophysics*, 28 (1), 33-109. doi:10.1007/s10712-007-9017-8, 2007.

- Chun, F. K., Knipp, D. J., McHarg, M. G., Lu, G., Emery, B. A., Vennerstrøm, S., and Troshichev, O. A.** (1999). Polar cap index as a proxy for hemispheric Joule heating. *Geophysical Research Letters*, 26 (8), 1101–1104. <http://doi.org/10.1029/1999GL900196>.
- Codrescu, M. V., Fuller-Rowell, T. J., Foster, J. C., Holt, J. M., and Cariglia, S. J.** (2000). Electric field variability associated with the Millstone Hill electric field model. *Journal of Geophysical Research: Space Physics*, 105 (A3), 5265-5273.
- Codrescu, M. V., Fuller-Rowell, T. J., Munteanu, V., Minter, C. F., and Millward, G. H.** (2008). Validation of the coupled thermosphere ionosphere plasmasphere electrodynamics model: CTIPE-mass spectrometer incoherent scatter temperature comparison. *Space Weather*, 6 (9), 1–10. <https://doi.org/10.1029/2007SW000364>.
- Codrescu, M. V., Negrea, C., Fedrizzi, M., Fuller-Rowell, T. J., Dobin, A., Jakowsky, N., ..., and Maruyama, N.** (2012). A real-time run of the Coupled Thermosphere Ionosphere Plasmasphere Electrodynamics (CTIPE) model. *Space Weather*, 10 (1), 1–10. <https://doi.org/10.1029/2011SW000736>
- Cohen, A., Daubechies, I., and Feauveau, J.-C.** (1992). Biorthogonal bases of compactly supported wavelets. *Communications on pure and applied mathematics*, 45 (5), 485-560.. doi:10.1002/cpa.3160450502.
- Committee on the Societal and Economic Impacts of Severe Space Weather Events and National Research Council** (2008). Severe Space Weather Events--Understanding Societal and Economic Impacts: workshop report. <http://www.nap.edu/catalog/12507.html>.
- Cowley, S. W. H.** (1996). The aurora ionosphere and its coupling to the magnetosphere and the solar wind. In Kohl, H., Rüster, R., and Schlegl, K.(Eds.), *Modern Ionospheric Science*, (pp. 32-66). EGS Publications, Katlenburg-Lindau.
- Crosby, N. B.** (2007). Major radiation environments in the heliosphere and their implications for interplanetary travel, In Bothmer, V., and Daglis, I. A (Eds), *Space Weather- Physics and Effects*, (pp. 131–171), Springer Business and Science Media, Berlin, Heidelberg.
- Crowley, G.** (2015) *Modeling the Upper Atmosphere and Ionosphere with TIMEGCM*, [PowePoint slides] Retrieved from: <https://docslide.com.br/documents/modeling-the-upper-atmosphere-and-ionosphere-with-timegcm-geoff-crowley-atmospheric.html>.

- Curto, J.J., Araki, T., and Alberca, L.F.** (2007). Evolution of the concept of Sudden Storm Commencements and their operative identification. *Earth, Planets and Space*, 59, i–xii. doi:10.1186/BF03352059
- Daly, E., Glover, A., and Hilgers, A.** (2007): Effects on spacecraft hardware and operations, In Bothmer, V., and Daglis, I. A (Eds), *Space Weather-Physics and Effects*, (pp. 353–381), Springer Business and Science Media, Berlin, Heidelberg.
- Daubechies, I.** (1992). *Ten lectures on wavelets* (Vol. 61). Siam.
- Davis, T., and Sugiura, M.** (1966). Auroral electrojet activity index AE and its universal time variations. *Journal of Geophysical Research*, 71 (3), 785–801. <http://doi.org/10.1029/JZ071i003p00785>
- De Zeeuw, D. L., Sazykin, S., Wolf, R. A., Gombosi, T. I., Ridley, A. J., and Tóth, G.** (2004). Coupling of a global MHD code and an inner magnetospheric model: Initial results. *Journal of Geophysical Research: Space Physics*, 109 (A12).
- Deng, Y., and Ridley, A. J.** (2007). Possible reasons for underestimating Joule heating in global models: E field variability, spatial resolution, and vertical velocity. *Journal of Geophysical Research*, 112 (A9), A09308. <http://doi.org/10.1029/2006JA012006>
- Deng, Y., Fuller-Rowell, T. J., Akmaev, R. A., and Ridley, A. J.** (2011). Impact of the altitudinal Joule heating distribution on the thermosphere. *Journal of Geophysical Research*, 116 (May), 1–7. <http://doi.org/10.1029/2010JA016019>
- Deng, Y., Fuller-Rowell, T. J., Ridley, A. J., Knipp, D., and Lopez, R. E.** (2013). Theoretical study: Influence of different energy sources on the cusp neutral density enhancement. *Journal of Geophysical Research: Space Physics*, 118 (5), 2340–2349. <https://doi.org/10.1002/jgra.50197>
- Deng, Y., Richmond, A. D., Ridley, A. J., and Liu, H.-L.** (2008). Assessment of the non-hydrostatic effect on the upper atmosphere using a general circulation model (GCM), *Geophysical Research Letters*, 35 (1), L01104, doi:10.1029/2007GL032182, 2008.
- Dickinson, R. E., Ridley, E. C. and Roble, R. G.** (1981). A three-dimensional general circulation model of the thermosphere, *Journal of Geophysical Research*, 86 (A3), 1499, doi:10.1029/JA086iA03p01499.
- Doumbia, V., Boka, K., Kouassi, N., Grodji, O.D.F., Amory-Mazaudier, C., and Menvielle, M.** (2017). Induction effects of geomagnetic disturbances in the geo-electric field variations at low latitudes. *Annales Geophysicae*, 35, 39–51. doi:10.5194/angeo-35-39-2017
- Duka, B., De Santis, A., Manda, M., Isac, A., and Qamili, E.** (2012). Geomagnetic jerks characterization via spectral analysis, *Solid Earth*, 3 (1), 131–148, doi:10.5194/se-3-131-2012.

- Emery, B. A., Lathuillere, C., Richards, P. G., Roble, R. G., Buonsanto, M. J., Knipp, D. J., ..., and Niciejewski, R.** (1999). Time dependent thermospheric neutral response to the 2-11 November 1993 storm period. *Journal of Atmospheric and Solar-Terrestrial Physics*, *61* (3–4), 329–350. [http://doi.org/10.1016/S1364-6826\(98\)00137-0](http://doi.org/10.1016/S1364-6826(98)00137-0).
- Emmert, J. T., and Picone, J. M.** (2011). Statistical uncertainty of 1967–2005 thermospheric density trends derived from orbital drag. *Journal of Geophysical Research*, *116* (May), A00H09. <https://doi.org/10.1029/2010JA016382>.
- Emmert, J. T., Warren, H. P., Segerman, A. M., Byers, J. M., and Picone, J. M.** (2017). Propagation of atmospheric density errors to satellite orbits. *Advances in Space Research*, *59* (1), 147–165. <https://doi.org/10.1016/j.asr.2016.07.036>.
- Eyigüler, E. C. K., and Kaymaz, Z.** (2017) Magnetic and electric field variations during geomagnetically active days over Turkey, *Advances in Space Research*, *60* (9), 1921-1948, doi:10.1016/j.asr.2017.07.019.
- Fedrizzi, M., Fuller-Rowell, T. J., and Codrescu, M. V.** (2012). Global Joule heating index derived from thermospheric density physics-based modeling and observations. *Space Weather*, *10* (3). <http://doi.org/10.1029/2011SW000724>.
- Fiori, R.A.D., Boteler, D.H., Gillies, D.M.** (2014). Assessment of GIC risk due to geomagnetic sudden commencements and identification of the current systems responsible. *Space Weather*, *12*, 76–91. doi:10.1002/2013SW000967.
- Foster, J. C., St-Maurice, J.-P., and Abreu, V. J.** (1983). Joule heating at high latitudes. *Journal of Geophysical Research*, *88* (A6), 4885. <http://doi.org/10.1029/JA088iA06p04885>.
- Frey, W. R.; Lin, C. S.; Garvin, M. B., and Acebal, A. O.** (2014). Modeling the thermosphere as a driven-dissipative thermodynamic system. *Space Weather*, *12* (3), 132–1.
- Fujii, R., Nozawa, S., Buchert, S. C., and Brekke, A.** (1999). Statistical characteristics of electromagnetic energy transfer between the magnetosphere, the ionosphere, and the thermosphere. *Journal of Geophysical Research*, *104* (A2), 2357. <http://doi.org/10.1029/98JA02750>.
- Fuller-Rowell, T. J., and Rees, D.** (1980). A three-dimensional time-dependent global model of the thermosphere. *Journal of the Atmospheric Sciences*, *37* (11), 2545-2567.
- Galand, M., and Richmond, A. D.** (2001). Ionospheric electrical conductances produced by auroral proton precipitation. *Journal of Geophysical Research: Space Physics*, *106* (A1), 117–125. <https://doi.org/10.1029/1999JA002001>.

- Geophysics Study Committee, & National Research Council** (1986). *The Earth's Electrical Environment*. National Academies Press. doi:10.17226/898.
- Gjerloev, J. W., and Hoffman, R. A.** (2000). Height-integrated conductivity in auroral substorms: 2. Modeling. *Journal of Geophysical Research*, 105 (A1), 227. <http://doi.org/10.1029/1999JA900353>.
- Gjerloev, J. W., Waters, C. L., and Barnes, R. J.** (2018). Deriving Global Convection Maps from SuperDARN measurements. *Journal of Geophysical Research: Space Physics*, 123 (4), 2902-2915. <http://doi.org/10.1002/2017JA024543>.
- Glocer, A., Fok, M., Meng, X., Toth, G., Buzulukova, N., Chen, S., and Lin, K.** (2013). CRCM + BATS-R-US two-way coupling. *Journal of Geophysical Research: Space Physics*, 118 (4), 1635–1650. <http://doi.org/10.1002/jgra.50221>.
- Gonzalez, W.D., Joselyn, J.A., Kamide, Y., Kroehl, H.W., Rostoker, G., Tsurutani, B.T., and Vasyliunas, V.M.** (1994). What is a geomagnetic storm? *Journal of Geophysical Research*, 99 (A4), 5771-5792.
- Gordeev, E., Facskő, G., Sergeev, V., Honkonen, I., Palmroth, M., Janhunen, P., and Milan, S.** (2013). Verification of the GUMICS-4 global MHD code using empirical relationships. *Journal of Geophysical Research: Space Physics*, 118 (6), 3138–3146. <http://doi.org/10.1002/jgra.50359>.
- Gordeev, E., Sergeev, V., Honkonen, I., Kuznetsova, M., Rastätter, L., Palmroth, M., ..., and Wiltberger, M.** (2015). Assessing the performance of community-available global MHD models using key system parameters and empirical relationships. *Space Weather*, 13 (12), 868–884. <http://doi.org/10.1002/2015SW001307>.
- Gordeev, E., Sergeev, V., Tsyganenko, N., Kuznetsova, M., Rastätter, L., Raeder, J., ..., and Wiltberger, M.** (2017). The substorm cycle as reproduced by global MHD models. *Space Weather*, 15 (1), 131–149. <http://doi.org/10.1002/2016SW001495>.
- Greenwald, R. A., Baker, K. B., Dudeney, J. R., Pinnock, M., Jones, T. B., Thomas, ..., and Yamagishi, H.** (1995). DARN/SuperDARN. *Space Science Reviews*, 71, 761–796. <http://doi.org/10.1007/BF00751350>.
- Hamilton, D.C., Gloeckler, G., Ipavich, F.M., Stüdemann, W., Wilken, B., and Kremser, G.** (1988). Ring current development during the great geomagnetic storm of February 1986. *Journal of Geophysical Research* 93, 14343-14355. doi:10.1029/JA093iA12p14343.
- Hardy, D. A., Gussenhoven, M. S., Raistrick, R., and McNeil, W. J.** (1987). Statistical and functional representations of the pattern of auroral energy flux, number flux, and conductivity. *Journal of Geophysical Research: Space Physics*, 92 (A11), 12275-12294.

- Hejduk, M. D., and Snow, D. E.** (2018). The Effect of Neutral Density Estimation Errors on Satellite Conjunction Serious Event Rates. *Space Weather*. <https://doi.org/10.1029/2017SW001720>
- Honkonen, I., Rastätter, L., Grocott, A., Pulkkinen, A., Palmroth, M., Raeder, J., Ridley, A.J., and Wiltberger, M.** (2013). On the performance of global magnetohydrodynamic models in the Earth's magnetosphere. *Space Weather*, 11 (5), 313-326.
- Huang, Y., Richmond, A. D., Deng, Y., and Roble, R.** (2012). Height distribution of Joule heating and its influence on the thermosphere. *Journal of Geophysical Research: Space Physics*, 117 (A8). <http://doi.org/10.1029/2012JA017885>
- Huang, C. Y., Su, Y.-J., Sutton, E. K., Weimer, D. R., and Davidson, R. L.** (2014). Energy coupling during the August 2011 magnetic storm. *Journal of Geophysical Research: Space Physics*, 119 (2), 1219–1232. <https://doi.org/10.1002/2013JA019297>
- Huttunen, K.E.J., Kilpua, S.P., Pulkkinen, A., Viljanen, A., and Tanskanen, E.** (2008). Solar wind drivers of large geomagnetically induced currents during the solar cycle 23. *Space Weather*, 6 (10). doi:10.1029/2007SW000374
- Joselyn, J.A., and Tsurutani, B.T.** (1990). Geomagnetic Sudden impulses and storm sudden commencements: A note on terminology. *Eos, Transactions of American Geophysical Union*, 71, 1808. doi:10.1029/90EO00350.
- Kallio, E. I., Pulkkinen, T. I., Koskinen, H. E. J., Viljanen, A., Slavin, J. A., and Ogilvie, K.** (2000). Loading-Unloading Processes in the nightside ionosphere. *Geophysical Research Letters*, 27 (11), 1627–1630.
- Kamide, Y., Richmond, A. D., and Matsushita, S.** (1981). Estimation of ionospheric electric fields, ionospheric currents, and field-aligned currents from ground magnetic records. *Journal of Geophysical Research: Space Physics*, 86(A2), 801-813.
- Kamide, Y., Ahn, B. H., Akasofu, S. I., Baumjohann, W., Friis-Christensen, E., Kroehl, H. W., ..., and Walker, J. K.** (1982). Global distribution of ionospheric and field-aligned currents during substorms as determined from six IMS meridian chains of magnetometers: Initial results. *Journal of Geophysical Research: Space Physics*, 87 (A10), 8228-8240.
- Kappenman, J.** (2010). *Geomagnetic storms and their impacts on the US power grid*. Metatech.
- Kappenman, J.G.** (2003). Storm sudden commencement events and the associated geomagnetically induced current risks to ground-based systems at low-latitude and midlatitude locations. *Space Weather*, 1 (3). doi:10.1029/2003SW000009.

- Kappenman, J.G.** (2006). Great geomagnetic storms and extreme impulsive geomagnetic field disturbance events – An analysis of observational evidence including the great storm of May 1921. *Advances in Space Research*, 38 (2), 188–199. doi:10.1016/j.asr.2005.08.055.
- Kataoka, R., and Pulkkinen, A.** (2008). Geomagnetically induced currents during intense storms driven by coronal mass ejections and corotating interacting regions. *Journal of Geophysical Research: Space Physics* 113, 1–8. doi:10.1029/2007JA012487.
- Kataoka, R.** (2013). Probability of occurrence of extreme magnetic storms, *Space Weather*, 11 (5), 214–218, doi:10.1002/swe.20044, 2013.
- Kauristie, K., Pulkkinen, T. I., Pellinen, R. J., and Opgenoorth, H. J.** (1997). What can we tell about global auroral-electrojet activity from a single meridional magnetometer chain?, *Annales Geophysicae*, 14 (11), pp. 1177–1185. <https://doi.org/10.1007/s00585-996-1177-1>.
- Kim, K. H., Moon, Y. J., Cho, K. S., Kim, H. D., and Park, J. Y.** (2006). Atmospheric drag effects on the KOMPSAT-1 satellite during geomagnetic superstorms. *Earth, Planets and Space*, 58 (12), 25–28. <https://doi.org/10.1186/BF03351968>.
- Knipp, D. J., Welliver, T., McHarg, M. G., Chun, F. K., Tobiska, W. K., and Evans, D.** (2005). Climatology of extreme upper atmospheric heating events. *Advances in Space Research*, 36 (12), 2506–2510. <http://doi.org/10.1016/j.asr.2004.02.019>.
- Knipp, D., Kilcommons, L., Hunt, L., Mlynczak, M., Pilipenko, V., Bowman, B., and Deng, Y.** (2013). Thermospheric damping response to sheath-enhanced geospace storms. *Geophysical Research Letters*, 40 (7), 1263–1267. <https://doi.org/10.1002/grl.50197>.
- Knipp, D. J.** (2016), Advances in Space Weather Ensemble Forecasting, *Space Weather*, 14, 52–53, doi:10.1002/2016SW001366.
- Kono, M.** (2007). *Geomagnetism, Treatise on Geophysics*. Elsevier. ISBN: 9780444527486.
- Korepanov, V.E.** (2011). A New Generation Magnetometer for the One second Standard of the INTERMAGNET System. *Proceedings of international conference “Artificial Intelligence in Studying the Terrestrial Magnetic Field: Russian Segment of the INTERMAGNET”*, Uglich, Russia.
- Kosch, M. J., and Nielsen, E.** (1995). Coherent radar estimates of average high-latitude ionospheric Joule heating. *Journal of Geophysical Research*, 100 (A7), 12201. <http://doi.org/10.1029/95JA00821>.
- Kumar, P., and Fofoula-Georgiou, E.** (1997). Wavelet analysis for geophysical applications. *Reviews of Geophysics*, 35 (4), 385–412. doi:10.1029/97RG00427.

- Kwak, Y. S., Richmond, A. D., Deng, Y., Forbes, J. M., and Kim, K. H.** (2009). Dependence of the high-latitude thermospheric densities on the interplanetary magnetic field. *Journal of Geophysical Research: Space Physics*, 114 (5), 1–7. <https://doi.org/10.1029/2008JA013882>.
- Kwak, Y. S., Kim, K. H., Deng, Y., and Forbes, J. M.** (2011). Response of thermosphere density to changes in interplanetary magnetic field sector polarity. *Journal of Geophysical Research: Space Physics*, 116 (11), A11316. <http://doi.org/10.1029/2011JA016938>.
- Langlois, P., Bolduc, L., and Chouteau, M.C.** (1996). Probability of Occurrence of Geomagnetic Storms Based on a Study of the Distribution of the Electric Field Amplitudes Measured in Abitibi, Quebec, in 1993-94. *Journal of geomagnetism and geoelectricity*, 48 (8), 1033-1041. doi:10.5636/jgg.48.1033.
- Lanzerotti, L. J.** (2007) Space Weather effects on communications, In Bothmer, V., and Daglis, I. A (Eds), *Space Weather- Physics and Effects*, (pp. 247–268), Springer Business and Science Media, Berlin, Heidelberg.
- Lathuillère, C., Menvielle, M., Marchaudon, A., and Bruinsma, S.** (2008). A statistical study of the observed and modeled global thermosphere response to magnetic activity at middle and low latitudes. *Journal of Geophysical Research: Space Physics*, 113 (7), 1–9. <https://doi.org/10.1029/2007JA012991>.
- Lei, J., Thayer, J. P., Lu, G., Burns, A. G., Wang, W., Sutton, E. K., and Emery, B. A.** (2011). Rapid recovery of thermosphere density during the October 2003 geomagnetic storms. *Journal of Geophysical Research: Space Physics*, 116 (3), 1–10. <https://doi.org/10.1029/2010JA016164>.
- Li, W., Knipp, D., Lei, J., and Raeder, J.** (2011). The relation between dayside local Poynting flux enhancement and cusp reconnection. *Journal of Geophysical Research: Space Physics*, 116 (8), 1–16. <http://doi.org/10.1029/2011JA016566>.
- Liou, K., Newell, P. T., Zhang, Y. L., and Paxton, L. J.** (2013). Statistical comparison of isolated and non-isolated auroral substorms. *Journal of Geophysical Research: Space Physics*, 118 (5), 2466–2477. <http://doi.org/10.1002/jgra.50218>.
- Liu, H., H. Lüher, V. Henize, and W. Köhler** (2005), Global distribution of the thermospheric total mass density derived from CHAMP, *Journal of Geophysical Research*, 110, A04301, doi:10.1029/2004JA010741.
- Liu, C.M., Liu, L.G., Pirjola, R., and Wang, Z.Z.** (2009). Calculation of geomagnetically induced currents in mid- to low-latitude power grids based on the plane wave method: A preliminary case study. *Space Weather*, 7 (4), 1–9. doi:10.1029/2008SW000439.

- Liu, C., Li, Y., Pirjola, R.** (2014). Observations and modeling of GIC in the Chinese large-scale high-voltage power networks. *Journal of Space Weather and Spae Climate*, 4, A03. doi:10.1051/swsc/2013057.
- Lopez, R. E., Gonzalez, W. D., Vasyliūnas, V., Richardson, I. G., Cid, C., Echer, E., ... , and Brandt, P. C.** (2015). Decrease in SYM-H during a storm main phase without evidence of a ring current injection. *Journal of Atmospheric and Solar-Terrestrial Physics*, 134, 118-129. doi:10.1016/j.jastp.2015.09.016
- Lu, G., Richmond, A. D., Emery, B. A., and Roble, R. G.** (1995). Magnetosphere-ionosphere-thermosphere coupling: Effect of neutral winds on energy transfer and field aligned current. *Journal of Geophysical Research*, 100 (A10), 19643–19659.
- Lu, G., Baker, D. N., McPherron, R. L., Farrugia, C. J., Lummerzheim, D., Ruohoniemi, J. M., ... , and Li, X.** (1998). Global energy deposition during the January 1997 magnetic cloud event. *Journal of Geophysical Research: Space Physics*, 103 (A6), 11685–11694. <http://doi.org/10.1029/98JA00897>.
- Lühr, H., Rother, M., Köhler, W., Ritter, P., and Grunwaldt, L.** (2004). Thermospheric up-welling in the cusp region: Evidence from CHAMP observations. *Geophysical Research Letters*, 31 (6). <https://doi.org/10.1029/2003GL019314>.
- Marshall, R.A., Dalzell, M., Waters, C.L., Goldthorpe, P., and Smith, E.A.** (2012). Geomagnetically induced currents in the New Zealand power network. *Space Weather*, 10 (8). doi:10.1029/2012SW000806.
- Matandirotya, E., Cilliers, P.J., Van Zyl, R.R.** (2015). Modeling geomagnetically induced currents in the South African power transmission network using the finite element method. *Space Weather*, 13 (3), 185–195. doi:10.1002/2014SW001135.
- McGranaghan, R., Knipp, D. J., McPherron, R. L., and Hunt, L. A.** (2014). Impact of equinoctial high-speed stream structures on thermospheric responses. *Space Weather*, 12 (4), 277–297. <https://doi.org/10.1002/2014SW001045>
- McHarg, M., Chun, F., Knipp, D., Lu, G., Emery, B., and Ridley, A.** (2005). High-latitude Joule heating response to IMF inputs. *Journal of Geophysical Research: Space Physics*, 110 (A8). <http://doi.org/10.1029/2004JA010949>
- McPherron, R.L.** (1991). Physical Processes Producing Magnetospheric Substorms and Magnetic Storms, in: Jacobs, J. (Ed.), *Geomagnetism*. London Academic Press, pp. 593–739.
- Mehta, P. M., Walker, A. C., Sutton, E. K., and Godinez, H. C.** (2017). New density estimates derived using accelerometers on board the CHAMP and

GRACE satellites. *Space Weather*, 15 (4), 558–576.
<https://doi.org/10.1002/2016SW001562>

- Mendes, O., Domingues, M.O., and Trivedi, N.B.** (2010). GIC-occurrence analysis: a case study. In *Proceedings of the 9th Brazilian Conference on Dynamics Control and Their Applications. Serra Negra, SP* (pp. 850-855).
- Merkin, V. G. and Lyon, J. G.** (2010). Effects of the low-latitude ionospheric boundary condition on the global magnetosphere, *Journal of Geophysical Research: Space Physics*, 115 (10), 1–15, doi:10.1029/2010JA015461.
- Millward, G. H., Müller-Wodarg, I. C. F., Aylward, A. D., Fuller-Rowell, T. J., Richmond, A. D., and Moffett, R. J.** (2001). An investigation into the influence of tidal forcing on F region equatorial vertical ion drift using a global ionosphere-thermosphere model with coupled electrodynamics. *Journal of Geophysical Research*, 106 (A11), 24733. <https://doi.org/10.1029/2000JA000342>.
- Moore, T. E., Brenneman, K. S., Chappell, C. R., Clemmons, J. H., Collinson, G. A., Cully, C., ..., and Kistler, L. M.** (2016). Future Atmosphere-Ionosphere-Magnetosphere Coupling Study Requirements. *Magnetosphere-Ionosphere Coupling in the Solar System*, 355-376.
- Murray, S. A.** (2018). The importance of ensemble techniques for operational Space Weather forecasting. *Space Weather*, 16 (7), 777-783. <https://doi.org/10.1029/2018SW001861>
- Naidu, G. D.** (2012). Magnetotellurics: Basic Theoretical Concepts. In *Deep Crustal Structure of the Son-Narmada-Tapti Lineament, Central India* (pp. 13-35). Springer, Berlin, Heidelberg.. doi:10.1007/978-3-642-28442-7.
- Newell, P. T., Sotirelis, T., and Wing, S.** (2009). Diffuse, monoenergetic, and broadband aurora: The global precipitation budget. *Journal of Geophysical Research: Space Physics*, 114 (A9). <https://doi.org/10.1029/2009JA014326>.
- Newell, P. T., Sotirelis, T., and Wing, S.** (2010). Seasonal variations in diffuse, monoenergetic, and broadband aurora. *Journal of Geophysical Research: Space Physics*, 115 (A3). <https://doi.org/10.1029/2009JA014805>
- Newell, P. T., Liou, K., Zhang, Y., Sotirelis, T., Paxton, L. J., and Mitchell, E. J.** (2014). OVATION Prime-2013: Extension of auroral precipitation model to higher disturbance levels. *Space Weather*, 12 (6), 368–379. <http://doi.org/10.1002/2014SW001056>.
- Oliveira, D. M., Zesta, E., Schuck, P. W., and Sutton, E. K.** (2017). Thermosphere Global Time Response to Geomagnetic Storms Caused by Coronal Mass Ejections. *Journal of Geophysical Research: Space Physics*, 122 (10), 10,762-10,782. <https://doi.org/10.1002/2017JA024006>.

- Mac-Mahon, R. M., and Gonzalez, W. D.** (1997). Energetics during the main phase of geomagnetic superstorms. *Journal of Geophysical Research*, 102 (A7), 14199. <http://doi.org/10.1029/97JA01151>.
- Olsson, A., Janhunen, P., Karlsson, T., Ivchenko, N., and Blomberg, L. G.** (2004). Statistics of Joule heating in the auroral zone and polar cap using Astrid-2 satellite Poynting flux. *Annales Geophysicae*, 22 (12), 4133–4142. <http://doi.org/10.5194/angeo-22-4133-2004>.
- Østgaard, N.** (2002). Energy analysis of substorms based on remote sensing techniques, solar wind measurements, and geomagnetic indices. *Journal of Geophysical Research*, 107 (A9), . <http://doi.org/10.1029/2001JA002002>.
- Palmroth, M., Janhunen, P., Pulkkinen, T. I., Aksnes, A., Lu, G., Østgaard, N., ..., and Germany, G. A.** (2005). Assessment of ionospheric Joule heating by GUMICS-4 MHD simulation, AMIE, and satellite-based statistics: towards a synthesis. *Annales Geophysicae*, 23 (6), 2051–2068. <http://doi.org/10.5194/angeo-23-2051-2005>.
- Pardini, C., Moe, K., and Anselmo, L.** (2012). Thermospheric density model biases at the 23rd sunspot maximum. *Planetary and Space Science*, 67 (1), 130–146. <https://doi.org/10.1016/j.pss.2012.03.004>
- Parlak, M., Fidan, A., Kızılcık, İ., and Koparan, H.** (2008). Determination of the fertility status of Eceabat-Çanakale agricultural soils. *Journal of Agricultural Sciences (Turkey)*.
- Perreault, P., and Akasofu, S.-I.** (1978). A study of geomagnetic storms. *Geophysical Journal International*, 54 (3), 547–573. <http://doi.org/10.1111/j.1365-246X.1978.tb05494.x>.
- Prölss, G. W.** (2011). Density Perturbations in the Upper Atmosphere Caused by the Dissipation of Solar Wind Energy. *Surveys in Geophysics*, 32 (2), 101–195. <https://doi.org/10.1007/s10712-010-9104-0>.
- Picone, J. M., Hedin, A. E., Drob, D. P., and Aikin, A. C.** (2002). NRLMSISE-00 empirical model of the atmosphere: Statistical comparisons and scientific issues. *Journal of Geophysical Research: Space Physics*, 107 (A12), SIA 15-1-SIA 15-16. <https://doi.org/10.1029/2002JA009430>.
- Pirjola, R.,** (2002). Review on the calculation of surface electric and magnetic fields and of geomagnetically induced currents in ground-based technological systems. *Surveys of Geophysics*, 23, 71–90. doi:10.1023/A:1014816009303.
- Poll, H.E., Weaver, J.T., and Jones, A.G.** (1989). Calculations of voltages for magnetotelluric modelling of a region with near-surface inhomogeneities. *Physics of the earth and planetary interiors*, 53 (3-4), 287-297. doi:10.1016/0031-9201(89)90013-7.

- Pröls, G. W.** (2011). Density Perturbations in the Upper Atmosphere Caused by the Dissipation of Solar Wind Energy. *Surveys in Geophysics*, 32 (2), 101–195. <https://doi.org/10.1007/s10712-010-9104-0>.
- Pulkkinen, A., Lindahl, S., Viljanen, A., and Pirjola, R.** (2005). Geomagnetic storm of 29-31 October 2003: Geomagnetically induced currents and their relation to problems in the Swedish high-voltage power transmission system. *Space Weather*, 3 (8). doi:10.1029/2004SW000123
- Pulkkinen, A., Thomson, A., Clarke, E., and McKay, A.** (2003). April 2000 geomagnetic storm: ionospheric drivers of large geomagnetically induced currents. *Annales Geophysicae*, Vol. 21(3), 709–717. doi:10.5194/angeo-21-709-2003
- Pulkkinen, A.**, (2003): Geomagnetic induction during highly disturbed Space Weather conditions studies of ground effects, Finnish Meteorological Institute. (PhD thesis) Retrieved from <http://ethesis.helsinki.fi/julkaisut/mat/fysik/vk/pulkkinen/> (Accessed 20 December 2017).
- Qian, L., Roble, R. G., Solomon, S. C., and Kane, T. J.** (2006). Calculated and observed climate change in the thermosphere, and a prediction for solar cycle 24. *Geophysical Research Letters*, 33 (23), 1–5. <https://doi.org/10.1029/2006GL027185>.
- Qian, L., and Solomon, S. C.** (2012). Thermospheric Density: An Overview of Temporal and Spatial Variations. *Space Science Reviews*, 168 (1–4), 147–173. <https://doi.org/10.1007/s11214-011-9810-z>
- Qian, L., Burns, A. G., Emery, B. A., Foster, B., Lu, G., Maute, A., ..., and Wang, W.** (2014). The NCAR TIE-GCM: A community model of the coupled thermosphere/ionosphere system. *Modeling the ionosphere-thermosphere system*, 201, 73-83.
- Quegan, S., Bailey, G. J., Moffett, R. J., Heelis, R. A., Fuller-Rowell, T. J., Rees, D., & Spiro, R. W.** (1982). A theoretical study of the distribution of ionization in the high-latitude ionosphere and the plasmasphere: First results on the mid-latitude trough and the light-ion trough. *Journal of Atmospheric and Terrestrial Physics*, 44 (7), 619-640.
- Quegan, S.** (1982). Theoretical studies of large-scale features of the Earth's mid- to high-latitude ionosphere, Sheffield Univ. (England). (PhD Thesis) Retrieved from: <http://adsabs.harvard.edu/abs/1982PhDT.....Q> (Accessed 22 December 2017), 1982.
- Rastätter, L., Shim, J. S., Kuznetsova, M. M., Kilcommons, L. M., Knipp, D. J., Codrescu, M., ..., and Wiltberger, M.** (2016). GEM-CEDAR challenge: Poynting flux at DMSP and modeled Joule heat. *Space Weather*, 14 (2), 113-135. <http://doi.org/10.1002/2015SW001238>.
- Rastogi, R.G., Rao, D.R.K., Alex, S., Pathan, B.M., and Sastry, T.S.** (1997). An intense SFE and SSC event in geomagnetic H, Y and Z fields at the

Indian chain of observatories. *Annales Geophysicae*, 15 (10), 1301–1308. doi:10.1007/s00585-997-1301-x.

- Reitz, G. and Facius, R. (2007):** Space Weather impacts on space radiation protection, In Bothmer, V., and Daglis, I. A (Eds), *Space Weather-Physics and Effects*, (pp. 289–352), Springer Business and Science Media, Berlin, Heidelberg.
- Richmond, A. D., and Kamide, Y. (1988).** Mapping electrodynamic features of the high-latitude ionosphere from localized observations: Technique. *Journal of Geophysical Research*, 93 (A6), 5741. <http://doi.org/10.1029/JA093iA06p05741>
- Richmond, A. D., Kamide, Y., Akasofu, S.-I., Alcaydé, D., Blanc, M., de la Beaujardière, O., ..., and Zaitzev, A. N (1990).** Global measures of ionospheric electrodynamic activity inferred from combined incoherent scatter radar and ground magnetometer observations. *Journal of Geophysical Research*, 95 (A2), 1061. <http://doi.org/10.1029/JA095iA02p01061>
- Richmond, A. D. (1992).** Assimilative mapping of ionospheric electrodynamics. *Advances in Space Research*, 12 (6), 59-68.
- Richmond, A. D., Ridley, E. C., and Roble, R. G. (1992).** A thermosphere/ionosphere general circulation model with coupled electrodynamics. *Geophysical Research Letters*, 19 (6), 601-604.
- Richmond, A. D. (2010).** On the ionospheric application of Poynting's theorem. *Journal of Geophysical Research: Space Physics*, 115 (10), 1–9. <http://doi.org/10.1029/2010JA015768>.
- Ridley, A. J. (2003)** Ionospheric control of the magnetospheric configuration: Thermospheric neutral winds, *Journal of Geophysical Research*, 108 (A8), 1328, doi:10.1029/2002JA009464.
- Ridley, A. J., Gombosi, T. I., and Dezeew, D. L. (2004).** Ionospheric control of the magnetosphere: conductance. *Annales Geophysicae*, 22 (2), 567–584. <http://doi.org/10.5194/angeo-22-567-2004>.
- Ridley, A. J., Deng, Y., and Tóth, G. (2006).** The global ionosphere–thermosphere model. *Journal of Atmospheric and Solar-Terrestrial Physics*, 68 (8), 839–864. <https://doi.org/10.1016/j.jastp.2006.01.008>
- Robinson, R. M., Vondrak, R. R., Miller, K., Dabbs, T., and Hardy, D. (1987).** On calculating ionospheric conductances from the flux and energy of precipitating electrons. *Journal of Geophysical Research*, 92 (A3), 2565. <https://doi.org/10.1029/JA092iA03p02565>
- Roble, R. G., Dickinson, R. E. and Ridley, E. C. (1982):** Global circulation and temperature structure of thermosphere with high-latitude plasma convection, *Journal of Geophysical Research*, 87 (A3), 1599, doi:10.1029/JA087iA03p01599.

- Rodger, A. S., Wells, G. D., Moffett, R. J., and Bailey, G. J.** (2001). The variability of Joule heating and its effects on the ionosphere and thermosphere, *Annales Geophysicae*, *19* (7), 773–781. <http://doi.org/10.5194/angeo-19-773-2001>.
- Roe, P.** (1981) . Approximate Riemann solvers, parameter vectors, and difference schemes, *Journal of Computational Physics*, *43* (2), 357–372, doi:10.1016/0021-9991(81)90128-5, 1981.
- Ruohoniemi, J. M., and Greenwald, R. A.** (1996). Statistical patterns of high-latitude convection obtained from Goose Bay HF radar observations. *Journal of Geophysical Research: Space Physics*, *101* (A10), 21743–21763. <http://doi.org/10.1029/96JA01584>.
- Ruohoniemi, J. M., and Baker, K. B.** (1998). Large-scale imaging of high-latitude convection with Super Dual Auroral Radar Network HF radar observations. *Journal of Geophysical Research: Space Physics*, *103* (A9), 20797–20811. <http://doi.org/10.1029/98JA01288>.
- Schrijver, C. J., Kauristie, K., Aylward, A. D., Denardini, C. M., Gibson, S. E., Glover, A., ..., and Vilmer, N.** (2015). Understanding Space Weather to shield society: A global road map for 2015–2025 commissioned by COSPAR and ILWS, *Advances in Space Research*, *55* (12), 2745–2807, doi:10.1016/j.asr.2015.03.023, 2015.
- Schulte in den Bäumen, H., Moran, D., Lenzen, M., Cairns, I., and Steenge, A.** (2014): How severe Space Weather can disrupt global supply chains, *Natural Hazards Earth System Science*, *14* (10), 2749–2759, doi:10.5194/nhess-14-2749-2014, 2014.
- Sheng, C., Deng, Y., Yue, X., and Huang, Y.** (2014). Height-integrated Pedersen conductivity in both E and F regions from COSMIC observations. *Journal of Atmospheric and Solar-Terrestrial Physics*, *115*, 79–86. <http://doi.org/10.1016/j.jastp.2013.12.013>.
- Shepherd, S. G., and Ruohoniemi, J. M.** (2000). Electrostatic potential patterns in the high-latitude ionosphere constrained by SuperDARN measurements. *Journal of Geophysical Research: Space Physics*, *105* (A10), 23005–23014. <http://doi.org/10.1029/2000JA000171>.
- Shepherd, S. G., Greenwald, R. A., and Ruohoniemi, J. M.** (2002). Cross polar cap potentials measured with Super Dual Auroral Radar Network during quasi-steady solar wind and interplanetary magnetic field conditions. *Journal of Geophysical Research: Space Physics*, *107* (A7).
- Shim, J. S., Kuznetsova, M., Rastätter, L., Hesse, M., Bilitza, D., Butala, M., ... Rideout, B.** (2011), CEDAR Electrodynamics Thermosphere Ionosphere (ETI) Challenge for systematic assessment of ionosphere/thermosphere models: NmF2, hmF2, and vertical drift using ground-based observations, *Space Weather*, *9*, S12003, doi:10.1029/2011SW000727.

- Shim, J. S., Kuznetsova, M., Rastätter, L., Bilitza, D., Butala, M., Codrescu, M., ..., Sutton, E.** (2012). CEDAR Electrodynamics Thermosphere Ionosphere (ETI) Challenge for systematic assessment of ionosphere/thermosphere models: Electron density, neutral density, NmF2, and hmF2 using space-based observations. *Space Weather*, 10 (10). <https://doi.org/10.1029/2012SW000851>
- Shim, J. S., Kuznetsova, M., Rastätter, L., Bilitza, D., Butala, M., Codrescu, M., ..., Manucci, A.J.** (2014). Systematic Evaluation of Ionosphere/Thermosphere (IT) Models : CEDAR electrodynamics thermosphere ionosphere (ETI) challenge (2009–2010). *Modeling the Ionosphere-Thermosphere System, Geophysical Monograph Series*, 201, 145-160.. <https://doi.org/10.1002/9781118704417.ch13>
- Shim, J. S., L. Rastaetter, K. M. Kuznetsova, E. C. Kalafatoglu, and Y. Zheng** (2015). Assessment of the predictive capability of IT models at the Community Coordinated Modeling Center. In *Ionospheric Effect Symposium*, Alexandria VA.
- Solomon, S. C., Qian, L., Didkovsky, L. V., Viereck, R. A., and Woods, T. N.** (2011). Causes of low thermospheric density during the 2007-2009 solar minimum. *Journal of Geophysical Research: Space Physics*, 116 (7), 1–14. <https://doi.org/10.1029/2011JA016508>.
- Stankovic, R.S., and Falkowski, B.J.** (2003). The Haar wavelet transform: its status and achievements. *Computers and Electrical Engineering*, 29, 25–44. doi:10.1016/S0045-7906(01)00011-8.
- Stauning, P.** (2013). The Polar Cap index: A critical review of methods and a new approach. *Journal of Geophysical Research: Space Physics*, 118 (8), 5021–5038. <http://doi.org/10.1002/jgra.50462>.
- Storz, M. F., Bowman, B. R., Branson, M. J. I., Casali, S. J., and Tobiska, W. K.** (2005). High accuracy satellite drag model (HASDSM). *Advances in Space Research*, 36 (12), 2497–2505.
- Suresh, P.** (2016). The thermospheric response to geomagnetic storms, (PhD thesis) Utah State University.
- Sutcliffe, P.R.** (2000). The development of a regional geomagnetic daily variation model using neural networks. *Annales Geophysicae*, 18, 120–128. doi:10.1007/s00585-000-0120-0.
- Sutton, E. K., Forbes, J. M., and Nerem, R. S.** (2005). Global thermospheric neutral density and wind response to the severe 2003 geomagnetic storms from CHAMP accelerometer data. *Journal of Geophysical Research: Space Physics*, 110 (A9), 1–10. <https://doi.org/10.1029/2004JA010985>
- Sutton, E. K., Forbes, J. M., Nerem, R. S., and Woods, T. N.** (2006). Neutral density response to the solar flares of October and November, 2003. *Geophysical Research Letters*, 33 (22), 1–5. <https://doi.org/10.1029/2006GL027737>

- Sutton, E. K., Nerem, R. S., and Forbes, J. M.** (2007). Density and Winds in the Thermosphere Deduced from Accelerometer Data, *Journal of Spacecraft and Rockets*, 44 (6), 1210–1219, doi:10.2514/1.28641.
- Sutton, E. K.** (2009), Normalized force coefficients for satellites with elongated shapes, *Journal of Spacecraft and Rockets*, 46 (1), doi:10.2514/1.40940.
- Sutton, E. K.** (2018). A New Method of Physics-Based Data Assimilation for the Quiet and Disturbed Thermosphere. *Space Weather*, 16 (6), 736–753. <https://doi.org/10.1002/2017SW001785>.
- Şeker, M., Sakaldaş, M., Akçal, A., Gündoğdu, M. A., Dardeniz, A., and Özcan, H.** (2009). Determination of nutritional status of dwarf apple orchards in Çanakkale. *TABAD, Tarım Bilimleri Arastırma Dergisi*, 2 (2), 31-36.
- Tanskanen, E. I.** (2009). A comprehensive high-throughput analysis of substorms observed by IMAGE magnetometer network: Years 1993-2003 examined. *Journal of Geophysical Research: Space Physics*, 114 (5), 1–11. <https://doi.org/10.1029/2008JA013682>.
- Tanskanen, E., Koskinen, H. E. J., Pulkkinen, T. I., Slavin, J. A., and Ogilvie, K.** (2002a). Dissipation to the joule heating: Isolated and stormtime substorms. *Advances in Space Research*, 30 (10), 2305–2311. [http://doi.org/10.1016/S0273-1177\(02\)80254-X](http://doi.org/10.1016/S0273-1177(02)80254-X).
- Tanskanen, E., Pulkkinen, T. I., Koskinen, H. E. J., and Slavin, J. A.** (2002b). Substorm energy budget during low and high solar activity: 1997 and 1999 compared. *Journal of Geophysical Research: Space Physics*, 107 (A6), 1–11. <http://doi.org/10.1029/2001JA900153>.
- Thayer, J. P., Vickrey, J. F., Heelis, R. A., and Gary, J. B.** (1995). Interpretation and modeling of the high latitude electromagnetic energy flux. *Journal of Geophysical Research*, 100 (A10), 19715–19728.
- Thayer, J. P.** (1998). Radar measurements of the electromagnetic energy rates associated with the Dynamic Ionospheric Load/Generator. *Geophysical Research Letters*, 25 (4), 469. <http://doi.org/10.1029/97GL03660>.
- Thayer, J. P., Lei, J., Forbes, J. M., Sutton, E. K., and Nerem, R. S.** (2008). Thermospheric density oscillations due to periodic solar wind high speed streams. *Journal of Geophysical Research: Space Physics*, 113 (6), A06307. <https://doi.org/10.1029/2008JA013190>.
- Torta, J.M., Serrano, L., Regué, J.R., Sánchez, A.M., and Roldán, E.** (2012). Geomagnetically induced currents in a power grid of northeastern Spain. *Space Weather*, 10 (6). doi:10.1029/2012SW000793.
- Torta, J., Marsal, S., and Quintana, M.** (2014). Assessing the hazard from geomagnetically induced currents to the entire high-voltage power network in Spain. *Earth, Planets and Space*, 66, 87. doi:10.1186/1880-5981-66-87.

- Tóth, G., Sokolov, I. V., Gombosi, T. I., Chesney, D. R., Clauer, C. R., De Zeeuw, D. L., ..., and Kóta, J.** (2005). Space Weather Modeling Framework: A new tool for the space science community. *Journal of Geophysical Research: Space Physics*, 110 (A12).
- Trivedi, N. B., Vitorello, Í., Kabata, W., Dutra, S. L. G., Padilha, A. L., Mauricio, S. B., ..., and Viljanen, A.** (2007). Geomagnetically induced currents in an electric power transmission system at low latitudes in Brazil: A case study, *Space Weather*, 5, 1–10, doi:10.1029/2006SW000282.
- Tsunomura, S.** (1998). Characteristics of geomagnetic sudden commencement observed in middle and low latitudes. *Earth, Planets and Space*, 50, 755–772. doi:10.1186/BF03352168.
- Turnbull, K.L., Wild, J.A., Honary, F., Thomson, A.W.P., and McKay, A.J.,** (2009). Characteristics of variations in the ground magnetic field during substorms at mid latitudes. *Annales Geophysicae*, 27, 3421–3428. doi:10.5194/angeo-27-3421-2009.
- Turner, N. E., Cramer, W. D., Earles, S. K., and Emery, B. A.** (2009). Geoefficiency and energy partitioning in CIR-driven and CME-driven storms. *Journal of Atmospheric and Solar-Terrestrial Physics*, 71 (10–11), 1023–1031. <http://doi.org/10.1016/j.jastp.2009.02.005>.
- Url-1** <https://ned.ipac.caltech.edu/level5/March03/Vallee2/Figures/figure5.jpg>, date of access 20.12.2017
- Url-2** <http://vt.superdarn.org/tiki-index.php?page=Radar+Overview>, date of access 20.07.2018
- Vasyliūnas, V. M., and Song, P.** (2005). Meaning of ionospheric Joule heating. *Journal of Geophysical Research: Space Physics*, 110 (1), 1–8. <http://doi.org/10.1029/2004JA010615>.
- Viljanen, A., Pirjola, R.** (1994). Geomagnetically induced currents in the Finnish high-voltage power system. *Surveys in Geophysics*, 15, 383–408. doi:10.1007/BF00665999.
- Viljanen, A.** (1997). The Relation Between Geomagnetic Variations and Their Time Derivatives and Implications for Estimation of Induction Risks. *Geophysical Research Letters*, 24, 631–634. doi:10.1029/97GL00538
- Viljanen, A., Nevanlinna, H., Pajunpää, K., and Pulkkinen, A.,** (2001). Time derivative of the horizontal geomagnetic field as an activity indicator. *Annales Geophysicae*, 19, 1107–1118. doi:10.5194/angeo-19-1107-2001.
- Viljanen, A., Pulkkinen, A., Amm, O., Pirjola, R., and Korja, T.** (2004). BEAR Working Group, 2004. Fast computation of the geoelectric field using the method of elementary current systems and planar Earth models. *Annales Geophysicae*, 22, 101–113. doi:10.5194/angeo-22-101-2004.

- Viljanen, A., Tanskanen, E.I., and Pulkkinen, A.** (2006). Relation between substorm characteristics and rapid temporal variations of the ground magnetic field. *Annales Geophysicae*, 24, 725–733. doi:10.5194/angeo-24-725-2006.
- Viljanen, A., Tanskanen, E.** (2011). Climatology of rapid geomagnetic variations at high latitudes over two solar cycles. *Annales Geophysicae*, 29, 1783–1792. doi:10.5194/angeo-29-1783-2011
- Wang, W., Wiltberger, M., Burns, a. G., Solomon, S. C., Killeen, T. L., Maruyama, N. and Lyon, J. G.** (2004). Initial results from the coupled magnetosphere-ionosphere-thermosphere model: Thermosphere-ionosphere responses, *Journal of Atmospheric and Solar-Terrestrial Physics*, 66, 1425–1441. doi:10.1016/j.jastp.2004.04.008, 2004.
- Wang, H., Ridley, A. J., and Lühr, H.** (2008). Validation of the Space Weather Modeling Framework using observations from CHAMP and DMSP. *Space Weather*, 6 (3), 1–16. <http://doi.org/10.1029/2007SW000355>.
- Wang, C., Zhang, J. J., Tang, B. B., and Fu, S. Y.** (2011). Comparison of equivalent current systems for the substorm event of 8 March 2008 derived from the global PPMLR-MHD model and the KRM algorithm. *Journal of Geophysical Research: Space Physics*, 116 (7), 1–9. <https://doi.org/10.1029/2011JA016497>.
- Watari, S., Kunitake, M., Kitamura, K., Hori, T., Kikuchi, T., Shiokawa, K., ..., and Tsuneta, Y.** (2009). Measurements of geomagnetically induced current in a power grid in Hokkaido, Japan. *Space Weather*, 7 (3). doi:10.1029/2008SW000417.
- Waters, C. L., Anderson, B. J., Greenwald, R. A., Barnes, R. J., and Ruohoniemi, J. M.** (2004). High-latitude poynting flux from combined Iridium and SuperDARN data. *Annales Geophysicae*, 22 (8), 2861–2875. <http://doi.org/10.5194/angeo-22-2861-2004>.
- Wei, L.H., Homeier, N., and Gannon, J.L.** (2013). Surface electric fields for North America during historical geomagnetic storms. *Space Weather*, 11, 451–462. doi:10.1002/swe.20073.
- Weimer, D. R.** (2001). An improved model of ionospheric electric potentials including substorm perturbations and application to the Geospace Environment Modeling November 24, 1996, event. *Journal of Geophysical Research: Space Physics*, 106 (A1), 407-416.
- Weimer, D. R.** (2005). Improved ionospheric electrodynamic models and application to calculating Joule heating rates. *Journal of Geophysical Research*, 110 (A5), A05306. <http://doi.org/10.1029/2004JA010884>.
- Wik, M., Viljanen, A., Pirjola, R., Pulkkinen, A., Wintoft, P., and Lundstedt, H.** (2008). Calculation of geomagnetically induced currents in the 400 kV power grid in southern Sweden. *Space Weather*, 6 (7). doi:10.1029/2007SW000343.

- Willmott, C. J., and Matsuura, K.** (2005). Advantages of the mean absolute error (MAE) over the root mean square error (RMSE) in assessing average model performance. *Climate Research*, 30, 79–82.
- Wilson, G. R., Weimer, D. R., Wise, J. O., and Marcos, F. A.** (2006). Response of the thermosphere to Joule heating and particle precipitation. *Journal of Geophysical Research: Space Physics*, 111 (10), 1–9. <http://doi.org/10.1029/2005JA011274>.
- Xi, S., Lotko, W., Zhang, B., Brambles, O. J., Lyon, J. G., Merkin, V. G., and Wiltberger, M.** (2015). Poynting flux-conserving low-altitude boundary conditions for global magnetospheric models. *Journal of Geophysical Research: Space Physics*, 120 (1), 384–400. <http://doi.org/10.1002/2014JA020470>.
- Xu, J., Wang, W., Lei, J., Sutton, E. K., and Chen, G.** (2011). The effect of periodic variations of thermospheric density on CHAMP and GRACE orbits. *Journal of Geophysical Research: Space Physics*, 116 (2), A02315. <https://doi.org/10.1029/2010JA015995>.
- Yiğit, E., and Ridley, A. J.** (2011). Effects of high-latitude thermosphere heating at various scale sizes simulated by a nonhydrostatic global thermosphere–ionosphere model. *Journal of Atmospheric and Solar-Terrestrial Physics*, 73 (5–6), 592–600. <http://doi.org/10.1016/j.jastp.2010.12.003>.
- Zesta, E., and Huang, C. Y.** (2016). Satellite orbital drag. In G. V. Khazanov (Ed.), *Space Weather fundamentals* (pp. 329–351). Boca Raton, FL: CRC Press.
- Zhang, J.J., Wang, C., Sun, T.R., Liu, C.M., and Wang, K.R.** (2015). GIC due to storm sudden commencement in low-latitude high-voltage power network in China: Observation and simulation. *Space Weather*, 13, 643–655. doi:10.1002/2015SW001263.
- Zhang, X. X., Wang, C., Chen, T., Wang, Y. L., Tan, A., Wu, T. S., ... Wang, W.** (2005). Global patterns of Joule heating in the high-latitude ionosphere. *Journal of Geophysical Research: Space Physics*, 110 (A12), 1–22. <http://doi.org/10.1029/2005JA011222>.
- Zhu, X., Talaat, E. R., Baker, J. B. H., and Yee, J.-H.** (2005). A self-consistent derivation of ion drag and Joule heating for atmospheric dynamics in the thermosphere. *Annales Geophysicae*, 23, 3313–3322. <http://doi.org/10.5194/angeo-23-3313-2005>.



APPENDICES

APPENDIX A : Baseline shifts for GEM-CEDAR events.

APPENDIX B : Temporal shifts for GEM-CEDAR events

APPENDIX C : Variations in E_y and B_x , E and dH/dt and E_x and E_y for the selected events



APPENDIX A : Baseline shifts for GEM-CEDAR events.

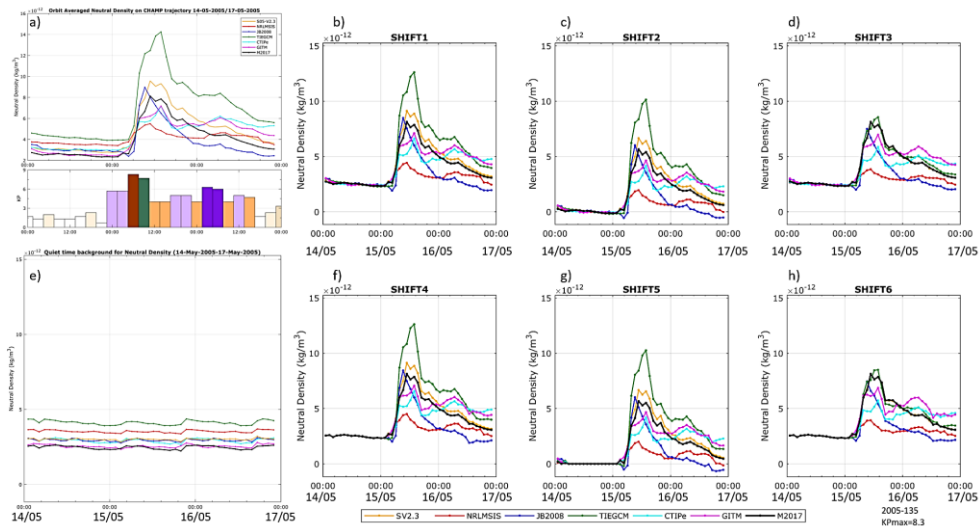


Figure A.1 : Baseline shifts: 2005-135.

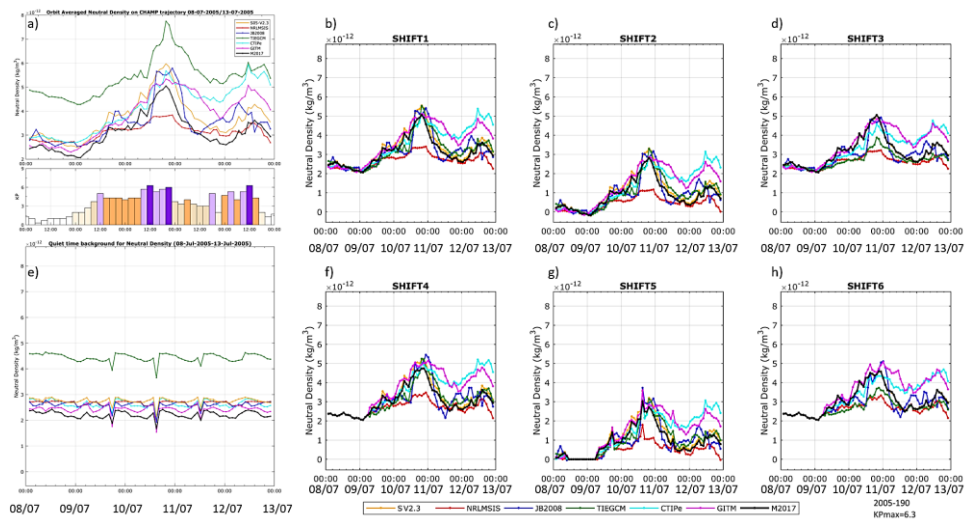


Figure A.2 : Baseline shifts: 2005-190.

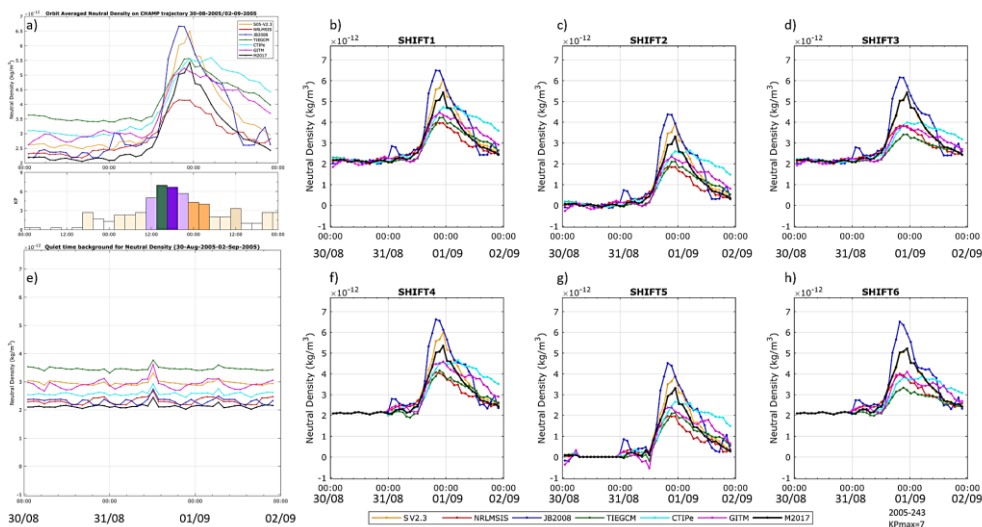


Figure A.3 : Baseline shifts: 2005-243.

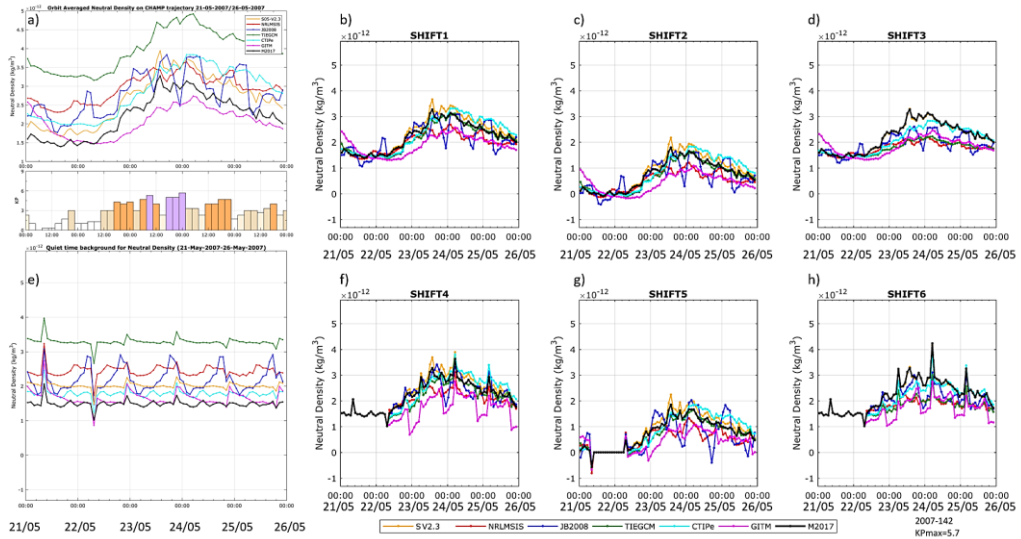


Figure A.4 : Baseline shifts: 2007-142.

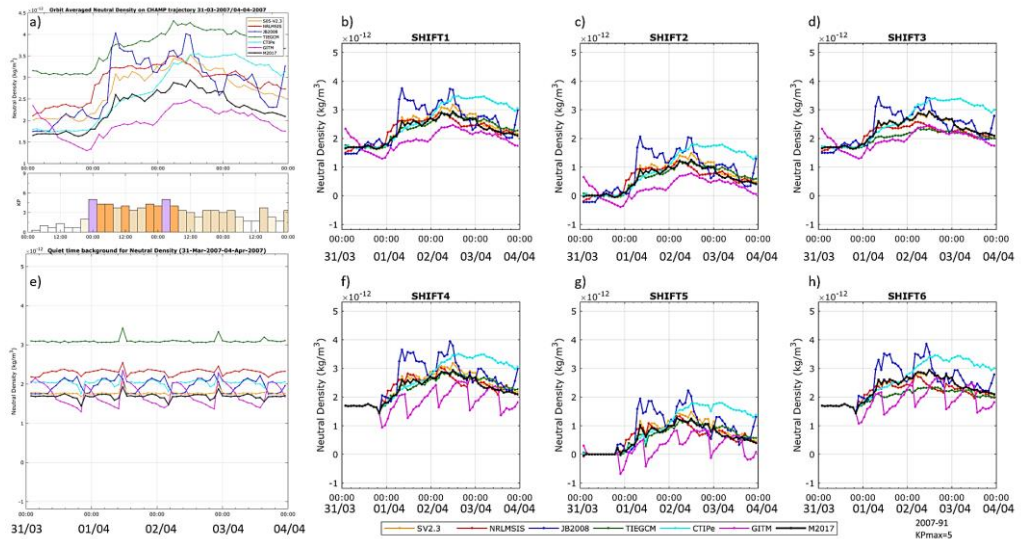


Figure A.5 : Baseline shifts: 2007-91.

APPENDIX B : Temporal shifts for GEM-CEDAR events

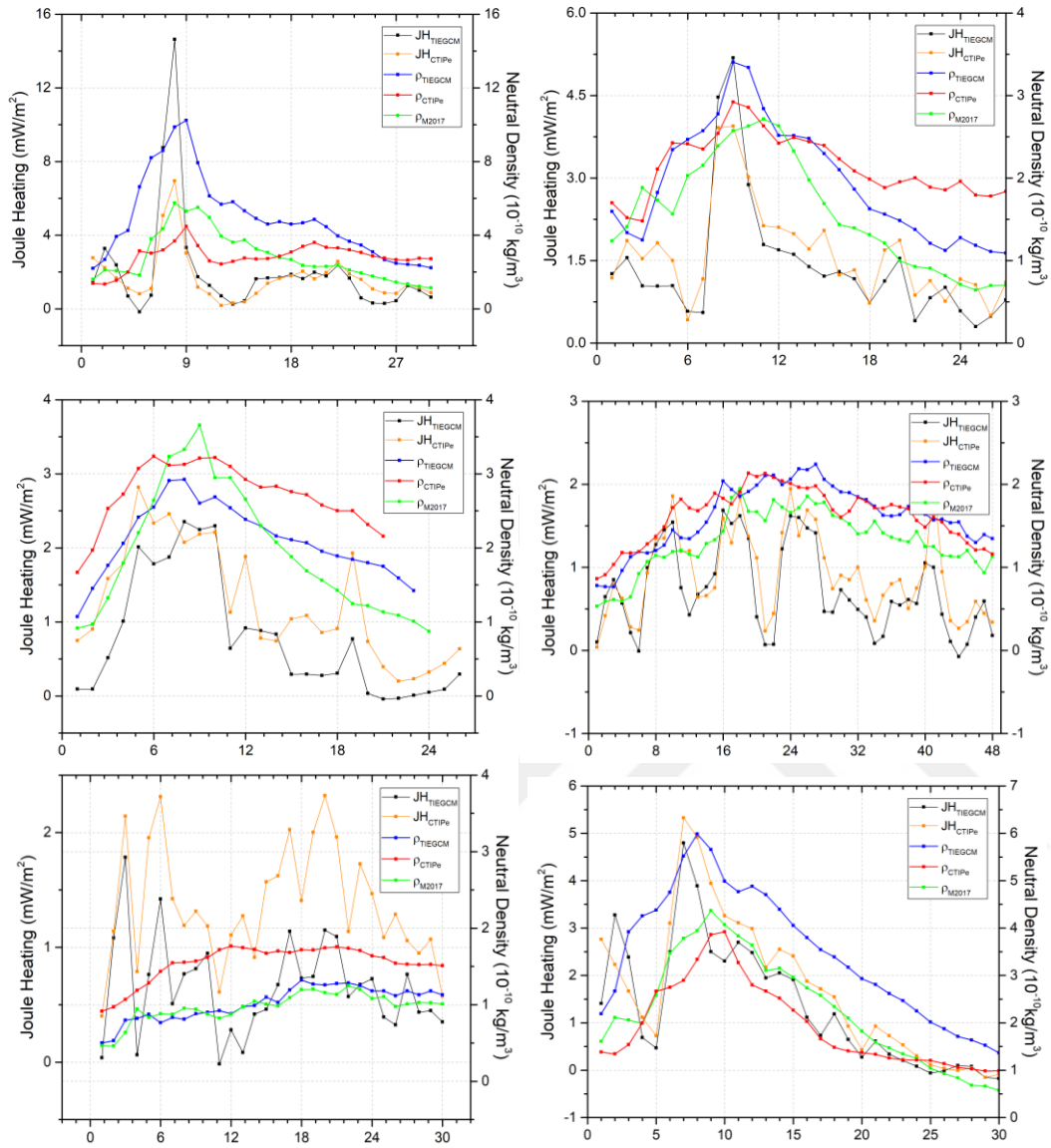


Figure B.1 : Temporal shifts for the GEM-CEDAR events. From left to right; Top: 2005-135 and 2005-190; Middle: 2005-243 and 2007-142 Bottom: 2007-91 and 2006-348.

APPENDIX C : Variations in E_y and B_x , E and dH/dt and E_x and E_y for the selected events

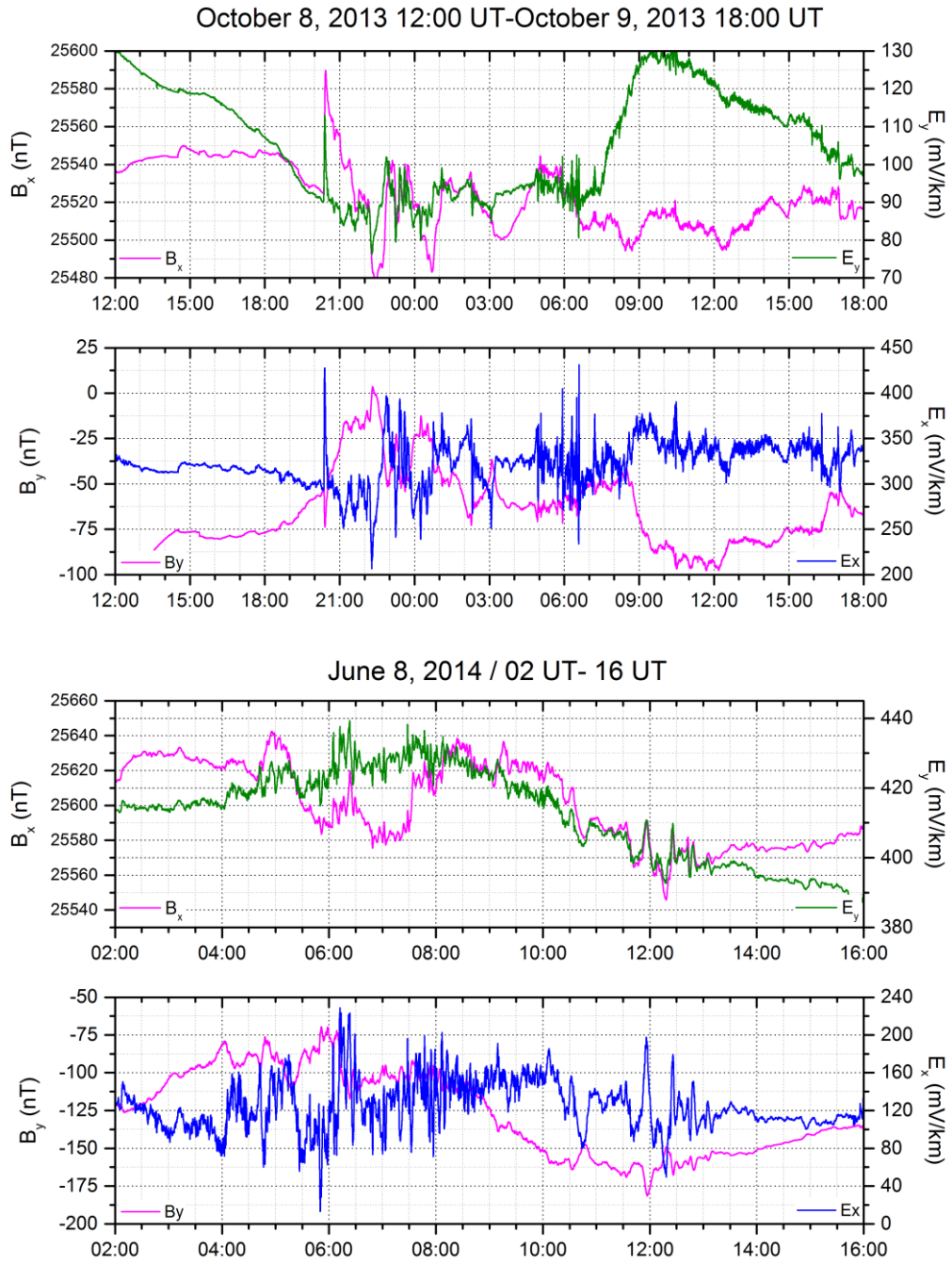


Figure C.1 : B_x , E_y and B_y , E_x . Top: October 8, 2013, bottom: June 8, 2014.

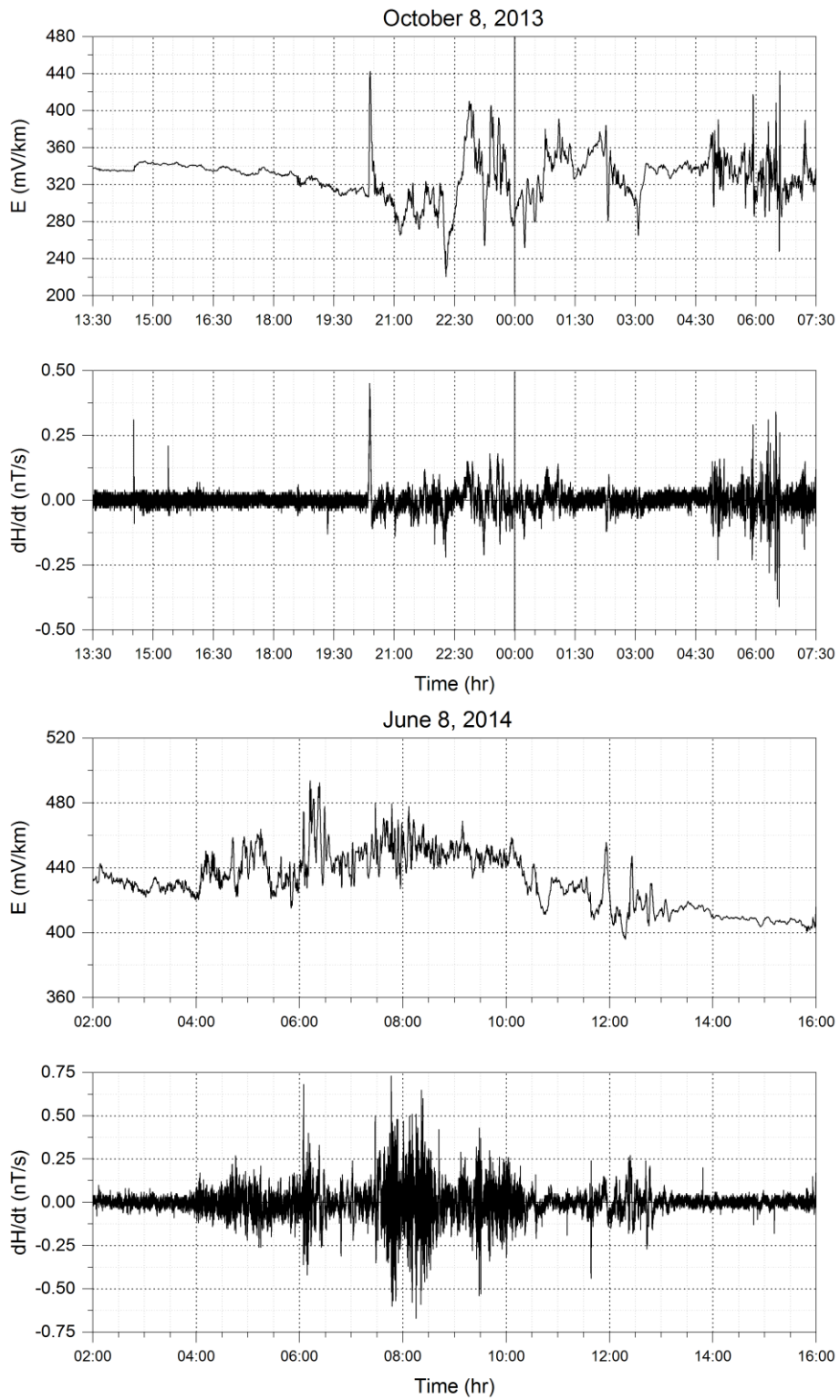


Figure C.2 : E and dH/dt. Top: October 8, 2013, bottom: June 8, 2014.

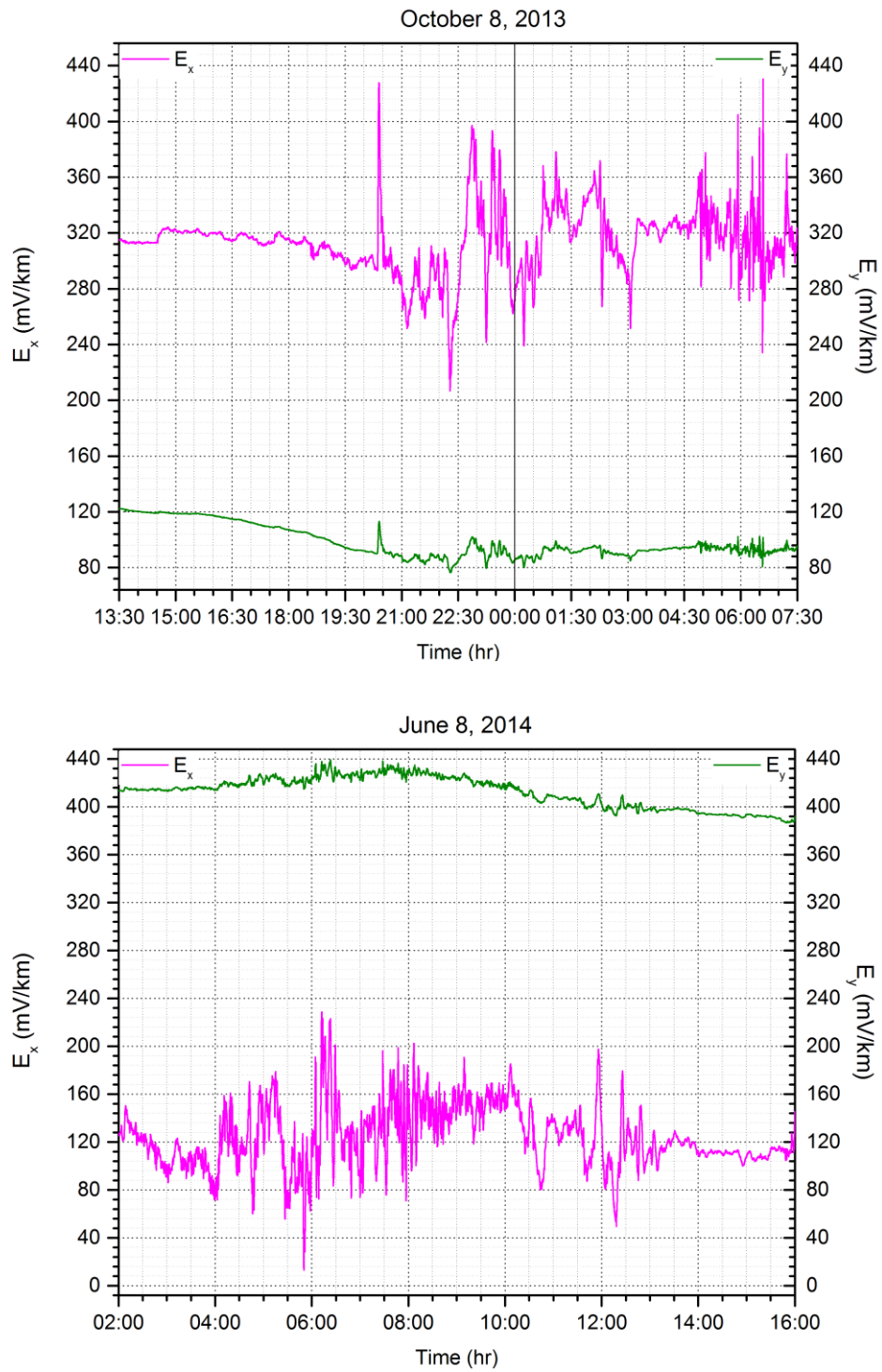


Figure C.3 : E_x and E_y . Top: October 8, 2013, bottom: June 8, 2014.





CURRICULUM VITAE

Name Surname : Emine Ceren EYİGÜLER
Place and Date of Birth : İstanbul, 19.07.1985
E-Mail : ceren.kalafatoglu@itu.edu.tr

EDUCATION:

- **B.Sc.** : 2006, İstanbul Technical University, Faculty of Aeronautics and Astronautics, Meteorological Engineering Department
2007, İstanbul Technical University, Faculty of Science and Letters, Physics Engineering Department
- **M.Sc.** : 2007-2008, University of Helsinki, Physics Department
2010, İstanbul Technical University, Graduate School of Science and Technology, Atmospheric Sciences Programme

PROFESSIONAL EXPERIENCE AND REWARDS:

- April 2017-Present: Specialist at ITU Upper Atmosphere and *Space Weather* Laboratory
- Jan 2009-Feb 2016: Research Assistant at ITU Meteorological Engineering Department
- TUBITAK Scholarship for Doctoral Research
- TİNÇEL scholarship for Research Assistants for Studies Abroad
- SW REDI Bootcamp 2014, Space Weather Prediction: Consequences on Earth, NASA Goddard Space Flight Center, 03.06.2014-13.06.2014
- Heliophysics Summer School 2012: Heliophysical Exploration, UCAR, Boulder, CO. 31.05.2012-07.06.2012.

- CISM Summer School 2009: Space Weather Phenomena, Consequences, and Modeling (or Reality, Harsh Reality, and Virtual Reality), Boston University, Boston, MA. July 20 – July 31, 2009.
- Graduation with 1st place from ITU Meteorological Engineering Department, 2006.
- High Honor Awards (2004, 2005, 2006)

PUBLICATIONS, PRESENTATIONS AND PATENTS ON THE THESIS:

1. **Kalafatoglu Eyiguler, E.C.**, Shim, J.S., Kuznetsova, M.M., Kaymaz, Z., Bowman, B. R., Codrescu, M. V., Solomon, S. C., ..., and Sutton, E. K., (2018). Quantifying the storm-time thermospheric neutral density variations using model and observations. Submitted to *Space Weather*. JULY 2018.
2. **Kalafatoglu Eyiguler, E. C.**, Kaymaz, Z., Frissell, N. A., Ruohoniemi, J. M., and Rastätter, L. (2018). Investigating upper atmospheric Joule heating using cross-combination of data for two moderate substorm cases. *Space Weather*, 16. <https://doi.org/10.1029/2018SW001956>.
3. **Eyigüler, E.C.K.** and Kaymaz, Z. (2017). Magnetic and Electric Field Variations during Geomagnetically Active Days over Turkey. *Advances in Space Research*. doi:10.1016/j.asr.2017.07.019.
4. **Eyiguler, E. C. K.**, Moral, A. C., Kaymaz, Z. and Caglar, R. (2015). Geomagnetically Induced Current (GIC) observations of geomagnetic storms in Turkey. In *Recent Advances in Space Technologies (RAST), 2015 7th International Conference*, on (pp. 501-503). IEEE.
5. Ja Soon Shim, Lutz Rastaetter, Maria M. Kuznetsova, **Emine C Kalafatoglu** and Yihua Zheng (2015). Recent assessment of the predictive capability of IT models at the Community Coordinated Modeling Center, *14th International Ionospheric Effects Symposium (IES2015)*, VA, USA.
6. **Kalafatoglu, E. C.**, and Kaymaz, Z. (2013, June). Neutral wind comparisons during substorms using TIEGCM and GITM models. In *Recent Advances in Space Technologies (RAST), 2013 6th International Conference* on (pp. 761-764). IEEE.
7. **Kalafatoglu, E.C.**, and Kaymaz, Z (2011, June). Spatial Variation of Joule Heating and its Relationship with the Motion of Polar Cap Boundary, In *Recent Advances in Space Technologies (RAST), 2011 5th International Conference* on (pp. 581-583). IEEE.
8. **Kalafatoglu E.C.**, Kaymaz, Z. . Quantitative assessment of the neutral wind contribution to Joule heating during geomagnetic storms, *CEDAR Workshop*, Seattle, USA, June 21-25, 2015. (poster)
9. **Kalafatoglu E.C.**, Kaymaz, Z. Effect of the neutral wind on Joule heating production rate estimated by different ionospheric models. *GEM Workshop*, Snowmass-CO, USA, June 14-19, 2015. (poster)
10. **Kalafatoglu E.C.**, Shim, Ja Soon, Kuznetsova, Maria M. and Kaymaz, Z. Quantitative Assessment of the Storm Time Performances of IT Models for

- the Orbit Averaged Neutral Densities on CHAMP orbit, *CEDAR Workshop*, Seattle, USA, June 22-26, 2014 (poster).
11. **Kalafatoglu E.C.**, Shim, Ja Soon, Kuznetsova, Maria M. and Kaymaz, Z. Towards a New Metric for Satellite Drag Studies: Neutral Density Validation, *CCMC Workshop*, Annapolis, MD, USA, March 31-April 04, 2014 (sözlü sunum).
 12. **Kalafatoglu E.C.**, Shim, Ja Soon, Kuznetsova, Maria M. and Kaymaz, Z. Quantifying the Storm Effects on the Modeled Neutral Density Variations on the CHAMP Satellite Track: Progress since the Mini-GEM, *Mini GEM-CEDAR Workshop*, Denver, CO, USA, April 07, 2014 (sözlü sunum).
 13. **Kalafatoglu E.C.**, Shim, Ja Soon, Kuznetsova, Maria M. and Kaymaz, Z. Quantifying the Storm Effects on the Thermospheric Neutral Density Using Orbital Averages on CHAMP Satellite Track, *Space Weather Workshop*, Denver, CO, USA, April 08-11, 2014 (poster).
 14. **Kalafatoglu, E.** & Kaymaz, Z. (2013, December). Investigation of Neutral Wind Effects on the Global Joule Heating Rate Using MHD and TI Models. In AGU Fall Meeting Abstracts. (poster)
 15. **Kalafatoglu E.C.**, Shim, Ja Soon, Kuznetsova, Maria M. and Kaymaz, Z. Quantifying the Storm Impact on the modeled Neutral Density Variations on the CHAMP satellite track, *Mini-GEM Workshop*, San Francisco, USA, December 08, 2013 (sözlü sunum).
 16. **Kalafatoglu, E.C.** & Kaymaz, Z. (2013, April). On the Role of Hall and Pedersen Conductivities in Determination of Ionospheric Joule Heating. In *EGU General Assembly Conference Abstracts (Vol. 15, p. 8875)*. (poster)
 17. **Kalafatoglu, E.C.**, Kaymaz, Z., Frissell, N.A., and Ruohoniemi, J.M. Ionospheric Dynamics During March 8, 2008 Substorms Using SuperDARN and MHD Models, *AOGS-AGU Joint Assembly*, Singapore, August 13-17, 2012. (poster)
 18. **Kalafatoglu, E.C.**, Kaymaz, Z., Frissell, N.A., Ruohoniemi, J.M and Rastaetter, L. A Comparative Study of Upper Atmospheric Joule Heating, *Geospace Environment Modeling (GEM-2012)*, Snowmass, Colorado, June 17-22, 2012. (poster)
 19. **Ceren Kalafatoglu, E.**, Kaymaz, Z., and Ruohoniemi, J. M. (2010, May). Estimating Joule Heating using Different Methods. In *EGU General Assembly Conference Abstracts (Vol. 12, p. 2943)*. (sözlü sunum)

OTHER PUBLICATIONS, PRESENTATIONS AND PATENTS:

1. *Meteoroloji/Atmosferimizi Anlamak, Bölüm adı: (Küresel Rüzgarlar)* (2015). **Eyigüler E.C.** Nobel Yayınevi, Editör: Kadioğlu Mikdat, Çakır Sedef, Türkçe (Book Translation), (Yayın No: 2272312)
2. *Meteoroloji/Atmosferimizi Anlamak, Bölüm adı: (Atmosferi Gözlemlemek)* (2015). **Eyigüler E.C.**, Sedef Çakır, Nobel Yayınevi, Editör: Kadioğlu Mikdat, Çakır Sedef, Türkçe (Book Translation), (Yayın No: 2272008)
3. **Kalafatoglu E.C.**, Kaymaz, Z., Moral, A.C., Çağlar, R., Elektrik ve Manyetik Alan Sinyalleri Kullanarak Yıldırım ve Şimşek Olaylarının Belirlenmesi, *ATMOS, 7th Atmospheric Science Symposium*, Istanbul Technical University, TR, 27-29 April 2015.
4. **Eyigüler, E.C.**, Ionosphere and Thermosphere (Basic Structure), Student Tutorials, *Geospace Environment Modeling (GEM) Workshop*, Portsmouth, Virginia, USA, June 15-20, 2014.
5. Moral, A.C., Kaymaz, Z. and **Kalafatoglu, E.C.**, Mid-latitude Electron Density Variations Under Magnetospheric Substorm Conditions as Determined From Istanbul Dynasonde Observations, *AOGS 2014*, Sapporo, Japan 28 July - 01 Aug 2014 (poster).
6. Kaymaz, Z. and **Kalafatoglu, E.C.**, İTÜ *Space Weather Lab* and CCMC Possible Collaborative Works, CCMC Workshop, Annapolis, MD, USA, March 31-April 04, 2014. (sözlü sunum).
7. Moral, A.C., Kaymaz, Z., Katırcıoğlu, F.T., **Kalafatoglu, E.C.**, and Zabolin N. Variations in mid-latitude ionospheric electron density using Istanbul Dynasonde observations", 2013, *CAWSES II (Climate and Weather of the Sun-Earth System II) Symposium*, Nagoya, Japan, November 18- 22, 2013 (poster).
8. Moral, A. C., **Eyiguler, E. C. K.** & Kaymaz, Z. (2013, June). Sudden Ionospheric Disturbances and their detection over Istanbul. In *Recent Advances in Space Technologies (RAST), 2013 6th International Conference* on (pp. 765-768). IEEE.
9. **Kalafatoglu E.C.** and Kaymaz, Z , Magnetospheric Energy Budget During Geomagnetic Storms: A Case Study, *ATMOS, 5th Atmospheric Science Symposium*, Istanbul Technical University, TR, 27-29 April, 2013.
10. **Kalafatoglu, E.C.**, Kaymaz, Z., Koçak, K. Manyetosferik Enerji Süreçlerinde Deterministik Kaos Rolünün İncelenmesi, *Proceedings of IV. Ulusal Havacılık Ve Uzay Konferansı (UHUK-2012)*, Hava Harp Okulu, Yeşilyurt, Istanbul, 12-14 Eylül 2012.
11. **Kalafatoglu, E.C.** and Kaymaz, Z., 2011. Estimation of the Change in Convection Using WRF and Statistical Fitting Methods during 11 August 1999 Solar Eclipse, *OSTIV Meteorological Panel*.
12. **Kalafatoglu, E.C.** and Kaymaz, Z. Characteristics of Magnetospheric Substorms From Case Studies, *Ankara International Aerospace Conference*, 2009, Ankara, Türkiye.

13. **Kalafatoglu, E. C.**, Kaymaz, Z., Angelopoulos, V. & Sibeck, D. G. (2009, April). On the Substorm-Upper Atmospheric Joule Heating using THEMIS Observations: A Case Study. In *EGU General Assembly Conference Abstracts* (Vol. 11, p. 8140).
14. **Kalafatoglu, E. C.**, Kaymaz, Z. & Tan, E. (2007, June). August 11, 1999 solar eclipse over Turkey and associated effects. In *Recent Advances in Space Technologies, 2007. RAST'07. 3rd International Conference on* (pp. 50-53). IEEE.





